



Universität
Zürich ^{UZH}

Physik-Institut



Annual Report
April 2014 - March 2015



**Universität
Zürich** ^{UZH}

Physik-Institut

Annual Report

April 2014 - March 2015

Front picture: the team that re-installed the CMS barrel pixel detector after maintenance work during the LHC upgrade (Sec. 11).

From left to right: Roland Horisberger (PSI), Jennifer Ngadiuba (UZH), Wolfram Erdmann (PSI), Lea Caminada (UZH), Nicola Bacchetta (Padova), Deborah Pinna (UZH), Silvan Streuli (PSI), Benedikt Vormwald (Uni Hamburg), Annapaola De Cosa (UZH), Willi Bertl (PSI), and Danek Kotlinski (PSI).

Picture on the back: one half of the barrel pixel detector after re-installation in CMS.
(Photo's by Michael Hoch)

Secretariat	044 635 5721	sekretariat@physik.uzh.ch
Prof. L. Baudis	044 635 5777	lbaudis@physik.uzh.ch
Prof. F. Canelli	044 635 5784	canelli@physik.uzh.ch
Prof. J. Chang	044 635 5748	johan.chang@physik.uzh.ch
Prof. V. Chiochia	022 767 6041	vincenzo.chiochia@cern.ch
Prof. H.-W. Fink	044 635 5801	hwfink@physik.uzh.ch
Prof. T. Gehrman	044 635 5818	thomas.gehrman@physik.uzh.ch
Prof. G. Isidori	044 635 5751	gino.isidori@physik.uzh.ch
Prof. H. Keller	044 635 5748	keller@physik.uzh.ch
Prof. B. Kilminster	044 635 5802	bjk@physik.uzh.ch
Prof. J. Osterwalder	044 635 5827	osterwal@physik.uzh.ch
Prof. S. Pozzorini	044 635 6014	pozzorin@physik.uzh.ch
Prof. A. Schilling	044 635 5791	schilling@physik.uzh.ch
Prof. N. Serra	044 635 5725	nicola.serra@physik.uzh.ch
Prof. A. Signer	056 310 3661	adrian.signer@psi.ch
Prof. D. Wyler	044 635 5817	wyler@physik.uzh.ch
Prof. U.D. Straumann	044 635 5768	strauman@physik.uzh.ch

The annual reports are available on the internet: <http://www.physik.uzh.ch/reports.shtml>.

Preface

This report summarizes past year's achievements of the Physik-Institut's sixteen research groups, covering both experimental and theoretical physics. Experimental activities include the physics of biological systems, nanometer structures and surface physics, fundamental properties of materials and high-temperature superconductivity as well as accelerator and non-accelerator based elementary- and astro-particle physics, while theoretical research concentrates on precision calculations of QCD processes and on fundamental aspects of elementary particle physics.

End of July 2014 Prof. Hugo Keller, a long-term member of the institute, retired. As an expert on magnetic properties of superconducting materials he used a variety of experimental techniques, such as μ SR and torque magnetometry, to improve our understanding of high- T_C superconductivity and other magnetic features in solids. Hugo is a gifted teacher, as for instance his lectures on modern physics are highly appreciated by the students. Hugo served as institute director for eight years and was member of numerous faculty and scientific committees. A detailed presentation of Hugo's scientific career follows further below.

In June 2014 Prof. Gino Isidori joined our department, working in the field of theoretical elementary particle physics. His research activities include dynamical flavor models, the search for physics beyond the standard model and the stability of the standard model Higgs potential and are summarized in Sec. 1.

In January 2015 Prof. Johan Chang joined our department. A new laboratory for research in hard condensed matter is being set-up, where his group will investigate fluctuations of correlated superconductors with thermoelectric experiments. It is planned to construct electronic surface transport instrumentation under ultra-high-vacuum conditions, with the possibility to dope with alkali-molecules. Furthermore, large-scale neutron and synchrotron facilities will be used to explore quantum matter physics. Phenomena such as high-temperature superconductivity and unconventional charge-density-wave ordering will be studied in transition-metal oxides.

We hosted no less than four assistant professors elected and funded by the Swiss National Science Foundation (SNF). Three of them received ERC - Starting or Consolidator Grants as additional support for their research activities.

The institute's 155 employees from 25 countries achieved an impressive number of results, documented in no less than 282 original publications, 216 seminars and presentations on international scientific conferences. Nineteen PhD, seven master, and ten bachelor theses have been completed.

Members of the department participate in many scientific organizations. These include the national research council, research committees of the Paul Scherrer Institut and advisory boards and panels of numerous international research institutions. Our professors also contribute to the academic self administration of the university and take part in many national and international search committees for new professors.

About 900 students have to be taught physics at any point in time. Students of the medical faculty and those of our science faculty in biology, chemistry, geography and mathematics learn about basic physics. We honor the traditional Humboldtian concept of unification of teaching and research, so all our physicists are involved in teaching. They are supported by typically fifteen undergraduate physics students and some senior physicists from other institutions.

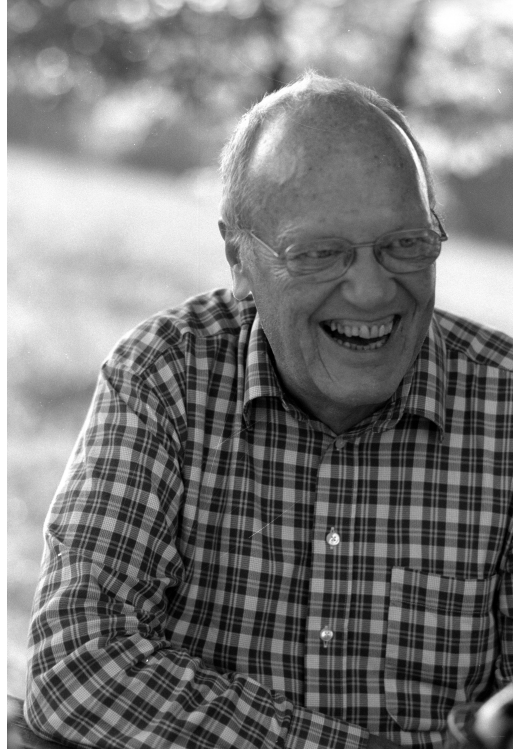
Following up on the G-Node summer school held in our institute in September 2013, in January 2015 again a one-week intensive course on advanced scientific programming with Python was given by Nicola Chiapolini, Christian Elsasser and Roman Gredig, attracting 32 participants from 14 institutes, mainly of ETHZ and UZH. Lectures on modern programming techniques were interleaved with practical exercises. The course was a great success and will be repeated in summer 2015.

Members of the institute actively contributed to information events for future students, gave presentations at schools and guided children through our labs. The department participates regularly in the European Masterclass for Particle Physics. There were 25 outreach events organized, corresponding to more than 700 working hours in total.

The success of our research and our international visibility is based to a large extent on the excellent technical infrastructure (mechanical and electronics workshop, information technology) and highly qualified and strongly motivated technical experts. This allows us to construct state-of-the-art laboratory equipment, and develop novel experimental methods further pushing the technical limits. Our success in research and teaching would not be possible without our reliable and efficient administrative staff.

Zürich, June 2015

Prof. Dr. Ueli Straumann



Retirement Prof. Hugo Keller

Hugo Keller was born in 1949 in Aarau. He studied Physics at the ETH Zürich before joining the group of Prof. Kündig at our institute, which was located in the Schönberggasse in those years.

In 1977 Hugo obtained his PhD with a thesis on *Phase transitions in low-dimensional magnetic systems*. In the following Hugo became a research associate in biophysics with Prof. Debrunner and Prof. Frauenfelder at the University of Illinois at Urbana-Champaign, where he studied the dynamics of iron in biomolecules using Mössbauer spectroscopy.

Even when several assistant professorships were offered to him in the US, Hugo was happy to accept the invitation to return to our institute as senior lecturer and research scientist, working on phase transitions with Mössbauer-spectroscopy techniques.

After his habilitation in 1984 Hugo started a very successful μ SR (muon spin rotation) research program at SIN (now part of the Paul Scherrer Institute) in Villigen.

In recognition of his forefront research together with Nobel prize winner Karl Alex Müller, his dedication to teaching and his service to the University, he became associate professor in 1995, and full professor in 2001.

Hugo Keller's research in solid-state physics, be it in μ SR or in other fields such as torque magnetometry or the study of isotope effects in superconductors, resulted in over 325 published articles which were well-received in the science community as demonstrated by numerous plenary talks at important international conferences.

Hugo contributed a lot to the institute and the faculty life, as the institute's director from 2003 to 2011, in the Fakultätsausschuss, or in his numerous and legendary lectures within the Kinderuniversität and at other instances, such as the *Tag der offenen Tür* in 2004, which he organized together with Paul Ward and John Robinson.

Hugo served on several scientific committees and is still an Associate Editor of the Journal on Superconductivity and Novel Magnetism. He was also very active in the supervision of the physics education at Swiss high schools.

Since August 2014, Hugo Keller is officially retired, but he agreed to teach Introductory Quantum and Atomic Physics for a few more semesters.

We thank Hugo Keller for everything he did for the institute, the students, the faculty and the university, and wish him many carefree and happy years as Professor Emeritus.

Personnel

Scientific personnel

Thea Klæboe	Årrestad	Sec. 11	PD Dr. Massimiliano	Grazzini	Sec. 1
Mirco	Ackermann	Sec. 16	Prof. Thomas	Greber	Sec. 14
PD Dr. Christof	Aegerter	Sec. 16	Roman	Gredig	Sec. 7
Dr. Hubertine	Aegerter-Wilmsen	Sec. 16	Dr. Michael	Greif	Sec. 14
Dr. Jonathan	Anderson	Sec. 10	Dr. Admir	Greljo	Sec. 1
Daniel	Assmann	Sec. 16	Dr. Henrik	Grundmann	Sec. 13
Francesco	Atzeni	Sec. 16	Dr. Zurab	Guguchia	Sec. 12
Simone	Balmelli	Sec. 2	Catalin	Hanga	Sec. 1
Peter	Barrow	Sec. 4	Dr. Adrian	Hemmi	Sec. 14
Prof. Laura	Baudis	Sec. 3, 4	Dr. Matthias	Hengsberger	Sec. 14
Giovanni	Benato	Sec. 3	Dr. Andreas	Hinzmann	Sec. 11
Dr. Markus	Bendele	Sec. 12	Dr. Alexander	Huss	Sec. 1
Carlo	Bernard	Sec. 14	Dr. Cédric	Huwylar	Sec. 2
Dr. Roland	Bernet	Sec. 10	Dr. Tomas	Hreus	Sec. 11
Marzia	Bordone	Sec. 1	Agnieszka	Ilnicka	Sec. 1
Dr. Ruxandra	Bondarescu	Sec. 2	Prof. Gino	Isidori	Sec. 1
Dr. Sophia	Borowka	Sec. 1	Prof. Philippe	Jetzer	Sec. 2
Espen	Bowen	Sec. 10	Matthieu	Jaquier	Sec. 1
Dr. Albert	Bursche	Sec. 10	Dr. Stefan	Kallweit	Sec. 1
Dr. Lea	Caminada	Sec. 11	Dominik	Kara	Sec. 1
Prof. Florencia	Canelli	Sec. 6, 11	Dr. Hafiza Rizwana	Kausar	Sec. 2
Dr. Fabio	Cascioli	Sec. 1	Dr. Arne	Keller	Sec. 16
Dr. Luca	Castiglioni	Sec. 14	Prof. Hugo	Keller	Sec. 12
Prof. Johan	Chang	Quantum Matter	Gaudenz	Kessler	Sec. 4
Dr. Nicola	Chiapolini	Sec. 10	Prof. Benjamin	Kilminster	Sec. 5, 11, 9
Prof. Vincenzo	Chiochia	Sec. 11	Dr. Alexander	Kish	Sec. 3, 4
Dr. Marcin	Chrzyszcz	Sec. 10	Pavlo	Kliuiev	Sec. 14
Dr. Huanyao	Cun	Sec. 14	Aram	Kostanyan	Sec. 14
Dr. James	Currie	Sec. 1	Rafael	Küng	Sec. 2
Dr. Annapaola	de Cosa	Sec. 11	Valère	Lambert	Sec. 11
Lorenzo	de Vittori	Sec. 2	Dr. Gabriel	Landolt	Sec. 14
Dr. Biplab	Dey	Sec. 10	Flavio	Lanfranconi	Sec. 16
David	Dreher	Sec. 16	Dr. Clemens	Lange	Sec. 11
Dominik	Eder	Sec. 16	Dr. Tatiana	Latychevskaia	Sec. 15
Dr. Christian	Elsasser	Sec. 10	Junhui	Liao	Sec. 5
Dr. Andreas	Engel	Sec. 13	Dr. Jonas	Lindert	Sec. 1
Dr. Conrad	Escher	Sec. 15	Federica	Lionetto	Sec. 10
Prof. Hans-Werner	Fink	Sec. 15	Dr. Jean-Nicolas	Longchamp	Sec. 15
Dr. Stefan	Förster	Sec. 14	Dr. Adriano	Lo Presti	Sec. 1
Dr. Domenico	Franco	Sec. 4	Marianna	Lorenzo	Sec. 15
Dr. Arno	Gadola	Sec. 6	Peter	Lowdon	Sec. 1, 10
Camilla	Galloni	Sec. 11	Dr. Philipp	Maierhöfer	Sec. 1
Dr. Michelle	Galloway	Sec. 4	Archana	Mallavalli	Sec. 16
Alsu	Gazizulina	Sec. 13	Dr. David	Marzocca	Sec. 1
Prof. Thomas	Gehrmann	Sec. 1	Andrea	Mauri	Sec. 10
Dr. Giulia	Ghielmetti	Sec. 16	Dr. Gerson	Mette	Sec. 14
Elena	Graverini	Sec. 9, 10	Daniel	Mayani Paras	Sec. 4

Dr. Elisa Miniussi	Sec. 14
Irshad Mohammed	Sec. 2
Dr. Claude Monney	Sec. 14
Niccolo Moretti	Sec. 1
Dr. Katharina Müller	Sec. 10
Jan Niehues	Sec. 1
Jennifer Ngadiuba	Sec. 11
Prof. Jürg Osterwalder	Sec. 14
Deniz Gizem Oeztürk	Sec. 1
Payam Pakarha	Sec. 4
Dr. Andreas Papaefstathiou	Sec. 1
Dr. Monalisa Patra	Sec. 1
Andrea Patteri	Sec. 1
Lionel Philippoz	Sec. 2
Francesco Piastra	Sec. 4
Deborah Pinna	Sec. 11
Prof. Stefano Pozzorini	Sec. 1
Sahil Puri	Sec. 16
Dirk Rathlev	Sec. 1
Dr. Peter Robmann	Sec. 5,7,8,11
PD Dr. Prasenjit Saha	Sec. 2
Daniel Salerno	Sec. 11
Mirna Saliba	Sec. 14
Hayk Sargsyan	Sec. 1
Andreas Schärer	Sec. 2
Prof. Andreas Schilling	Sec. 13
Timo Schmidt	Sec. 1
Dr. Jale Schneider	Sec. 16
Dr. Marek Schönherr	Sec. 1
Adrian Schuler	Sec. 14
Dr. Lara Selvaggi	Sec. 16
Prof. Nicola Serra	Sec. 9,10
Prof. Adrian Signer	Sec. 1
Roland Stania	Sec. 14
Dr. Olaf Steinkamp	Sec. 10
Dr. Evelyn Stilp	Sec. 12
Dr. Barbara Storaci	Sec. 9,10
Prof. Ulrich Straumann	Sec. 6,7,10
Dr. Lorenzo Tancredi	Sec. 1
Dr. Silvia Taroni	Sec. 11
Dr. Alessandro Torre	Sec. 1
Dr. Paolo Torrielli	Sec. 1
Marco Tresch	Sec. 10
Dr. Severine Urdy	Sec. 16
Dr. Andries van der Schaaf	Sec. 8
Dr. Mauro Verzetti	Sec. 11
Andreas Visconti	Sec. 1
Dr. Achim Vollhardt	Sec. 6,10,18
Dr. Fabian von Rohr	Sec. 13
Dr. Zvonimir Vlah	Sec. 1

Manuel Walter	Sec. 3
Dr. Rasmus Westerström	Sec. 14
Dr. Yuehuan Wei	Sec. 4
Andreas Weiden	Sec. 10
Erich Weihs	Sec. 1
Flavio Wicki	Sec. 15
Dr. Marius Wieseemann	Sec. 1
Julien Wulf	Sec. 4
Prof. Daniel Wyler	Sec. 1
Dr. Yong Yang	Sec. 11
Wolf-Dietrich Zabka	Sec. 14
Xiaofu Zhang	Sec. 13

Technical and administrative personnel

Dr. Carlos Abellan Beteta	Sec. 10
Kurt Bösiger	Sec. 17
Tiziano Crudeli	Technical support
Daniel Florin	Sec. 18,6
Dario Gabrielli	Sec. 17
Carmelina Genovese	Secretariat
Ruth Halter	Secretariat
Andreas James	Sec. 3,4
Thomas Kälin	Sec. 14
Hanspeter Koch	Lecture demonstrations
Bruno Lussi	Sec. 17
Reto Maier	Sec. 17
Brandon Markwalder	Sec. 17
Esther Meier	Secretariat
Lucien Pauli	Lecture demonstrations
Jan Ten Pierick	Sec. 2
Monika Röllin	Secretariat
Sandra Saornil Gamarra	Sec. 10
Marcel Schaffner	Sec. 17
Silvio Scherr	Sec. 17
Regina Schmid	Secretariat
Andrea Schneider	IPhO
Stefan Siegrist	Sec. 13,12
Peter Soland	Sec. 18
Stefan Steiner	Sec. 6,10
Jonas Verges	Sec. 15
Pascal Weyeneth	Sec. 17
David Wolf	Sec. 18

Contents

Physics of Fundamental Interactions and Particles	1
1 Theory of Elementary Particles	1
2 Astrophysics and General Relativity	6
3 GERDA: Neutrinoless Double Beta Decay in Ge	9
4 Cold Dark Matter Search with XENON and DARWIN	13
5 DAMIC: search for dark matter using CCD detectors	20
6 Very High Energy Gamma Ray Astronomy with CTA	24
7 Search for the rare decay $\mu^+ \rightarrow e^+ e^- e^+$	28
8 The $\pi^+ \rightarrow e^+ \nu_e / \pi^+ \rightarrow \mu^+ \nu_\mu$ branching ratio	31
9 Particle Physics with the proposed SHiP experiment	34
10 Particle Physics with LHCb	37
11 Particle physics with the CMS experiment at CERN	42
Condensed Matter Physics	52
12 Superconductivity and Magnetism	52
13 Phase transitions and superconducting photon detectors	55
14 Surface Physics	59
15 Physics of Biological Systems	64
16 Disordered and Biological Soft Matter	70
Infrastructure and Publications	75
17 Mechanical Workshop	75
18 Electronics Workshop	80
19 Publications	82

1 Theory of Elementary Particles

M. Bordone, S. Borowka, F. Cascioli, J. Currie, T. Gehrmann, M. Grazzini, A. Greljo, A. Ilnicka, G. Isidori, M. Jaquier, S. Kallweit, D. Kara, J. Lindert, A. Lo Presti, P. Lowdon, P. Maierhöfer, D. Marzocca, N. Moretti, J. Niehues, G. Oeztürk, A. Papaefstathiou, M. Patra, A. Patteri, S. Pozzorini, D. Rathlev, H. Sargsyan, M. Schönherr, A. Signer, L. Tancredi, A. Torre, P. Torrielli, A. Visconti, E. Weihs, M. Wiesemann, D. Wyler

in collaboration with: Durham University, INFN Firenze, University of Buenos Aires, Freiburg University, Mainz University, INFN Milano, MPI Munich, INFN Padova, Peking University, Oxford University, INFN Roma, SLAC, ETH Zürich, Desy Hamburg, TU Dresden

The particle theory group at the Physik-Institut is primarily involved in research projects dealing with the interpretation of data from high energy particle colliders. Topics are precision calculations of benchmark observables, simulation of full collider events, identification of optimal observables for searches and measurements, physics beyond the Standard Model, as well as development of calculational techniques.

We summarize some highlights of last year's research below.

1.1 Vector boson pair production at NNLO

The Tevatron experiments have measured cross sections for vector-boson pair production at invariant masses beyond those probed at LEP2, setting limits on anomalous couplings, and this program is continued at the LHC [1].

The study of the production of vector-boson pairs (VV') is relevant for physics both within and beyond the Standard Model (SM). First of all, any deviation of the vector boson trilinear couplings from the structure predicted by $SU(2) \otimes U(1)$ gauge invariance would be a signal of new physics. At the same time vector boson pairs provide a dominant background in new physics searches. Although the Higgs resonance was observed well below the WW and ZZ thresholds, off-shell WW and ZZ backgrounds must be taken into account when extracting the Higgs signal and width.

Until just one year ago, theoretical predictions for VV' production were essentially limited to next-to-leading order (NLO) in perturbative QCD. The bottleneck has been the knowledge of the relevant two-loop amplitudes. At next-to-next-to-leading order (NNLO) tree-level scattering amplitudes with two additional (unresolved) partons, one-loop amplitudes with one additional parton, and one-loop-squared and two-loop corrections to the Born subprocess $q\bar{q} \rightarrow VV'$ must be evaluated.

Recently, a major step forward was made with the evaluation of all two-loop planar [2, 3] and non-planar [4, 5] master integrals relevant for the production of off-shell vector boson pairs, and the calculation of the corresponding helicity amplitudes has been completed [6]. Still, the computation of the NNLO corrections is non-trivial. Infrared (IR) singularities at intermediate stages of the calculation forbid straightforward numerical techniques. To handle and cancel these singularities the q_T subtraction formalism [7] is well suited since it is fully developed to work in the hadronic production of heavy colorless final states.

In the following we present results for ZZ [8] and WW [9] production in pp collisions with \sqrt{s} ranging from 7 to 14 TeV. The required tree-level and one-loop amplitudes were obtained with the OPENLOOPS [10] generator, which employs the Denner-Dittmaier algorithm for the numerical evaluation of one-loop integrals and implements a fast numerical recursion for the calculation of NLO scattering amplitudes within the SM.

As for the EW couplings, we use the so-called G_μ scheme, with $G_F = 1.16639 \times 10^{-5} \text{ GeV}^{-2}$, $m_W = 80.399 \text{ GeV}$ and $m_Z = 91.1876 \text{ GeV}$. Additional input, $m_t = 173.2 \text{ GeV}$ and $m_H = 125 \text{ GeV}$, enters through the loop-induced gluon fusion contribution. We use the MSTW 2008 [11] sets of parton distributions, with densities and α_S evaluated at each corresponding order (i.e., we use $(n+1)$ -loop α_S at $N^n\text{LO}$, with $n = 0, 1, 2$), and we consider $N_f = 5$ massless quark flavors. The default renormalization (μ_R) and factorization (μ_F) scales are set to $\mu_R = \mu_F = m_Z$.

1.1.1 ZZ

The resulting LO, NLO and NNLO ZZ cross sections as a function of \sqrt{s} are shown in Fig. 1.1. For comparison, we also show the NLO result supplemented with the loop-induced gluon fusion contribution ("NLO+gg") com-

puted with NNLO parton distribution functions (PDFs). The NLO corrections increase the LO result by about 45%. The impact of NNLO corrections with respect to the NLO result ranges from 11% ($\sqrt{s} = 7$ TeV) to 17% ($\sqrt{s} = 14$ TeV), see lower panel in Fig. 1.1. Using NNLO PDFs throughout, the gluon fusion contribution exhausts between 58% and 62% of the full NNLO correction. The theoretical predictions are compared with the ATLAS and CMS values measured at $\sqrt{s} = 7$ TeV and $\sqrt{s} = 8$ TeV. The experimental results still have relatively large uncertainties and are compatible with both the NLO and NNLO predictions with the possible exception of the ATLAS measurement at $\sqrt{s} = 8$ TeV which seems to prefer a lower cross section. Such comparisons should be interpreted with care since the LHC experiments base their ZZ production cross section on four-lepton final states with dilepton invariant mass around the Z boson mass: the contribution from far off-shell Z bosons is excluded. Furthermore, EW corrections are not included in our calculation and are expected to lower the inclusive cross section.

In Table 1.1 we list the LO, NLO and NNLO cross sections and scale uncertainties, evaluated by varying μ_R and μ_F simultaneously and independently in the range $0.5m_Z < \mu_R, \mu_F < 2m_Z$ with the constraint $0.5 < \mu_F/\mu_R < 2$. Scale uncertainties are $O(\pm 3\%)$ for both NLO and NNLO. Note that the NLO scale uncertainty does not cover the NNLO effect which is no surprise since the gluon fusion channel, which provides a rather large contribution, opens up at NNLO only.

1.1.2 WW

Contrary to what happens in ZZ production, the higher-order QCD corrections to WW production include partonic channels with b -quarks in the final state, which leads to a subtle interplay between WW and top production. In the five-flavor-number scheme (5FNS), where b -quarks are included in the parton distribution functions with their mass set to zero, the presence of real b -quark emission is crucial in order to cancel collinear singularities that arise from $g \rightarrow b\bar{b}$ splittings in the virtual corrections. At the same time, the occurrence of Wb pairs in the real-emission matrix elements induces top-quark resonances that lead to a problematic contamination of WW production. This problem can be circumvented in the four-flavor scheme (4FNS) where, since b -quarks are massive and collinear divergences are not present, we can define top-free WW production by simply omitting b -quark emissions.

We present LO, NLO and NNLO predictions for $pp \rightarrow W^+W^-X$ in the 4FNS with \sqrt{s} ranging from 7 to 14 TeV. We use the MSTW2008 sets of PDFs with four active flavors. The default renormalization (μ_R) and factorization

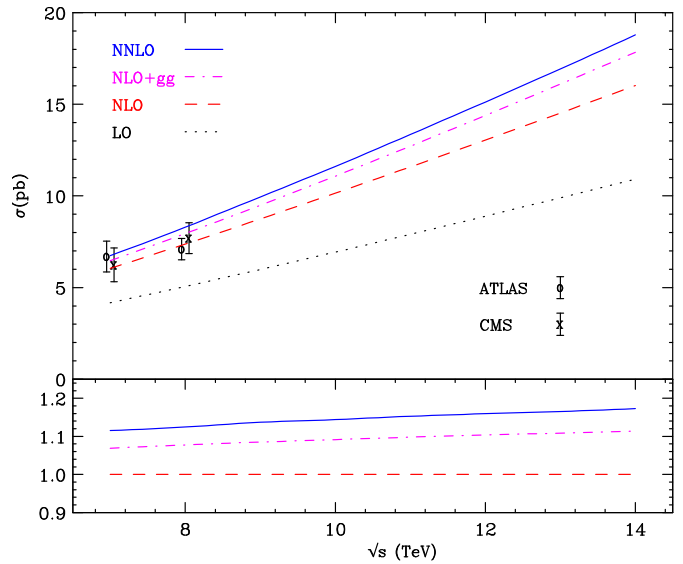


FIG. 1.1 –

Top: ZZ cross section at LO, NLO, NLO+gg and NNLO as a function of \sqrt{s} . The ATLAS and CMS results at $\sqrt{s} = 7$ TeV and $\sqrt{s} = 8$ TeV are shown for comparison.

Bottom: NNLO and NLO+gg results normalized to the NLO prediction.

TAB. 1.1 –

Inclusive cross section for ZZ production at the LHC at LO, NLO and NNLO with $\mu_F = \mu_R = m_Z$. The uncertainties are obtained by varying the renormalization and factorization scales in the range $0.5m_Z < \mu_R, \mu_F < 2m_Z$ with the constraint $0.5 < \mu_F/\mu_R < 2$.

\sqrt{s} (TeV)	σ_{LO} (pb)	σ_{NLO} (pb)	σ_{NNLO} (pb)
7	$4.167^{+0.7\%}_{-1.6\%}$	$6.044^{+2.8\%}_{-2.2\%}$	$6.735^{+2.9\%}_{-2.3\%}$
8	$5.060^{+1.6\%}_{-2.7\%}$	$7.369^{+2.8\%}_{-2.3\%}$	$8.284^{+3.0\%}_{-2.3\%}$
9	$5.981^{+2.4\%}_{-3.5\%}$	$8.735^{+2.9\%}_{-2.3\%}$	$9.931^{+3.1\%}_{-2.4\%}$
10	$6.927^{+3.1\%}_{-4.3\%}$	$10.14^{+2.9\%}_{-2.3\%}$	$11.60^{+3.2\%}_{-2.4\%}$
11	$7.895^{+3.8\%}_{-5.0\%}$	$11.57^{+3.0\%}_{-2.4\%}$	$13.34^{+3.2\%}_{-2.4\%}$
12	$8.882^{+4.3\%}_{-5.6\%}$	$13.03^{+3.0\%}_{-2.4\%}$	$15.10^{+3.2\%}_{-2.4\%}$
13	$9.887^{+4.9\%}_{-6.1\%}$	$14.51^{+3.0\%}_{-2.4\%}$	$16.91^{+3.2\%}_{-2.4\%}$
14	$10.91^{+5.4\%}_{-6.7\%}$	$16.01^{+3.0\%}_{-2.4\%}$	$18.77^{+3.2\%}_{-2.4\%}$

TAB. 1.2 –

LO, NLO and NNLO cross sections for on-shell W^+W^- production in the 4FNS and reference results for $gg \rightarrow H \rightarrow WW^*$ from Ref. [12].

\sqrt{s} (TeV)	σ_{LO} (pb)	σ_{NLO} (pb)	σ_{NNLO} (pb)	$\sigma_{gg \rightarrow H \rightarrow WW^*}$ (pb)
7	$29.52^{+1.6\%}_{-2.5\%}$	$45.16^{+3.7\%}_{-2.9\%}$	$49.04^{+2.1\%}_{-1.8\%}$	$3.25^{+7.1\%}_{-7.8\%}$
8	$35.50^{+2.4\%}_{-3.5\%}$	$54.77^{+3.7\%}_{-2.9\%}$	$59.84^{+2.2\%}_{-1.9\%}$	$4.14^{+7.2\%}_{-7.8\%}$
13	$67.16^{+5.5\%}_{-6.7\%}$	$106.0^{+4.1\%}_{-3.2\%}$	$118.7^{+2.5\%}_{-2.2\%}$	$9.44^{+7.4\%}_{-7.9\%}$
14	$73.74^{+5.9\%}_{-7.2\%}$	$116.7^{+4.1\%}_{-3.3\%}$	$131.3^{+2.6\%}_{-2.2\%}$	$10.64^{+7.5\%}_{-8.0\%}$

(μ_F) scales are set to $\mu_R = \mu_F = m_W$, and, as done for ZZ production, to assess scale uncertainties they are varied in the range $0.5 m_W < \mu_{R,F} < 2 m_W$ with $0.5 < \mu_F/\mu_R < 2$. In the 4FNS we use the pole mass $m_b = 4.75$ GeV. Our NLO and NNLO predictions involve resonant top quarks and off-shell Higgs bosons where we use $m_t = 173.2$ GeV, $\Gamma_t = 1.443$ GeV, $m_H = 125$ GeV and $\Gamma_H = 4.09$ MeV. Higgs contributions, included via squared one-loop amplitudes in the $gg \rightarrow H^* \rightarrow W^+W^-$ channel, are strongly suppressed since the Higgs boson is off-shell.

In Table 1.2 we present LO, NLO and NNLO predictions for inclusive W^+W^- production in the 4FNS. We see that at 7 (14) TeV the LO predictions receive a positive NLO shift of 53 (58)%, and the NNLO corrections induce a further enhancement by 9 (12)%. This decent perturbative convergence must be relativized, since the scale uncertainty does not decrease significantly when moving from LO to NLO and NNLO. Still, the NNLO corrections exceed the scale uncertainty by about a factor 3.

The fact that the NLO scale variations underestimate higher-order effects can be attributed to the fact that the gluon-gluon partonic channel appears only beyond NLO. The NNLO is the first order at which all partonic channels are contributing. The NNLO scale dependence, which amounts to about 3%, can thus be considered a realistic estimate of the theoretical uncertainty due to missing higher-order effects.

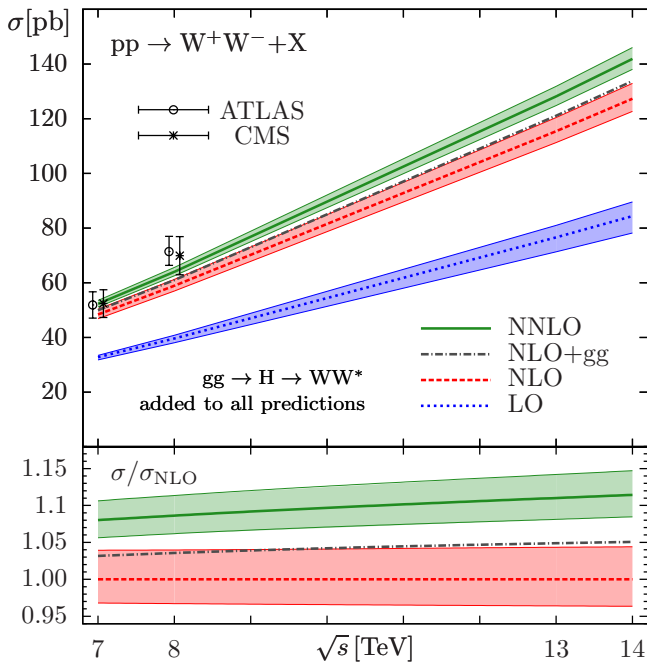


FIG. 1.2 – Top: the on-shell W^+W^- cross section in the 4FNS at LO, NLO, NLO+gg and NNLO combined with $gg \rightarrow H \rightarrow WW^*$ is compared with recent ATLAS and CMS results. Bottom: NNLO and NLO+gg results, normalized to NLO. The bands indicate scale variations.

In Fig. 1.2, theoretical predictions in the 4FNS are compared to CMS and ATLAS measurements at 7 and 8 TeV. For a consistent comparison, our results for on-shell W^+W^- production are combined with the $gg \rightarrow H \rightarrow WW^*$ cross sections reported in Table 1.2. It turns out that the inclusion of the NNLO corrections leads to an excellent description of the data at 7 TeV and decreases the significance of the observed excess at 8 TeV. In the lower frame of Fig. 1.2, predictions and scale variations at NNLO are compared to NLO ones, and also the individual contribution of the $gg \rightarrow W^+W^-$ channel is shown. Using NNLO PDFs throughout, the loop induced gluon fusion contribution is only about 35% of the total NNLO correction.

In the light of the small scale dependence of the 4FNS NNLO cross section, the ambiguities associated with the definition of a top-free W^+W^- cross section might represent a significant source of theoretical uncertainty at NNLO. In Ref. [13] we show that the W^+W^- cross-section can be computed within the 5FNS, through an appropriate subtraction of the top contamination based on the scaling behavior of the (N)NLO cross section in the limit of vanishing top-quark width. The obtained results agree within 2% with those obtained in the 4FNS.

The calculation of the second-order QCD corrections described here was accomplished during the past year in a collaborative effort involving many of the researchers at our institute. The timely completion of this project (well ahead of competing groups) is due to unique synergies in our institute, which pools together high-level competences on many different aspects of precision calculations.

- [1] J. Wang [ATLAS, D0, CDF and CMS Collaborations], Int. J. Mod. Phys. Conf. Ser. **31** (2014) 1460279.
- [2] T. Gehrmann, L. Tancredi and E. Weihs, JHEP **1308** (2013) 070.
- [3] J. M. Henn, K. Melnikov and V. A. Smirnov, JHEP **1405** (2014) 090.
- [4] T. Gehrmann, A. von Manteuffel, L. Tancredi and E. Weihs, JHEP **1406** (2014) 032.
- [5] F. Caola, J. M. Henn, K. Melnikov and V. A. Smirnov, JHEP **1409** (2014) 043.
- [6] T. Gehrmann, A. von Manteuffel and L. Tancredi, arXiv:1503.04812 [hep-ph].
- [7] S. Catani and M. Grazzini, Phys. Rev. Lett. **98** (2007) 222002.
- [8] F. Cascioli, T. Gehrmann, M. Grazzini, S. Kallweit, P. Maierhöfer, A. von Manteuffel, S. Pozzorini and D. Rathlev *et al.*, Phys. Lett. B **735** (2014) 311.
- [9] T. Gehrmann, M. Grazzini, S. Kallweit, P. Maierhöfer, A. von Manteuffel, S. Pozzorini, D. Rathlev and L. Tancredi, Phys. Rev. Lett. **113** (2014) 21, 212001.

- [10] F. Cascioli, P. Maierhöfer and S. Pozzorini, Phys. Rev. Lett. **108** (2012) 111601.
- [11] A. D. Martin, W. J. Stirling, R. S. Thorne and G. Watt, Eur. Phys. J. C **63** (2009) 189.
- [12] S. Heinemeyer *et al.* [LHC Higgs Cross Section Working Group Collaboration], arXiv:1307.1347 [hep-ph].
- [13] T. Gehrmann, M. Grazzini, S. Kallweit, P. Maierhöfer, A. von Manteuffel, S. Pozzorini, D. Rathlev and L. Tancredi, Phys. Rev. Lett. **113** (2014) 21, 212001.

1.2 Differential cross sections for top pair production beyond NLO

At the LHC, top quarks are produced predominantly as ($t\bar{t}$) pairs. A precise theoretical understanding of this process is important both for the determination of the top quark mass and for numerous studies in which the process forms a background. Since top quarks decay almost instantly through $t \rightarrow W^+b$ and $\bar{t} \rightarrow W^-\bar{b}$, with subsequent W decay, they are detected indirectly through their decay products. Hence, for a realistic description it is essential to include the top decay and allow for cuts mimicking the experimental selection procedures.

In Ref. [1] results for fully differential top-pair production have been presented that go beyond a full NLO calculation: approximate NNLO correction terms (denoted by nNLO) in the production of a $t\bar{t}$ -pair have been included. Renormalization-group techniques were applied to determine NNLO terms that are enhanced by logarithms. Near threshold, these terms are expected to dominate and thus give a reliable estimate of the full correction. The precise form of these logarithmic corrections depends on the kinematic situation and several options have been investigated, giving consistent results.

As an example, in Fig. 1.3 two distributions are shown for the 8 TeV LHC. The k_T -cluster algorithm has been applied to define b -jets J_b and as an illustration the following standard cuts on the decay products J_b , l and ν have been applied: $p_T(J_b) > 15$ GeV, $E_T(l) > 15$ GeV and $\cancel{E}_T > 20$ GeV. The comparison of the full NLO result with the approximate NLO result strongly indicates that the nNLO results are a reliable improvement beyond NLO.

- [1] A. Broggio, A. S. Papanastasiou and A. Signer, JHEP **1410** (2014) 98.

1.3 Pseudo observables in Higgs decays

After the discovery phase, Higgs physics has entered the era of precision measurements. Characterizing the particle properties accurately and with minimal theoretical bias, is of utmost importance when investigating the nature of physics beyond the Standard Model. For this reason we have developed a formalism characterizing Higgs decays in generic extensions of the SM with heavy new particles. Ref. [1]. The method uses a set of *pseudo observables* (PO) defined by the momentum expansion of the on-shell Higgs decay amplitudes. More precisely, the PO of a generic Higgs to n -body decay are defined by the expansion of the decay amplitude around the single-particle poles (in all $m < n$ relevant subsystems) due to the exchange of SM particles.

The PO are well-defined physical parameters that can

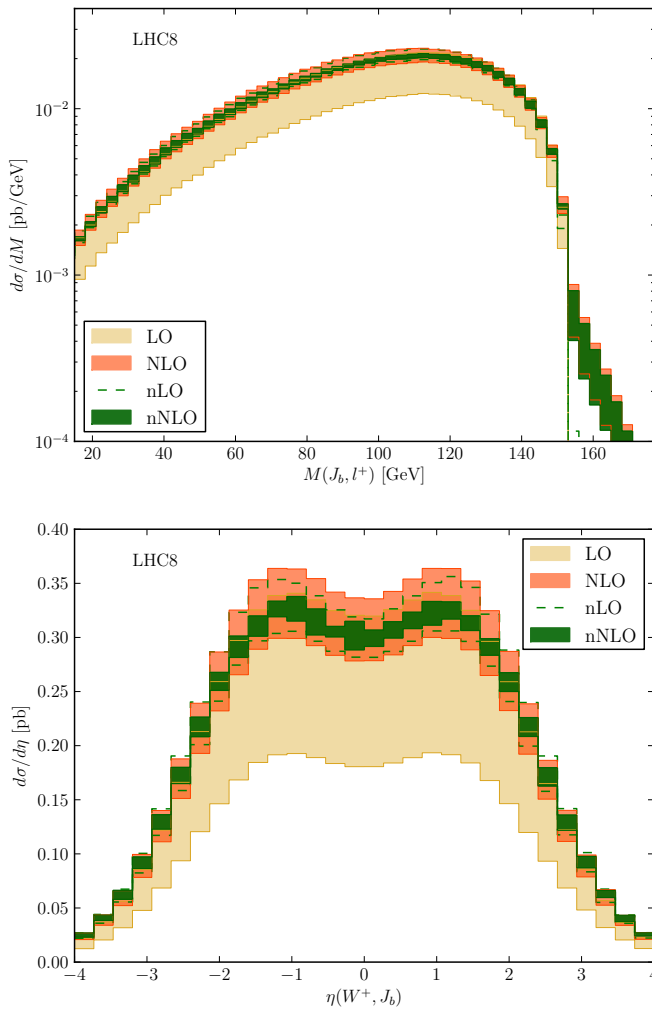


FIG. 1.3 – Invariant mass of the b -jet lepton pair (top panel) and pseudo-rapidity of the reconstructed top (bottom panel) for the 8 TeV LHC with standard cuts as described in the text. The approximate NNLO prediction is denoted by nNLO

be directly extracted from data, providing a natural generalization of the so-called “ κ -framework” introduced so far by the LHC collaborations. Moreover, they allow for a systematic inclusion of higher-order QED and QCD corrections and can be computed in any Effective Field Theory (EFT) approach to Higgs physics. The number of independent PO reduces when applying certain hypotheses such as lepton-universality, CP invariance, custodial symmetry, and linearly realized electroweak symmetry breaking.

- [1] M. Gonzalez-Alonso, A. Greljo, G. Isidori and D. Marzocca, *Eur. Phys. J. C* **75** (2015) 3, 128.

1.4 Extending the Standard Model up to Infinite Energy

Attempts to solve naturalness by having the weak scale as the only breaking of classical scale invariance have to deal with two severe difficulties: gravity and the absence of Landau poles. We have shown that solutions to the first problem require premature modifications of gravity at scales no larger than 10^{11} GeV, while the second problem calls for many new particles around the weak scale Ref. [1].

In order to build models that fulfill these properties, we have classified the four-dimensional Quantum Field Theories that satisfy the criterion of Total Asymptotic Freedom (TAF), namely theories that hold at any energy scale, with all coupling constants flowing to zero. We have developed a method identifying such theories and determining their low-energy predictions. Since the Standard Model turns out to be asymptotically free only under unphysical conditions, we have explored some of its weak-scale extensions that satisfy the requirements for TAF. Interestingly, the latter predict a large number of new particles around the TeV scale which are, however, severely constrained by low-energy flavor data. In that perspective, a significant amount of fine-tuning is required.

- [1] G. F. Giudice, G. Isidori, A. Salvio and A. Strumia, *JHEP* **1502** (2015) 137.

2 Astrophysics and General Relativity

R. Angélim, S. Balmelli, R. Bondarescu, L. De Vittori, C. Huwlyer, Ph. Jetzer, R. Kauser, R. Küng, I. Mohammed, L. Philippoz, P. Saha and A. Schärer

Astrophysics could be defined as the branch of physics where gravity is important. For much of astrophysics, Newtonian gravity is adequate, but for phenomena involving very strong gravitational fields, cosmological distances, the effect of gravity on light, or just extremely precise measurements, relativistic gravity is needed. After a hundred years, Einsteinian gravity continues to pass all tests, and meanwhile reveals new manifestations. Exploring these is the area of our research.

2.1 Gravitational waves and LISA

Although the existence of gravitational waves (GW) can be inferred indirectly, from the spin-down of binary pulsar systems, the first direct detection of gravitational waves is an eagerly-awaited event. Within our group we addressed various topics on gravitational wave physics.

Motivated by a recently proposed parameterized post-Einsteinian (ppE) scheme, which introduces corrections to the post-Newtonian coefficients of the frequency domain gravitational waveform in order to emulate alternative theories of gravity, we computed analytical time domain waveforms that, after a numerical Fourier transform, aim to represent (phase corrected only) ppE waveforms. In this formalism, alternative theories manifest themselves via corrections to the phase and frequency, as predicted by General Relativity (GR), at different post-Newtonian (PN) orders. In order to present a generic test of alternative theories of gravity, we assumed that the coupling constant of each alternative theory is manifestly positive, allowing corrections to the GR waveforms to be either positive or negative. By exploring the capabilities of massive black hole binary GR waveforms in the detection and parameter estimation of corrected time domain ppE signals, using the current proposed eLISA configuration, we demonstrated that for corrections arising at higher than 1 PN order in phase and frequency, GR waveforms are sufficient for both detecting and estimating the parameters of alternative theory signals. However, for theories introducing corrections at the 0 and 0.5 PN order, GR waveforms are not capable of covering the entire parameter space, requiring the use of non-GR waveforms for detection and parameter estimation.

Compact binaries in hyperbolic orbits are plausible GW sources for the upcoming and planned GW observatories. We developed an efficient prescription to compute post-Newtonian (PN) accurate ready-to-use GW polar-

ization states for spinning compact binaries, influenced by the dominant order spin-orbit interactions, in hyperbolic orbits. This is achieved by invoking the 1.5 PN accurate quasi-Keplerian parameterization for the radial sector of the orbital dynamics. We probed the influences of spins and gravitational radiation reaction on h_+ and h_x during the hyperbolic passage. It turns out that both polarization states exhibit the memory effect for GWs from spinning compact binaries in hyperbolic orbits. In contrast, only cross polarization state exhibits the memory effect for GWs from non-spinning compact binaries. Additionally, we computed 1 PN accurate amplitude corrected GW polarization states for hyperbolic non-spinning compact binaries in a fully parametric manner and performed initial comparisons with the existing waveforms.

We proposed a way of including the next-to-leading (NLO) order spin-spin coupling into an effective-one-body (EOB) Hamiltonian, extending our work, which was restricted to the case of equatorial orbits and aligned spins, to general orbits with arbitrary spin orientations. To achieve this goal we applied appropriate canonical phase-space transformations to the NLO spin-spin Hamiltonian in Arnowitt-Deser-Misner (ADM) coordinates, and systematically added effective quantities at NLO to all spin-squared terms appearing in the EOB Hamiltonian. As required by consistency, the introduced quantities reduce to zero in the test-mass limit. We exposed the result both in a general gauge and in a gauge-fixed form, chosen to minimize the number of new coefficients that have to be inserted into the effective spin squared. As a result, the 25 parameters that describe the ADM NLO spin-spin dynamics get condensed into only 12 EOB terms.

We studied binary neutron star mergers using nonlinear 3+1 numerical relativity simulations and the analytical effective-one-body (EOB) model. The EOB model predicts quasi-universal relations between the mass-rescaled GW frequency and the binding energy at the moment of merger, and certain dimensionless binary tidal coupling constants depending on the stars Love numbers, compactnesses and the binary mass ratio. These relations are quasi-universal in the sense that, for a given value of the tidal coupling constant, they do not depend significantly on the equation of state and on the mass ratio, though they do depend on stars spins. The spin dependence is approximately linear for small spins aligned with the orbital angular momentum. The quasi-universality is

a property of the conservative dynamics; nontrivial relations emerge as the binary interaction becomes tidally dominated. This analytical prediction is qualitatively consistent with new, multi-orbit numerical relativity results for the relevant case of equal-mass irrotational binaries. Universal relations are thus expected to characterize neutron star mergers dynamics. In the context of GW astronomy, these universal relations may be used to constrain the neutron star equation of state using waveforms that model the merger accurately.

2.1.1 LISA Pathfinder

We are member of the LISA Pathfinder science team and of the eLISA consortium board. LISA Pathfinder (see Fig. 2.1) is a dedicated technology demonstrator for the evolved Laser Interferometer Space Antenna (eLISA) ESA mission. The technologies required for eLISA are extremely challenging. LISA Pathfinder essentially

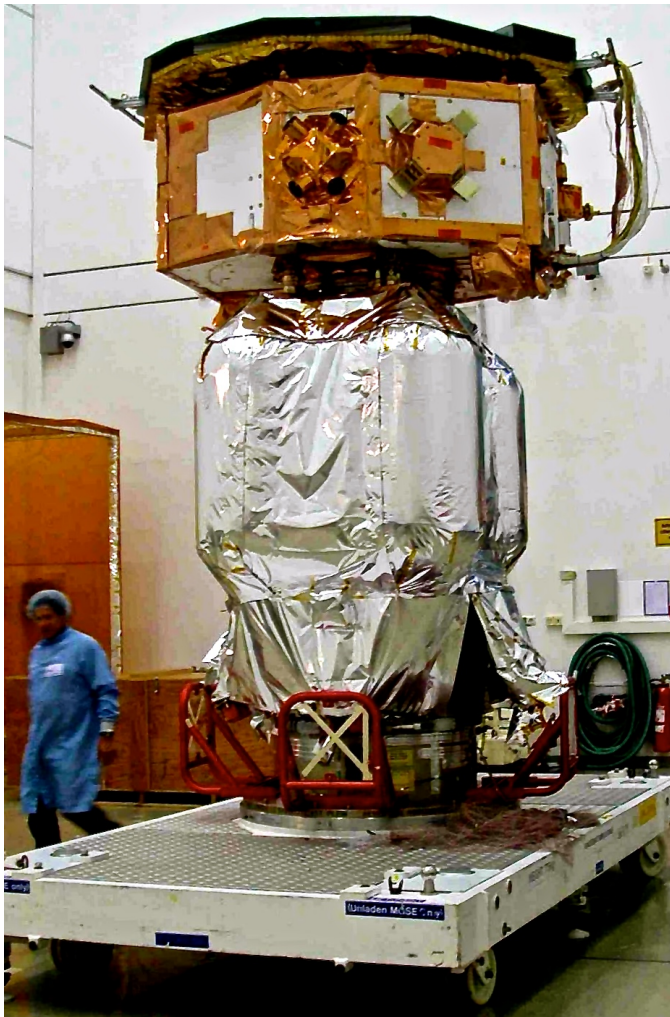


FIG. 2.1 – LISA-Pathfinder at the top of the propulsion module which will bring it at the L1 point (first Sun-Earth Lagrange point).

mimics one arm of the eLISA constellation by shrinking the 1 million kilometer arm length down to a few tens of centimeters, giving up the sensitivity to gravitational waves, but keeping the measurement technology: the distance between the two test masses is measured using a laser interferometric technique similar to one aspect of the eLISA interferometry system. The scientific objective of the LISA Pathfinder mission consists then of the first in-flight test of low frequency gravitational wave detection metrology. LISA Pathfinder is currently under final integration and tests and is scheduled to be launched in fall 2015 to the L1 Sun-Earth point in space.

2.2 Gravitational Lensing

That gravitational lensing — specifically that light is affected by both space and time parts of the metric, unlike Newtonian bodies, which are affected only by the time part — is too well known to need elaborating here. Nowadays, however, gravitational lensing is valued, more than as a test of general relativity, as a way of detecting matter that would be otherwise invisible.

On the scale of galaxies and clusters of galaxies, gravitational lensing is very important as a probe of dark matter. Extracting the information on mass distributions, however, requires solving a non-trivial inverse problem. R. Küng, I. Mohammed and P. Saha, together with external collaborators, have worked on the problem of mapping a mass distribution from lensing observables. One part of this work is the development of an improved method for modeling galaxy lenses and furthermore, a theoretical formulation and computational interface to enable modeling in a citizen-science context. The other aspect is mapping and interpreting dark-matter structure in strong-lensing galaxy-clusters

2.2.1 Microlensing

We studied the polarization of the star light that may arise during microlensing events due to the high gradient of magnification across the atmosphere of the source star, by exploring the full range of microlensing and stellar physical parameters. Since it is already known that only cool evolved giant stars give rise to the highest polarization signals, we computed the polarization as due to the photon scattering on dust grains in the stellar wind. Motivated by the possibility to perform a polarization measurement during an ongoing microlensing event, we considered the recently reported event catalog by the OGLE collaboration covering the 2001-2009 campaigns (OGLE-III events), that makes available the largest and more comprehensive set of single lens microlensing events towards the Galactic bulge. The study of these events, integrated by a Monte Carlo analysis, allowed us to esti-

mate the expected polarization profiles and to predict for which source stars and at which time it is most convenient to perform a polarization measurement in an ongoing event. We found that about two dozens of OGLE-III events (about 1 percent of the total) have maximum degree of polarization in the range $0.1\% < P_{max} < 1\%$, corresponding to source stars with apparent magnitude $I \leq 14.5$, being very cool red giants. This signal is measurable by using the FORS2 polarimeter at VLT telescope with about 1 hour integration time.

2.3 Space clocks and relativity

A surprising natural orbiting clock is provided by stars in orbit around a black hole at the centre of our Galaxy. Some of these stars are on very eccentric orbits, and around their point of closest approach to the black hole, they move at a few percent of light speed. The spectra of these stars should exhibit effects of space curvature and black-hole spin. R. Angèlil and P. Saha have studied the relevant observational signatures, and how they could be disentangled from the Newtonian effects of other stars and gas in the Galactic-centre region.

We computed the PPN parameters γ and β for general scalar-tensor theories in the Einstein frame, which we compared to the existing PPN formulation in the Jordan frame for alternative theories of gravity. This computation is important for scalar-tensor theories that are expressed in the Einstein frame, such as chameleon and symmetron theories, which can incorporate hiding mechanisms that predict environment-dependent PPN parameters. We introduced a general formalism for scalar-tensor theories which is constrained by the limit on γ given by the Cassini experiment. In particular we discussed massive Brans-Dicke scalar fields for extended sources. Next, using a recently proposed Earth satellite experiment in which atomic clocks are used for spacecraft tracking, we computed the observable perturbations in the redshift induced by PPN parameters deviating from their general relativistic values.

We studied in detail the scientific objectives in fundamental physics of the Space-Time Explorer and Quantum Equivalence Space Test (STE-QUEST) mission, which was proposed within the framework of the ESA call for missions. It carries out tests of different aspects of the Einstein Equivalence Principle using atomic clocks, matter wave interferometry and long distance time/frequency links, providing fascinating science at the interface between quantum mechanics and gravitation that cannot be achieved, at that level of precision, in ground experiments. We discussed the strong interest of performing equivalence principle tests in the quantum regime, i.e. using quantum atomic wave interferometry.

3 GERDA: Neutrinoless Double Beta Decay in Ge

Laura Baudis, Giovanni Benato, Andreas James, Alexander Kish,
Michael Miloradovic, Manuel Walter

in collaboration with: INFN Laboratori Nazionali del Gran Sasso LNGS, Jagellonian University Cracow, Institut für Kern- und Teilchenphysik Technische Universität Dresden, Joint Institute for Nuclear Research Dubna, Institute for Reference Materials and Measurements Geel, Max Planck Institut für Kernphysik Heidelberg, Università di Milano Bicocca e INFN Milano, Institute for Nuclear Research of the Russian Academy of Sciences, Institute for Theoretical and Experimental Physics Moscow, Russian Research Center Kurchatov Institute, Max-Planck-Institut für Physik München, Dipartimento di Fisica dell Università di Padova e INFN, Physikalisches Institut Eberhard Karls Universität Tübingen.

(GERDA Collaboration)

Neutrino oscillation experiments show that neutrinos mix so neutrino mass eigenstates differ from weak eigenstates, *i.e.* neutrinos have mass and the Standard Model (SM) must be extended to include the observed lepton flavor violation. One possibility is to allow left-handed neutrinos only so the mass eigenstates are Majorana fermions, and the 3×3 mixing matrix depends on six independent parameters, the three mixing angles and three physical phases. Meanwhile the magnitudes of all elements of the leptonic mixing matrix are determined [1].

While oscillation experiments provide information on the mass squared differences, and on the leptonic mixing angles, they are insensitive to the absolute mass scale of neutrinos. Such information can be extracted from kinematic studies of Tritium (and other) beta decays, and from the neutrinoless double beta decay ($0\nu\beta\beta$). More importantly this decay, if observed, would proof that the neutrino is a Majorana fermion and that total lepton number is not conserved in nature. The rate of the extremely rare nuclear process is proportional to the effective Majorana neutrino mass, $\langle m \rangle_{eff} = \sum_i U_{ei}^2 m_i$, where the sum is over the three generations and U_{ei} , the elements of the lepton mixing matrix, are complex numbers.

Limits on $\langle m \rangle_{eff}$ have been obtained for a variety of nuclei, see [2] for a recent review. The most stringent upper limit for ^{76}Ge comes from GERDA [3], as detailed below, while the best limits for ^{130}Te and ^{100}Mo , $\langle m \rangle_{eff} \leq 0.2 - 0.7 \text{ eV}$, and $\langle m \rangle_{eff} \leq 0.45 - 0.9 \text{ eV}$, respectively, come from the Cuoricino and NEMO-3 experiments. Recently, experiments using xenon in its liquid form, EXO, and mixed with a scintillator, KamLAND-ZEN, provided very competitive upper limits of $\sim 0.2 - 0.25 \text{ eV}$ and $\sim 0.2 - 0.5 \text{ eV}$, respectively.

3.1 The GERDA experiment

The GERDA experiment at LNGS searches for the $0\nu\beta\beta$ -decay of ^{76}Ge . High-purity germanium (HPGe) detectors

enriched in ^{76}Ge are operated bare, immersed in liquid argon (LAR). The argon is surrounded by a 3 m thick water Cherenkov shield. A clean room for Ge diode handling is installed on top of the water tank, with a lock at its center for transferring detectors into the Ar [4].

GERDA phase I took data at LNGS from 2011-2013 with about 18 kg of enriched HPGe detectors, accumulating an exposure of 21.6 kg.y. Pulse shape discrimination (PSD) is used to distinguish signal events which have primarily a single interaction site within the detector bulk from background events which are dominated by interactions on the surface or by multiple interactions. A flat background was predicted in the 1930-2190 keV region of interest [5]. No events above background are observed in the resulting energy spectrum, shown in Fig. 3.1. The resulting lower limit (90% C.L.) on the half-life, $2.1 \times 10^{25} \text{ y}$ corresponds to an upper limit on the effective neutrino

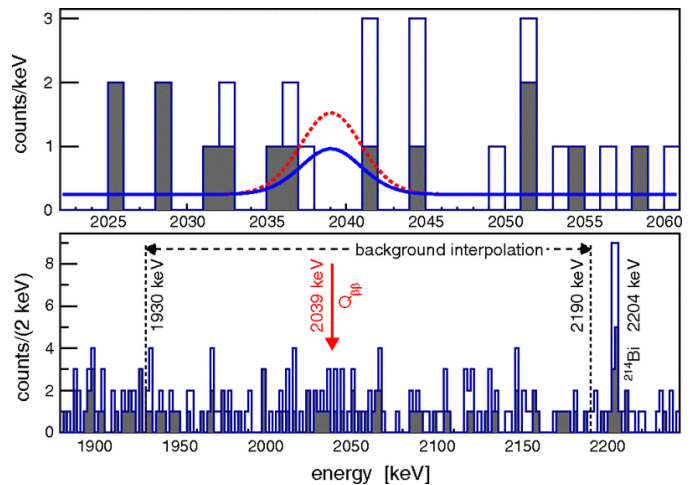


FIG. 3.1 – Combined energy spectrum from all Ge detectors without (with) PSD, indicated by the open (filled) histogram. A zoom around $Q_{\beta\beta}$ is shown in the upper panel, along with the expectation from $T_{1/2} = 1.19 \times 10^{25} \text{ y}$ (red dashed) [6] and the the 90% upper limit $T_{1/2} < 2.1 \times 10^{25} \text{ y}$ (blue solid) derived from this measurement.

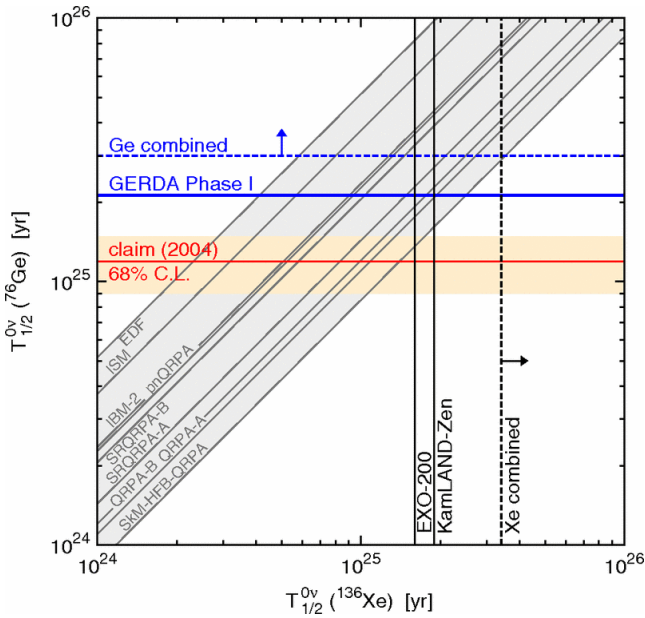


FIG. 3.2 – Limits (90% C.L.) on $T_{1/2}$ from ^{76}Ge and ^{136}Xe , compared with the signal claim for ^{76}Ge [6]. The lines in the shaded grey band are the predictions for the correlation of the half-lives according to different NME calculations. Figure from [3].

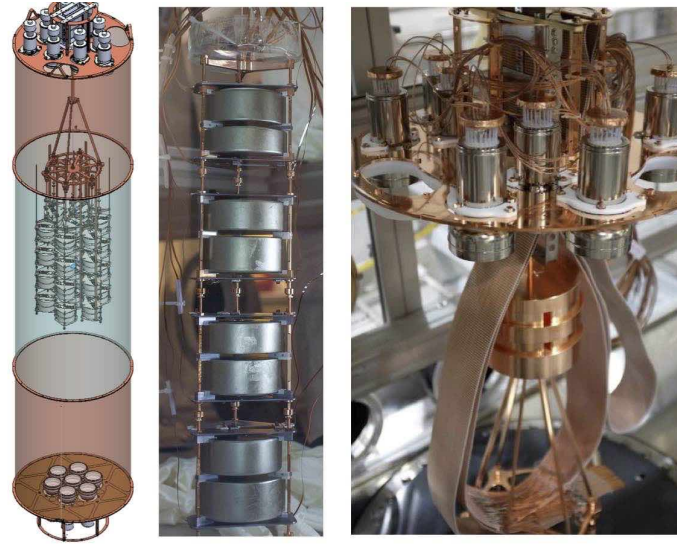


FIG. 3.3 – Left: Schematic view of the GERDA phase II Ge detector and LAr veto arrangement. Centre: A string of eight BEGe detectors in GERDA phase II. These are grouped in pairs within one holder. Right: Part of the phase II liquid argon veto during its installation at LNGS. The top PMT array (of Hamamatsu R11065, low-radioactivity type) can be clearly seen.

10

mass of $\langle m \rangle_{\text{eff}} \leq 0.2 - 0.4 \text{ eV}$, depending on the nuclear matrix element [3]. This result strongly challenges the claim of a signal by part of the Heidelberg-Moscow collaboration [6], as shown in Fig. 3.2. Recently, results on the decay with emission of Majorons were submitted for publication [7].

The second phase of the experiment aims at a total exposure of $100 \text{ kg}\cdot\text{y}$ with a background around $Q_{\beta\beta}$ reduced by a factor ten to $10^{-3} \text{ counts}/(\text{keV}\cdot\text{kg}\cdot\text{y})$. The half-life sensitivity is $2 \times 10^{26} \text{ y}$ and the corresponding range of effective neutrino masses is $\leq 0.09 - 0.15 \text{ eV}$, taking into account the uncertainty in the matrix element and neglecting new lepton number violating interactions.

All thirty (20.5 kg) enriched phase II detectors, of broad-energy germanium (BEGe) type, were produced, characterised [8] and are now under commissioning in the LAr cryostat at LNGS. Figure 3.3 shows a schematic view of the arrangement, and pictures of a BEGe detector string and the liquid argon veto. The latter will allow to reduce background events with depositions in both the LAr and a Ge detector (see below). We expect to start data taking in late summer 2015.

3.2 Analysis of calibration and physics measurements

We are strongly involved in the analysis of the GERDA calibration and physics data. During phase I the energy resolution suffered from low-frequency baseline fluctua-

tions. A digital filter with enhanced low-frequency noise rejection was developed and tested as an alternative to the standard Gaussian shaping. It consists of a cusp filter with a central flat-top for maximizing the charge integration. The distortion induced by the preamplifier is removed via a deconvolution with the preamplifier response function. The effect of this Zero-Area finite-length Cusp filter (referred as ZAC filter) is illustrated in Figs. 3.4 and 3.5. The energy is estimated as the peak value of the shaped signal.

We have tuned the filter parameters for each detector separately, and all phase I data have been successfully reprocessed, leading to an average improvement of 0.3 keV at $Q_{\beta\beta}$ for the calibration data [9]. The impact on the physics reach of GERDA phase I is $\sim 5\%$ in median sensitivity. The reprocessed phase I data will be combined with the new results from phase II.

Since the PSD performance is strongly affected by the noise conditions as well a noise-reduction algorithm was implemented which transforms the raw wavelet as shown in Fig. 3.6). The algorithm can calculate a threshold based on the noise observed in each individual event. We will test this method on the current pulse instead of using the raw trace (charge pulse).

The larger number of Ge detectors and the longer duration of phase II make the use of a robust, fully automated and well documented analysis software mandatory. In order to minimize the proliferation of single purpose

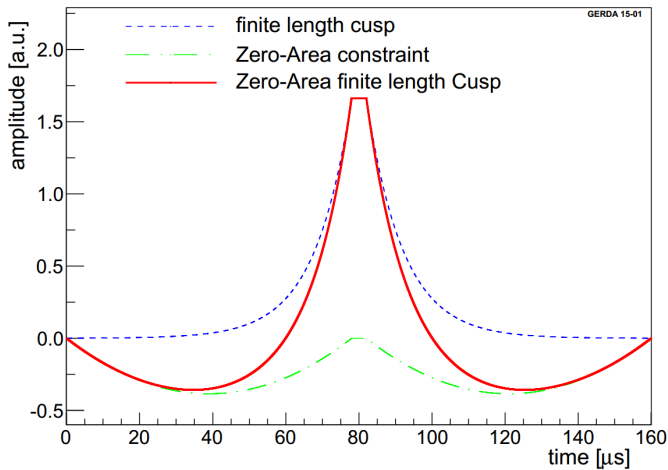


FIG. 3.4 – ZAC filter composed of the finite-length cusp from which two parabolas are subtracted on the sides.

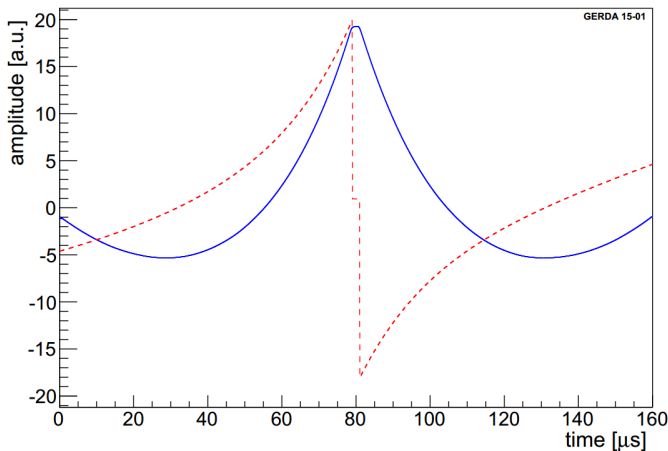


FIG. 3.5 – The ZAC filter after the de-convolution with the preamplifier response function (red) and the resulting waveform (blue).

software packages we are developing a multi-purpose software framework. Main tasks are the optimization of the filters for energy reconstruction and PSD discussed above, the event selection through dedicated quality cuts and the energy calibration. Tools are being developed to

constantly monitor the noise conditions which will automatically tag data periods with stable noise features, for which a single filter can be employed. The software will be interfaced to a CouchDB database for the storage of the main output parameters, *e.g.* the quality cuts values, the calibration curves, as well as the PSD and LAr veto selections.

3.3 Production and characterization of the calibration sources for phase II

We are responsible for the calibration system hardware and software [10]. In preparation for the start of GERDA phase II we produced four low neutron emission ^{228}Th sources by depositing the radioactive material on high purity gold foils. The emitted neutron flux was measured with a ^3He counter and a low background LiI(Eu) detector, located underground at LNGS. As an example, Fig. 3.7 shows the spectrum recorded by our LiI(Eu) detector with the four phase II sources and background spectrum recorded during 142 days. These results proof for the first time that LiI(Eu) can detect very low neutron fluxes. The neutron rates measured with the LiI(Eu) and the ^3He detectors are 8.2 ± 2.3 n/s/Bq and 9.4 ± 2.3 n/s/Bq, respectively, which is an order of magnitude

11

less than observed with standard ^{228}Th sources measured with the same procedure. Moreover, this result confirms the reproducibility of our source production, developed for phase I. ^{228}Th sources with reduced neutron strength are of interest for other low background experiments too, when the activation of material close to the detector is of relevance.

The γ activity of each source was measured with the Gator facility at LNGS. The "zero background" condition, along with a detailed knowledge of the detector geometry, allowed us to obtain a very good agreement between measured and simulated spectra, with a total uncertainty of $\sim 4\%$. In the future, we thus plan to perform a detailed validation of the GERDA Monte Carlo framework MAGE, which is a necessary step for the development of a reliable background model used in the $2\nu\beta\beta$ and $0\nu\beta\beta$ decay analyses.

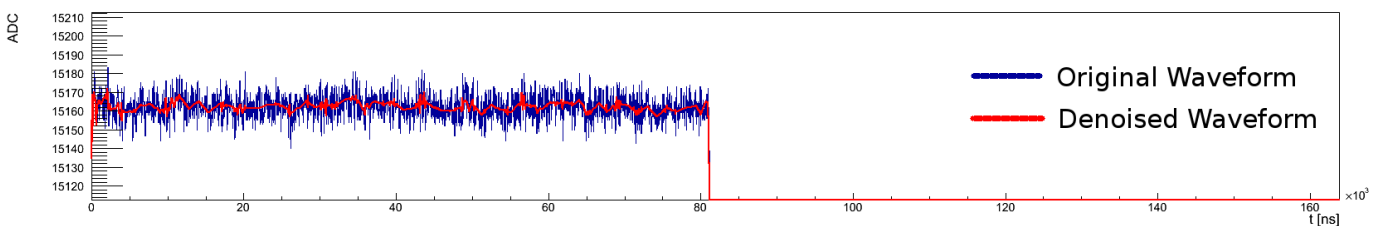


FIG. 3.6 – Wavelet trace in GERDA: baseline before and after noise reduction.

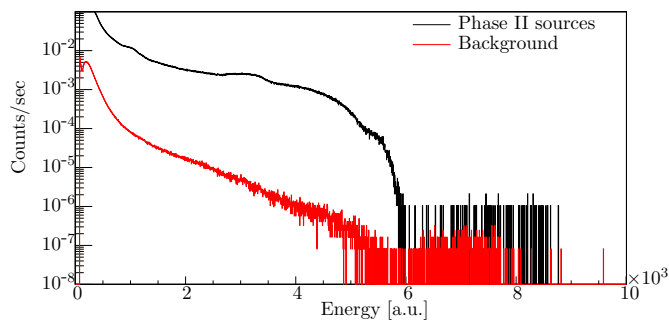


FIG. 3.7 – Energy spectra of the LiI(Eu) detector at LNGS with/without the four GERDA Phase II ^{228}Th sources. While the γ contribution shows an endpoint at ~ 6000 , a thermal neutron signal is present around channel 8000. The faint peak in the background spectrum around channel 7000 might be due to an α contamination of the crystal.

3.4 The liquid argon veto

As mentioned already, in phase II the background level is to be reduced by one order of magnitude compared to phase I. Some sources of background deposit energy in the LAr surrounding the Ge detectors. The LAr instrumentation system was installed in the GERDA cryostat in early 2015. It uses two arrays of low-radioactivity Hamamatsu R11065 PMTs and SiPMs coupled to an optical fibre curtain for the light readout. Since the PMTs have a quartz window absorbing the 128 nm scintillation light and the optical fibers are not sensitive to this wavelength either, foils with wavelength shifting coatings surround the LAr.

We have produced and tested several wavelength shifting reflector foils, and Tetratex dip-coated with ~ 0.8 mg TPB/cm² showed the optimal performance [11]. We then produced ten 46 cm \times 64 cm sheets of TPB coated Tetratex and installed them in Gerda. The Tetratex foil was stitched to the copper cylinders with nylon wire. This method introduces a minimal amount of additional material and thus radioactive contamination. The completed bottom cylinder with installed PMTs is shown in Fig. 3.8.

With our LAr chamber at UZH, built for the WLS work, we will test a new version of the R11065 PMT which has a MgF₂ window. Since MgF₂ transmits 128 nm light, these PMTs could obviate the use of WLS, potentially increasing the veto signal and thus reducing the energy threshold.

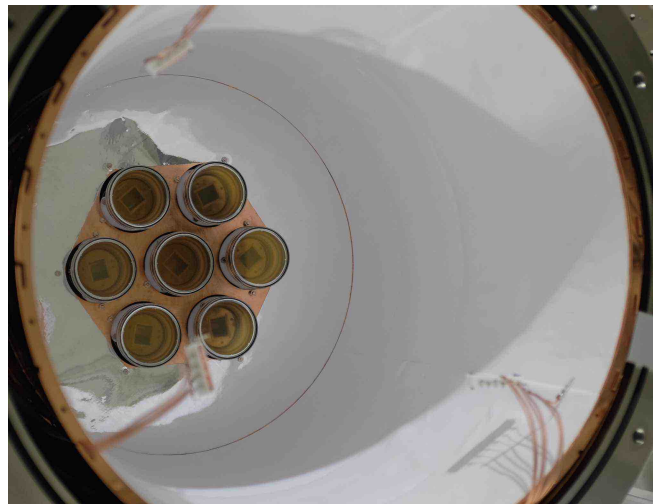


FIG. 3.8 – Bottom part of the liquid Ar veto system in GERDA, with installed Tetratex coated with TPB and the 3-inch PMT array.

12

- [1] M. Gonzalez-Garcia, Phys. Dark Univ. 4 (2014) 1–5.
- [2] S. Bilenky, C. Giunti, Int. J. Mod. Phys. A30 (2015) 0001.
- [3] M. Agostini *et al.*, GERDA Collaboration, Phys. Rev. Lett. 111 (2013) 122503.
- [4] K. Ackermann *et al.*, GERDA Collaboration, Eur. Phys. J. C73 (year?) page?
- [5] M. Agostini *et al.*, GERDA Collaboration, Eur. Phys. J. C74 (2014) 2764.
- [6] H. Klapdor-Kleingrothaus, I. Krivosheina, A. Dietz, O. Chkvorets, Phys. Lett. B586 (2004) 198–212.
- [7] M. Agostini *et al.*, GERDA Collaboration, Results on $\beta\beta$ decay with emission of two neutrinos or Majorons in ^{76}Ge from GERDA Phase I, <http://arxiv.org/abs/1501.02345>
- [8] M. Agostini *et al.*, GERDA Collaboration, Eur. Phys. J. C75 (2015).
- [9] M. Agostini *et al.*, GERDA Collaboration, Improvement of the Energy Resolution via an Optimized Digital Signal Processing in GERDA Phase I, <http://arxiv.org/abs/1502.04392>
- [10] L. Baudis, A. Ferella, F. Froberg, M. Tarka, Nucl. Instrum. Meth. A729 (2013) 557–564.
- [11] L. Baudis, G. Benato, R. Dressler, F. Piastra, I. Usoltsev *et al.*, Fluorescence Efficiency and Stability of Radio-Pure Tetraphenyl-butadiene Based Coatings for VUV Light Detection in Cryogenic Environments, <http://arxiv.org/abs/1503.05349>

4 Cold Dark Matter Search with XENON and DARWIN

Laura Baudis, Peter Barrow, Sandro D’Amato, Domenico Franco, Michelle Galloway, Andrea Gmuer, Gaudenz Kessler, Alexander Kish, Andreas James, Daniel Mayani, Francesco Piastra, Julien Wulf and Yuehuan Wei

in collaboration with: Albert Einstein Center for Fundamental Physics Bern, Columbia University, UCLA, INFN, University of Münster, Coimbra University, Subatech, The Weizmann Institute of Science, University of Mainz, SJTU, MPIK Heidelberg, Stockholm University, Rice University, University of Chicago, University of Bologna, Nikhef, Purdue University, NYU of Abu Dhabi

(XENON Collaboration)

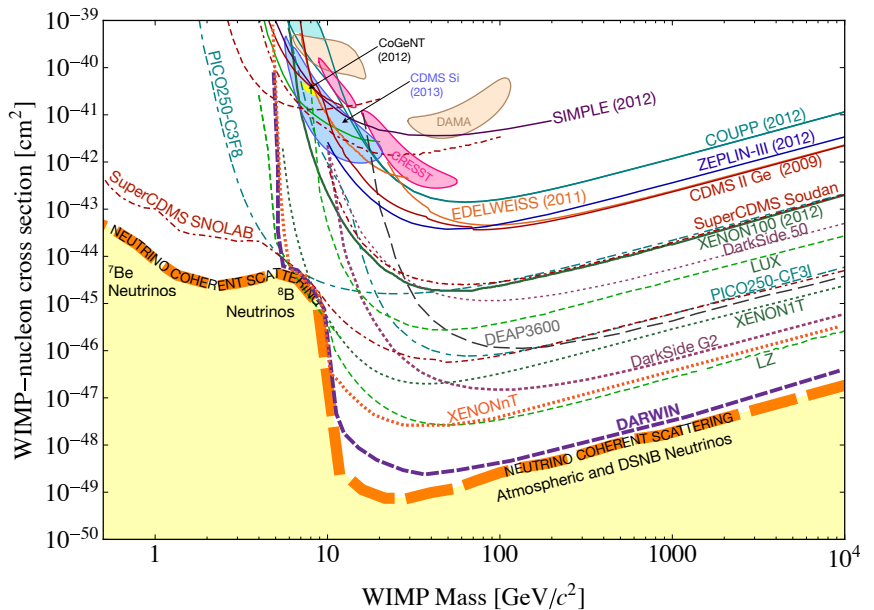
After decades of increasingly precise astronomical observations, we have unequivocal evidence that the matter forming galaxies, clusters of galaxies and the largest observed structures in the universe is mostly non-luminous, or dark. These observations include galactic rotation curves, orbital velocities of individual galaxies, cluster masses from gravitational lensing, cosmic microwave background acoustic fluctuations, the abundance of light elements, and the mapping of large scale structures. Cosmological simulations based on the Λ CDM model do predict the observed large-scale structures in the universe. In this model, which so far provides the only paradigm that can explain all observations, our universe is spatially flat and composed of $\sim 5\%$ atoms, $\sim 27\%$ dark matter and $\sim 68\%$ dark energy [1].

Understanding the nature of dark matter poses a significant challenge to astroparticle physics. Its solution may involve new particles with masses and cross sections characteristic of the electroweak scale, so-called Weakly Interacting Massive Particles (WIMPs). WIMPs may be directly detected by scattering off nuclei in ultra-sensitive

laboratory detectors [2]. Since the predicted cross sections and hence expected signal rates are very low, large detector masses and extremely low backgrounds are necessary ingredients of any experiment aiming to discover WIMPs [3]. Existing upper limits and projected sensitivities for the spin-independent WIMP-nucleon interaction cross section as a function of the WIMP mass are summarized in Fig. 4.1.

Liquid xenon offers an excellent medium for building non-segmented, homogeneous, compact and self-shielding dark matter detectors: it is a good scintillator and ionizer in response to the passage of radiation, and the simultaneous detection of ionization and scintillation signals allows to identify the primary particle interacting in the liquid. In addition, the 3D position of an interaction can be determined with sub-mm (in the z-coordinate) to mm (in the x-y-coordinate) precisions in a time projection chamber (TPC), where the prompt light (S1) and charge (S2, in general via proportional scintillation) signals are detected. These features, together with the relative ease of scale-up to large masses, have contributed

FIG. 4.1 – Spin-independent WIMP-nucleon scattering results: Existing limits from the ZEPLIN-III [4], XENON10 [5], XENON100 [6], and LUX [7] experiments, along with projections for DarkSide-50 [8], LUX [7], DEAP3600 [9], XENON1T, DarkSide G2, XENONnT, LZ [10], and DARWIN [11]. DARWIN is designed to probe the entire parameter region for WIMP masses above $\sim 6 \text{ GeV}/c^2$, until the neutrino background (yellow region) will start to dominate the recoil spectrum. Experiments based on the mK cryogenic technique such as SuperCDMS [12] and EURECA [13] have access to lower WIMP masses. Adapted from [14].



to make LXe a powerful target for WIMP searches [15]. The dual-phase LXe TPCs ZEPLIN-III [4, 16], XENON10 [5], XENON100 [6, 17] and LUX [7] are successful implementations of the technique. XENON1T, the next step of the XENON program, is in construction at LNGS. The next phase in the LUX program, LUX-ZEPLIN (LZ), foresees a 7 t LXe detector at SURF, with the goal of reaching a sensitivity of $2 \times 10^{-48} \text{ cm}^2$ after three years of data taking [10]. The upgrade of XENON1T, XENONnT, is to reach a similar sensitivity, with planned operation between 2018-2021. DARK matter Wimp search with Noble liquids (DARWIN) is an initiative to build an ultimate, multi-ton dark matter detector at LNGS [11, 18], to probe the spin-independent WIMP-nucleon cross section down to the 10^{-49} cm^2 region. It would thus explore the experimentally accessible parameter space, which eventually be limited by irreducible neutrino backgrounds.

4.1 The XENON dark matter program

The primary goal of the XENON program is to directly detect WIMP dark matter in ultra-sensitive low-background detectors. XENON100 is a 161 kg double-

phase Xe TPC, still in operation at the Gran Sasso Laboratory (LNGS), for calibration measurements and R&D for the next phase of the project. XENON1T is in an advanced construction stage in hall B of LNGS. All its major components have been designed such that an upgrade to a detector which is at least twice more massive is rather straight-forward. For this stage of the program, called XENONnT, the main challenges will be to develop a new, larger TPC and to lower the backgrounds further. With a planned exposure of $\sim 20 \text{ t} \times \text{y}$ the expected sensitivity is roughly one order of magnitude below the one of XENON1T, shown schematically in Fig.4.2.

XENON1T houses a $\sim 3.3 \text{ t}$ LXe, of which 2.0 t constitute the active mass of the dual-phase TPC. The background goal is less than one event in $2 \text{ t} \times \text{y}$ in the central fiducial region of $\sim 1.0 \text{ t}$ which leads to a sensitivity to spin-independent WIMP-nucleon cross sections of $2 \times 10^{-47} \text{ cm}^2$ for $50 \text{ GeV}/c^2$ WIMPs.

The underground building, the Cherenkov muon veto, the cryostat support, the outer and inner cryostats, as well as the xenon storage, purification and recovery systems are in place, see Fig. 4.3. The TPC is under construction, first cryogenic tests will be performed at UZH; its assembly at LNGS is planned for summer 2015. After the detector commissioning first data is to be acquired within that same year.

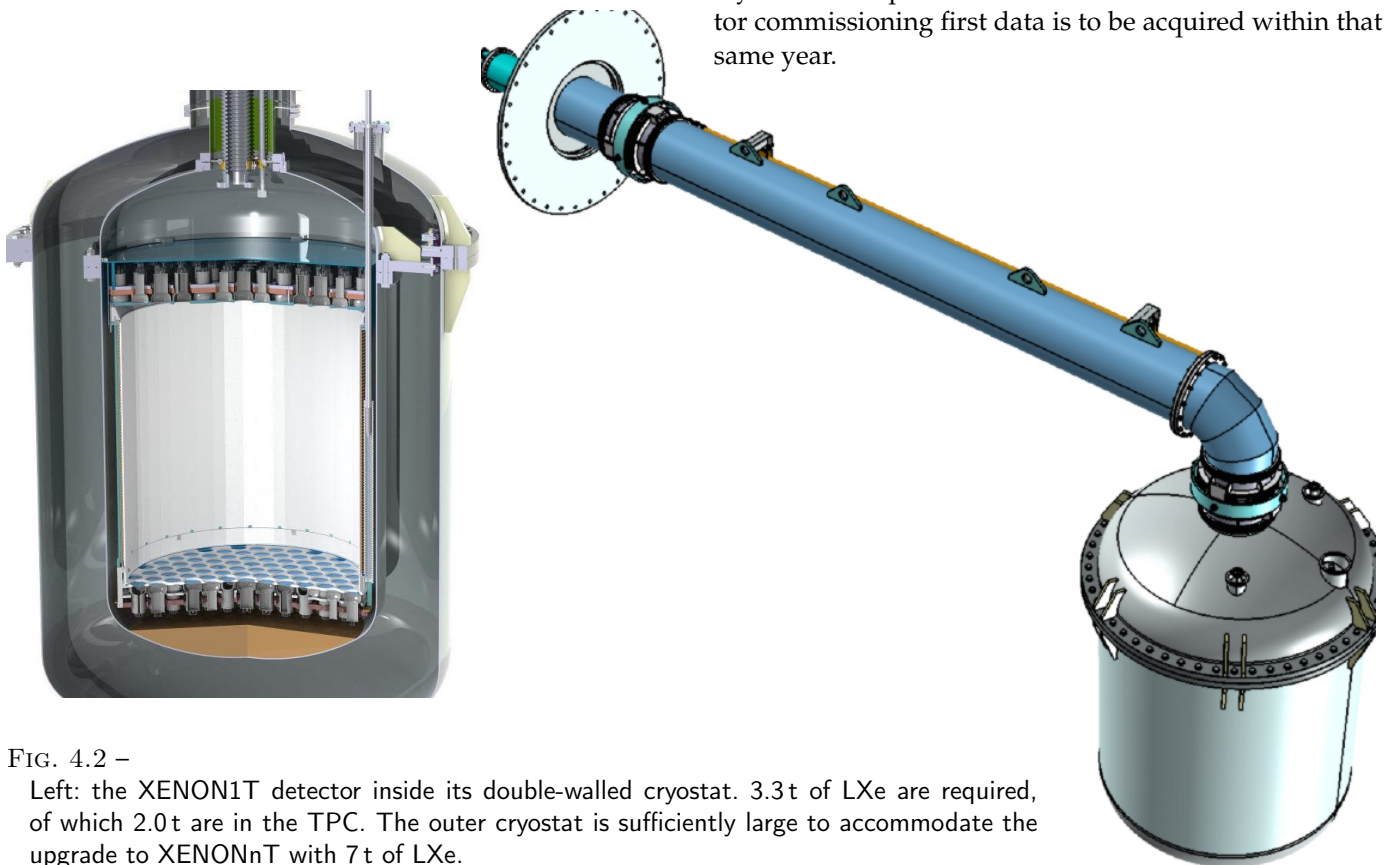


FIG. 4.2 –

Left: the XENON1T detector inside its double-walled cryostat. 3.3 t of LXe are required, of which 2.0 t are in the TPC. The outer cryostat is sufficiently large to accommodate the upgrade to XENONnT with 7 t of LXe.

Right: the detector with its single connecting pipe, containing both the transmission lines for gaseous and liquid xenon and all electronic cables.

FIG. 4.3 –

Left: the XENON1T inner and outer cryostats are installed underground at LNGS, inside a 9.6 m diameter water Cherenkov muon veto.

Right: The main underground infrastructures, as well as the building with DAQ, xenon storage, purification and cryogenic systems are in place.



4.2 Analysis of XENON100 science data

We participate in various aspects of the analysis of the XENON100 data, from the development of data quality and physics cuts, to the final physics analysis. Our current focus is on inelastic WIMP-nucleus scatters, on the search for bosonic SuperWIMPs, on background studies of the latest, still blinded, dark matter run, and on the YBe and ^{83m}Kr calibrations.

4.2.1 Inelastic analysis

In collaboration with theorists from Darmstadt, we worked out the signature of dark matter scattering inelastically off xenon nuclei, where the nucleus is excited to a low-lying state with subsequent fast de-excitation $\text{Xe}^* \rightarrow \text{Xe} + \gamma$ (39.6 keV). The observation of both elastic and inelastic channels in a xenon detector could provide information on the nature of the interaction, on the mass of the dark matter particle and eventually on the dark matter halo, as the two channels probe different regions of the dark matter velocity distribution [19].

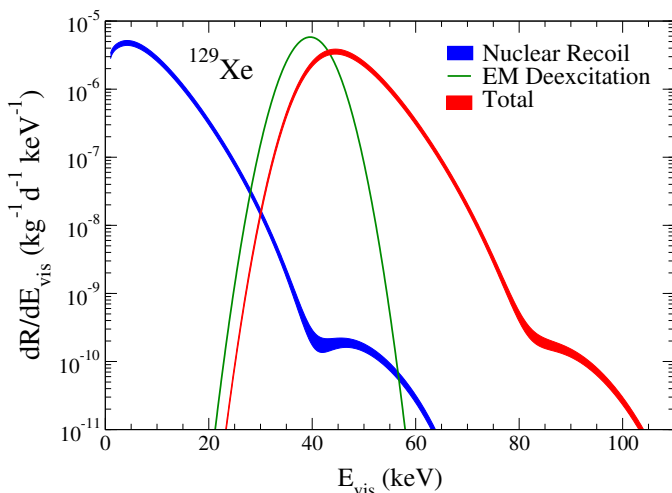


FIG. 4.4 – Decomposition of the energy spectrum for inelastic scattering off ^{129}Xe (see text) assuming a 100 GeV WIMP with $\sigma_{\text{nucleon}} = 10^{-40} \text{ cm}^2$, see [19].

In Fig.4.4, we show the expected components of the energy spectrum for inelastic scattering off ^{129}Xe . We are working on the analysis of the latest XENON100 physics data, where we study the total deposited energies in the S2 and S1 planes. The signal region is determined with AmBe neutron calibration data, see Fig.4.5. Since the search window differs from our standard WIMP analysis, we developed new cuts and studied their efficiency. We are performing a maximum likelihood analysis to determine the sensitivity of XENON100, which reaches down to $4.8 \times 10^{-38} \text{ cm}^2$ for 100 GeV WIMPs, improving upon earlier results by XMASS [20].

4.2.2 Bosonic SuperWIMPs

Bosonic SuperWIMPs are light (10-100 keV), super-weakly interacting dark matter candidates [21]. In the XENON100 detector, these could be observed via the axio-electric effect, where a SuperWIMP would be completely absorbed by a xenon atom, depositing an energy in the detector approximately equal to its rest mass. Such a signal would thus be found within the electronic re-

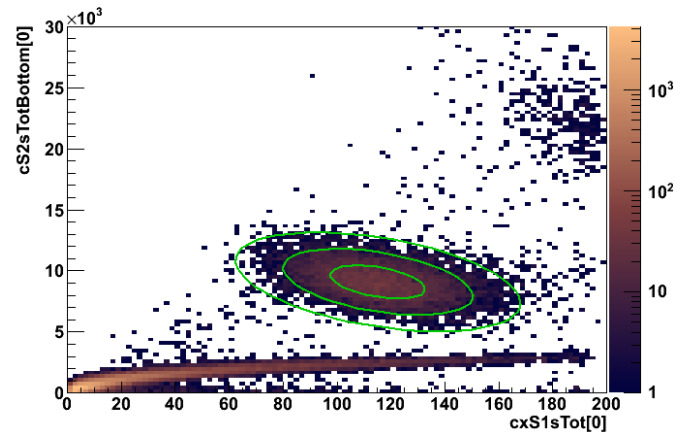


FIG. 4.5 – The signal region in S2 versus S1, determined with AmBe neutron calibration data with a two-dimensional Gaussian fit. The green ellipses indicate the 1-, 2- and 3- σ contours (for 39.6 keV γ + NR).

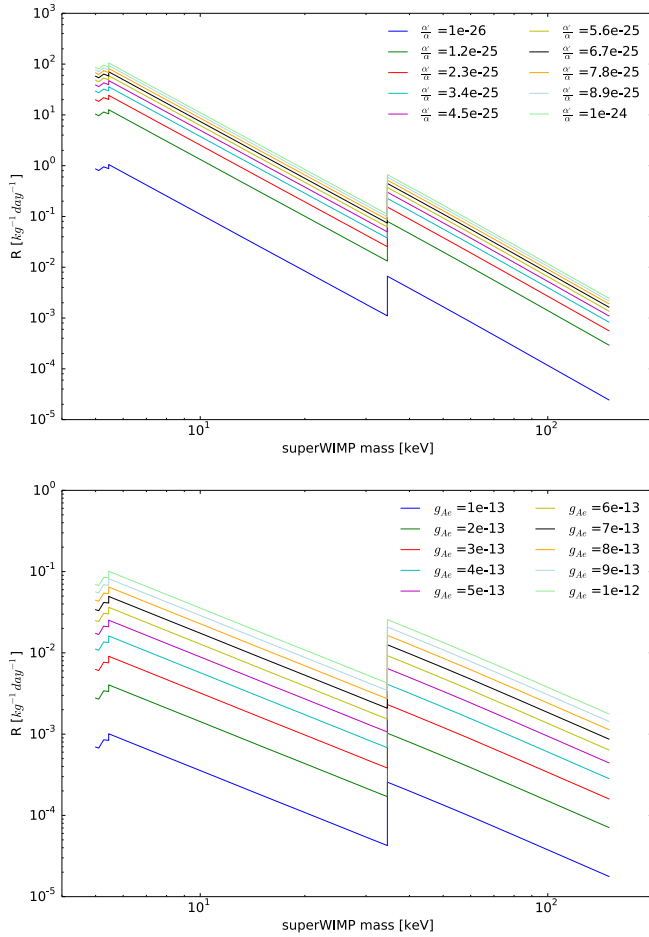


FIG. 4.6 – Predicted integral rates to be observed in the XENON100 detector for vector (top) and pseudo-scalar (bottom) bosonic SuperWIMPs for a range of couplings to electrons which are not (yet) excluded.

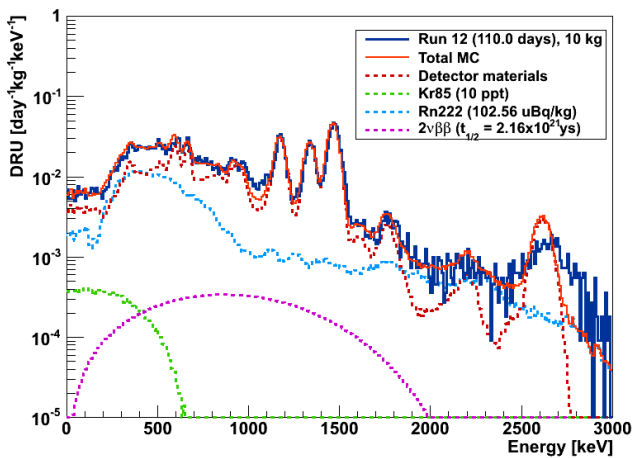


FIG. 4.7 – Measured and simulated energy distributions for a 10 kg LXe fiducial mass in XENON100. The simulation is based on material screening results. The main contributions are from detector materials and internal radon. The contributions from ^{85}Kr and ^{136}Xe decays are also shown.

coil band of events. The rate at which SuperWIMPs interact inside the detector depends on their type (pseudoscalar or vector), their coupling to electrons and their mass [21]. In Fig.4.6 we show the predicted integral rates in XENON100, for an assumed exposure of $225 \text{ d} \times 34 \text{ kg}$. We are analyzing the electronic recoil band of XENON100 for these type of signatures, with the goal of improving upon the sensitivity of XMASS [22] due to a larger exposure, a lower background and an extended energy region for the search. We have defined the physics cuts for the analysis, and are now developing a profile likelihood approach to calculate our sensitivity.

4.2.3 Background analysis

The main sources for the electronic recoil background in the XENON100 detector are radioactive contaminations in the detector materials, the intrinsic ^{222}Rn and ^{85}Kr radioactivity in LXe, and the decays of ^{222}Rn daughters inside the shield cavity. Extensive Monte Carlo simulations of the XENON100 detector were performed by our group with the GEANT4 software, using a detailed geometry and the measured radioactivity of all components [23]. Using this simulation, we are now comparing the predictions with the dark matter data taken during the latest science run, that lasted 153.8 live days. Figure 4.7 shows a preliminary comparison between the data acquired in this run and the MC predictions. To further improve the matching between data and MC, in particular at high energies, the position reconstruction of events in the various selected fiducial volumes is being investigated. Because the PMTs saturate for large S2 signals, this effect can lead to a misplacement of the interaction vertex at high energies, and thus affects the measured rate for a given fiducial volume.

4.3 The XENON1T time projection chamber

We participate in the design, production, assembly, and testing of the XENON1T TPC. The field cage, to be assembled at our institute, is made of high purity copper as the conductor and PTFE as insulator which also acts as an efficient reflector for LXe scintillation light. The TPC is designed with interlocking PTFE panels to account for the contraction when cooled down to -95°C . The cage has a height of 970 mm and a diameter of 960 mm, and may contain an active LXe mass of $\sim 2 \text{ t}$. To achieve a TPC drift field of $0.5 - 1 \text{ kV/cm}$, the cathode at the bottom, made from $200 \mu\text{m}$ wires, will be biased with -50 to -100 kV . The required field homogeneity is obtained with the help of 74 massive field shaping rings made from oxygen-free high conductivity (OFHC) copper. The geometry was optimized by simulation.

The field cage will be subjected to cryogenic and struc-

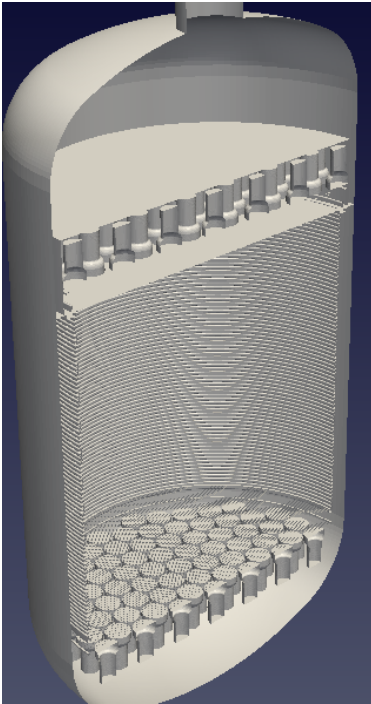


FIG. 4.8 – The implementation of the XENON1T geometry inside the newly developed field simulation software.

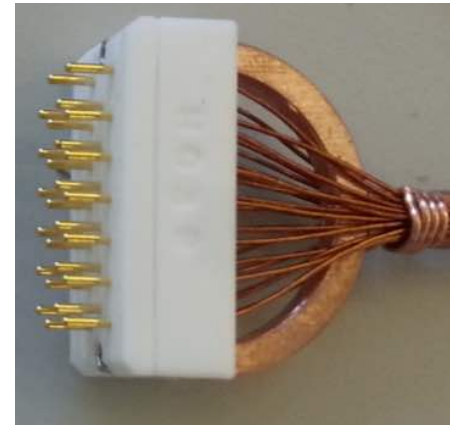
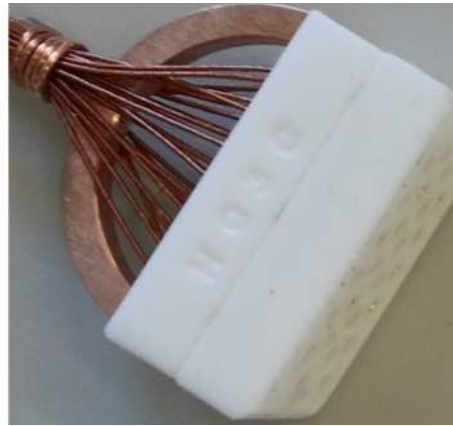


FIG. 4.9 – Custom-made connectors for XENON1T. Above: High voltage connector with Kapton cables and strain relief. Right: Signal coaxial cables with MMCX connectors in a PTFE holder structure.



tural integrity tests in a large dewar that can be cooled down to -95°C . Upon the successful completion of these tests, the cage will be disassembled and shipped to LNGS.

As indicated above, the design of the TPC was based on accurate electric field simulations. We had used the commercial simulation software *COMSOL Multiphysics* to simulate a first, axial symmetrical geometry of the detector. Because more detailed simulations were needed, a new software has been developed by our group. It uses the boundary element method, a numerical solution technique to solve Maxwell's equation and it is mainly based on the Kasper simulation package developed by the KA-TRIN [24] experiment. We are now able to calculate very large and complex geometries on fast parallelized computing platforms using GPUs. With the iterative Robin Hood [25] methods as charge density solver, the memory consumption has been greatly reduced. With this software, non axial symmetrical geometries of the detector were simulated, leading to the identification of the optimal electrode structures in the TPC. Fig.4.8 shows the implementation of the XENON1T geometry into our simulation software. We will extend it to include particle tracking, with the goal of increasing the reconstruction precisions of an interaction vertex inside the TPC. We will also provide the field corrections maps, needed after the commissioning of the TPC, once data taking starts.

We are responsible for the cables and connectors (signal and HV) on the xenon side, to power the PMTs and

extract the signal from the TPC. Due to strict background requirements of the experiment, and since the cabling will be located near the active volume of the TPC, ultra-low radioactivity cables and connectors are used. For the high voltage, we employ Kapton insulated copper wires connected with custom-made connectors (see Fig.4.9) made of PTFE and copper. The connector was tested to withstand up to 2.0 kV under realistic operating conditions. For the signal cable, a full coaxial connection is provided using PTFE insulated coax cables and MMCX connectors. The bunches of 24 signal cables each are held together by a PTFE structure, as shown in Fig.4.9.

The vacuum feed-throughs, shown in Fig.4.10, are made of epoxy with high thermal conductivity and low out-gassing. These are mounted on the so-called *porcupine*, Fig.4.11, a stainless steel vessel with several CF flanges. This vessel is directly connected to the large cable pipe through a CF100 elbow at the level of the cryogenic room.

In mid 2014, we have installed 900 cables into the pipe that guides them from the top of the TPC through the water tank, to the underground building. Because later access is complicated, we have already installed the required number of cables for XENONnT, including some contingency, as well. At the beginning of 2015, the cables with the feed-throughs were mounted on the porcupine and connected to the cables in the pipe. The porcupine was installed onto the pipe, and all the connections



FIG. 4.10 – Example vacuum feed-throughs for 10 high voltage and 10 signal cables.

were successfully tested. In mid 2015 the last sections of the cables will be connected to the PMT voltage dividers (bases) at UZH, then installed inside the TPC, connected and tested once more.

4.4 The XENON1T PMTs

The final version of the photomultiplier tube selected for XENON1T is the Hamamatsu R11410-21. It has been developed by Hamamatsu with extensive feedback from us regarding the requirements for dark matter searches, based on radioactivity measurements of all production components, and of the final product [26], and extensive tests performed in LXe. It is a 3-inch diameter tube and operates stably at -100°C and 2 atm [27]. Apart from a greatly reduced intrinsic radioactivity level, a major ad-

vantage is its high quantum efficiency (QE) at the xenon scintillation wavelength of 175 nm. With our HPGe facility at LNGS, we have screened 240 out of 283 PMTs. The results are satisfactory for XENON1T [26]. A mean value of $\text{QE} = 35\%$ has been observed with a few tubes reaching 40%. All tubes to be installed in XENON1T are tested at room temperature and at -100°C . Around 10% of them are tested at UZH in LXe to measure their performance in the conditions of a dark matter experiment. The main features that we monitor are the dark count rate, the gain evolution and the afterpulse rate before, during and after each cool down in LXe, which have a typical duration of a few weeks. In XENON1T all PMTs will be equalized in gain with the aim of achieving a peak-to-valley ratio in the SPE spectrum of around 4. This ensures a good separation of the single photoelectron signal from the noise component of the spectrum. As we show in Fig.4.12, this is achieved at gains above 2×10^6 .

After completing the cryogenic tests for the remaining tubes for XENON1T, all PMTs will be mounted on their support structures of the top and bottom arrays, tested once again and then brought to LNGS for integration into the TPC.

18

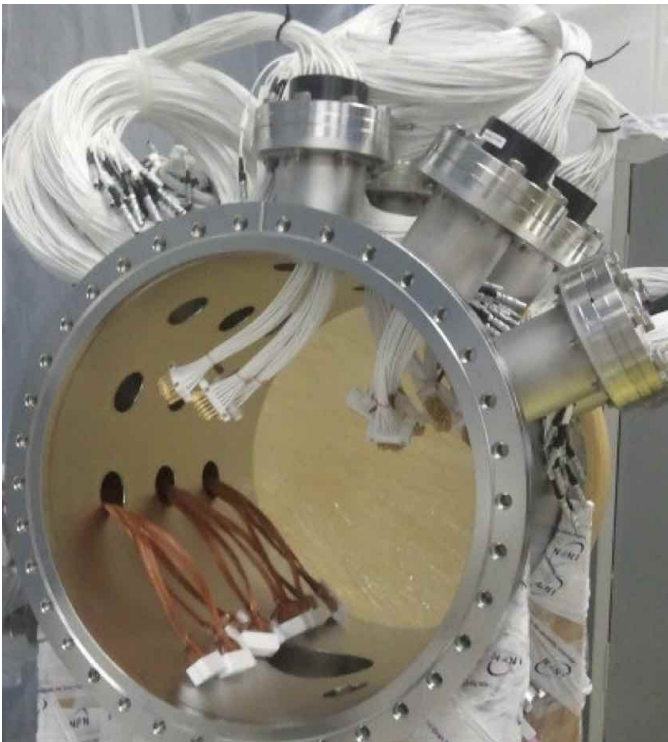


FIG. 4.11 – Porcupine with mounted signal and high voltage feed-throughs (nipples on the side open).

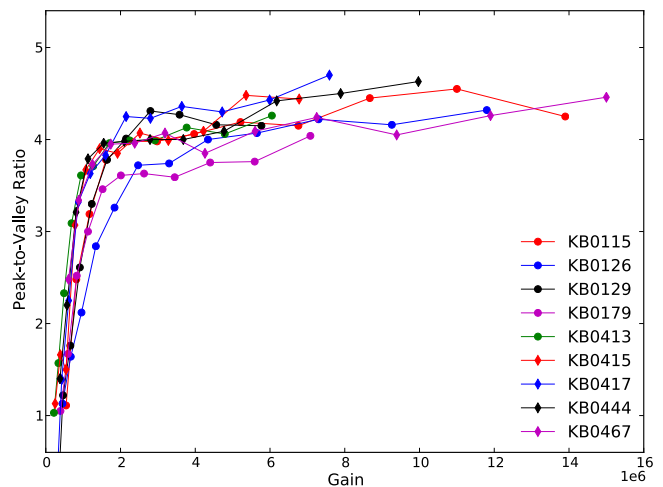


FIG. 4.12 – Peak-to-valley ratio as a function of gain. At a gain of about 2×10^6 the PMTs reach a sufficiently high peak-to-valley ratio.

Several voltage-divider layouts have been tested resulting in a design with a power dissipation of $<0.025\text{ W/PMT}$ showing good linearity over the full DAQ range at low rate. Currently, the printed circuits are being produced. Once these arrive at UZH, we will produce all bases for XENON1T, test them and mount them onto the PMTs. We will also perform final linearity tests.

In the next two years, we will develop the bases for XENONnT, which have even stricter requirements on the radioactivity levels of the components.

4.5 The XENONnT and DARWIN projects

Most major XENON1T components are designed such that a doubling of the detector mass will be feasible once the science goals of XENON1T have been achieved. The underground infrastructure, in particular the water shield, the xenon storage vessel, the cryogenic system, the cryostat support, the outer cryostat vessel and the connection pipe to the building can be reused for XENONnT. The DAQ system for XENON1T is designed such that it can be upgraded for the ~ 200 extra channels of XENONnT without new developments. The main remaining work will be to design and build a new TPC capable of being biased with higher cathode voltages, and to lower the intrinsic backgrounds from radon and krypton further. XENONnT will be developed and various parts will be constructed while XENON1T is taking science data, utilizing the experience gained from the new experiment, and is expected to take science data by 2018.

DARWIN is an ultimate WIMP detector with a sensitivity down to 10^{-49} cm^2 . At these cross-sections, neutrino interactions, which cannot be reduced by target fiducialization, will limit the sensitivity to WIMP interactions [11]. With a target mass of about 20 tons, this project would be the successor of XENONnT, possibly installed inside the XENON1T water tank. Currently our R&D is focused on topics where we have experience from XENON: design and prototyping of the time projection chamber, Monte Carlo simulations of the radioactive background, new light read-out schemes and tests of light sensors in noble liquids, material screening with high-purity germanium spectroscopy, as well as the science impact of the facility. We additionally perform charge and light yield measurements of nuclear and electronic recoils in LXe at low energies, which are necessary to define accurate energy scales in noble liquid dark matter detectors. The R&D and design phase will end by 2019, after which the construction phase of the various sub-systems is to start. The detector would be installed and commissioned underground starting in 2021, with a first science run to start by 2023. The facility would be operated for at least 5 years, thus until 2027, possibly longer.

- [1] Planck Collaboration, *Planck 2015 results. XIII. Cosmological parameters*, (2015) arXiv:1502.01589.
- [2] M.W. Goodman and E. Witten, *Phys. Rev. D* 31 (1985) 3059.
- [3] L. Baudis, *Phys. Dark Univ.* 1 (2012) 94.
- [4] D.Yu. Akimov *et al.*, *Phys. Lett. B* 709 (2012) 14.
- [5] J. Angle *et al.*, XENON Collaboration, *Phys.Rev.Lett.* 100 (2008) 021303.
- [6] E. Aprile *et al.*, XENON100 Collaboration, *Phys. Rev. Lett.* 109 (2012) 181301.
- [7] D.S. Akerib *et al.*, LUX Collaboration (2013) arXiv:1310.8214.
- [8] M. Bossa, DarkSide Collaboration, *JINST* 9 (2014) C01034.
- [9] M.G. Boulay, DEAP Collaboration, *J.Phys.Conf.Ser.* 375 (2012) 012027.
- [10] D.C. Mallin *et al.*, *After LUX: The LZ Program*, (2011) ARXIV:1110.0103.
- [11] L. Baudis, DARWIN Consortium, *J.Phys.Conf.Ser.* 375 (2012) 012028.
- [12] R. Agnese *et al.*, SuperCDMS Collaboration, *Search for Low-Mass WIMPs with SuperCDMS* (2014) ARXIV:1402.7137.
- [13] H. Kraus *et al.*, *PoS IDM2010* (2011) 109.
- [14] P. Cushman *et al.*, *Snowmass CF1 Summary: WIMP Dark Matter Direct Detection* (2013) ARXIV:1310.8327.
- [15] Elena Aprile and Laura Baudis, *Liquid noble gases, in Bertone, G. (ed.): Particle dark matter* (2010) 413.
- [16] D.Yu. Akimov *et al.*, ZEPLIN-III Collaboration, *Nucl.Instrum.Meth.* A623 (2010) 451.
- [17] E. Aprile *et al.*, XENON100, *Astropart. Phys.* 35 (2012) 573.
- [18] Laura Baudis, *PoS IDM2010* (2011) 122.
- [19] L. Baudis *et al.*, *Phys.Rev.* D88 (2013) 115014.
- [20] H. Uchida *et al.*, XMASS-I Collaboration, *PTEP* 6 (2014) 063C01.
- [21] M. Pospelov, A. Ritz and M.B. Voloshin, *Phys.Rev.* D78 (2008) 115012.
- [22] K. Abe *et al.*, XMASS Collaboration, *Phys. Rev. Lett.* 113 (2014) 121301.
- [23] E. Aprile *et al.*, XENON100 Collaboration (2011) *Phys.Rev.* D83 (2011) 082001.
- [24] R.G. Robertson *et al.*, KATRIN Collaboration, *KATRIN: an experiment to determine the neutrino mass from the beta decay of tritium* (2013) ARXIV:1307.5486.
- [25] J.A. Formaggio *et al.*, *Solving for Micro- and Macro-Scale Electrostatic Configurations Using the Robin Hood Algorithm*, ARXIV:1111.5035.
- [26] E. Aprile *et al.*, XENON Collaboration *Lowering the radioactivity of the photomultiplier tubes for the XENON1T dark matter experiment* (2015) arXiv:1503.07698.
- [27] L. Baudis *et al.*, *JINST* 8 (2013) P04026.

5 DAMIC: search for dark matter using CCD detectors

J. Liao, B. Kilminster, and P. Robmann

in collaboration with: Fermi National Accelerator Laboratory, University of Chicago, University of Michigan, Universidad Nacional Autónoma de México, Universidad Nacional de Asunción de Paraguay

(DAMIC Collaboration)

The main challenge in searching for low mass DM is measuring the low energy deposit of the associated nuclear recoils in the detection material. DAMIC (Dark Matter in CCDs) aims at the search for WIMPs in the mass region below 5 GeV by detection the feeble ionization signals produced by WIMPs colliding with nuclei inside low noise CCDs. DAMIC uses CCDs with an electronics noise of $\sigma=7.2$ eV. This leads to a $5\sigma=36$ eV threshold, which is the lowest of any current DM detector.

CCD detectors are silicon pixel detectors that shift charge from the capacitor of one pixel to the next by generating potential wells until reaching a charge amplifier which converts the charge to voltage (see Fig. 5.1). The DAMIC CCD detectors were fabricated by Lawrence Berkeley National Laboratory [1] originally for the Dark Energy Camera (DECam) [2, 3]. DECam CCDs [4] are good candidates for a DM search since they are 30 times thicker (500 - 650 μm) than commercial CCDs, leading to proportionally higher interaction rates. Each CCD has up to 16 million 15 $\mu\text{m} \times 15 \mu\text{m}$ pixels and is read by two amplifiers in parallel. The electronic gain is $\sim 2.5 \mu\text{V}/e$. The signal is digitized after correlated double sampling and the noise performance improves by reducing the readout speed. The lowest noise, $\sigma < 2e^-$ (R.M.S.) per pixel, was achieved with readout times of 50 μs per pixel [5].

First results were obtained with a single 0.5 g CCD, installed ≈ 100 m underground in the NuMI [6] near-detector hall at Fermilab. Data were collected during 11 months in 2011. Standard techniques were used to

interpret the results as a cross section limit for spin-independent DM interactions [7], and parameterizations were used allowing the direct comparison with other limits on low mass DM particles. At the time, the DAMIC results constituted the best limits for dark matter mass below 4 GeV.

- [1] S.E. Holland *et al.*, IEEE Trans. Electron Dev., **50** 225 (2003).
- [2] B. Flaugher, *Ground-based and Airborne Instrumentation for Astronomy*, Ian S. McLean editor; Iye, Masanori, Proceedings of the SPIE, Volume 6269, (2006).
- [3] Dark Energy Survey Collaboration, astro-ph/0510346.
- [4] J. Estrada and R. Schmidt, *Scientific Detectors for Astronomy 2005*, J.E. Beletic, J.W. Beletic and P. Amico editors, Springer (2006).
- [5] Estrada *et al.*, Proceedings of SPIE 2010.
- [6] <http://www.numi.fnal.gov/PublicInfo/forscientists.html>.
- [7] J. Barreto *et al.* (DAMIC Collaboration), Phys. Lett. B **711**, 264 (2012).

20

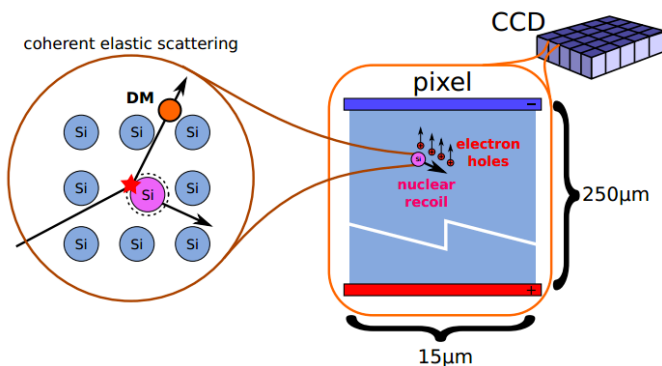


FIG. 5.1 – DAMIC detection principle: hypothetical dark matter particles scatter coherently off silicon nuclei, producing a nuclear recoil that is recorded as charge on pixels in the CCD.

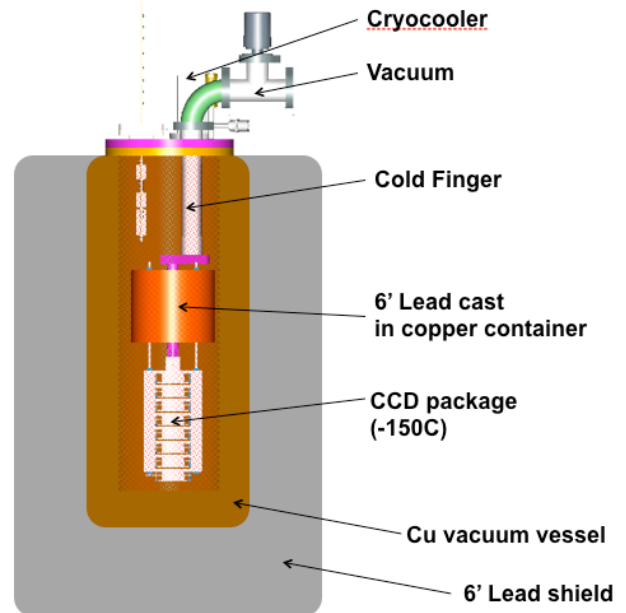


FIG. 5.2 – Schematic of the DAMIC-100 vacuum vessel with copper and lead shielding.

DAMIC

Charge-coupled devices (CCDs) as low threshold, low background particle detectors.

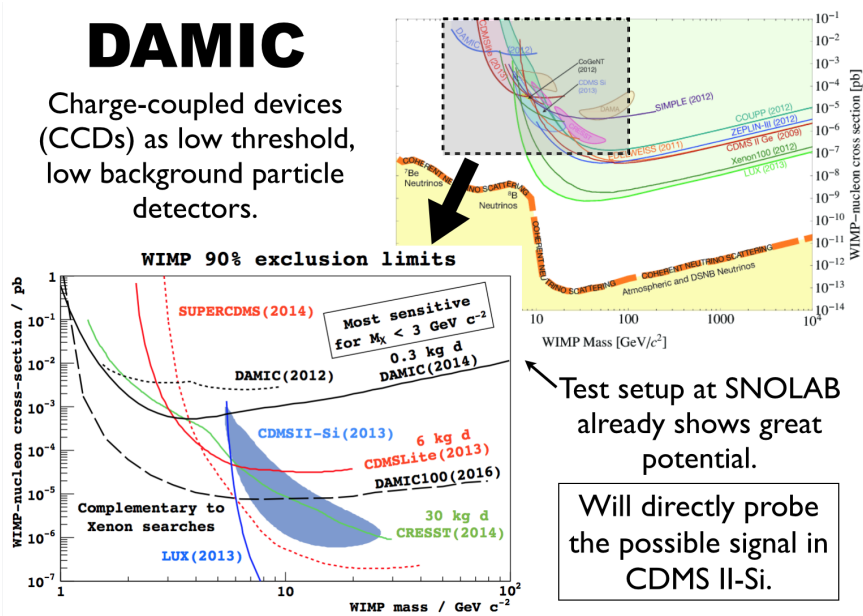


FIG. 5.3 – Result of DAMIC 0.3 kg · days and the expected sensitivity of DAMIC-100 (2016).

5.1 DAMIC-100

The next phase is DAMIC-100, which has begun collecting commissioning data in the summer of 2014. The experiment has been moved underground to SnoLab, which has a 6000 meter water equivalent shielding from cosmic rays, the shielding has been upgraded, and new, thicker detectors have been fabricated. A schematic of the new setup is shown in Fig. 5.2. The CCDs, with a total mass of 100 g, are installed inside a copper box cooled to -150°C to reduce dark current. The cold copper also shields the detectors against infrared radiation. A closed cycle helium gas refrigerator is used to maintain the low temperature. The detector is connected through a readout cable to the preamplifiers located outside the lead shield. The detector package is housed in a cylindrical vacuum vessel fabricated with oxygen-free copper, and maintained at 10^{-7} Torr with a turbo molecular pump. Lead and polyethylene shield against γ -rays and neutrons.

The detector has been iteratively improved in 2014, with a low background lead shield machined at the University of Zurich, and newly designed readout cables provided by the University of Zurich. Using 0.3 kg·day of DAMIC data taken from three CCDs in 2014, DAMIC has obtained a preliminary limit which constitutes the best constraint on DM particles with mass below 4 GeV, Fig. 5.3. Expectations with the full 100 grams of CCDs, and some additional reductions of backgrounds are also shown as DAMIC 100.

5.1.1 Calibration and testing

Energy calibration for DM in the detector is factorized into the ionization energy calibration as determined from

direct X-rays and carbon and oxygen fluorescent X-rays from a Fe^{55} source and the signal quenching observed for ionizing nuclear recoils. The quenching factor has been measured in Si for recoil energies above 4 keV [1], showing good agreement with the Lindhard model [2, 3].

We have helped design and test an experiment at the Tandem Van der Graaf of the University of Notre Dame in which monochromatic neutrons are scattered off a silicon target and the scattering angle and neutron time-of-flight are used to determine the nuclear recoil energy. The scattered neutrons are detected with 19 scintillating bar counters placed at angles between 20 and 70 degrees (see Fig. 5.4) corresponding to the low recoil energies of interest between 1 and 30 keV.

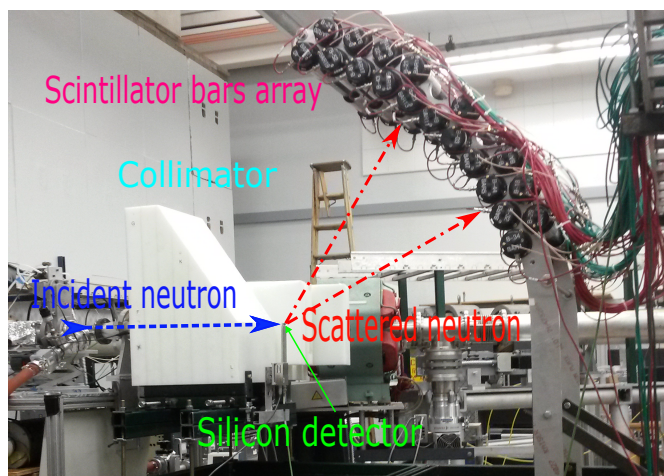


FIG. 5.4 – The setup of the quenching factor measurements at Notre Dame.

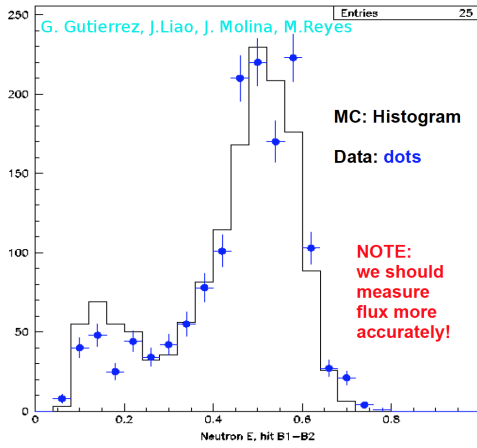


FIG. 5.5 – Neutron flux comparison between data and Geant4 simulation for 2013 beam test.

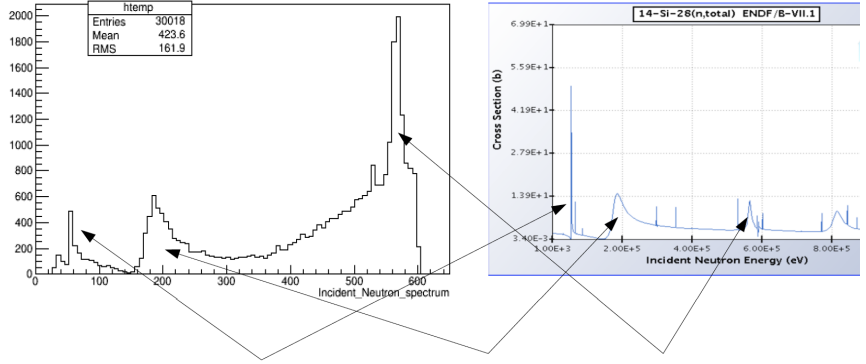


FIG. 5.6 – Neutron resonances shown in Geant4 simulation (left) and NNDC database (right) [4]. Note that the left plot is the convolution of our incident neutron flux (Fig. 5.5) and the neutron silicon cross-section (right plot).

We also developed a Geant simulation of the setup to confirm the neutron beam flux (Fig. 5.5), and to determine the resonance structure for the cross-section of ~ 100 keV incident neutrons on silicon, as shown in Fig. 5.6. With this model we were able to solve some unexpected discrepancies in the data. Based on the beam test of 2013 and the Geant4 simulation for the 2015 beam test, we expect to produce uncertainties greatly improved compared to previous measurements as in Fig. 5.7.

22

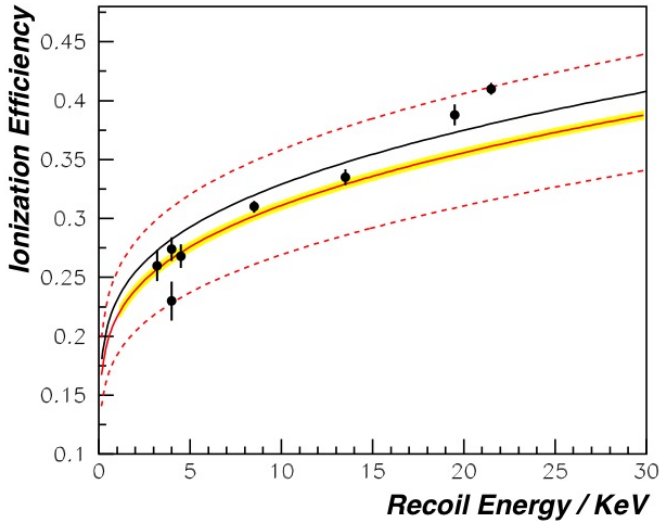


FIG. 5.7 – Silicon quenching factor versus recoil energy. Black dots with error bars: data measured in 2013. Solid red line: single parameter χ^2 fit based on the Lindhard model [2]. Dashed red lines: 1σ error band of the fit. Yellow band: 1σ error band expected for 2015, when the recoil energy will cover the region 1-30 keV.

5.1.2 CCD CTI study

The charge deposited in a CCD pixel is shifted across thousands of pixels by row and column to two corners of the CCD and read out by amplifiers. The ratio of lost to total charge is called Charge Transfer Inefficiency (CTI) [5]. We determine the CTI with 5.9 keV X-rays from Fe-55, which produces about 1600 e^- . We found the CTI of DAMIC CCDs to be $3.0E^{-7}$, as compared to a typical CTI from 2001 of $\sim 1.0E^{-6}$ [5].

5.1.3 Monitoring and data analysis

To reach the projected sensitivity of DAMIC-100 we need to determine the noise, dark current, energy response, backgrounds, map of dead and hot pixels for each CCD, with optical light and X-ray sources. We have developed a monitoring system of the data quality which allows to correlate temperature, voltage, and pressure inside the detector cryostat, with dark current, RMS detector noise and X-ray radio-impurities of each individual CCD for each of the thousands of exposures expected during one year of data taking. There is a web page interface to visualize the information in real time, and store everything for off-line data analysis when the signal efficiency and background rejection will be optimized.

5.1.4 EFT analysis of DAMIC data

The momentum transfer q in direct detection is typically a few hundred MeV/c or less so DM-nucleus scattering can be described by a non-relativistic effective potential depending on DM velocity $v \sim 10^{-3}c$ and q/Λ , where Λ is some scale involved, such as the DM mass, the nuclear mass or a heavy mediator mass [6]. Detected energy is affected by quenching, as discussed above, and by the

detector response. The quenching factor was calculated using the Lindhard model [2].

EFT (Effective Field Theory) provides a general scheme to characterize the experimental results with a small set of parameters, such as the WIMP mass and the effective coupling constants [7–9]. There exist 14 “useful” EFT operators with varying powers of v, q and mass scales and we have determined the event rate versus detected energy for each of them. Two examples are shown in Fig. 5.8. This will allow us to determine limits on cross-section versus DM mass for the various operators. Thanks to the low energy threshold of DAMIC certain EFT operators will be probed for the first time.

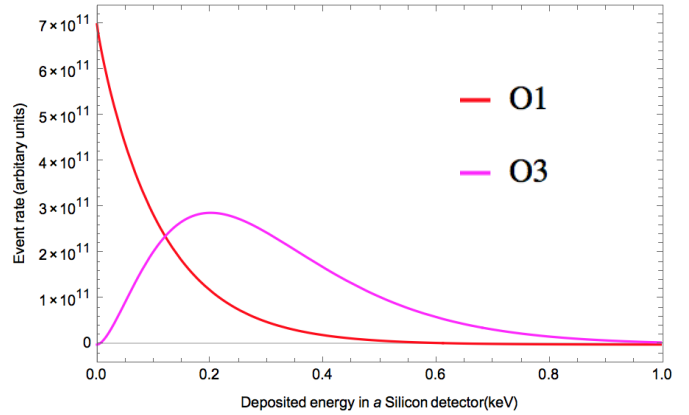


FIG. 5.8 – Comparison of the distributions of deposited energy for the $\mathcal{O}1$ and the $\mathcal{O}3$ operator, assuming a 3 GeV incident WIMP. The DAMIC energy threshold is 0.04 keV.

- [1] J.D. Lewin and P.F. Smith, *Astropart. Phys.* 6, 87 (1996).
- [2] J. Lindhard, V. Nielsen, M. Scharff, and P.V. Thomsen, *Mat. Fys. Medd. Dan. Selsk* 33, 10 (1963).
- [3] H. Chagani *et al.*, *JINST* 3 (2008) P06003.
- [4] <http://www.nndc.bnl.gov/sigma/index.jsp>.
- [5] J. R. Janesick, *Scientific Charge-Coupled Devices* (SPIE Press, Bellingham, WA), 101 (2001).
- [6] J. Fan, M. Reece and L.-T. Wang, *JCAP* 11 (2010) 042.
- [7] B. A. Dobrescu and I. Mocioiu, *JHEP* 0611, 005 (2006).
- [8] Nikhil Anand *et al.*, *Phys. Rev. C* 89. 065501(2014).
- [9] A. Liam Fitzpatrick *et al.*, *JCAP* (2013) 004.

6 Very High Energy Gamma Ray Astronomy with CTA

F. Canelli, D. Florin, A. Gadola, S. Steiner, U. Straumann, A. Vollhardt, D. Wolf

in collaboration with: ETH Zürich, Jagiellonian University Cracow, MPI für Kernphysik Heidelberg, Universität Tübingen, Universität Erlangen, Universität Innsbruck and over hundred institutes from 31 countries

(CTA)

The Cherenkov Telescope Array (CTA) is our best candidate for the next generation of Imaging Atmospheric Cherenkov Telescopes (IACTs). IACTs are used to detect very high energy gamma rays (from GeV to tens of TeV). Sources for such gamma rays are both galactic and extragalactic, including quasars, supernovae and their remnants, gamma-ray bursts, and possibly dark matter annihilations. The signal to be detected is a faint and very fast Cherenkov light flash, allowing the reconstruction of the primary gamma ray's energy and direction.

CTA is approaching the final R&D stage aiming at a first telescope on site in 2016/17. We contribute primarily to the production of a mirror alignment system (see report from 2011/12) and the design and production of the body and the photomultiplier-based detector modules of the first fully digital IACT camera. The past year was devoted mainly to the completion of the camera body mechanics and safety system, preparations for the production of the large series of detector prototype modules and to the writing of the technical design report which will be completed soon.

6.1 FlashCam

FlashCam [1] is a camera design suited for the mid-size telescopes of CTA. The output signals of 1764 photomultiplier tubes are amplified and transmitted via commercial CAT6 cables to the readout electronics which digitizes them at a rate of 250 MS/s and with a dynamic range of 12 bit. The digitized signals are then combined to form patches of up to 21 channels uniformly distributed over the whole pixel area. The real-time evaluation of the patch-information generates a trigger for the readout of the whole camera. The pixel data are sent to a server for post-processing to be collected by the array's computer farm where the information of several telescopes may be combined.

FIG. 6.1 – Camera seen from the back with doors open.

The four bluish modules mounted at bottom and top of the two electronic racks are the heat exchangers with associated fan drawers. The safety control cabinet (see Sec. 6.1.2) is seen in the lower half of the left rack. The remaining rack space is allocated to readout crates. Two empty crates can be seen in the rack on the right.

The main parts developed at UZH are the detector modules and the camera body including the mechanics, the cooling system and the safety control system. Last year mainly engineering tasks have been performed and a big step was made towards a fully functional camera.

6.1.1 The camera body mechanics and cooling

The camera body (see Fig. 6.1), a 3x3x1 m³ shelter for the camera electronics, has been completed during the last year and is now at a stage where different tests of the electronics and the mechanics can be performed.



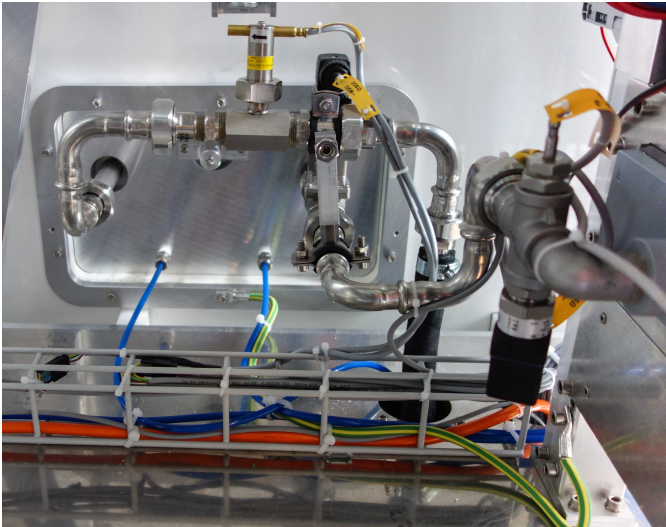


FIG. 6.2 – Panel with in- and outlet of the cooling liquid for the heat-exchangers. The necessary temperature, pressure and flow sensors are installed.

The cooling of the electronics is realized with water-air heat exchangers. The readout electronics and the safety control cabinet are installed into two racks forming four sectors. Each sector has its own heat exchanger including speed-regulated fan drawers. Figure 6.2 shows the piping of the cooling system installed in the camera body. First tests have shown a good performance. Figure 6.3 shows for instance the dependency of the cooling system pressure drop on the liquid flow. Such characterizations of the system are needed later for the operation in the moving telescope to compensate for the elevation of the camera.

A camera window protecting the sensitive electronics and optics against water, dust, and even animals was foreseen from the beginning. It turned out difficult to find a producer of large UV-transparent windows with the required optical quality. A 'dummy' Plexiglas test window was installed recently instead (see Fig. 6.4), doubling the thermal resistance ($R_{th} \sim 8.5$ K/kW before and

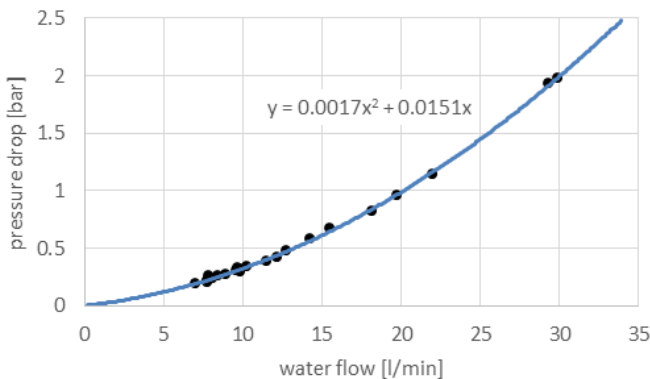


FIG. 6.3 – Pressure drop of the camera cooling system versus liquid flow, as measured with the sensors of the control system (black dots). The data show a quadratic dependency.

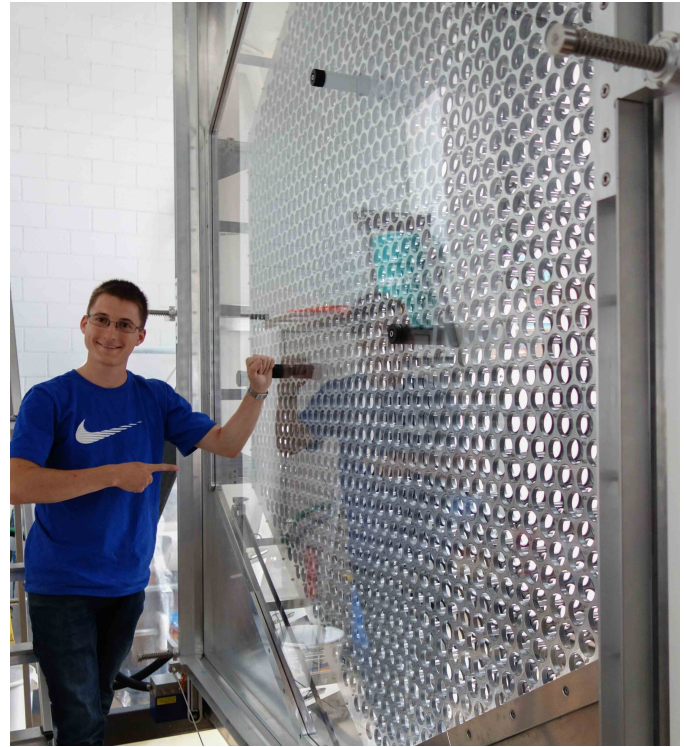


FIG. 6.4 – David Wolf in front of the Plexiglas test window mounted on the detector support. Three pixels had to be sacrificed to support the window and prevent damage under its own weight while the camera is rotated.

~ 18.0 K/kW after installation).

The equipment must resist heavy rain and even hail. While the water tightness will be tested by the end of May 2015, the hail tests have already started as a bachelor work with encouraging results so far.

The camera body will be mounted into a prototype telescope structure in Adlershof near Berlin (see also last year's report). The loading and unloading of the camera into the telescope's camera frame, the cooling performance under different elevation angles, and the mechanical compatibility will be tested. These results may lead to some modifications in the two planned pre-series camera bodies.

6.1.2 The camera safety control

The safety control system of the camera (shown in Fig. 6.5) must protect the camera electronics under all circumstances. The system, containing a variety of sensors for parameters like ambient light, temperature, pressure, water leaks, current and power supply performance, is built around the rugged and compact FPGA based compact RIO (cRIO) system of National Instruments. In very critical cases the implementation is totally hardwired. Elaborate sequences involving all possible situations, for instance the opening and closing of the cam-



FIG. 6.5 – The safety control cabinet with circuit breakers for the 230 VAC safety and 3x400 VAC physics power and the redundant 24 VDC power supplies. The cRIO control system is installed at the top left side.

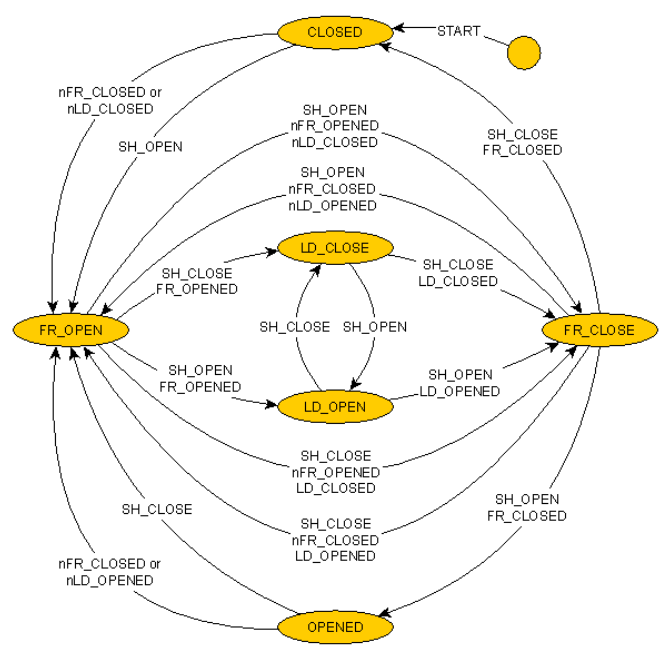


FIG. 6.6 – State diagram for the opening and closing procedure of the camera lid as hardwired in the safety control.

26

era lid (Fig. 6.6), have been developed. A Labview graphical user interface steers all functionalities.

Figure 6.7 shows the block diagram of the safety system as currently implemented in the prototype camera. Tests of the different functionalities have been performed successfully.

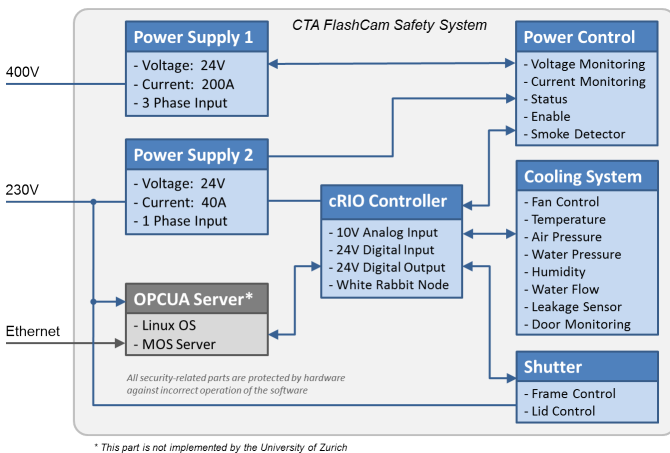


FIG. 6.7 – Block diagram of the camera safety system as implemented in the prototype camera.

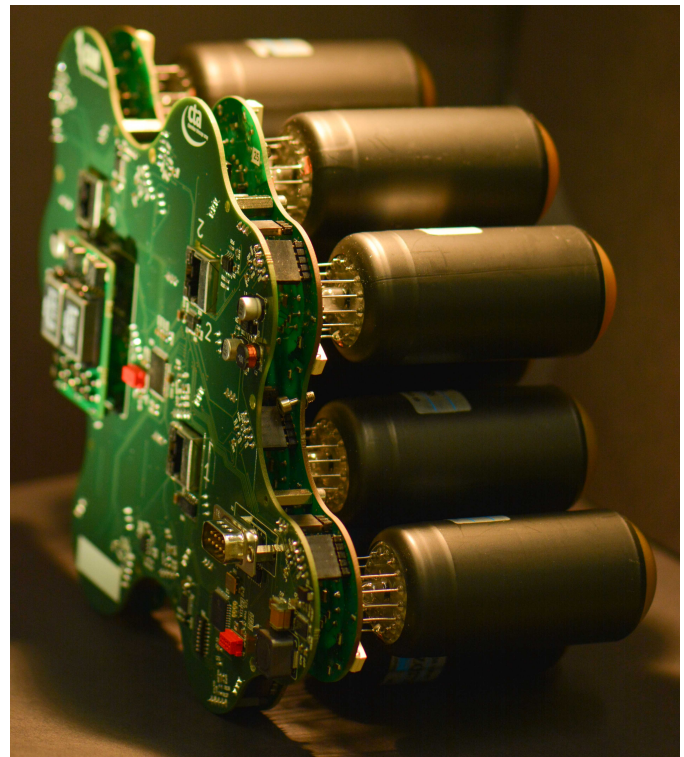


FIG. 6.8 – The latest version of the detector module with twelve PMTs. The small piggyback board houses the high-voltage generators.

6.1.3 The photon-detector module

The photon-detector module (Fig. 6.8) has already been presented in more detail in last year's report. The module has twelve photomultiplier tubes, high-voltage generators, amplifiers, a CAN-bus controller and a micro-controller on board. The amplified analogue signals of the detectors are transmitted via commercial CAT6 cables to the readout electronics. Since last year, small improvements have been made on the electronics and finally the electronics for 70 modules have been ordered. This will fill half of the camera (in total there will be 147 modules installed). Half of this order will be equipped with 8-dynode PMTs while the other half will have 7-dynode PMTs, which have the same dimensions but different pinout and a marginally better timing performance. The mixed assembly in the prototype camera will allow a cross-check of the two PMTs and their performance and help to choose the best candidate for the final version of the photon-detector module.

The wire-up scheme of the over 440 cables from the photon-detector modules to the readout is a tricky task especially without having enough modules at hand where the cables can be plugged into. Cheap dummy boards with heating resistors to simulate the power dissipation and a CAN-bus controller to test the CAN bus chain have been developed and installed in the camera (Fig. 6.9). Together with the real modules they will complement the camera to test the possible wire-up options, which currently are evaluated. More dummy boards have been ordered to complete the whole camera and to finalize the cabling without having to use the more fragile photon-detector modules.

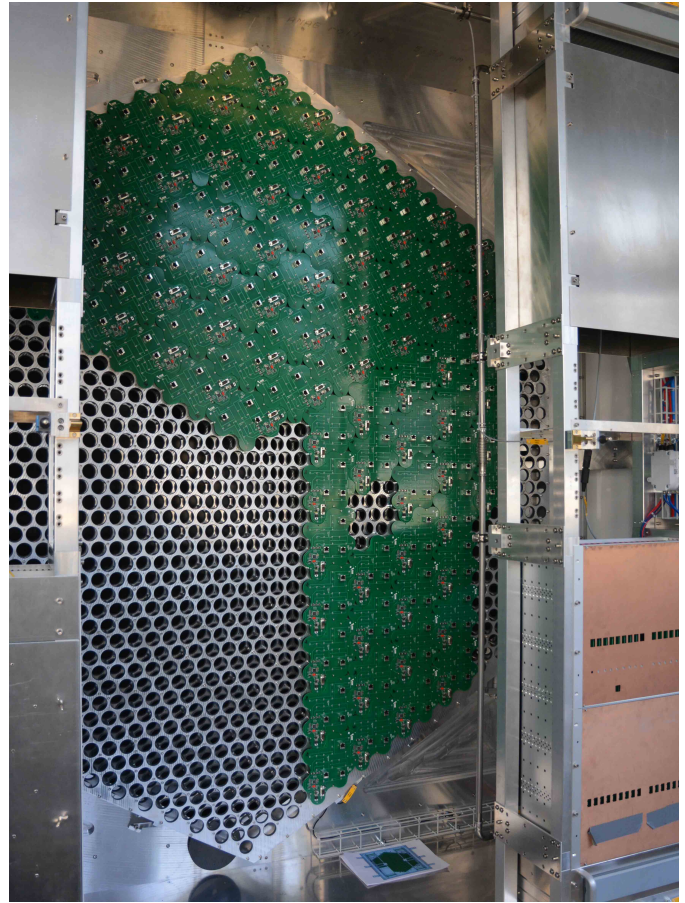


FIG. 6.9 – Rear view of the open camera. About half of the photon-detector plane is already equipped with dummy heating boards.

- [1] G. Pühlhofer *et al.*, (FlashCam Collaboration), arXiv 1211.3684 [astro-ph.IM] (2012).

7 Search for the rare decay $\mu^+ \rightarrow e^+ e^- e^+$

R. Gredig, P. Robmann, and U. Straumann

in collaboration with: University of Geneva, Paul Scherrer Institute, ETH Zürich, University of Heidelberg, University of Mainz, Karlsruhe Institute of Technology

(Mu3e Collaboration)

Mu3e is a proposed experiment searching for the charged-lepton-flavour violating decay $\mu^+ \rightarrow e^+ e^- e^+$, aiming at a sensitivity to its branching ratio B down to 10^{-16} and better [1]. In the standard model charged lepton flavour violation is highly suppressed, so a discovery would clearly present physics beyond the standard model. The aimed sensitivity is four orders of magnitude beyond the limit set by the SINDRUM experiment [2]. Muon number violation has already been searched in many channels and recently MEG, for example, set an upper limit of 5.7×10^{-13} in the $\mu^+ \rightarrow e^+ \gamma$ channel [3].

7.1 Scintillating Fibres

28

The University of Zurich is mainly involved in developing a scintillating fibre detector located in the center module of the detection setup (see Fig. 7.1). The fibres will be combined to 16 mm wide ribbons, containing three or four layers. Currently, different types of fibres are under investigation. Whereas the universities of Geneva and Zurich and ETHZ focus on round 250 μm thick doubly cladded fibres, with the option of an additional titanium dioxide coating, the Paul Scherrer Institute (PSI) investigates square fibres.

7.2 Fibre Ribbon Performance Testing

In the past year a test setup has been developed for the examination of several multi-layer fibre ribbons matching the final design (three to four layers, 16 mm wide). 32 fibres can be read out on both ends. The photons are detected with a modular three stage system. The first stage is a board holding the silicon photomultipliers (SiPMs) and a high voltage distribution system. The second stage is a PCB directly connected to this sensor-board, containing a signal amplifier that can drive a 50 Ω signal cable. The third stage digitizes the data with eight daisy chained DRS4 evaluation boards [4] and an additional DRS4 board recording the trigger signals.

The ribbon performance has been tested by irradiation with a ^{90}Sr -source and at the PSI piM1 test-area with a beam momentum of 161 MeV/c. The goal was to measure the light yield and time resolution and check the simulation results presented in last years Annual Report.

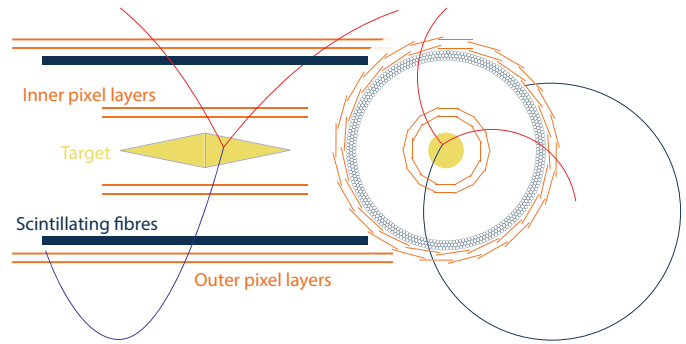


FIG. 7.1 – Central region of the Mu3e setup in the zy and xy projections. The central fibre tracker consists of three layers of 250 μm fibres with a length of 36 cm.

7.2.1 Readout electronics

The second generation sensor-board, shown in Fig.7.2 holds 16 individual SiPMs (the first generation board had a monolithic 4x4 SiPM module) that can be biased individually. The small sensitive area of only $1 \times 1 \text{ mm}^2$ results in a relatively low dark-count rate of $\mathcal{O}(10^5)$ photoelectrons. A third version of the board will allow to connect a variety of DAQ systems including different ASICs considered for the final design.

Because of the lack of a common clock on all boards, it was unclear how precisely the trigger signal propagates through them, so this had to be measured. A test-pulse was split in two and the resolution of the time difference Δt was found to be $\sigma_{\Delta t} \approx 232 \text{ ps}$. Assuming that all channels have a resolution σ_t , the resolution of the DAQ system is $\sigma_t = \sigma_{\Delta t} / \sqrt{2} \approx 165 \text{ ps}$.

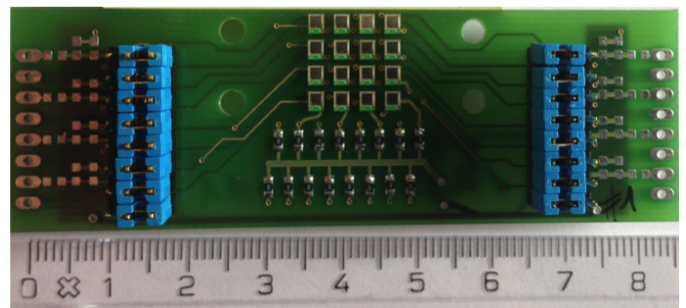


FIG. 7.2 – Second generation sensor-board with 16 individual $1 \times 1 \text{ mm}^2$ sensors.

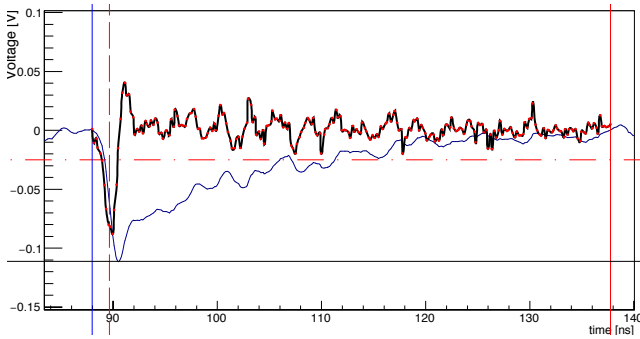


FIG. 7.3 – A fibre waveform. Both the original (blue) and the differentiated signal (black) are shown. Various observables are determined. The signal amplitude (horizontal black line) is the minimal value of the original waveform. The signal time (vertical dashed red line) is the centroid of the negative peak in the differentiated waveform. The signal integral is the sum of the original waveform over the window marked by the vertical blue and red lines.

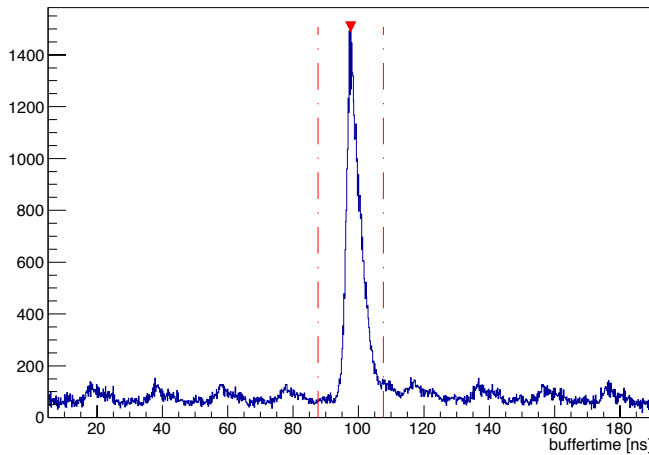


FIG. 7.4 – Time difference between fibre signals crossing a threshold just above the electric noise and a reference trigger counter. The periodic structure of accidental coincidences results from the 50 MHz PSI cyclotron frequency. The red markers show the window used in this analysis.

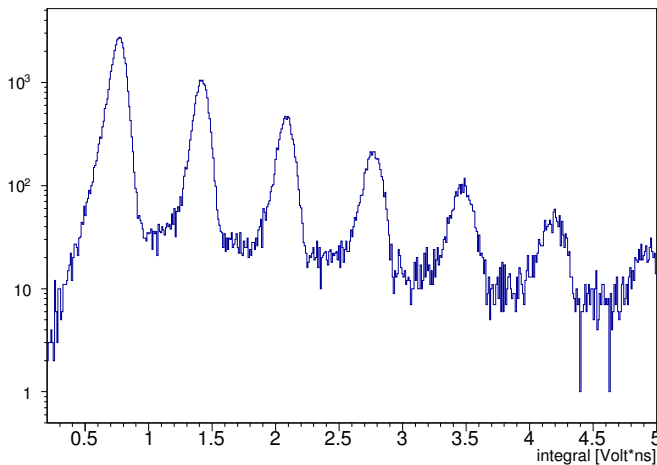


FIG. 7.5 – Histogram of signal integrals for one of the fibres showing well-separated peaks associated with the number of observed photo-electrons.

7.2.2 Signal Analysis

Figure 7.3 shows a typical waveform produced with the PSI positron beam. Under investigation was Kurary SCSF-81 Multi Clad. In most events the positron triggering a small downstream beam counter did not cross the fibre under study so off-line a -25 mV threshold was set on the amplitude (red dash-dotted line in Fig.7.3) to remove events with noise only. The distribution of the times when the signal crossed that threshold for the first time (Fig.7.4) shows a pronounced prompt peak on a random background. For further analysis events are selected from the prompt window indicated in Fig.7.4. The distribution of the signal integral (Fig.7.5) shows a series of peaks associated with the number of detected photo-electrons. These distributions allow an accurate gain calibration for each fibre. In further discussions the number of photo-electrons is used as a measure of the signal amplitude.

7.3 Results

7.3.1 Photon Yield

The observed distribution of the number of photo-electrons is compared with the results of a simulation in Fig.7.6. The current simulation significantly overestimates the signal. It accounts for the SiPM window index of refraction and assumes a photon detection efficiency of 35%. We have checked that the observed light attenuation over a distance of 355 mm is reproduced by the simulation and suspect that the mismatch is due either to an overestimation of the scintillation yield or an underestimation of light trapping at the beginning.

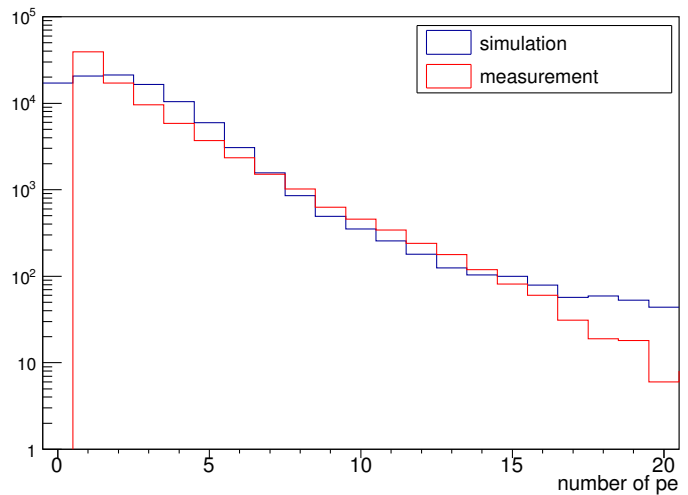


FIG. 7.6 – Measured and predicted distributions of the number of photo-electrons at one fibre end for central ribbon crossing. In the measurement the number of entries with no signal can not be determined from these measurements. The comparison indicates an unknown loss by a factor 3.

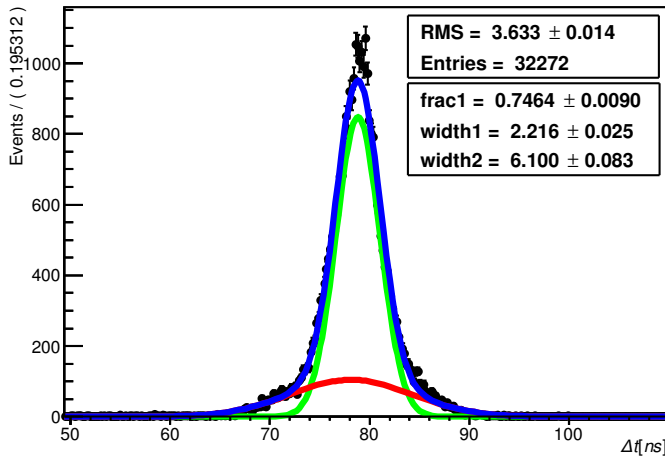


FIG. 7.7 – Distribution of the time difference between the signals from both ends for central ribbon crossing. The observed distribution has been described by two Gaussians with σ =width.

7.3.2 Time resolution

The time resolution for a single fibre, given by the observed resolution of the time difference between the signals at both ends of a fibre (Fig.7.7) divided by two, is still above the design goal of 1 ns for a single fibre. An ongoing measurement of the time resolution of SiPM and amplifier alone will help to identify the main contribution to the time resolution.

7.3.3 2015 PSI Test Beam Campaign

For 2015 another test beam campaign at PSI is planned with new ribbons coated with titanium dioxide that will increase the photon yield. In this beam period one of the ASIC candidates, the STiC chip [5], will be tested as well.

- [1] A. Blondel *et al.* (Mu3e Collaboration), *Research Proposal for an Experiment to Search for the Decay $\mu \rightarrow 3e$* , submitted to PSI (2013), ArXiv 1301.6113.
- [2] U. Bellgardt *et al.* (SINDRUM Collaboration), *Nucl. Phys. B* 299 (1988) 1.
- [3] J. Adam *et al.* (MEG Collaboration), *Phys. Rev. Lett.* 110, 201801.
- [4] S. Ritt *et al.*, *Nucl. Instrum. Methods A* 623 486488.
- [5] T. Harion *et al.*, 2014 JINST 9 C02003.

8 The $\pi^+ \rightarrow e^+ \nu_e / \pi^+ \rightarrow \mu^+ \nu_\mu$ branching ratio

P. Robmann, A. van der Schaaf and P. Truöl

in collaboration with University of Virginia, Charlottesville, USA; Institute for Nuclear Studies, Swierk, Poland; JINR, Dubna, Russia; PSI, Villigen, Switzerland and Rudjer Bošković Institute, Zagreb, Croatia

(PEN Collaboration)

The theoretical value of the $\pi^+ \rightarrow e^+ \nu_e / \pi^+ \rightarrow \mu^+ \nu_\mu$ branching ratio, calculated assuming a universal $Wl_i v_i$ coupling strength and the $V - A$ structure of the electroweak interaction, is $1.2353(1) \times 10^{-4}$ [1]. A measurement of the branching ratio would allow sensitive tests of these two fundamental ingredients of the Standard Model. The present experimental result $1.2312(37) \times 10^{-4}$ dates back over thirty years [2] and two new experiments [3] aim at a reduction of the error by almost an order of magnitude.

- [1] V. Cirigliano and I. Rosell, JHEP **10** (2007) 5; Phys. Rev. Lett. **99** (2007) 231801.
- [2] G. Czapek *et al.*, Phys. Rev. Lett. **70** (1993) 17; D. I. Britton *et al.*, Phys. Rev. Lett. **68** (1992) 3000.
- [3] PEN Collaboration, PSI experiment R-05-01 (2005), D. Počanić and A. van der Schaaf, spokespersons; PIENU Collaboration, TRIUMF proposal 1072 (2006), D. Bryman and T. Numao, spokespersons.

8.1 PEN data taking

The PEN experiment took data at PSI during the years 2008 - 2010. The setup varied slightly over the years and the 2010 version is shown in Fig. 8.1. Pions from the π E1 beam line are brought to rest in a plastic scintillator after having crossed a thin scintillator in an intermediate focus 4 m upstream and a degrader scintillator, situated close to the target scintillator. A small time-projection chamber (mini TPC) is used to record the trajectories of the incoming pions.

Decay positrons from $\pi \rightarrow e \nu$ and the sequence $\pi \rightarrow \mu \nu, \mu \rightarrow e \nu \bar{\nu}$, are tracked in two cylindrical MWPCs. The positron energy is determined with the help of a spherical 3π Sr pure-CsI calorimeter. A cylindrical plastic scintillator hodoscope in front of the calorimeter is used both for timing and for particle identification (in particular to separate decay positrons and protons from pion reactions) through $\Delta E - E$.

Figure 8.2 illustrates how beam pions can be identified by their characteristic velocity and energy loss.

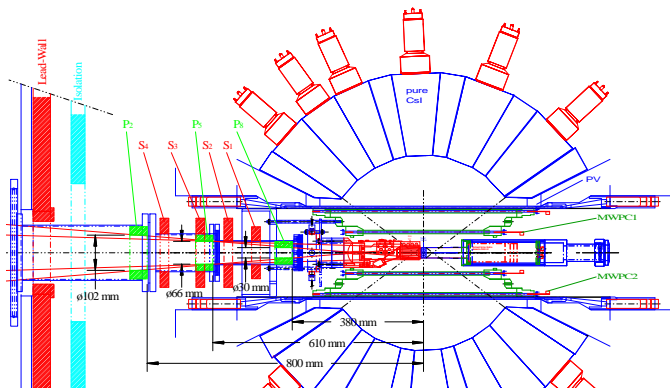


FIG. 8.1 – Cross sections through the PEN setup.

On the right: the target region showing (1) degrader and (3) target scintillators, (2) mini TPC and (4) inner MWPC.

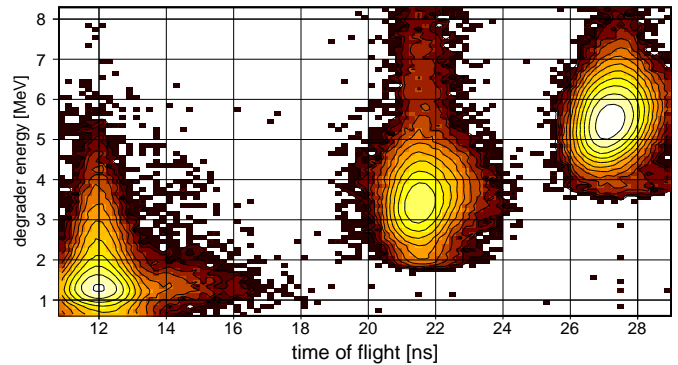
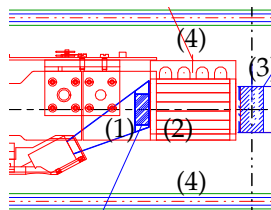


FIG. 8.2 – Degrader energy versus time of flight between an upstream beam counter and the degrader. Events were selected in which a second beam particle is observed, next to the pion required in the readout trigger. The event concentrations, corresponding to (from the left) positrons, muons and pions, reflect the π E1 beam contaminations around 75 MeV/c.

Time of flight is used for an accurate absolute pion energy determination, event by event.

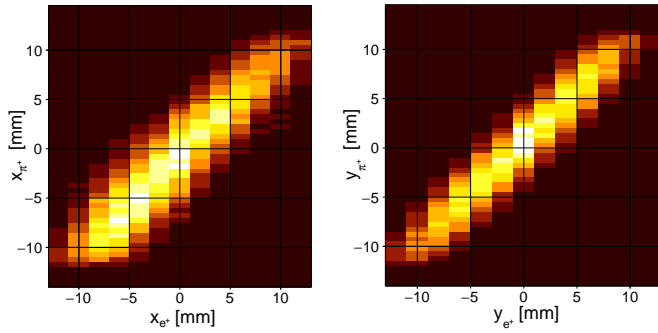


FIG. 8.3 – Correlation between the position coordinates of π^+ and e^+ for e^+ moving vertically (left) and horizontally (right). The correlation, broadened by detector resolutions and by the travel of the intermediate muon, allows for an accurate calibration of the mTPC (x_{π^+} and y_{π^+} are based on charge-division and drift time, respectively).

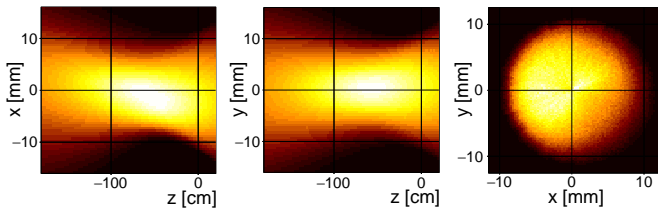


FIG. 8.4 – Pion trajectories as reconstructed with the miniTPC. For these 2009 data the observed target spot is limited radially by a circular $\varnothing = 20$ mm lead collimator situated a few cm upstream of the target. The distribution is off-center in x giving best suppression of the higher-momentum beam positrons situated further to the left.

32

8.2 The mini TPC beam tracker

Pion trajectories were recorded with the small 4-wire time-projection chamber (TPC) shown in Fig. 8.1. The drift field is in y direction so the y coordinate is determined by drift time. The x coordinate is deduced by charge-division (ratio of signals on both ends of the resistive anode wires). Calibrations were done with selected e^+ MWPC trajectories, as illustrated in Fig. 8.3.

The pion stop location (see Fig. 8.4) is needed (i), to check whether the pion stopped sufficiently far from the target surface to make sure that a decay muon would stay inside the target and (ii), to determine the e^+ path length inside the target.

8.3 The Zurich cylindrical hodoscope

Our workshop contributed all plastic scintillators, in particular the 20-element cylindrical hodoscope. A study was made of its performance by determining the response to protons which give a well-defined dE/dx signal. As can be seen from Fig. 8.5 the position dependence of the light yield differs significantly from the expected smooth exponential distribution and each module has its own “fingerprint”, a performance that did not vary over the

years. These maps are used numerically in the data analysis and also taken into account in the detector simulation.

8.4 Target waveform analysis

The classical observables discriminating between the two decay branches are the positron energy and the delay between pion stop and positron emission. The major systematic uncertainty is associated with the few percent of $\pi \rightarrow e\nu$ decays depositing less than 52 MeV in the calorimeter where the $\mu \rightarrow e\nu\bar{\nu}$ decay dominates by far.

The target waveform analysis aims at testing the occurrence of an intermediate 4.1 MeV muon. The strategy is to remove the signals predicted for pion and positron. The pion time is predicted primarily from the degrader waveform and the pion energy from time-of-flight and degrader energy loss. The positron time is predicted primarily from the plastic hodoscope TDC’s and the positron energy from the target trajectory.

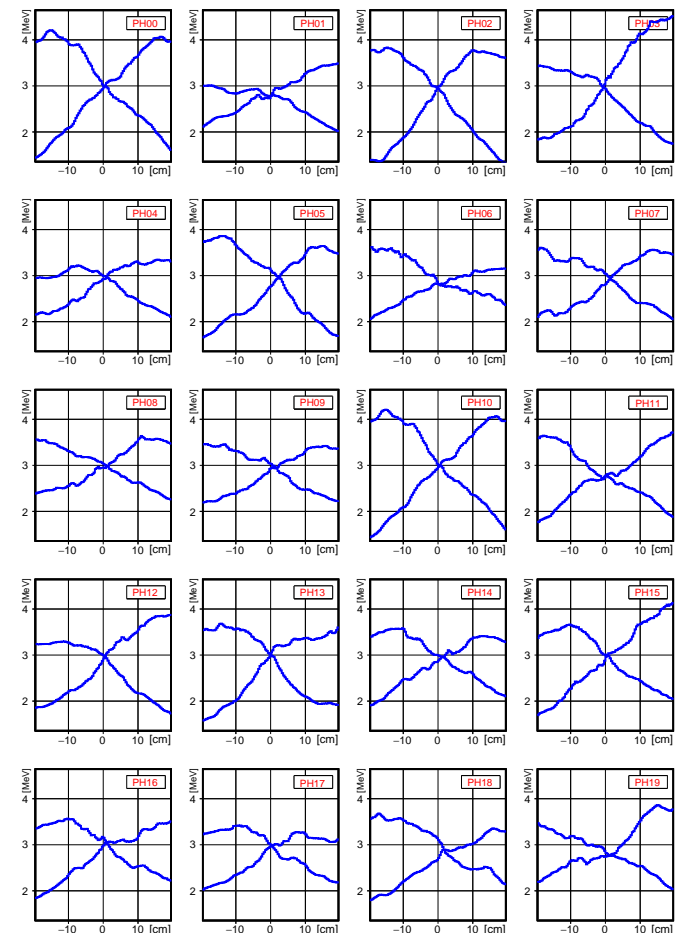


FIG. 8.5 – Position dependence of the light yield observed at the ends of each of the twenty hodoscope staves. Events were selected with 100 MeV protons from pion reactions in the target. Note the irregular behavior varying considerably between the modules.

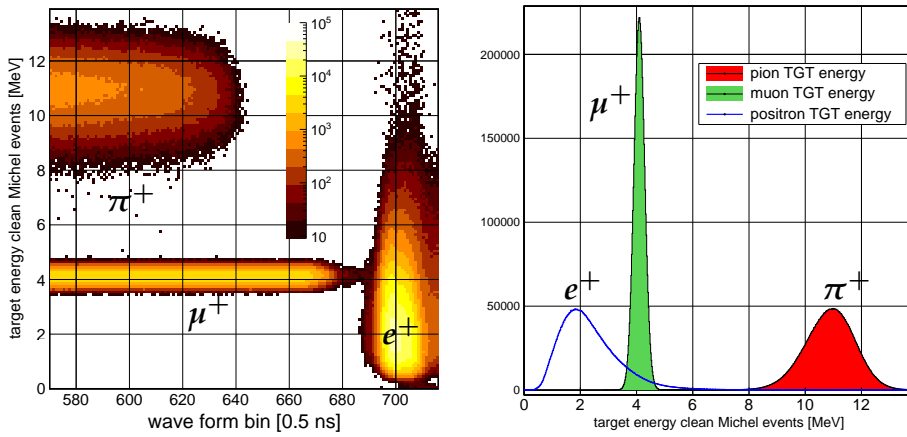


FIG. 8.6 – Results of the target waveform analysis for $\pi \rightarrow \mu \rightarrow e$ decay chains in which the three target signals are well-separated. Positrons, which timed the trigger through their signals in the plastic hodoscope, are situated around waveform bin 700. Their parents, the muons, are situated to their left and mono-energetic with $T = 4.1$ MeV since they originate in the decay of a pion at rest. The pions, preceding the muons, deposit typically 11 MeV.

The scheme is optimized by studying events nicknamed “gold-plated Michel events” i.e., events in which the muon signal is well separated from both the parent pion and the daughter positron so all energies can be determined. Figure 8.6 shows for such events the energies and peak positions in the target waveform. Energies have been corrected here for the detector quenching (signal loss for high ionization densities) taken directly from simulation.

Figure 8.7 shows for such events the perfect linear correlations between predicted and observed π^+ and e^+ energies. The left panel of Fig. 8.8 shows how well the pion signal is predicted in time as well. It is very reassuring that all these results depend on nothing but the muon energy calibration. Finally, the right panel of Fig. 8.8 shows how the scheme works when signals do overlap.

8.5 Outlook

PEN finished data-taking five years ago and has been studying these data in great detail ever since. Energy, time and geometry calibrations are done and most features observed are understood and reproduced by simulation.

The question remains when we might expect to “open the box” and finish the project by publishing the branching ratio. Unfortunately, we can’t answer that question yet but do hope it happens within the next 1-2 years. Pushing systematic errors far below 0.1% is not easy but really time-consuming is convincing ourselves and the scientific world that we reached that point, in particular if the result should turn out to be unexpected...

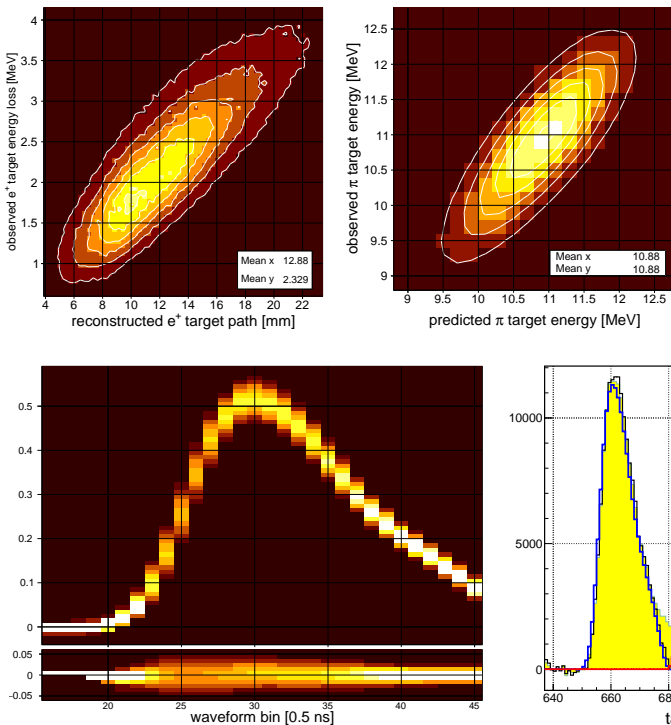


FIG. 8.7 – Left: e^+ target energy versus path length. Observed mean dE/dx is 1.81 MeV/cm, or 1.73 MeV/g. Right: π^+ target energy versus the predicted value based on time of flight and observed degrader energy. In both cases no adjustments were made other than the energy calibration from the 4.1 MeV muon peak.

FIG. 8.8 – Left: pion waveforms before (upper panel) and after (lower panel) subtraction of the predicted signal. These are thousands of waveforms plotted on top of each other.

Right: example of the waveform analysis of an event in which the muon lived only 3.5 ns.

9 Particle Physics with the proposed SHiP experiment

N. Chételat (since March 2015), E. Graverini, B. Kilminster, N. Serra, B. Storaci

The full SHiP collaboration consists of 45 institutes from Bulgaria, Chile, Denmark, France, Germany, Italy, Japan, Russia, Sweden, Switzerland, Turkey, Ukraine, the United Kingdom and the United States of America.

(SHiP Collaboration)

Apart from the observed neutrino oscillations the Standard Model (SM) describes all known microscopic physics phenomena with great precision. The existence of Dark Matter and the matter-antimatter asymmetry in the Universe give additional evidence that the SM is not a complete theory. All these deficiencies could be addressed by adding (at least three) right-handed neutrinos to the SM particle content, particles also known as sterile or Majorana neutrinos or Heavy Neutral Leptons (HNLs).

SHiP is a newly proposed general purpose fixed target experiment at the CERN SPS accelerator with as primary goal the search for HNLs in the mass region below 5 GeV, improving by roughly four orders of magnitude the present experimental sensitivities. SHiP would operate with a beam energy of 400 GeV dumped into a heavy target. A total of 2×10^{20} Proton on Target (PoT) would be studied during 5 years of data taking.

In addition to the search for HNLs, for which the experiment was optimized, SHiP can test several other models of physics beyond the SM, involving very weakly interacting long-lived particles. A detailed description of the SHiP physics case can be found in Ref. [1].

Our group has been active in SHiP since the submission of the Expression of Interest in 2013 [2]. We play a leading role by taking responsibility of the physics programme (Nicola Serra is the physics convener) and of part of the detector design and R&D (Barbara Storaci is convener for the upstream veto and timing detectors).

9.1 the SHiP detector

A dedicated beam line extracted from the SPS will convey a 400 GeV/c proton beam at the SHiP facility [2, 3]. The beam will be stopped in a Molybdenum and Tungsten target, at a center-of-mass energy $E_{CM} = \sqrt{2E_b m_p} \simeq 27$ GeV. Figure 9.1 shows an overview of the setup. The target will be followed by a hadron stopper and by a system of sweeping magnets primarily to keep muons away from the fiducial decay volume. A neutrino detector consisting of OPERA-like bricks of laminated lead and emulsions, followed by a tracker and a muon spectrometer, will allow to detect charged particles produced in charged current neutrino interactions. An upstream tagger will help to veto charged particles entering the main decay volume, defined by a 60 m long vacuum vessel of elliptical cross section with semi-axes 2.5 m and 5 m. A straw tagger is placed 5 m downstream of the entrance window of the vessel. A liquid-scintillator background tagger surrounds the fiducial decay volume. A straw tagger is placed 5 m downstream of the entrance window of the vessel. A liquid-scintillator background tagger surrounds the fiducial decay volume.

The Hidden Sector (HS) detector will comprise: a tracking system placed in vacuum at the end of the vessel, made of 5 m long straw tubes organized in 4 stations in

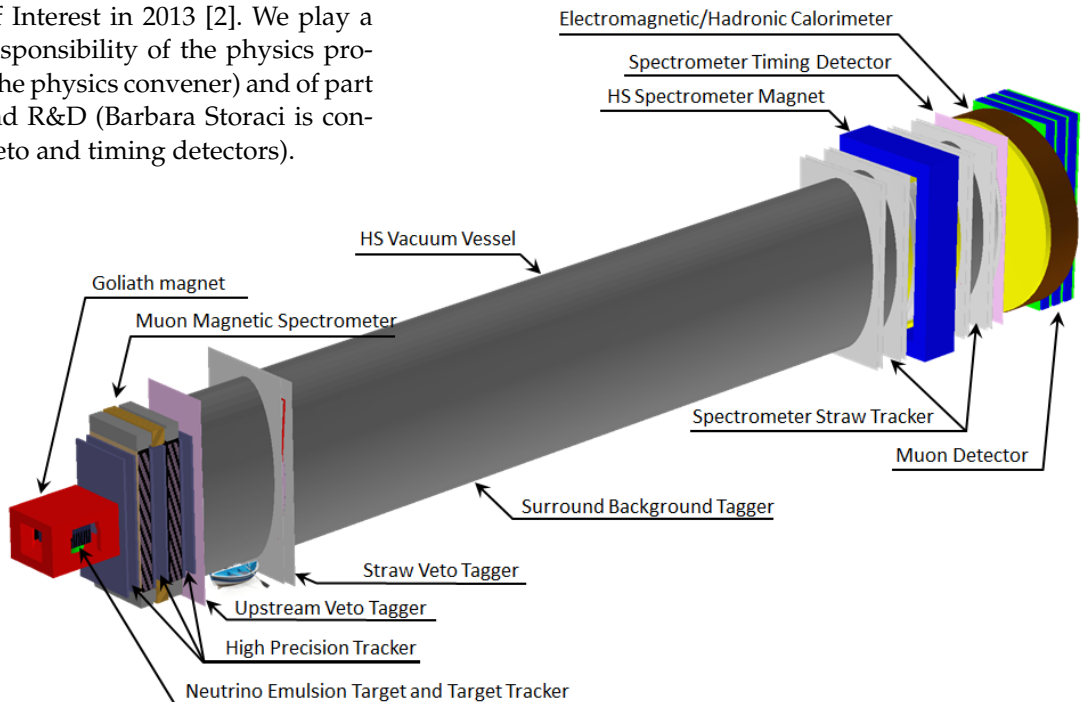


FIG. 9.1 – Ship overview.

a magnetic field of 1 Tm, a precision timing detector, a particle identification system featuring electromagnetic and hadronic calorimeters and, finally, a muon system consisting of four active layers interlaced with iron.

Our group has lead the optimization studies for the shape of the vacuum vessel. The length of the decay volume was obtained by maximizing the acceptance to the hidden particle decay products given the transvers dimensions, dictated by the upstream sweeping magnet.

9.1.1 Upstream Veto and Timing detector

E. Graverini, B. Kilminster, N. Serra and B. Storaci

A potential background source is associated with neutral kaons produced by neutrino and muon interactions upstream of the vacuum vessel, in the passive material of the tau-neutrino detector. The muon spectrometer that follows the tau-neutrino detector is not optimized to act as veto, and does not cover the full acceptance of the decay volume. An upstream veto tagger will reduce this background to negligible levels, and ensure a good level of redundancy of veto systems.

Muons crossing the decay volume represent a dangerous source of combinatorial background which can be removed by requiring that the two tracks mimicking a genuine signal event are coincident in time. A time resolution ≤ 100 ps is required for which a dedicated timing detector is needed.

Two technologies are considered: plastic scintillating bars and multi-gap resistive plate chambers (MRPC). For both technologies well-studied designs are available [3]. In collaboration with the group of the University of Geneva we are the main proponent of a veto timing detector with plastic scintillating bars, read out with silicon photomultipliers. This technology would profit from synergy for R&D and production since the same technology is considered for the muon detector and for the timing detector.

9.2 SHiP physics performance

At the energy accessible at the SPS, the hidden particles are predominantly produced in decays of hadrons, in particular in decays of charmed and beauty hadrons

above the kaon mass, and in proton bremsstrahlung. In comparison with the couplings between the particles of the SM, the hidden sector couplings with SM particles are highly suppressed, resulting in production rates of $\mathcal{O}(10^{-10})$ or less. The principal background to the hidden particle decay signal originates from the inelastic scattering of neutrinos and muons in the vicinity of the detector, producing long-lived V^0 particles. Another source of background comes from random combinations of tracks in the fiducial volume from the residual muon flux, or other charged particles from interactions in the proximity, which enter the decay volume and together mimic signal events. The contribution of cosmic muons to both types of background is expected to be small [3].

9.2.1 Background studies

N. Chételat, E. Graverini, N. Serra and B. Storaci

Our group has conducted a thorough study of the neutrino-induced background and coordinated the analyses of the other background sources. Studies conducted with the full SHiP Monte Carlo simulation indicate that a level of background of 0.1 events for 5 years of data taking is achievable with making use of appropriate veto systems. The flux of neutrinos is estimated to be 1.0×10^{11} neutrinos per spill, with an energy spectrum ranging from 2 GeV to about 100 GeV. A large sample of neutrino interactions with the detector material was simulated, corresponding to expectations during the full five years of SHiP operation. Neutrino interactions were found to take place mainly in the muon magnetic spectrometer of the tau neutrino detector, and in the entrance window and the surrounding walls of the vacuum vessel. Neutrino interactions with the residual gas in the decay volume are negligible if the vacuum pressure is below 10^{-6} bar. Preliminary studies show that the background can be suppressed further by simple selection criteria, which would allow to relax the requirements on the vacuum pressure. In general the interaction products do not point at the target, do not have a reconstructed vertex inside the decay volume, and have very poor track quality. The requirement of having two tracks with a reduced χ^2 below 5, forming a vertex with a maximum width of 30 cm, and with an impact parameter with respect to the proton target below 5 m (see Fig. 9.2) allows rejects 99.4% of the

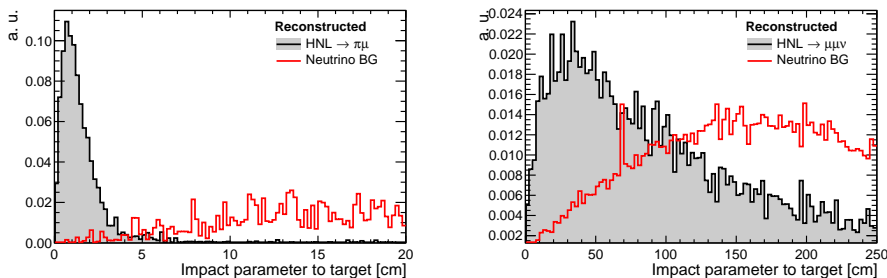


FIG. 9.2 – Simulated distributions of the impact parameter with respect to the proton target of reconstructed HNL events decaying into $\pi\mu$ (left) and $\mu\mu\nu$ (right) with the neutrino-induced backgrounds superimposed.

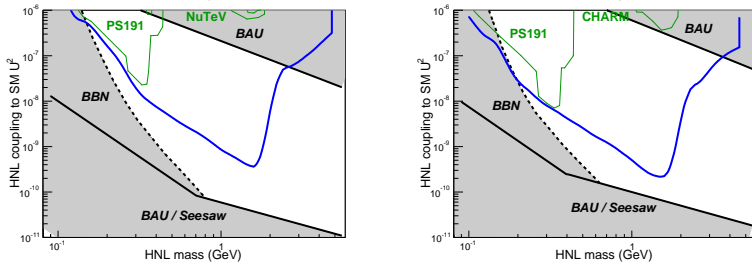


FIG. 9.3 – SHiP’s sensitivity to HNLs assuming normal (left) or inverted (right) hierarchy of standard neutrino masses. The parameter space of the ν MSM is shown as well.

reconstructed background-induced candidate events. At the level of online selection, the requirement of having at least one veto detector with a positive response, together with a loose requirement on the pointing of the interaction products to the target, rejects about 99.5% of events originating in neutrino interactions.

Together, the combination of veto detectors and offline selections allows to reduce the neutrino induced background to zero. The set of selections applied is highly redundant and can be trimmed down to study specific channels.

9.2.2 SHiP sensitivity

E. Graverini, N. Serra and B. Storaci

Our group has been responsible for studying the SHiP sensitivity to HNLs and for dark photons. The latter are gauge bosons of a minimalistic theory based on the breaking of a $U(1)$ symmetry in the hidden sector (for theoretical details see [1]).

The SHiP physics sensitivities are evaluated using the FAIRSHIP package which is based on the FAIRROOT [4] package, a lightweight software framework based on ROOT. Our group contributed substantially to the development of FAIRSHIP. In addition, we developed a fast simulation to interpolate the results of the full simulation.

The FAIRSHIP simulation makes use of the package GEANT4 to simulate the interaction between stable particles and the material and is therefore relatively high CPU consuming. The fast simulation has been validated with the full simulation and corrected for the reconstruction efficiency. The use of the fast simulation allows to scan a large set in the models phase space of the various. The sensitivity to HNLs as a function of their mass and couplings, for normal and inverted hierarchy of SM neutrinos, is shown in Fig. 9.3.

A very similar method, analogous the one used by the authors of [5], was used to estimate SHiP sensitivity to dark photons, shown in Fig. 9.4.

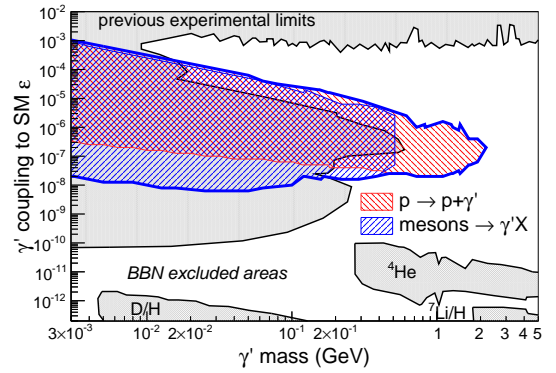


FIG. 9.4 – SHiP’s sensitivity to dark photons superimposed on present limits including those from cosmological observations.

- [1] S. Alekhin *et al.*, *A facility to Search for Hidden Particles at the CERN SPS: the SHiP physics case*, arXiv:1504.04855.
- [2] W. Bonivento *et al.*, *Proposal to Search for Heavy Neutral Leptons at the SPS*, arXiv:1310.1762.
- [3] M. Anelli *et al.*, SHiP collaboration, *A facility to Search for Hidden Particles (SHiP) at the CERN SPS*, arXiv:1504.04956.
- [4] Al-Turany *et al.*, J. Phys. Conf. Ser. 396 (2012) 022001.
- [5] J. Blümlein and J. Brunner, Phys. Lett. **B** (2014) 731.

10 Particle Physics with LHCb

C. Abellan (since May 2014), J. Anderson (until September 2014), R. Bernet, E. Bowen, A. Bursche (until December 2014), N. Chiapolini (until December 2014), M. Chrzęszcz¹, B. Dey (since April 2014), Ch. Elsasser, E. Graverini, F. Lionetto, P. Lowdon, A. Mauri (since June 2014), K. Müller, S. Saornil (until September 2014), N. Serra, St. Steiner, O. Steinkamp, B. Storaci, U. Straumann, M. Tresch, A. Vollhardt and A. Weiden (since January 2015)

¹ also at Henryk Niewodniczanski Institute of Nuclear Physics, Kraków, Poland (until February 2015)

The full LHCb collaboration consists of 69 institutes from Brazil, China, Colombia, France, Germany, Ireland, Italy, Poland, Romania, Russia, Spain, Switzerland, the Netherlands, Turkey, Ukraine, the United Kingdom and the United States of America.

(LHCb Collaboration)

The LHCb experiment [1] at CERN's Large Hadron Collider (LHC) is dedicated to the study of rare decays of hadrons containing a b or c quark and to precision measurements of CP violating observables. Major goals are the study of the flavour structure in the quark sector and the search for physics beyond the Standard Model (BSM) of particle physics.

The LHCb detector is a single-arm forward spectrometer covering an acceptance close to the LHC beam pipe. This allows to measure particles propagating with a small angle with respect to the direction of the colliding hadrons, which is a typical feature of hadrons containing b or c quarks produced in hadron colliders at energies reached by the LHC.

The Zurich group takes responsibility for the operation and maintenance of silicon detectors in the tracking system. Furthermore, our group significantly contributes to measurements of rare B and τ decays as well as measurements involving W and Z bosons.

[1] A. A. Alves Jr. *et al.* [LHCb Collab.], JINST 3 S08005 (2008).

10.1 LHCb detector

The main features of the detector are an excellent momentum and impact parameter resolution for charged particles achieved by the tracking system consisting of silicon and gaseous sub-detectors. Furthermore, two Ring Imaging Cherenkov detectors can identify charged pions and kaons as well as protons.

The Zurich group played a major role in the construction of the Silicon Tracker (ST) system, especially for the Tracker Turicensis (TT), a large area micro-strip detector located upstream of the LHCb dipole magnet. The group

is also responsible for its operation and maintenance. Information about the detector and its performance can be found in previous annual reports [1].

During the Long Shutdown 1 (LS1) of LHC between spring 2013 and 2015, consolidation work was done on several sub-detectors. Additionally, a system based on scintillating detectors was installed covering very small angles with respect to the direction of the beams. This allows to better identify proton-proton collisions where at least one of the colliding protons has stayed intact.

[1] <http://www.physik.uzh.ch/reports.shtml>

10.1.1 Detector operation and performance

C. Abellan, E. Bowen, B. Dey, E. Graverini, S. Saornil, O. Steinkamp, and B. Storaci

During the LHC Run 1, the ST had a very high fraction of working channels, which was on average more than 99.6% for TT and 98.4% for the Inner Tracker (IT), the second detector in the ST system. After maintenance work in LS1 these numbers are 99.7% and 99.1%, respectively.

During the LS1 new monitoring algorithms were developed in order to allow an even more detailed analysis of the ST performance. This software will be included in the official LHCb framework and allow to spot issues with the detector alignment or track reconstruction software. Since LHCb will use a novel alignment procedure running online in the upcoming data taking period, these algorithms will play an important role. Their first applications have already revealed possible sources of inaccuracies in the detector description whose correction will allow to improve the LHCb detector alignment. As a consequence, Elena Graverini developed in collaboration with the École Polytechnique Fédérale de Lausanne several in-

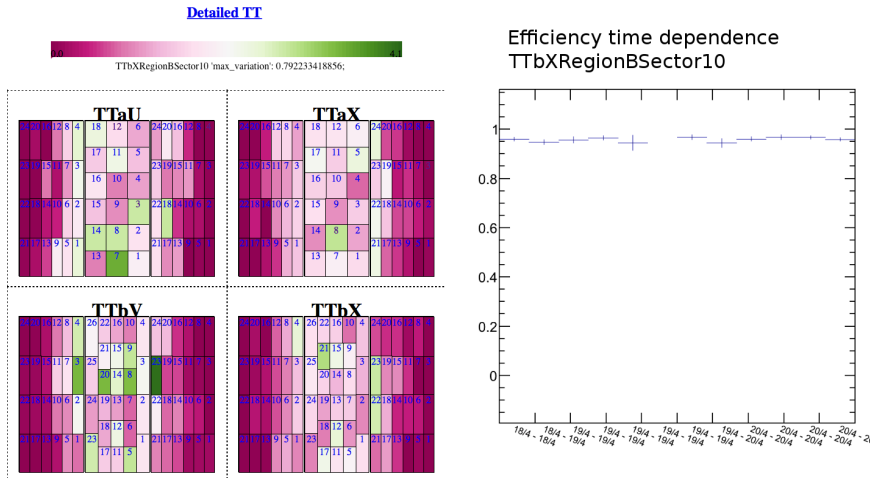


FIG. 10.1 – A view of the new ST interactive monitoring interface. The left panel shows the summary of a certain performance indicator for the whole TT on read-out sector (i.e. a group of sensors) level. Hovering over a region of the detector in the left panel allows to visualize more details about the performance for that specific region, shown in the right panel.

interactive monitoring tools, which allow to study the detector performance down to a single-sensor, even during data taking (cf. Fig. 10.1). The restart of the LHC for Run 2 will pose new challenges for the operation of the ST. The increase in collision energy from 8 TeV to 13 TeV will affect the detector occupancy, and the change of bunch spacing from 50 ns to 25 ns makes it necessary to re-evaluate ST's operation parameters in order to properly deal with the spill-over of detector signals between consecutive bunch crossings.

10.1.2 Luminosity measurements

K. Müller and A. Weiden

Among the LHC experiments, LHCb performed the most precise determinations of the luminosity. One method is based on the change in interaction rate when the overlap of the two proton beams is varied by scanning their relative position (van der Meer scan) [1]. Alternatively one measures the collision rate of protons from a single beam with residual gas atoms inside the beam pipe [2]. The combined uncertainty on the luminosity measurement is 1.12% [3].

Since a precise determination of the luminosity in LHCb is a pre-requisite for cross-section measurements, effort is ongoing to get an accurate evaluation already a few weeks after the start of the Run 2 data taking. Andreas Weiden is working on the optimization of the dedicated trigger setup to identify collisions of protons with residual gas atoms and will be responsible for the analysis of the Van der Meer scans in the upcoming running period.

- [1] S. van der Meer, CERN-ISR-PO68-31 (1968).
- [2] M. Ferro-Luzzi, Nucl. Instrum. Meth. A553 (2005) 388.
- [3] R. Aaij *et al.* [LHCb Collab.], JINST 9 (2014), P12005.

10.2 LHCb upgrade

C. Abellan, B. Dey, F. Lionetto, S. Saornil, and O. Steinkamp

The upgraded LHCb detector [1], planned to be installed in the LHC cavern in 2019, will cover the same pseudo-rapidity region but run at an instantaneous luminosity five times higher than in the current configuration. The readout time will have to be reduced from the present 1 μ s to 25 ns which means that several sub-detectors have to be redesigned.

The TT was a major responsibility of our group and so is its upgraded version, the Upstream Tracker (UT) [2]. The UT will contribute to speed up the formation of the trigger decision. It will have a finer granularity, required to stand the higher particle density after 2019. The Zurich group is developing a test board used to examine the functionalities of the new read-out chip developed for a rate of 40 MHz, is contributing to the design and development of the high- and low voltage distribution systems, and is responsible for detector control and safety and for environmental monitoring.

10.2.1 Test stand

Last year, a laser test stand has been assembled in Zurich, allowing R&D activities on silicon micro-strip sensors. It is used to characterize the prototype sensors with different geometries (cf. Fig. 10.2). A large effort was made in automating the measurement procedures and in a precise monitoring of the environmental variables (temperature, humidity, and dew point), which will ultimately allow to inspect the sensors before installation in the LHC cavern.

10.2.2 Test beam

Federica Lionetto and Biplab Dey joined the first two beam tests organized in the context of the UT project. An exploratory campaign in July and August allowed to

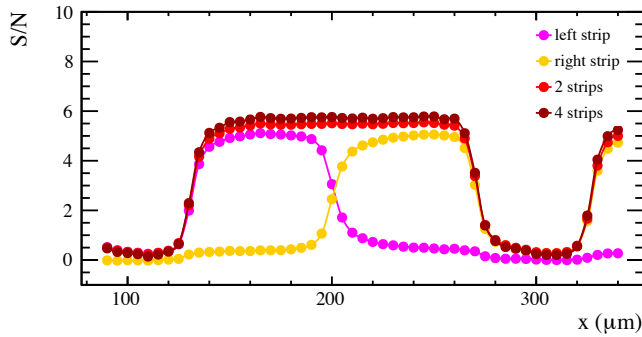


FIG. 10.2 – Charge signal, in terms of signal over noise ratio, versus the position of the laser beam between two adjacent strips. No charge is lost in this situation. Shown are the signal over noise ratio measured on these two strips, their sum and the sum over four adjacent strips. The low but finite values on the sides are caused by laser light reflected by the aluminum read-out strips.

test the readout system and the synchronisation between the detector under test and the beam telescope. Later that year sensors of both p-in-n and n-in-p type, irradiated with doses up to 23.3 MRad, were tested at the CERN SPS with a 180 GeV/c proton beam. Charge collection properties and spatial resolution were studied [3].

- [1] LHCb Collab., CERN-LHCC-2012-007, LHCb-TDR-012.
- [2] LHCb Collab., CERN-LHCC-2014-001, LHCb-TDR-015.
- [3] A. Abba *et al.*, CERN-LHCb-PUB-2015-006.

10.3 Track reconstruction at software trigger level

E. Bowen, E. Graverini, B. Storaci, and M. Tresch

Until now the interaction rate of up to 40 MHz has been reduced to an acceptable detector read-out rate of 1 MHz in an electronic trigger system based on rough signatures such as energy deposits in the calorimeters. This scheme inhibits the operation of the detector at higher luminosities as trigger rates for decays with only hadronic final state particles would saturate. As a major goal of the LHCb upgrade a trigger system, based purely on software, should remove this bottleneck. Such a software trigger allows great flexibility in defining selection topologies. The resulting efficient triggering on low momentum tracks is normally beyond the scope of a hadron collider.

There exist strict requirements on the execution time of the applied pattern recognition algorithms. An algorithm [1], developed by our group, using information from the two most upstream tracking sub-detectors gives a factor three reduction of the execution time of the overall tracking sequence, well within the allowed CPU budget, maintaining very high efficiency. At the same time the fraction of ghost tracks is lower by a factor 4. The new algorithm has therefore been adopted into the baseline tracking sequence of the upgrade trigger [2] and a modified version will be implemented in the software trigger of Run 2 already.

- [1] E. Bowen and B. Storaci, CERN-LHCb-PUB-2013-023.
- [2] LHCb Collab., CERN-LHCC-2014-016, LHCb-TDR-016.

10.4 Physics results

During the past twelve months LHCb published more than 70 physics papers [1] covering a broad range of topics. Here some results will be presented followed by more detailed discussions of our own contributions.

During the reporting period LHCb discovered two baryons, $\Xi'_b{}^-$ and Ξ_b^{*-} , containing one beauty, one strange and one down quark. While the first state has spin 1/2, the spins of the quarks in the second state line up, leading to a 3/2 spin of the baryon [2]. LHCb also discovered a spin-3 hadron containing a charm quark, called $D_{sJ}^*(2860)^-$, with a mass of about 2.86 GeV/c² [3].

LHCb combined several of its measurements of the angle γ in CKM-triangle. This angle is a measure of the amount of CP violation in the SM and is a sensitive observable in a search for BSM physics. The resulting $\gamma = 72.9^\circ_{-9.9^\circ}^{+9.2^\circ}$ [4, 5] is more accurate than the combined value from the B-factories Belle and BaBar.

Another important observable in the study of CP violation is the phase ϕ_s describing CP violation in $B_s^0 \rightarrow J/\psi K^+ K^-$ and $B_s^0 \rightarrow J/\psi \pi^+ \pi^-$ decays. The value obtained by LHCb, $\phi_s = -0.010 \pm 0.039$ rad, is in agreement with the very low SM prediction [6].

The branching ratio R_K , between the decays $B^+ \rightarrow K^+ \mu^+ \mu^-$ and $B^+ \rightarrow K^+ e^+ e^-$, was measured for an invariant mass of the lepton pair squared in the range 1 to 6 GeV²/c⁴. This observable has small theoretical uncertainties and lepton universality postulated in the SM predicts $R_K = 1 \pm \mathcal{O}(10^{-3})$. The LHCb value of $R_K = 0.745_{-0.074}^{+0.090}$ represents a 2.6 σ deviation from unity [7].

- [1] <http://lhcb.web.cern.ch/lhcb/>
- [2] R. Aaij *et al.* [LHCb Collab.], Phys. Rev. Lett. **114** (2015), 062004.
- [3] R. Aaij *et al.* [LHCb Collab.], Phys. Rev. Lett. **113** (2014), 162001.
- [4] R. Aaij *et al.* [LHCb Collab.], JHEP **10** (2014), 097.
- [5] LHCb Collab., LHCb-CONF-2014-004.
- [6] R. Aaij *et al.* [LHCb Collab.], Phys. Rev. Lett. **114** (2015), 041801.
- [7] R. Aaij *et al.* [LHCb Collab.], Phys. Rev. Lett. **113** (2014), 151601.

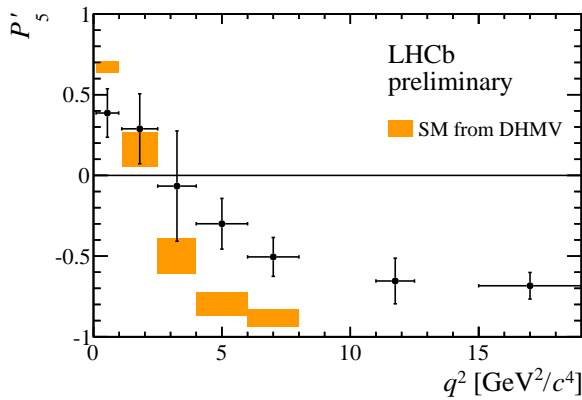


FIG. 10.3 – The angular observable P'_5 in the decay $B^0 \rightarrow K^{*0}\mu^+\mu^-$ measured by LHCb with a data set corresponding to 3 fb^{-1} compared to the SM predictions from Ref. [8].

10.4.1 $B^0 \rightarrow K^{*0}\mu^+\mu^-$

E. Bowen, M. Chrzszcz, B. Dey, N. Serra, B. Storaci, and M. Tresch

The rare decay $B^0 \rightarrow K^{*0}\mu^+\mu^-$ is a flavour-changing neutral current process that is very sensitive to BSM physics [1]. The kinematics can be described by three helicity angles and the invariant mass of the muon pair. The analysis performed on the 1 fb^{-1} data sample showed a 3.7σ discrepancy with respect to SM predictions [2].

Our group played a key role in an updated measurement with the full 3 fb^{-1} data set. We were responsible for particle identification and event selection, based in part on training algorithms in which data subsets alternate for training and testing. This way the data are used most efficiently and with high discriminating power. We introduced the method of moments to determine the angular observables [3] which appears more stable than a conventional likelihood fit and allows finer mass binning. Preliminary results [4] confirm the discrepancy mentioned above (cf. Fig. 10.3).

Several explanations for the deviation have been brought up [5] such as the existence of an additional boson, Z' , with a mass above 10 TeV [6]. It has also been pointed out that the discrepancy might be explained by QCD effects ignored in the SM predictions [7].

- [1] J. Matias *et al.*, JHEP 04 (2012) 104.
- [2] R. Aaij *et al.* [LHCb Collab.], JHEP 1308 (2013) 131.
- [3] F. Beaujean, M. Chrzszcz, N. Serra and D. van Dyk, arXiv:1503.04100 [hep-ex].
- [4] LHCb Collab., LHCb-CONF-2015-002.
- [5] S. Descotes-Genon *et al.*, arXiv:1503.03328 [hep-ph].
- [6] R. Gauld, F. Goertz and U. Haisch, JHEP 1401 (2014) 069.
- [7] J. Lyon and R. Zwicky, arXiv:1406.0566 [hep-ph].
- [8] S. Descotes-Genon *et al.*, JHEP 01 (2013) 048.

10.4.2 Search for $\tau^- \rightarrow \mu^- \mu^+ \mu^-$

M. Chrzszcz and N. Serra

A huge number of τ leptons are produced in the acceptance of LHCb which makes LHCb well suited to perform, for example, a search for the Lepton Flavour Violating (LFV) decay $\tau^- \rightarrow \mu^- \mu^+ \mu^-$. In the SM this decay occurs via neutrino mixing but the branching ratio of $\mathcal{O}(10^{-40})$ is far below experimental sensitivity. Several BSM models including an extended neutrino sector [1] can enhance the branching fraction to values that are in reach of LHCb.

Our group had a leading role in a search in the full 3 fb^{-1} data set collected by LHCb. The sensitivity was raised with a new multivariate selection technique, called blending, which combines information from different classifiers and different τ sources (e.g. promptly produced, produced in decay of b hadrons, etc.). A new limit $\mathcal{B}(\tau^- \rightarrow \mu^- \mu^+ \mu^-) < 4.6 \times 10^{-8}$ at 90% CL [2] was set.

Marcin Chrzszcz is member of PDG's Heavy Flavour Averaging Group (HFAG) focusing on τ lepton properties including LFV τ decays [3].

- [1] R. H. Bernstein and P. S. Cooper, Phys. Rep. 532 (2013) 27.
- [2] R. Aaij *et al.* [LHCb Collab.], JHEP 1502 (2015) 121.
- [3] Y. Amhis *et al.* [Heavy Flavor Averaging Group (HFAG) Collab.], arXiv:1412.7515 [hep-ex].

10.4.3 Search for new scalar particles in B decays

M. Chrzszcz, A. Mauri, and N. Serra

The LHCb experiment offers the possibility to search for long lived particles produced in B decay with higher sensitivity than reached by Belle [1]. Many BSM models [2, 3] predict the existence of light particles, such as an inflaton or a dark matter mediator, that, mixing with the Higgs boson, can couple to the visible SM sector.

We are analyzing the 3 fb^{-1} of data collected in 2011 and 2012 looking for the decay sequence $B^+ \rightarrow K^+ \chi$, $\chi \rightarrow \mu^+ \mu^-$ with χ a light scalar particle. The lifetime of such a particle can be long so that it could travel several centimeters before decaying. Simulations were made for different mass and lifetime values as a guidance to the optimal event selection based on machine-learning algorithms.

- [1] J.-T. Wei *et al.* [Belle Collab.], Phys.Rev.Lett.103:171801 (2009).
- [2] J. D. Clarke, R. Foot and R. R. Volkas, JHEP 02 (2014) 123.
- [3] K. Schmidt-Hoberg, F. Staub and M. W. Winkler, Phys. Lett. B727 (2013) 506-510.

10.4.4 $B_{(s)}^0 \rightarrow \mu^+\mu^-$ in combination with CMS

Ch. Elsasser

In 2013 both LHCb and CMS presented results on the rare decays $B_s^0 \rightarrow \mu^+\mu^-$ and $B^0 \rightarrow \mu^+\mu^-$ [1, 2]. These decays are sensitive to BSM physics since the non-SM particles can act as propagator.

The two collaborations aligned their procedures and the combined measurement resulted in the first observation of the decay $B_s^0 \rightarrow \mu^+\mu^-$ and the first evidence for $B^0 \rightarrow \mu^+\mu^-$ [3] with measured branching fractions in agreement with the SM prediction at the 1.2σ and 2.2σ level, respectively [4].

- [1] R. Aaij *et al.* [LHCb Collab.], Phys. Rev. Lett. **111** (2013) 101805.
- [2] S. Chatrchyan *et al.* [CMS Collab.], Phys. Rev. Lett. **111** (2013) 101804.
- [3] V. Khachatryan *et al.* [LHCb+CMS Collab.], arXiv:1411.4413.
- [4] C. Bobeth *et al.*, Phys. Rev. Lett. **112** (2014) 101801

10.4.5 Electroweak boson and low mass Drell-Yan production

J. Anderson, A. Bursche, N. Chiapolini, Ch. Elsasser, K. Müller, and M. Tresch

Measurements on W and Z production constitute sensitive SM tests at LHC energies. We were largely involved, determining detection efficiencies, estimating background contaminations, and calculating theoretical predictions which are presently computable at next-to-next-to-leading order (NNLO) in perturbative QCD. They rely on the parametrisations of the parton distributions inside the proton – described by the parton density functions (PDF), which are determined from experiment. The ratio of the W^+ to W^- production cross sections, for example, allows a determination of the ratio of up to down valence quark densities since both the experimental and the theoretical systematic uncertainties tend to cancel.

The measurements of the W production in the muon channel have been updated with the full 2011 dataset [1]. The precision improved significantly due to the larger data sample, a better understanding of the detector, and an improved luminosity determination. The measurement of Z production using the full dataset benefits from a similar improvement in precision and will be published shortly. The systematic uncertainties of the inclusive cross sections are below 1% and even for the differential measurements the experimental errors are comparable or below the theoretical uncertainties. Figure 10.4 shows the ratio of the W^+ to W^- cross section as a function of the pseudo-rapidity of the muon, in good agreement with NNLO predictions for various PDF parametrisations.

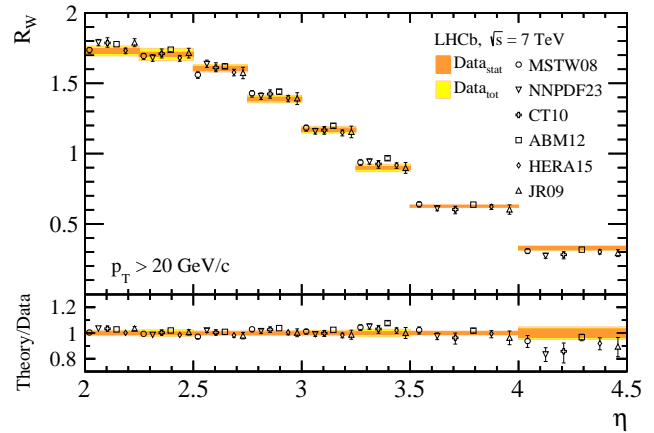


FIG. 10.4 – R_W , the ratio of W^+ to W^- cross sections in bins of muon pseudo-rapidity. Measurements, represented as bands corresponding to the statistical and total uncertainty, are compared to NNLO predictions for various parametrisations of the PDFs (black markers, displaced horizontally for presentation).

The analysis of low mass Drell-Yan production in the dimuon channel is described in the thesis of Nicola Chiapolini [2]. This measurement is sensitive to Bjorken- x values (the momentum fraction carried by the quark taking part in the actual scattering) as low as 8×10^{-6} . These measurements are challenging since the backgrounds are very high. The purity is estimated from a fit to a variable describing the amount of activity in the detector close to the two muons. The variable can be determined from the background free sample of Z decays. The systematic studies will be finalized by Marcin Chrzęszcz before results can be published. A refined analysis is planned with the data to be collected in Run 2.

Further ongoing studies in our group are:

- production of K_S^0 , Λ^0 and protons in events with a Z boson (Marco Tresch),
- $Z\gamma$ diboson production (Moritz Küng (Master student 2013-2014) [3] and Christian Elsasser), and
- low energy $W \rightarrow \mu^+\nu^-$ (Christian Elsasser) and $Z \rightarrow \mu^+\mu^-$ (Albert Bursche [4]) production at 2.76 TeV.

- [1] R. Aaij *et al.* [LHCb Collab.], JHEP **12** (2014) 079.
- [2] Nicola Chiapolini, PhD thesis, 2014.
- [3] Moritz Küng, Master thesis, 2014.
- [4] Albert Bursche, PhD thesis, 2014.

10.5 Summary and Outlook

With the end of LHC's long shutdown LHCb is ready for Run 2. The experiment will continue, primarily, to shed light on the field of physics involving c and b quarks.

In parallel preparations for the next upgrade, planned to begin in 2019, are running at full steam including the work by the Zurich group on the new Upstream Tracker.

11 Particle physics with the CMS experiment at CERN

T. Årestad, L. Caminada, F. Canelli, V. Chiochia, A. de Cosa, C. Galloni, A. Hinzmann, T. Hreus, B. Kilminster, C. Lange, J. Ngadiuba, D. Pinna, P. Robmann, D. Salerno, S. Taroni, M. Verzetti, and Y. Yang

in collaboration with the:

CMS - Collaboration

After the recent discovery at the LHC of a Higgs-like particle [1, 2], studying its properties is among the primary goals and challenges of the next LHC run. Another goal are searches for new particles with masses around a TeV that could be produced directly at the LHC, after its upgrade.

Cosmological and astronomical observations have uncovered the existence of dark matter (DM). If DM is indeed a stable neutral weakly interacting particle with mass less than around a TeV as expected, we must produce it at the LHC so the LHC may well bridge the gap between the shortest and the largest distance scales.

42

The LHC delivered proton collisions until February 2013 concluding the first three-year running period (Run 1) in which CMS collected an integrated luminosity of $23.3(6.1) \text{ fb}^{-1}$ at the centre-of-mass energy $\sqrt{s} = 8(7) \text{ TeV}$.

The next data-taking period (Run 2) at a higher center-of-mass energy of 13 TeV should have started by the time this report came to print.

[1] CMS collaboration, Phys. Lett. B **716** (2012) 30.

[2] ATLAS collaboration, Phys. Lett. B **716** (2012) 29.

11.1 The CMS detector

CMS [1, 2] is a multipurpose detector designed for a variety of particle physics studies at the LHC. CMS consists of different detector layers (see Fig. 11.1). An all-silicon tracker, an electromagnetic calorimeter, and a hadronic sampling calorimeter are all contained within a large-bore 3.8 T superconducting solenoid. Beyond the solenoid are four layers of muon detectors. The CMS

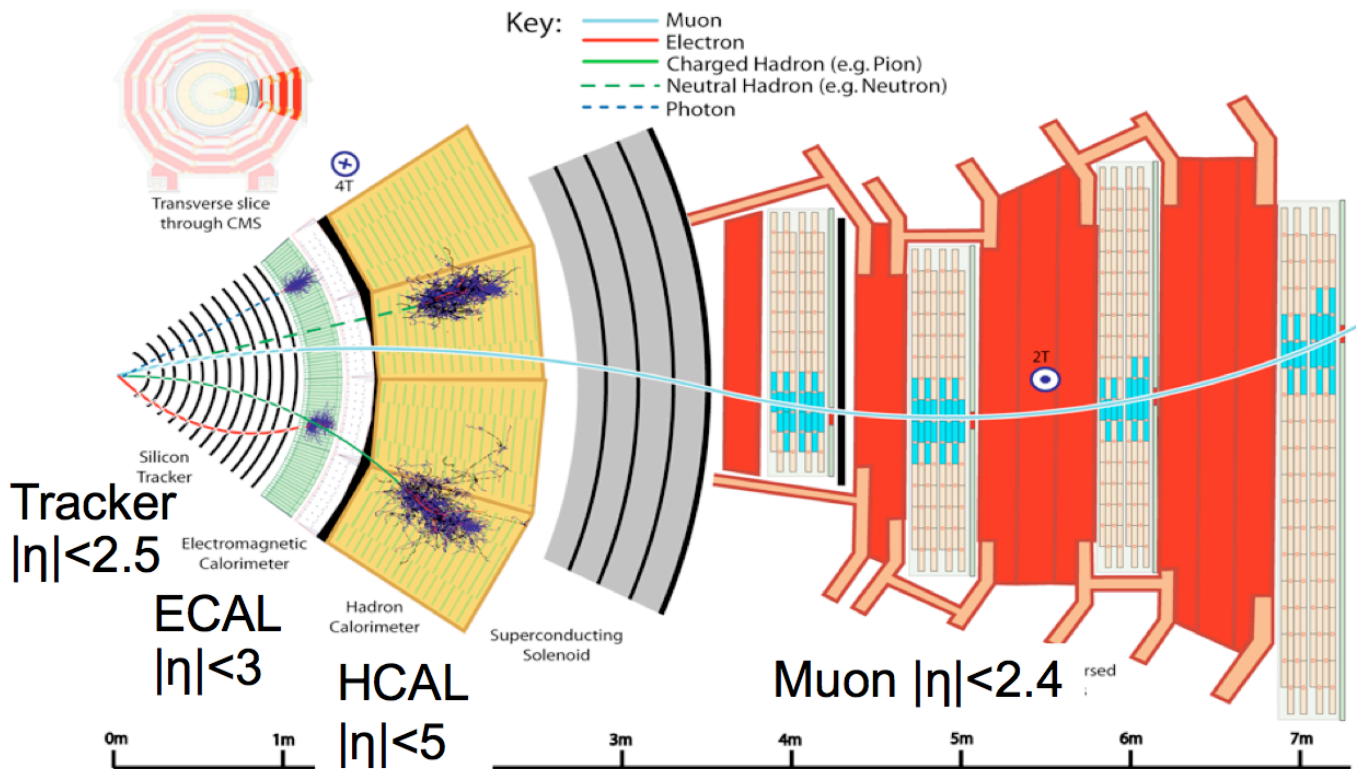


FIG. 11.1 – Schematic view of a sector of the CMS detector, illustrating how muons, electrons, charged hadrons, neutral hadrons and photons are reconstructed.

tracker is composed of the inner pixel detector and the outer silicon strip detector. The pixel detector consists of three barrel layers (BPIX) at 4.4, 7.3, and 10.2 cm, and two forward/backward disks (FPIX) at longitudinal positions of ± 34.5 cm and ± 46.5 cm and extending in radius from about 6 to 15 cm. BPIX was built by the CMS Swiss Consortium: PSI, ETH and the University of Zurich.

The high segmentation of the pixel detector permits the building of seed clusters for the tracking algorithm reconstruction and also for the fast online track reconstruction in the high level trigger (HLT). The pixel detector is used for electron/photon identification and muon reconstruction, and its high resolution is crucial for accurate vertex reconstruction, which also allows the identification of long-lived τ -leptons and B -hadrons traveling a few millimeters before decaying.

Members of our group cover important coordination roles within the CMS collaboration. A. de Cosa is the level3 pixel monitor coordinator, C. Lange acts as convener of the CMS pixel data acquisition group, L. Caminada coordinates the supply tube subgroup within the CMS pixel phase 1 upgrade project and serves as ex-officio member of the Tracker conference committee, A. Hinzmann is former co-convener of the Exotica in jet final states physics group and current convener of the the JetMET algorithms and reconstruction group, Y. Yang serves as the CMS Monte Carlo request manager, B. Kilminster is co-convener of the phase 2 upgrade future Higgs physics group, F. Canelli is co-convener of the Beyond 2 Generations Very Heavy Fermions subgroup, T. Hreus coordinates the Tracker Detector Performance Group, in charge of the tracker offline software and operations, while V. Chiochia is a member of the CMS conference committee and B-physics steering group. In addition, L. Caminada (taking over from S. Taroni) and C. Lange are members of the Swiss CMS Tier3 steering committee. Currently F. Canelli holds the position of group leader.

[1] CMS collaboration, CERN-LHCC 2006-001.

[2] CMS collaboration, JINST 3 (2008) S08004.

In what follows, we describe the contributions of our group, which were focused in three main areas of research: physics measurements and searches, analysis techniques that benefit these physics analyses, and the operation and upgrade of one of the detectors vital to these measurements. A primary physics focus was on the better understanding of the Higgs sector. We also searched for new particles motivated by DM, SUSY, and extra dimensions, which could be in reach of LHC energies and luminosities.

11.2 Higgs boson couplings to top quark pairs

The Higgs boson was first observed through its decay into ZZ and $\gamma\gamma$. Also in the decay channel to WW a significant signal could be established. Furthermore, evidence for Higgs couplings to up-type fermions was found at the Tevatron in the decay $H \rightarrow b\bar{b}$ [1], and, more recently, in $H \rightarrow b\bar{b}$ and $H \rightarrow \tau\tau$ at the LHC [2–5] where our group contributed significantly, as documented in last year’s annual report. Since the properties of Higgs bosons belonging to extended Higgs sectors differ from SM predictions, accurate measurements of Higgs couplings are important to identify possible deviations that indicate new physics scenarios.

Evidence of a direct coupling to up-type fermions, in particular to top quarks, is still lacking. Since the top quark is the heaviest particle of the SM, the only way to directly probe such coupling is by studying the associated production of a Higgs boson and a pair of top quarks ($t\bar{t}H$). This channel is challenging, given the small cross section and high QCD background. The $H \rightarrow b\bar{b}$ decay is most promising thanks to the large branching ratio and the high efficiency of tagging jets from b -quark hadronization. Nevertheless, the QCD background $pp \rightarrow t\bar{t} + b\bar{b}$ remains irreducible with respect to b -tagging, and dominates the signal by far [6].

We are leading a search for $t\bar{t}H$ based on the analytical Matrix Element Method (MEM) [7] for optimal separation of $t\bar{t}H$ signal and $pp \rightarrow t\bar{t} + b\bar{b}$ background. We use the 8 TeV data from 2012, corresponding to an integrated luminosity of 19.0 fb^{-1} [8]. Events are selected, in which at least one top quark decays leptonically through $t \rightarrow bW$, with $W \rightarrow \ell\nu_\ell$, $\ell = e, \mu$, and the other W decay may proceed hadronically ($W \rightarrow q'\bar{q}$). Event classes are defined according to lepton and jet multiplicities to take advantage of the different signal to background ratios. Single-lepton (SL) and double-lepton (DL) events contain exactly one lepton or an opposite-sign lepton pair, respectively. The b -tagger discriminator of jets is based on secondary vertex information. For each event, a b -tag likelihood ratio is calculated, which optimally separates the hypotheses that either exactly four or two jets originate from b -quarks. Signal events as well as those from the irreducible $t\bar{t} + b\bar{b}$ background contain four b -quarks and thus have values of b_{LR} close to 1.0. Backgrounds containing light quarks tend to have values closer to zero.

The ratio of probability densities under the two competing hypotheses $t\bar{t}H$ and $t\bar{t} + b\bar{b}$ together with the b -tagging information is used to constrain the *signal strength modifier* $\mu \equiv \sigma/\sigma_{\text{SM}}$, shown in Fig. 11.2. No evidence of a signal is found. The 95% CL upper limit under background-only hypothesis is $\mu < 3.3$. The observed limit, $\mu < 4.2$, corresponding to a best-fit value of

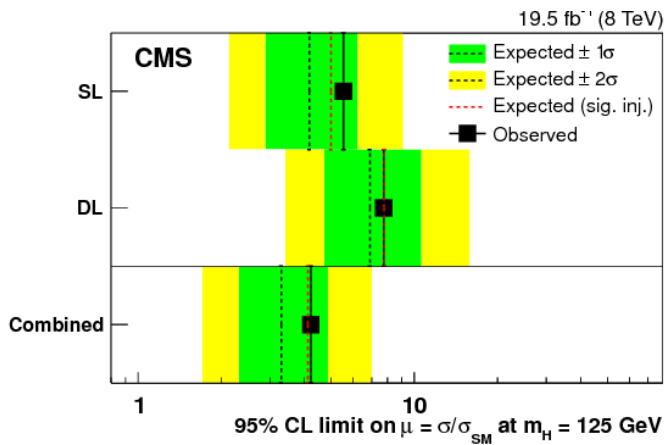


FIG. 11.2 – The 95% CL upper limit on μ , the $t\bar{t}H$ rate normalized to the SM prediction. Observed values are compared to the median expected limits under the background-only and the signal-plus-background hypotheses, both for the individual channels (see text) and their combination.

$\mu = 1.2_{-1.5}^{+1.6}$ represents an improvement by more than 20% over the result published previously.

Our focus now turns towards the higher energy data at 13 TeV becoming available in the coming months. We plan to include the all-hadronic decay channels of the top-quark pair, with a branching ratio as large as 46%, giving a significant increase in statistical accuracy.

44

[1] CDF and D0 collaborations, Phys. Rev. Lett. **109** (2012) 071804.
 [2] CMS collaboration, JHEP **05** (2014) 104.
 [3] ATLAS collaboration, JHEP **04** (2015) 117.
 [4] CMS collaboration, Phys. Rev. D **89** (2014) 012003.
 [5] ATLAS collaboration, JHEP **01** (2015) 069.
 [6] A. Bredstein, Phys. Rev. Lett. **103**, (2009) 012002.
 [7] D0 collaboration, Nature **429**, 638-642 (2004); Phys. Lett. B **617** (2005) 23; M.F. Canelli, FERMILAB-THESIS-2003-22; CDF collaboration, Phys. Rev. Lett. **101** 252001 (2008); Phys. Rev. Lett. **103** 092002 (2009); Phys. Rev. Lett. **105** 042002 (2010); Phys. Rev. Lett. **99** 182002 (2007); Phys. Rev. D **84** 071105(R) (2011); Phys. Rev. Lett. **103** 101802 (2009); Phys. Rev. D **85** 072001 (2012).
 [8] CMS collaboration, arXiv:1502.02485.

11.3 MSSM Higgs boson search

The low mass of the SM Higgs boson demands a mechanism for its stabilization, since naively radiative corrections should make it many orders of magnitude higher. SUSY, for instance, provides loop corrections to the Higgs mass that cancel divergent loops from known SM particles. Within the MSSM (Minimal Supersymmetric Model), there are four additional, heavier, Higgs bosons (two oppositely-charged scalars, one neutral scalar, and a neutral pseudoscalar) which could be in reach of the LHC since the favored masses are just above current limits. We are searching for neutral Higgs bosons decaying to $b\bar{b}$ within the MSSM framework, in association with a b -jet. The cross section is enhanced compared to SM value by a factor of $\tan^2(\beta)$, which could be as large as 1000. For $\tan^2(\beta) \geq 3$ the decay to $b\bar{b}$ has a branching ratio of about 90%.

A previous search at 7 TeV set lower limits on the MSSM Higgs mass up to 350 GeV [1], the most stringent bounds on MSSM Higgs-production in this final state. At 8 TeV $H \rightarrow b\bar{b}$ becomes more boosted and the fraction of events in which two B -hadron jets merge is significant. We found that the sensitivity improves by a special evaluation of such events. We have investigated variables (secondary vertex variables such as vertex mass) discriminating between single- b and two- b jets. Online b -tagging based on impact-parameter significance can cope with the large hadronic interaction rate at the LHC. Different mass ranges have been defined, for which we have optimized the event trigger. We also evaluated the non-QCD-multijet background events, and estimated the associated systematic uncertainties. With the help of recent higher-order MC event generator programs for the MSSM $b\bar{b}H$ process [2], we found that the acceptance differences between the leading and next-to-leading order predictions are small, which is of interest for all related MSSM Higgs analyses.

The new discriminant, called event b -tag, gives a handle on the background composition. The background consists largely of QCD multijet events which can be studied in the measured double- b -tag events. Our group performed exhaustive MC studies confirming the validity of this approach. A full 2D maximum likelihood fit to the invariant mass of the leading two b -jets and the event b -tag fixes the event yields, where a signal would show up as a bump. Results from the full 2012 dataset at 8 TeV will soon be published. We will extend the mass range of this search using the upcoming 13 TeV data.

[1] CMS collaboration, Phys. Lett. B **722**, 207 (2013).
 [2] M. Wiesemann *et al.*, JHEP **02**, 2015, 132.

11.4 Search for $H \rightarrow e\tau$

The effective couplings of the Higgs particle with the SM fermions and gauge bosons are still poorly known. If the scalar sector of the theory is different from the SM expectation (e.g. in presence of more scalars), sizable deviations might occur. In particular, the suppressed couplings of the massive Higgs field to the light SM fermions do not need to be proportional to their masses and do not need to be flavor diagonal. Upper limits on such possible flavor-changing couplings have been derived from the precise low-energy constraints on FCNC processes, both in the quark and in the lepton sector [1, 2], before any attempt to directly access them in Higgs decay. Flavor-changing couplings in the quark sector, and the $h \rightarrow \bar{\mu}e, \bar{e}\mu$ couplings appear severely constrained already. Indirect constraints for couplings involving the τ lepton are, however, quite weak and $\mathcal{B}(h \rightarrow \tau\bar{\mu} + \bar{\mu}\tau)$ and $\mathcal{B}(h \rightarrow \tau\bar{e} + \bar{e}\tau)$ could be as large as 10%, well within reach of the LHC.

We have recently performed a direct search for $H \rightarrow \mu\tau$, resulting in a 2.5σ excess over the background expectation [3]. This result generated a great interest in the physics community and triggered the interest in other final states, such as the $e\tau$, discussed here.

The search was performed in the 19.7 fb^{-1} data sample at 8 TeV, looking at both $\tau \rightarrow \mu\nu_\mu\nu_\tau$ and $\tau \rightarrow \nu_\tau + \text{hadrons}$. We coordinate the analysis of the hadronic channel. Candidate events for Higgs production are grouped according to the number of jets: no jet gluon-gluon fusion (GGF), one jet boosted production, and two jets vector boson fusion (VBF). The main backgrounds are $W + \text{jets}$ events, when a jet is misidentified as electron or τ , and Drell-Yan. Minor backgrounds involve $t\bar{t}$, single top and di-boson (WW, ZW and ZZ) production and $H \rightarrow \tau\tau$.

Both channels use the collinear mass, $M_{coll} = M_{vis} / \sqrt{x_{vis}}$ where M_{vis} is the mass reconstructed using only the visible decay products and x_{vis} is the fraction of τ momentum carried by the visible decay products. Events are selected requiring an electron with $p_T > 45$ (35, 35) GeV and τ_{had} candidates with $p_T > 30$ (40, 30) GeV for the 0 (1, 2) jet category. The electron and the τ are required to have opposite charge. A veto on the presence of additional leptons and jets is applied. No jets tagged as b -jets are allowed to reduce the $t\bar{t}$ and single top backgrounds. The additional requirements on the transverse mass of τ to the missing transverse energy ($\tau \text{ MET } M_T$), $M_T < 70$ (40, 50) GeV for the 0 (1, 2) jet category and, on the $\Delta\Phi$ of the $e - \tau$ pair for the 0-jet category, are applied to better discriminate the signal from $W + \text{jets}$ and Drell-Yan backgrounds.

The collinear mass for the GGF category is shown in Fig. 11.3, where the data in the signal region are kept blind. The measured distribution in the mass sidebands is consistent with the sum of all backgrounds. Expected and ob-

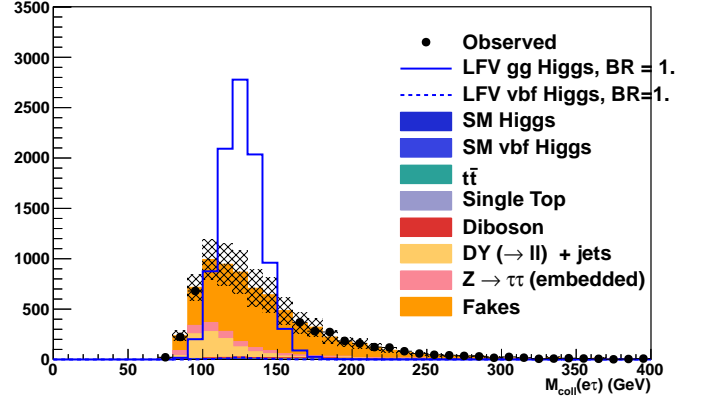


FIG. 11.3 – Collinear mass of the $e\tau_{had}$ final state (see text) in the zero-jet category after applying all the selection cuts. The measured distribution (still blinded in the signal region) is compared with the expected background contributions. The LFBV Higgs signal is enhanced for better visualization.

served limits are calculated in the CLs approach for a Higgs boson mass of 126 GeV. The expected upper limit on the branching ratio is found to be $(1.69 \pm 0.85)\%$ for the $H \rightarrow e\tau_{had}$. Combining both τ_{had} and τ_μ channels the expected upper limit is $(0.74 \pm 0.38)\%$. The study is currently in the final review phase and will be submitted for publication soon.

- [1] G. Blankenburg, J. Ellis and G. Isidori, Phys. Lett. B **712** (2012) 386.
- [2] R. Harnik, J. Kopp and J. Zupan, JHEP **1303** (2013) 026.
- [3] CMS collaboration, CMS-PAS-HIG-14-005.

11.5 Search for dark matter particles with top quarks

In several BSM models, like SUSY, a weakly interacting massive particle (WIMP) arises naturally as a DM candidate. So far, however, there is no established knowledge about its properties, including its mass and interactions with ordinary matter [1, 4].

The interaction Lagrangian between DM particles and quarks can be described by an effective field theory (EFT) with an interaction scale M_* , where the form of the Lagrangian depends on the type of the interaction. For scalar interaction, the coupling strength scales with the quark mass,

$$\mathcal{L}_{\text{int}} = \frac{m_q}{M_*^3} \bar{q}q\bar{\chi}\chi$$

so couplings to light quarks are suppressed and traditional inclusive mono-jet searches are not very sensitive [4–11].

In our analysis, we look for DM produced in association with a top-quark pair. The search is performed in the dilepton [12] and single-lepton channel [13], with large

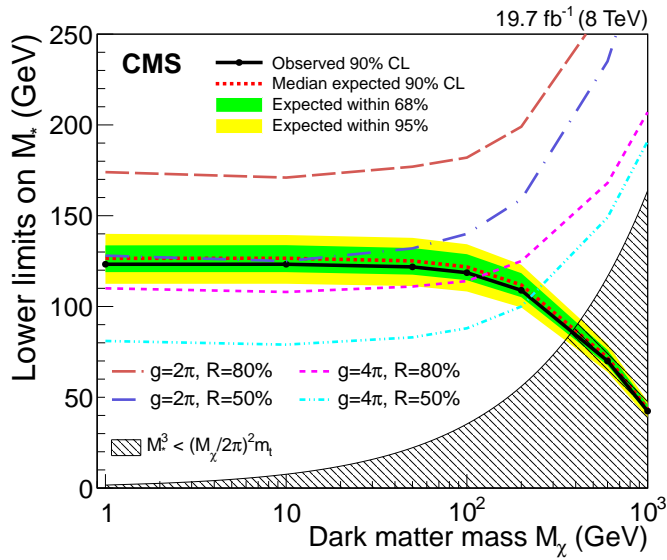


FIG. 11.4 – Observed 90% CL exclusion limits in the plane of DM particle mass and interaction scale. The background-only expectation and the 68% and 95% CL bands are indicated. A lower bound of the validity of the EFT is indicated by the upper edge of the hatched area. The four curves represent the lower bound on M_* for which 50% and 80% of signal events have a pair of DM particles with an invariant mass less than $g\sqrt{M_*^3/m_t}$.

46

transverse missing energy (E_T^{miss}). The single-lepton channel, which is particularly sensitive, shows no signal above SM background, excluding cross sections larger than 22 to 55 fb (90% CL) for DM particles with mass between 1 GeV and 1 TeV. These results translate into new lower limits on M_* , as shown in Fig. 11.4.

In preparation of DM searches for Run 2 the analysis has been extended to the fully hadronic channel. The sensitivity is comparable to the single-lepton channel.

In addition to top quarks, DM can also be produced in association with bottom quark pairs, providing a striking signature. DM signals are characterized by large E_T^{miss} , one or two b-tagged jets and no other significant activities in the detector. The channel is expected to have sensitivity similar to the previous one.

The limits on the interaction scale M_* have been translated into limits on the DM-nucleon scattering cross section for the scalar operator considered here (see Fig. 11.5): 90% CL upper limits are a few times 10^{-42}cm^2 and represent the most stringent limits below 6 GeV.

- [1] Planck collaboration, arXiv:astro-ph/1303.5076.
- [2] V. Trimble, *Ann. Rev. Astrophys.*, **25** (1987) 425.
- [3] E. Komatsu *et al.*, *Astrophys. J. Suppl.*, **192** (2011) 18.
- [4] J. L. Feng, *Ann. Rev. Astron. Astrophys.*, **48** (2010) 495.
- [5] J.M. Beltran *et al.*, *JHEP* **17** (2010) 1.

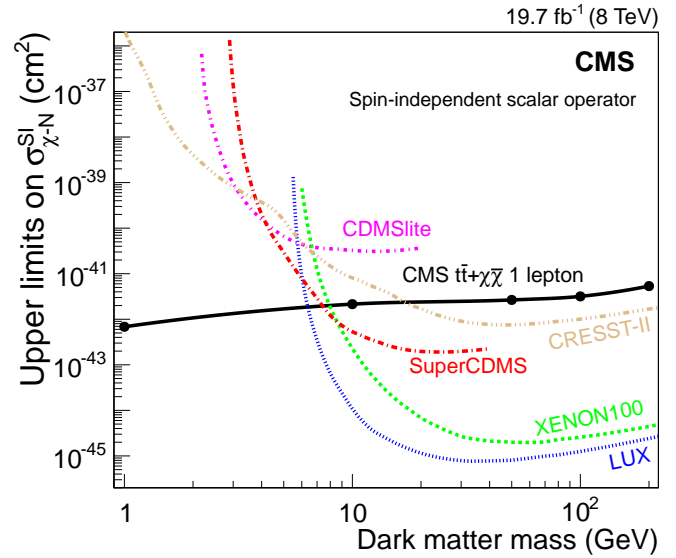


FIG. 11.5 – The 90% CL upper limits on the DM-nucleon spin-independent scattering cross section ($\sigma_{\chi-N}^{\text{SI}}$) as a function of the DM particle mass for the scalar operator considered here. Also shown are 90% CL limits from various direct DM search experiments.

- [6] J. Goodman *et al.*, *Phys. Lett. B* **695** (2011) 185; *Phys. Rev. D*, **82** (2010) 116010.
- [7] P. J. Fox *et al.*, *Phys. Rev. D* **85** (2012) 056011; *Phys. Rev. D* **86** (2012) 015010.
- [8] Rajaraman *et al.*, *Phys. Rev. D* **84** (2011) 095013.
- [9] T. Lin, E.W. Kolb, and L.-T. Wang, *Phys. Rev. D* **88** (2013) 063510.
- [10] CMS collaboration, Tech. Rep. CMS-PAS-EXO-12-048, 2012.
- [11] ATLAS collaboration, *JHEP*, **1304**, 2013; Tech. Rep. ATLAS-CONF-2012-147, CERN, Nov 2012.
- [12] CMS collaboration, CMS-PAS-B2G-13-004.
- [13] CMS collaboration, arXiv:1504.03198.

11.6 Dijet angular distributions and search for new physics

High momentum-transfer proton-proton collisions at the CERN LHC probe the dynamics of the underlying interaction at distances below 10^{-19}m . Often these collisions produce a pair of jets (dijets) approximately balanced in transverse momentum. These dijet events provide an ideal testing ground to probe the validity of perturbative QCD and to search for new phenomena such as quark compositeness or additional, compactified spatial dimensions. A particularly suitable observable for this purpose is the dijet angular distribution expressed in terms of $\chi_{\text{dijet}} = \exp(|y_1 - y_2|)$, where y_1 and y_2 are the rapidities

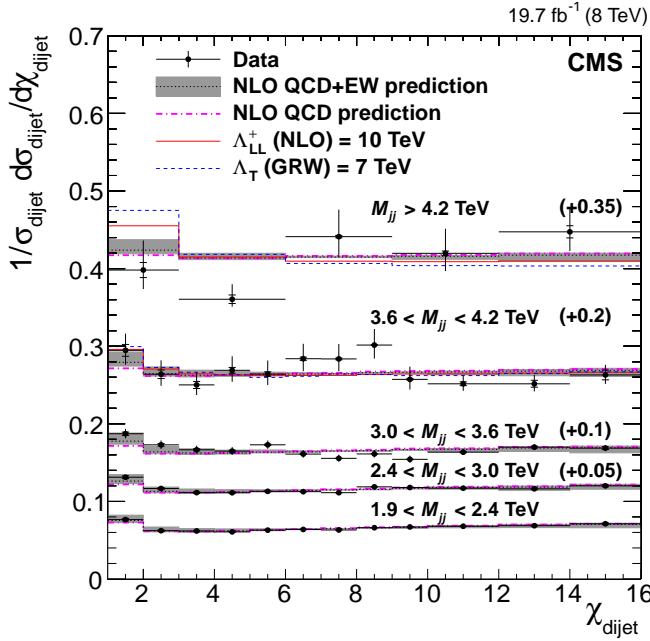


FIG. 11.6 – Normalized χ_{dijet} data distributions corrected for detector effects are compared to NLO predictions with electroweak corrections and no significant deviation is found. The predictions for a signal from quark compositeness Λ_{LL}^+ and extra dimensions Λ_T are overlaid.

of the two jets with the highest transverse momenta. In perturbative QCD the dijet angular distribution at small c.m. scattering angles is approximately independent of the underlying partonic level process and exhibits behavior similar to Rutherford scattering, characteristic of spin-1 particle exchange. Signatures of new physics, such as quark compositeness visible to us as quark contact interactions or virtual exchange of Kaluza–Klein excitations of the graviton in extra dimension models, that exhibit angular distributions that are more isotropic than those predicted by QCD, could appear as an excess of events at low values of χ_{dijet} .

We performed a search based on a data set corresponding to an integrated luminosity of 19.7 fb^{-1} [1]. Dijet angular distributions unfolded for detector effects are found to be in agreement with the perturbative QCD predictions that include electroweak corrections (see Fig. 11.6). Limits on the contact interaction scale from a variety of models at next-to-leading order in QCD corrections are obtained. A benchmark model in which only left-handed quarks participate is excluded up to a scale of 9.0 (11.7) TeV for destructive (constructive) interference at 95% CL. Lower limits between 5.9 and 8.4 TeV on the scale of virtual graviton exchange are extracted for the Arkani-Hamed–Dimopoulos–Dvali model of extra spatial dimensions.

[1] CMS collaboration, arXiv:1411.2646.

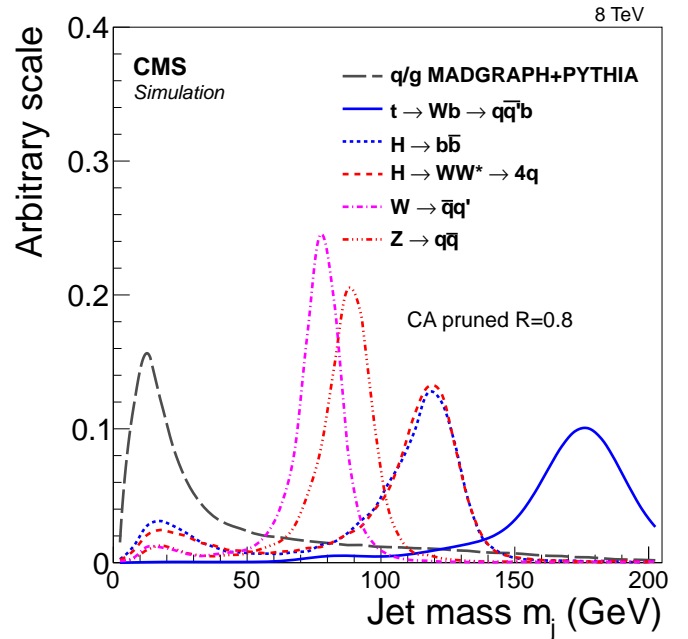


FIG. 11.7 – Distribution of pruned jet mass in simulation of signal and background processes.

11.7 Search for heavy resonances in diboson events

The SM does not explain why the strengths of the electroweak force and gravity differ by 36 orders of magnitude. Composite Higgs models and models of large extra dimensions [1, 2], which do provide a natural solution to this hierarchy problem, predict many new particles such as additional W' and Z' gauge bosons. These bosons can have large branching ratios for decays into W , Z and H bosons, while the decay to fermions is suppressed.

We have searched for such new heavy particles decaying to pairs of bosons in the 2012 data. The recently proposed Heavy Vector Triplet (HVT) model [3] generalizes a large class of explicit models predicting new heavy spin-1 vector bosons and we use it to interpret our search results in a more general framework.

11.7.1 Exploiting jet substructure

The final states described above are accessible through novel jet substructure techniques identifying the bosons by what is called W/Z - or Higgs-tagging. The bosons decay predominantly into quarks which transform into sprays of particles (jets). Unfortunately, for heavy resonances reachable at the LHC, the bosons have such high momenta that their decay products merge into a single jet. In order to distinguish the substructure of these jets we have demonstrated and tested a variety of W/Z -tagging algorithms. The best scheme is based on the Lorentz invariant jet mass with the so-called pruning algorithm [4] and the jet shape variable N -subjettiness [5], which is an

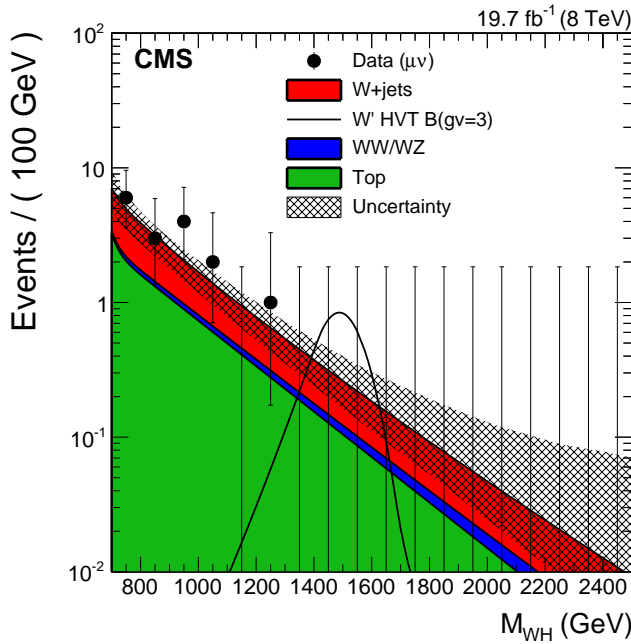


FIG. 11.8 – Distribution of m_{WH} for data and expected backgrounds for the muon category. Also shown is a hypothetical W' signal with mass of 1500 GeV.

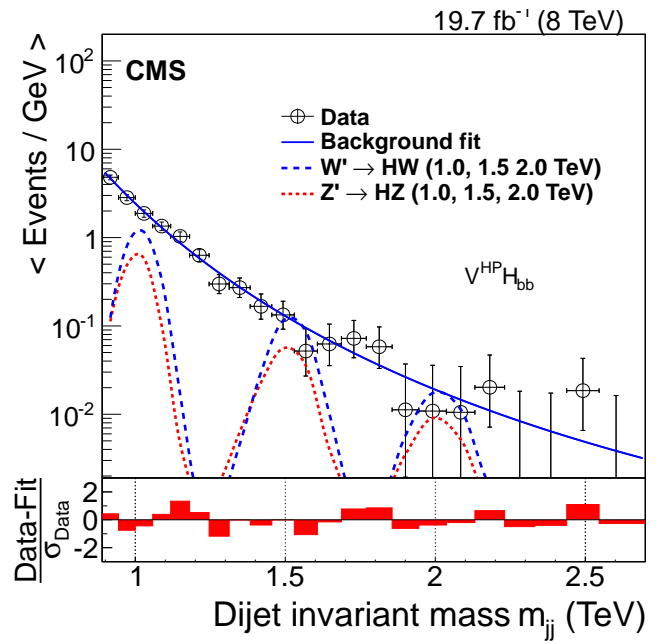


FIG. 11.9 – The final dijet mass distribution fit for a signal-like resonance. No signal is observed, and upper limits on the cross-section are set.

48

indicator for the number of hard quarks in the jet. The pruning algorithm separates the particles from quarks originating in boson decay from those consistent with background-like QCD radiation are filtered out (see Fig. 11.7). Our technique has been employed in the most recent CMS searches.

11.7.2 Search for new heavy bosons with b -tagged jets and tau leptons in the boosted regime

We investigated the decay of a charged heavy vector boson W' into a W and a Higgs boson, which is one of the first studies of an exotic final state with a Higgs boson. For a W' mass between 1 and 3 TeV, the resulting energetic decay products tend to be very collimated. The selected signature, a leptonic W decay in combination with a Higgs decaying into two b -quarks, is characterized by an isolated high p_T lepton, large missing transverse energy and two high p_T jets which are expected to be highly collimated into a single jet. The jet pruning and N-subjettiness algorithms mentioned above have been implemented and the presence of b -quarks is exploited. Additional challenges emerge when the secondary vertices from the B hadrons overlap. As illustrated in Fig. 11.8, no signal was observed and a strongly coupled vector resonance with mass below 1.5 TeV has been excluded [6]. Using the same techniques for $W/Z/H$ identification, our group also performed a search for heavy resonances, denoted as X , in the process $X \rightarrow ZH \rightarrow q\bar{q}b\bar{b}$ and $X \rightarrow WH \rightarrow q\bar{q}'b\bar{b}$,

looking for a bump on a smoothly falling background as shown in Fig. 11.9. This search yields the current most stringent limits in this final state on a strongly coupled vector resonance with mass up to 1.7 TeV [7].

We also search for heavy resonances, in the process $X \rightarrow ZH \rightarrow q\bar{q}\tau\tau$ and $X \rightarrow HH \rightarrow b\bar{b}\tau\tau$. The fact that the τ leptons decay products may overlap makes the τ reconstruction challenging. The hadronic τ identification is performed by algorithms based on jet reconstruction with particle-flow techniques [9]. Since this might fail for overlapping energy deposits we have developed special reconstruction techniques. We remove from consideration energy deposits from each subdetector associated with each identified τ , and recalculate the isolation.

No BSM signals were found in the $Z + H$ final state [8]. From a combination of all possible decay modes of the τ leptons, production cross sections in a range between 0.9 and 27.8 fb are excluded at 95% CL, depending on the resonance mass. The $X \rightarrow HH \rightarrow b\bar{b}\tau\tau$ is currently nearing completion and will have similar sensitivity.

11.7.3 Preparation studies for Run II

The increased beam intensities and energies in Run 2 adversely affect the performance of substructure quantities for V tagging. Typically 30 to 40 proton-proton collisions will accompany an event of interest giving pileup. Moreover, the increase in center-of-mass collision energy from 8 TeV to 13 TeV will raise the production rate and energies

of highly boosted objects challenging the jet reconstruction algorithms and degrading the discriminating power of V tagging variables. Such degradation was observed for jet momenta above 1.5 TeV with the algorithms used in Run 1, due to breakdowns in particle reconstruction techniques [10].

The CMS ECAL granularity is five times finer than HCAL in both η and ϕ , which improves the ability to detect high- p_T jet substructure. We studied different scenarios with different treatment of reconstructing neutral particles from ECAL and HCAL energy left after charged hadron reconstruction [11] and we are able to maintain the current V tagging performance up to $p_T = 3.5$ TeV at an average of 40 pileup interactions. It follows that CMS will effectively provide substructure observables across the full range of jet p_T expected in Run 2.

The di-boson resonance searches our group has performed during Run 1 are a very useful preparation for Run 2 when the sensitivity to new physics signals will overtake the Run 1 results within a couple of months. We are prepared for the search for high mass diboson resonances setting up the full analysis work-flows to be run immediately once the data comes in.

- [1] L. Randall and R. Sundrum, *Phys. Rev. Lett.* **83** (1999) 3370.
- [2] K. Agashe, H. Davoudiasl, G. Perez *et al.*, *Phys. Rev. D* **76** (2007) 036006.
- [3] D. Pappadopulo *et al.*, arXiv:1402.4431.
- [4] S.D. Ellis, C.K. Vermilion, and J.R. Walsh, *Phys. Rev. D* **81** (2010) 094023.
- [5] J. Thaler and K. Van Tilburg, *JHEP* **1103** (2011) 015.
- [6] CMS collaboration, CMS-PAS-EXO-14-010.
- [7] CMS collaboration, CMS-PAS-EXO-14-009.
- [8] CMS collaboration, CMS-PAS-EXO-13-007.
- [9] CMS collaboration, CMS-PAS-PFT-09-001 (2009).
- [10] CMS collaboration, *JHEP* **12** (2014) 017.
- [11] CMS collaboration, CMS-PAS-JME-14-002.



FIG. 11.10 – One half of the barrel pixel detector after re-installation in CMS.

11.8 Detector maintenance, operations, and upgrades

Our group is dedicated to operating, maintaining, and upgrading the barrel pixel detector (BPIX), which our institute helped to build. The detector allows for high precision tracking and to reconstruct secondary vertices from heavy quark or τ -lepton decays and is a key element for most analyses in our research portfolio. Its location closest to the interaction point results in a high track multiplicity and heavy irradiation.

11.8.1 Pixel detector maintenance and operation

The pixel detector, installed in 2008, showed excellent performance during the first LHC run with more than 97.7% of the channels working. After Run 1 finished in 2012, the detector was stored at low temperature in a dedicated clean room, equipped with all infrastructure needed to control and readout the detector. Faulty modules and optical components were replaced and preparations were made for Run 2.

In the course of its operation, the pixel detector suffered radiation damage, resulting in an increase of leakage current and bias voltage, charge trapping and signal degradation. We determined the optimal settings for the irradiated detector and tested the full detector at 0°C . Some sectors were also tested at -15°C as foreseen in Run 2 to mitigate radiation effects.

We took part in the reinstallation (see Fig. 11.10) and were responsible for the commissioning and calibration. A picture of the team, formed by our group and colleagues from PSI, INFN Padova and Hamburg University, is shown in Fig. 11.11. The installation of the BPIX was completed within a week, allowing to quickly proceed with the installation of the FPIX detector and the subsequent closure of CMS.



FIG. 11.11 – Pixel installation team after the successful completion of its task.

Furthermore, we are improving the software used to calibrate, monitor, record data, and reconstruct hits. During the long shutdown of the LHC, we migrated the software to the new infrastructure at the experimental site, and continuously improved its components. Changes in the CMS trigger and timing system made a new control software necessary ensuring the synchronization with the other CMS subdetectors.

11.8.2 Detector studies and improvements to the hit reconstruction

During the year 2012 the BPIX hit resolution in the transverse plane changed gradually from $8\ \mu\text{m}$ to $9\ \mu\text{m}$ (see Fig. 11.12). This degradation is attributed to changes in the detector conditions, such as alignment, gain calibration, Lorentz angle and irradiation. The pixel hit resolution is measured using the so called pixel triplet method [1] in which the actual hit position is compared with the value predicted by the two neighboring layers. This way we are also able to measure the hit efficiency for different detector conditions and irradiation scenarios and their impact on the hit resolution. So far we found no explanation for the degradation but studies are ongoing.

50 Our group has also worked on improving the reconstruction of pixel hits in collimated particle jets. When two charged particles traverse the sensors in close proximity, the pixel hits may overlap and merge into one larger cluster. The resulting merged hit is displaced with respect to the correct position and can lead to deterioration of tracking resolution and efficiency. More details are given in last year's report.

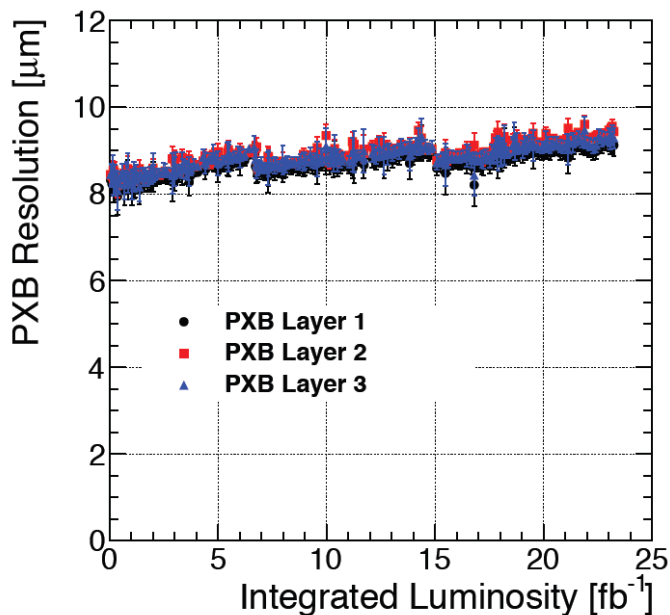


FIG. 11.12 – Hit resolution of the BPIX detector in the transverse plane ($r\phi$) as a function of the delivered integrated luminosity in the year 2012 [1].

11.8.3 Barrel pixel detector phase I upgrade

The current BPIX detector consists of three 57 cm long layers of silicon pixel modules serviced by 2.2 m of supply tubes which transport cooling tubes, electrical power, and optical signals. The University of Zurich designed, built and tested the mechanical support structure and the supply tubes, including the mechanical structure, cooling and service lines, and boards to transfer optical signals. For the BPIX phase 1 upgrade [2] we are again in charge of these components. The upgrade combines a new pixel readout chip with several other improvements to keep up performance during Run 2: The current 3-layer central pixel barrel, 2-disk forward pixel detectors are to be replaced with 4-layer central pixel barrel, 3-disk forward pixel detectors (Fig. 11.13) which makes a complete re-design of the detector and supply tube mechanics necessary. In order to reduce the amount of dead material which has a negative impact on the detector performance a new, light-weight cooling system will be installed. The new cooling system uses two-phase CO_2 cooling instead of single-phase C_6F_{14} liquid cooling. The tubes are much narrower, operate at 60 times higher pressure and show a complicated looping structure.

We have now constructed two prototype half-barrels (four will be needed for the final phase 1 pixel system) including both detector and supply tube parts as shown in Fig. 11.14. The prototypes are currently tested at CERN. The mechanical construction of the cooling system is very challenging, in particular the brazing of thin, stainless steel tubes in dense and inclined positions. We are still performing stress tests at the workshop here at the University of Zurich and investigate aging effects to confirm the reliability and the longterm stability of the brazing process in view of final construction.

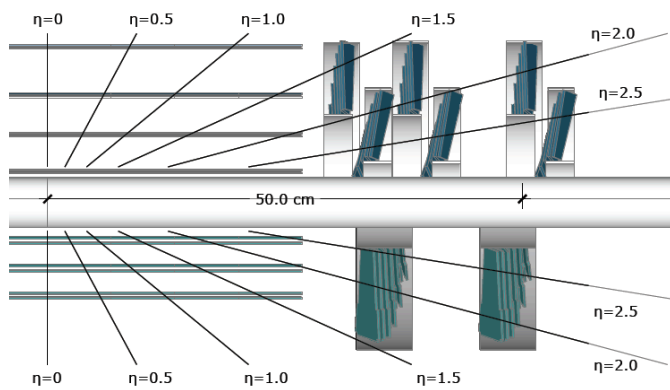


FIG. 11.13 – Schematic of barrel pixel upgrade. Bottom half represents current 3-layer BPIX system, top half shows upgraded 4-layer system in which the innermost detector plane is located within 3 cm of the beam axis.

In addition to the commitment in the construction of the mechanical support system of the CMS pixel phase 1 upgrade, our group is also responsible for the integration of the supply tube readout electronics and the testing of the complete system. The barrel pixel supply tube supports ten types of electronics boards which communicate with the pixel modules to handle control signals, DC-DC power conversion and power distribution, data readout, electrical to optical signal conversions, communication with the DAQ, as well as the cooling loop structure.

In order to test the performance of the complete pixel system we are installing a full CMS-pixel DAQ system at the University of Zurich, commission it and write the necessary software. The system makes use of power supplies, control modules, a DCS system, two readout systems (VME until 2016, μ TCA 2017 and after) as well as additional equipment to handle the complex fiber arrangements and to check the fiber connections.

Prototypes of all electronics components have become available during this past year and were integrated together with two pixel detector modules in our system test as shown as shown in Fig. 11.15. Our goal is to gain experience in the operation of the new system and validate the individual components in view of the final production. Testing has started, but considerable work is still needed over the coming months to operate together all the detector parts and in the development of sophisticated software algorithms for testing, calibration and monitoring of all detector components.

- [1] A. Burgmeier and D. Pitzl, CMS-AN-13-356.
- [2] CMS collaboration, CERN-LHCC-2012-016 (2012).



FIG. 11.14 – One of the two half-barrel prototypes of the phase 1 pixel upgrade cooling system.

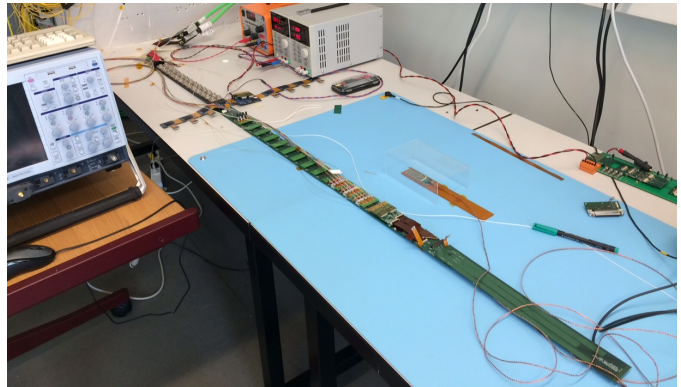


FIG. 11.15 – The CMS pixel phase 1 system test setup at University of Zurich. The test setup includes a detector module connected to the chain of readout electronics that will be hosted on the supply tube.

12 Superconductivity and Magnetism

M. Bendele (January 2014 to September 2014), Z. Guguchia (until July 2014),
H. Keller (until July 2014), E. Stilp (until December 2014)

Visiting scientists: R. Puzniak, A. Shengelaya

Emeritus members: M. Mali, K. A. Müller, J. Roos, T. Schneider

in collaboration with:

Kazan Federal University (B. I. Kochelaev), Leibniz Institute for Solid State and Materials Research Dresden (R. Hühne), Max-Planck-Institute for Solid State Research Stuttgart (A. Bussmann-Holder, J. Köhler), Paul Scherrer Institute (K. Conder, R. Khasanov, E. Morenzoni, E. Pomjakushina, A. Suter), Polish Academy of Sciences (R. Puzniak), Tbilisi State University (A. Shengelaya), University of Rome La Sapienza (A. Bianconi, N.L. Saini), University of British Columbia (W. Hardy, R.F. Kiefl), University of Fribourg (C. Bernhard)

We report on research projects in the field of high-temperature superconductors (HTS's) and materials with novel electronic properties. Our studies involve a number of complementary techniques, such as muon-spin rotation (μ SR), neutron diffraction, X-ray absorption spectroscopy (XAS), and various standard magnetometry techniques.

52

12.1 Oxygen isotope effect on the static spin stripe order in $\text{La}_{2-x}\text{Ba}_x\text{CuO}_4$ ($x = 1/8$)

After the discovery of high-temperature superconductivity in $\text{La}_{2-x}\text{Ba}_x\text{CuO}_4$ (LBCO) numerous comprehensive studies have revealed a complex interplay between charge, spin, orbital, and lattice degrees of freedom [1]. In LBCO the superconducting (SC) transition temperature T_c shows a pronounced minimum at $x \simeq 1/8$ [2], known as the 1/8 anomaly. Here a structural transition from a low-temperature orthorhombic (LTO) to a low-temperature tetragonal (LTT) phase was observed [3]. Neutron diffraction experiments revealed two-dimensional charge and spin order in $\text{La}_{1.48}\text{Nd}_{0.4}\text{Sr}_{0.12}\text{CuO}_4$ [4]. It was proposed [4] that the dopant induced charge carriers, showing a periodically modulated spatial distribution forming a self-organized alternating array of charge and spin stripes, are pinned by the lattice modulation in the LTT phase, and T_c is suppressed. Later experimental studies indicate that uni-directional stripe-like ordering is in fact common to cuprates [5]. Despite of various attempts [6, 7], no consensus on the microscopic mechanism of stripe formation and the relevance of stripe correlations for high-temperature superconductivity in cuprates has been achieved. Exploring the mechanism of stripe formation may help to clarify the situation. The stripe phase may be caused by a purely electronic and/or electron-lattice in-

teraction. There is increasing experimental evidence that a strong electron-lattice interaction is essential in cuprates (see, e.g., [8]) which may, however, not play a role in the formation of the stripe phase.

Isotope-effect experiments played a crucial role for understanding superconductivity. For conventional superconductors they clearly demonstrated that the electron-phonon interaction is responsible for the electron pairing. In the cuprate HTS's unconventional oxygen isotope ($^{16}\text{O}/^{18}\text{O}$) effects (OIE's) on various fundamental quantities were observed [8]. However, no OIE investigation on the charge and spin order in the stripe phase of cuprates has been reported.

We combined magnetization, zero-field as well as transverse-field μ SR experiments in order to study the

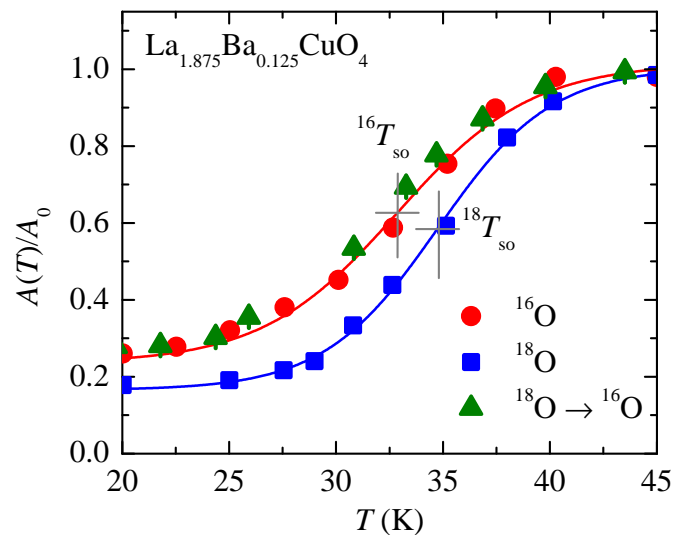


FIG. 12.1 – Normalized transverse-field μ SR asymmetry A/A_0 versus temperature for ^{16}O , ^{18}O , and back-exchanged ($^{18}\text{O} \rightarrow ^{16}\text{O}$) samples of LBCO-1/8.

The crosses mark the spin-stripe order temperatures T_{so} , of both ^{16}O and ^{18}O (from [9]).

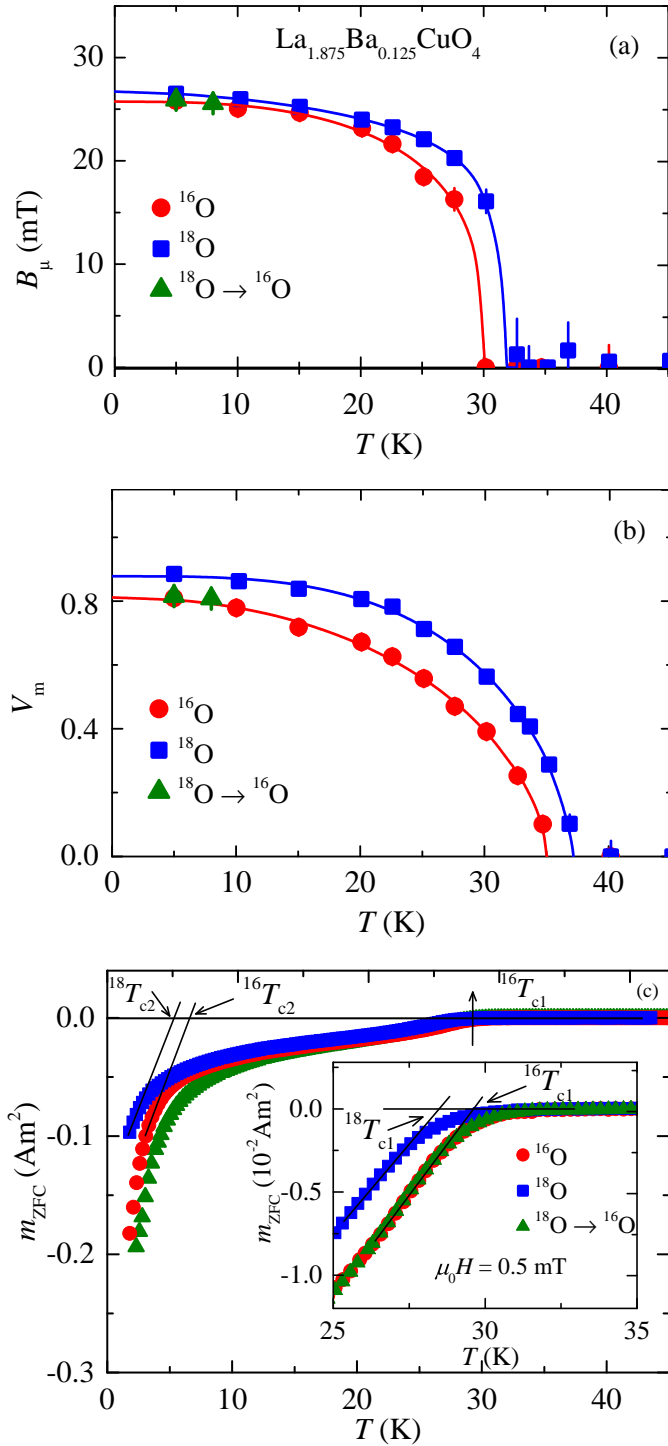


FIG. 12.2 – Comparative studies of ^{16}O , ^{18}O , and back-exchanged ($^{18}\text{O} \rightarrow ^{16}\text{O}$) samples of LBCO-1/8 (from [9]). Shown are the temperature dependences of various observables.

Panels (a) and (b) show the average internal magnetic field B_μ at the muon site and the magnetic volume fraction V_m , respectively. Solid lines represent empirical power-law fits. Panel (c) shows the diamagnetic moment m_{ZFC} . The superconducting transition temperatures T_{c1} and T_{c2} are indicated. The inset gives a closer view of the SC transition near T_{c1} .

OIE's on magnetic and SC quantities related to the static stripe phase of LBCO-1/8 [9]. μSR allows to determine separately the magnetic volume fraction and the order parameter in magnetically ordered materials. We found that the static spin-stripe order temperature T_{so} (see Figs. 12.1 and the magnetic volume fraction $V_m(0)$ (see Fig. 12.2b) exhibit a large negative OIE which is novel and unexpected. This indicates that the electron-lattice interaction plays an essential role for the stripe formation in cuprate HTS's. Furthermore, the observed oxygen-isotope shifts of the superconducting transition temperature T_c (see Fig. 12.2) and the spin-ordering temperature T_{so} have almost the same magnitude, but opposite signs [9]. This provides clear evidence that bulk superconductivity and static spin-order are competitive phenomena in the stripe phase of LBCO-1/8, and that the electron-lattice interaction is a crucial factor controlling this competition. The present results may contribute to a better understanding of the complex microscopic mechanism of stripe formation and of high-temperature superconductivity in the cuprates in general.

- [1] A. Bussmann-Holder *et al.*, Phys. Rev. Lett. **67**, 512 (1991).
- [2] A.R. Moodenbaugh *et al.*, Phys. Rev. B **38**, 4596 (1988).
- [3] J.D. Axe *et al.*, Phys. Rev. Lett. **62**, 2751 (1989).
- [4] J.M. Tranquada *et al.*, Nature (London) **375**, 561 (1995).
- [5] M. Vojta *et al.*, Adv. Phys. **58**, 699 (2009).
- [6] J.M. Tranquada *et al.*, Phys. Rev. B **78**, 174529 (2008).
- [7] Z. Guguchia *et al.*, New Journal of Physics **15**, 093005 (2013).
- [8] H. Keller *et al.*, Materials Today **11**, 9 (2008).
- [9] Z. Guguchia *et al.*, Phys. Rev. Lett. **113**, 057002 (2014).

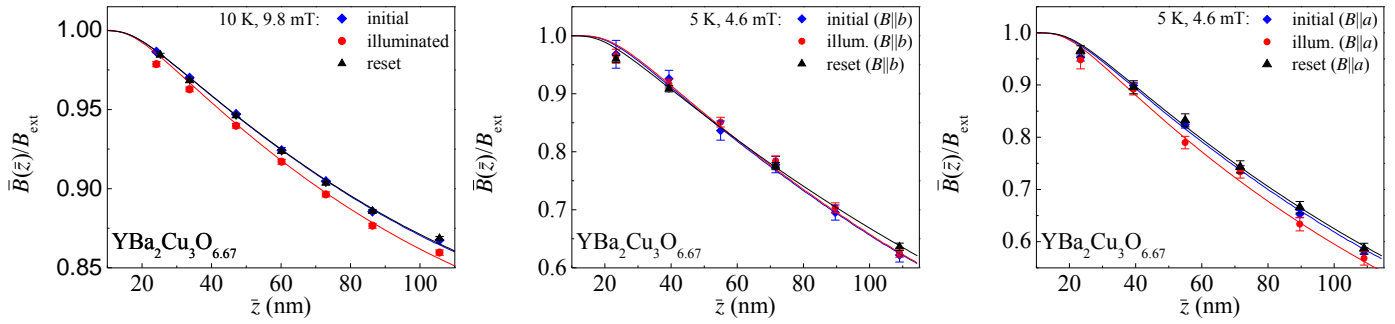


FIG. 12.3 – Magnetic penetration profiles $\bar{B}(\bar{z})$ normalized to the applied magnetic field B_{ext} for the thin-film set (left) and the detwinned ortho-VIII single crystal mosaic (other panels) of $\text{YBa}_2\text{Cu}_3\text{O}_{6.67}$. B_{ext} is oriented parallel to either the crystallographic c axis (left), b axis (center), or a axis (right). The profiles correspond to the states before and after illumination and to the recovered state after one day at room temperature (from [5]).

12.2 Photo-induced effects on $\text{YBa}_2\text{Cu}_3\text{O}_{6+x}$ studied by low-energy μSR

Irradiation with light weakens the superconducting ground state in classical superconductors. Remarkably, studies on $\text{YBa}_2\text{Cu}_3\text{O}_{6+x}$ (YBCO) with reduced oxygen content ($x < 1$) show a persistent increase in the electrical conductivity after continuous illumination with visible light, both in thin films [1, 2] and in single crystals [3]. The critical temperature T_c increases for $0.4 \leq x \leq 0.9$ by up to 15 K [4].

We investigated the changes in the superfluid density n_s using the low-energy μSR technique. Muons were implanted at four different depths in a set thin-film samples ($x = 0.67$) for a determination of the magnetic screening profile $\bar{B}(\bar{z})$ in the Meissner state (see Fig. 12.3, left) [5]. Initially $\bar{B}(\bar{z})$ behaves as expected for a thin film in the Meissner state. After illumination $\bar{B}(\bar{z})$ shows a pronounced change in shape, shifted to lower values. After thermal reset the original screening profile is recovered so the photo persistent changes are fully reversible. Careful analysis of these data revealed that the changes of n_s appear on a length scale of only 50 – 60 nm, corresponding to the light penetration depth determined in ellipsometry measurements [5].

Studies of single crystals reveal the role of disorder in the photo-induced effects. The investigated YBCO ortho-VIII single crystals consist of alternating Cu-O chains which are either empty or full, forming a superstructure. Therefore, the amount of disorder is greatly reduced compared to the thin-film sample set with equal doping level ($x = 0.67$). Moreover, the single crystals are detwinned which allows us to investigate the anisotropy of the photo-induced effects. In the ortho-VIII single crystal mosaic, the superfluid density at the vacuum interface is only increased if the magnetic field is applied along the crystallographic a axis (shielding currents flow along the Cu-O chains). Thus the magnetic screening profile is

shifted to lower values for $B||a$ -axis, but not for $B||b$ -axis (see Fig. 12.3 center and right).

This anisotropic photo persistent behavior can be related to the in-plane anisotropy (different penetration depths λ_a and λ_b) present in YBCO. The large in-plane anisotropy is discussed in the context of multi-band effects. This picture suggests a contribution of the Cu-O chains to the superfluid screening current along the chain direction, leading to a lower λ_b . Since it is assumed that the illumination rearranges the Cu-O chains, the additional charge carriers may modify the contribution of the Cu-O chains to the superfluid density. Therefore, the photo-persistent effect would be clearly observed when the shielding currents flow along the chains ($B||a$), but would be virtually absent for $B||b$, as observed.

In conclusion we observed an anisotropic photo persistent effect in under-doped YBCO. The superfluid density is enhanced mainly close to the sample surface. These results can be explained by a self-organization of the Cu-O chains.

- [1] A. I. Kirilyuk *et al.*, JETP Letters **52**, 49 (1990)
- [2] V. I. Kudinov *et al.*, Phys. Lett. A **151**, 358 (1990).
- [3] G. Yu *et al.*, Solid State Comm. **72**, 345 (1989).
- [4] K. Tanabe *et al.*, Phys. Rev. Lett. **72**, 1537 (1994).
- [5] E. Stilp *et al.*, Sci. Rep. **4**, 6250 (2014).

13 Phase transitions and superconducting photon detectors

A. Gazizulina, X. Zhang, F. von Rohr, H. Grundmann, S. Siegrist, A. Engel and A. Schilling

in collaboration with: University of Bern (K. Krämer), Karlsruhe Institut für Technologie (K. Il'in), Deutsches Zentrum für Luft- und Raumfahrt (H.-W. Hübers, A. Semenov), University of Wellington (E. Anton, B. Ruck), Leiden University (J. Renema, M. van Exter, M. de Dood), University of Geneva (F. Bussières, H. Zbinden), FIRST Lab ETH Zürich, PSI Villigen (M. Medarde, K. Conder), McMaster University (H. Dabkowska), IFW Dresden (V. Kataev, A. Alfonsov), High Field Magnet Laboratory Nijmegen (L. Peters), Hochfeld-Magnetlabor Dresden-Rossendorf (T. Förster), University of Sao Paulo (A. Paduan-Filho), Institute of Nuclear Physics, Tashkent (A. Rakhimov), ETH Zürich (R. Nesper & J. Novotny), Princeton University (R. J. Cava)

(PTMA)

In the past few years, a growing number of superconducting materials have been suggested for use in Superconducting nanowire single-photon detectors (SNSPD), including amorphous materials, see for example [1]. Amorphous films are interesting because they are easier to fabricate on a larger variety of substrates, since no close matching between the two crystal structures is necessary. Amorphous films can also be more easily integrated into more complex micro- and nanostructures, such as optical cavities or multilayers, because they typically do not require elevated substrate temperatures during film deposition. Therefore they are more likely to be compatible with other materials and lithographic technologies. Last but not least, one can expect more homogeneous films and nanostructures on length scales from a few nanometers to micrometers because there are no grain boundaries, for example. W_xSi_{1-x} is particularly interesting as a material for X-SNSPD because of the good X-ray absorption properties of W which has motivated us to investigate W_xSi_{1-x} films of different composition and thickness.

The W_xSi_{1-x} films were prepared by co-sputtering of pure W and Si targets in an Ar atmosphere at room temperature. The deposition parameters have been optimized to obtain maximum T_c for thin (down to 5 nm) and thick films (> 100 nm) and varying composition $0.15 \leq x \leq 0.3$. The resulting film thicknesses have been measured with a step-profiler and an AFM from which we calculated the deposition rates. The compositions of the films have been verified with EDX. We are now able to produce W_xSi_{1-x} films with the desired thickness and composition with high reproducibility. The measured T_c values of thick and thin films compare favorably with published data [2, 3]. A comprehensive set of normal-state and superconducting material parameters were determined from magneto-conductivity measurements as

shown in Fig. 13.1, which are important for the design and the operation of SNSPD and X-SNSPD [4]. Typical values for the most important parameters are given in Table 13.1, together with values for NbN and TaN films.

The knowledge of the W_xSi_{1-x} material parameters allowed us to apply our recently developed detection model [5, 6]. We have found strong indications that in W_xSi_{1-x} a much lower energy (corresponding to mid-infrared photons) is necessary to completely suppress superconductivity in a significant part of the strip cross-section. The enhanced sensitivity to low-energy photons is a consequence of the reduced T_c and the lower density of states of W_xSi_{1-x} as compared to NbN and may explain some of the peculiar differences between W_xSi_{1-x} and nitride based SNSPD [6].

55

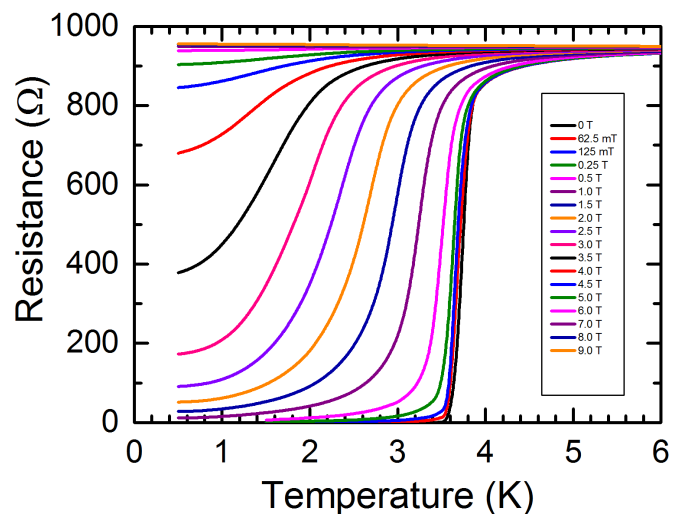


FIG. 13.1 – Resistance as a function of temperature and magnetic field for a typical $W_{0.8}Si_{0.2}$ film of 10 nm thickness.

Tab. 13.1 – Summary of the most important material parameters of a typical thin $W_{0.8}Si_{0.2}$ film compared to the respective parameters of similarly thick NbN and TaN films.

Material	Energy gap (meV)	Coherence length (nm)	Penetration depth (nm)	Diffusion coefficient (nm^2/ps)
NbN	2.3	4.2	430	52
TaN	1.3	5.2	520	60
WSi	0.53	8.0	1400	75

- [1] V. B. Verma *et al.*, Appl. Phys. Lett., **105**, (2014) 022602.
 [2] S. Kondo, J. Mater. Res., **7**, (1992) 853.
 [3] B. Baek *et al.*, Appl. Phys. Lett., **98**, (2011) 251105.
 [4] J. Lonsky, Bachelor thesis, Universität Zürich (2014).
 [5] A. Engel and A. Schilling, J. Appl. Phys., **114**, (2013) 214501.
 [6] A. Engel, J. Lonsky, X. Zhang, and A. Schilling, IEEE Trans. Appl. Supercon. **25**, (2015) 2200407.

56

13.1 Influence of doping on the BEC-phase boundary in $Ba_{3-x}Sr_xCr_2O_8$

In the previous annual report, we described how chemical disorder influences the structure and magnetic interactions in the solid solution $Ba_{3-x}Sr_xCr_2O_8$. The Cr^{5+} ions are arranged in pairs, forming dimers with a strong interaction constant J_0 between the spin- $\frac{1}{2}$ electrons inside the dimers and weaker interdimer interactions J' . For

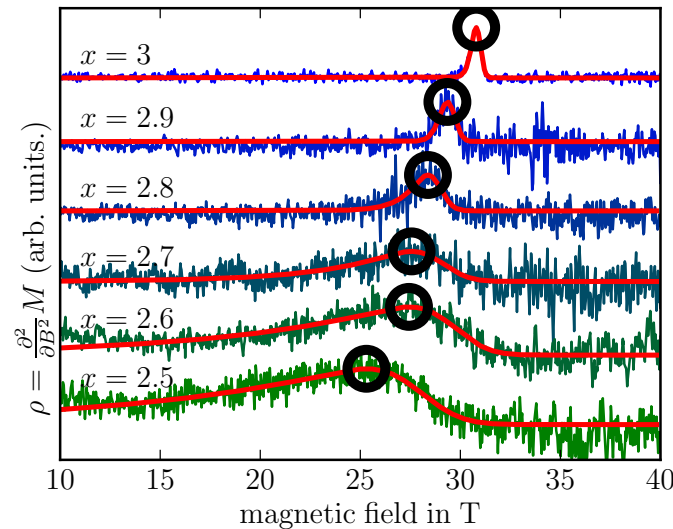


FIG. 13.2 – The derivative $\rho \equiv d\chi/dB$ of the susceptibility χ versus applied magnetic field B , for several compositions of $Ba_{3-x}Sr_xCr_2O_8$. Results from pulsed field magnetometry experiments at $T \approx 1.5$ K. The black circles indicate the extrema which mark the value of the critical field B_c .

the mother compounds, $Ba_3Cr_2O_8$ and $Sr_3Cr_2O_8$, the electronic system has been reported to show a field-induced ordering phase transition which has been described in terms of a Bose-Einstein-condensation (BEC) of magnetic quasiparticles (triplons) [1, 2] which are formed by the above described dimerized electronic spins in the lattice. The critical field above which this condensation occurs depends largely on the value of J_0 .

For $Ba_{3-x}Sr_xCr_2O_8$, J_0 varies in a peculiar way with Sr content x [3]. Based on a neutron-diffraction analysis of the structural properties at room temperature and at $T = 2$ K, we could show that the stoichiometry dependent disorder leads to a gradual suppression of a structural phase transition in $Ba_{3-x}Sr_xCr_2O_8$ which strongly influences the magnetic properties of the spin system, allowing us to explain these results [4].

As the change of the magnetic interactions should also modify the critical fields B_c for the magnetic ordering ($B_c \approx 12.5$ T in $Ba_3Cr_2O_8$ and $B_c \approx 30.5$ T in $Sr_3Cr_2O_8$), we have performed low temperature magnetometry experiments in high magnetic fields. To estimate the dependence of B_c on x , we have performed pulsed field magnetometry experiments in fields up to 65 T at the *Hochfeld-Magnetlabor Dresden-Rossendorf* for x in the range 2.5 - 3.0. As the phase transition of the spin system is supposed to be of second order, the derivative $\rho(B)$ of the measured susceptibility $\chi(B)$ should peak at the transition field. In Fig. 13.2, we have plotted $\rho(B) = d^2M/dB^2 = d\chi/dB$. Note that $B_c(x)$ increases with x .

The variation of B_c due to the variation of the magnetic interactions with x should be accompanied by a shift of the critical temperature $T_c(B)$ of the magnetic ordering. To examine T_c in more detail, we have performed cantilever magnetometry experiments in high magnetic

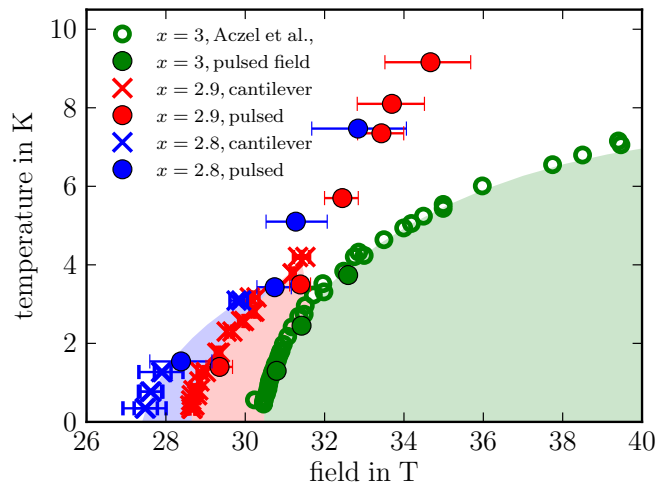


FIG. 13.3 – The critical temperature T_c for the triplon condensation as a function of the applied magnetic field for $x \in \{3, 2.9, 2.8\}$. The open circles represent data points from [2]. The colored areas are guides to the eye only.

fields at temperatures down to $T = 350$ mK for $x=2.8$ and $x=2.9$. From the second derivative of the obtained magnetization M we have calculated $\rho(B) = d^2M/dB^2$. The critical field corresponds to the value at which $\rho(B)$ reaches its maximum, as in the above described pulsed field experiments.

In Fig. 13.3, we have plotted $T_c(B)$, resulting from these measurements for $\text{Ba}_{0.1}\text{Sr}_{2.9}\text{Cr}_2\text{O}_8$, $\text{Ba}_{0.2}\text{Sr}_{2.8}\text{Cr}_2\text{O}_8$ and pure $\text{Sr}_3\text{Cr}_2\text{O}_8$. The observed phase boundaries are shifted towards lower magnetic fields when lowering x , in accordance with Fig. 13.2. To verify these results from magnetometry experiments, we are currently performing high field heat capacity experiments for $x = 2.9$.

- [1] M. Kofu *et al.*, Phys. Rev. Lett., **102**, (2009) 177204.
- [2] A. A. Aczel *et al.*, Phys. Rev. Lett., **103**, (2009) 207203.
- [3] H. Grundmann, A. Schilling, C. A. Marjerrison, H. A. Dabkowska, B. D. Gaulin, Mat. Res. Bull. **48**, (2013) 3108.
- [4] H. Grundmann, A. Schilling, M. Medarde, D. Sheptyakov, Phys. Rev. B., **90**, (2014) 075101.

13.2 Superconductivity and correlated Fermi liquid behavior in noncentrosymmetric $\text{Ca}_3\text{Ir}_4\text{Ge}_4$

Inversion symmetry is an important concept for understanding superconductivity, allowing to classify superconductors by the order parameter symmetry as conventional (*s*-wave) or unconventional (*p*-, *d*-, *f*-wave). However, for structures lacking inversion symmetry, the classification loses its strict meaning and parity-violating superconductivity is allowed. Thereby, a mixture of spin-singlet and spin-triplet pairing states within the same orbital channel can occur (see, e.g., [1, 2]).

CePt_3Si , the most discussed noncentrosymmetric superconductor, displays pronounced unconventional properties, such as the coexistence of magnetism and superconductivity, the large H_{c2} , and a very unusual spin-relaxation rate $1/T_1$. CePt_3Si is, however, also a heavy-fermionic superconductor, so its unconventional properties may not only come from the lack of inversion symmetry [3]. Other noncentrosymmetric compounds with indications for unconventional superconducting properties are $\text{Li}_2\text{Pt}_3\text{B}$, $\text{Mo}_3\text{Al}_2\text{C}$, and LaNiC_2 . In the other noncentrosymmetric superconductors, *s*-wave pairing appears to be dominant and no unconventional properties were observed [4]. To improve our understanding it is important to explore novel types of noncentrosymmetric superconductors.

The cubic noncentrosymmetric $\text{Na}_3\text{Pt}_4\text{Ge}_4$ structure-type with the space group $I\bar{4}3m$, is a rather rare structure with only five known examples: $\text{Na}_3\text{Pt}_4\text{Ge}_4$ [5], $\text{Eu}_3\text{Ni}_4\text{Ga}_4$ [6], $\text{Ca}_3\text{Ir}_4\text{Si}_4$ [7], $\text{Sr}_3\text{Ir}_4\text{Sn}_4$ [8], and $\text{Ca}_3\text{Ni}_4\text{Ga}_4$ [9]. So far a detailed study has been per-

formed for $\text{Eu}_3\text{Ni}_4\text{Ga}_4$ [10] only and electronic structure calculations only exist for $\text{Sr}_3\text{Ir}_4\text{Sn}_4$ [8].

We have now reported [11] the discovery, the crystal structure, and the elementary physical properties of $\text{Ca}_3\text{Ir}_4\text{Ge}_4$, which is a new member of the $\text{Na}_3\text{Pt}_4\text{Ge}_4$ structure type. We show that this compound is a low-temperature superconductor, while above T_c it is a paramagnetic metal, with Fermi liquid behavior, showing indications of strong electron-electron correlation.

In Fig. 13.4, we show the powder x-ray diffraction pattern at ambient temperature of a sample with the nominal composition $\text{Ca}_3\text{Ir}_4\text{Ge}_4$. The compound is found to crystallize in the $\text{Na}_3\text{Pt}_4\text{Ge}_4$ structure type with the cubic body centered $I\bar{4}3m$ space group with the lattice parameter $a = 7.56895(4)$ Å. The material is found to be air sensitive and a small CaO impurity (2%) is observed in the x-ray diffraction pattern, but all other experimentally observed intensities are in very good agreement with the $\text{Na}_3\text{Pt}_4\text{Ge}_4$ structure type. The crystal structure of $\text{Ca}_3\text{Ir}_4\text{Ge}_4$ is shown in Fig. 13.5a. The Ir atoms are surrounded by the Ge atoms in a tetrahedral coordination. These edge-sharing and corner-sharing IrGe_4 tetrahedra form a 3D network. The channels in the structure are occupied by Ca atoms; this channel-type array resembles that found in NaPd_3Ge_2 and NaPd_4Si_4 and related structures [12, 13]. The Ir-Ge framework consists of Ir_4Ge_4 polyanions built from tetrahedral stars, as shown in Fig. 13.5b. These tetrahedral stars do not contain any interstitial atoms, as expected from the short Ir-Ir distance.

In Fig. 13.5c, we show the Ir tetrahedron found both at the center and at the origin of the unit cell of the compound. The tetrahedral structural motifs present, and

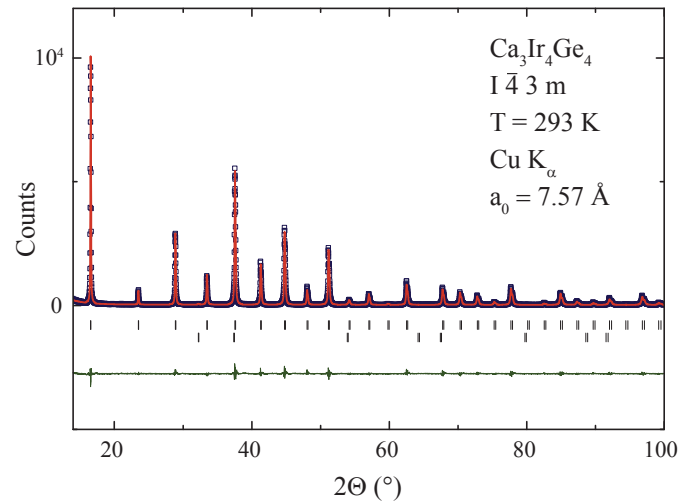


FIG. 13.4 – Powder x-ray diffraction pattern of $\text{Ca}_3\text{Ir}_4\text{Ge}_4$ at room temperature. Dark-blue squares: measurement; red curve: calculation; upper tic marks: calculated peak positions for $\text{Ca}_3\text{Ir}_4\text{Ge}_4$; lower tic marks: same for 2% CaO impurity; lower curve, difference between observed and calculated pattern.

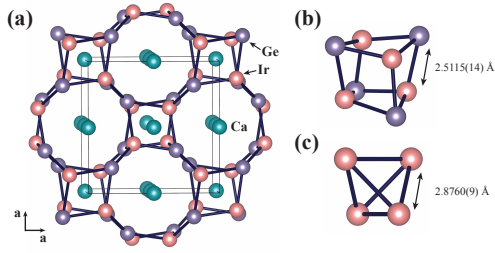


FIG. 13.5 –

(a) Crystal structure of $\text{Ca}_3\text{Ir}_4\text{Ge}_4$, the Ge-Ir bonds are depicted, (b) Ir_4Ge_4 polyanion in the shape of a tetrahedral star, (c) Ir tetrahedron in the center of the unit cell.

their arrangement in the cell, result in $\text{Ca}_3\text{Ir}_4\text{Ge}_4$ having a noncentrosymmetric crystal structure.

In Fig. 13.6, we present the normalized resistivity $\rho(T)/\rho(6\text{ K})$ of $\text{Ca}_3\text{Ir}_4\text{Ge}_4$ in zero external magnetic field and in a temperature range 0.6 - 6 K. A clear transition to superconductivity is observed, with a critical temperature mid-point of $T_{c,\text{mid}} \approx 1.7\text{ K}$, reaching zero resistance at $T_c(\rho = 0) \approx 1.4\text{ K}$. The bulk nature of the superconductivity, confirmed by the specific heat (see Fig. 13.6b), is suppressed in an external magnetic field of $\mu_0 H = 1\text{ T}$.

Based on the Debye model and Fermi statistics the specific heat of the normal state can be calculated according to

$$C = C_e + C_l = \gamma T + \beta T^3,$$

where, γ and β denote the electronic and the phonon contributions, respectively. The electronic contribution is, under the assumption of a degenerate electron gas of non-interacting particles, linear in the density of states at the Fermi-level $D(E_F)$:

$$\gamma = \frac{\pi^2}{3} k_B^2 D(E_F).$$

With $k_B \approx 1.38 \times 10^{-23}\text{ J}\cdot\text{K}^{-1}$, we obtain for $\text{Ca}_3\text{Ir}_4\text{Ge}_4$ with $\gamma \approx 25\text{ mJ}\cdot\text{mol}^{-1}\cdot\text{K}^{-2}$ a $D(E_F) \approx 10.6\text{ states/eV}$, and with $\beta \approx 1.64\text{ mJ}\cdot\text{mol}^{-1}\cdot\text{K}^{-4}$ a Debye temperature of $\Theta_D \approx 235\text{ K}$.

In the inset of Fig. 13.6b, we show the measured C_e/T data after subtraction of the phonon contribution. The superconducting transition temperature is determined to be $T_c \approx 1.8\text{ K}$, by an entropy conserving construction (solid line in the inset of figure 13.6b), in agreement with the transition temperature observed in the resistivity measurement. The discontinuity at T_c is found to be $\Delta C/T_c \approx 38\text{ mJ}\cdot\text{mol}^{-1}\cdot\text{K}^{-2}$, in good agreement with comparable intermetallic compounds. For the normalized discontinuity in the specific heat, we obtain a value of $\Delta C/\gamma T_c \approx 1.52$, which is close to the standard weak-coupling BCS value of $\Delta C/\gamma T_c = 1.43$. Well above T_c , the compound is

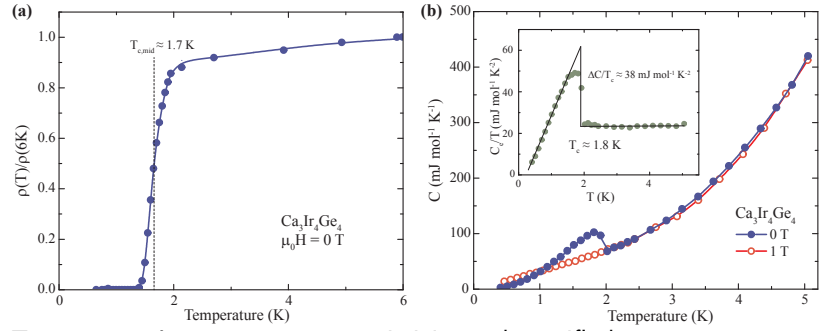


FIG. 13.6 – Low-temperature resistivity and specific heat measurements on a polycrystalline sample of $\text{Ca}_3\text{Ir}_4\text{Ge}_4$ in the vicinity of the superconducting phase transition.

a paramagnetic metal, with Fermi liquid behavior (data not shown). The value of the Kadowaki-Woods ratio and Stoner enhancement factor indicate a significant electron-electron correlation in this compound.

In conclusion, we have synthesized a new compound $\text{Ca}_3\text{Ir}_4\text{Ge}_4$ by high-temperature solid-state synthesis in the noncentrosymmetric $\text{Na}_3\text{Pt}_4\text{Ge}_4$ structure type. We observe a clear transition to superconductivity below 2 K in the resistivity and in the specific heat. The physical properties display indications for electron-electron correlation and correlated Fermi-liquid behavior. Therefore, $\text{Ca}_3\text{Ir}_4\text{Ge}_4$ is a new candidate material for the investigation of the admixture of spin-singlet and spin-triplet pairing states in noncentrosymmetric superconductors.

58

- [1] M. Sigrist, K. Ueda, *Rev. Mod. Phys.* **63** (1991) 239.
- [2] E. Bauer and M. Sigrist, *Non-Centrosymmetric Superconductors*, (Springer-Verlag, Berlin, Heidelberg, 2012).
- [3] E. Bauer *et al.*, *Phys. Rev. Lett.* **92** (2004) 027003.
- [4] M. Isobe *et al.*, *Chemistry of Materials* **26** (2014) 2155, and citations therein.
- [5] W. Thronberens and H. Schuster, *Z. Naturforsch. B* **34** (1979) 781.
- [6] A. E. Dwight, *Materials Research Bulletin* **22** (1987) 305.
- [7] S. Schoolaert and W. Jung, *ZAAC* **628** (2002) 1806.
- [8] R. Hoffmann *et al.*, *International Journal of Inorganic Materials* **2** (2000) 135.
- [9] S. Kim *et al.*, *Dopov. Akad. Nauk Ukr. RSR, Ser. B*, **13**, (1983).
- [10] C. Anupam *et al.*, *J. Phys.: Condens. Matter* **24** (2012) 326002.
- [11] F. von Rohr *et al.*, *Phys. Rev. B* **89** (2014) 224504.
- [12] W. Thronberens *et al.*, *Journal of the Less-Common Metals* **76** (1985) 99.
- [13] M. N. Ali, F. von Rohr, C. Campana, A. Schilling, R. J. Cava, *to be published*.

14 Surface Physics

M. Hengsberger, G. Mette, L. Castiglioni, H. Cun, S. Förster, E. Miniussi, C. Monney, R. Westerstöm, C. Bernard, M. Greif, A. Hemmi, P. Kliuiev, A. Kostanyan, G. Landolt, A. Schuler, R. Stania, W.D. Zabka, R. Arulanantham, M. Baumgartner, D. Becker-Koch, M. Graf, A. Spescha, T. Kälin, T. Greber, and J. Osterwalder

The group investigates surface and interface phenomena at the atomic level. For this purpose the laboratory is well equipped for the preparation and characterization of clean single-crystalline surfaces as well as metal and molecular monolayer films, using a wide variety of experimental techniques. Moreover, the group is participating actively in the buildup and commissioning of the new SLS beam-line PEARL (PhotoEmission and Atomic Resolution Laboratory).

We hosted four postdocs with their own grants: H. Cun (UZH Forschungskredit): *Freestanding monolayers of boron nitride, graphene and their heterostructures*, S. Förster (P.R.I.M.E program of the DAAD): *Looking inside a 2D quasicrystal*, C. Monney (SNF Ambizione): *Time- and angle-resolved photoemission spectroscopy on correlated materials*, and R. Westerström (Swedish Research Council): *A new family of single-molecule magnets: Structural and magnetic characterization of self-assembled monolayers*.

During the report period the research was performed in the following four groups of projects:

- 2D Materials

The long term project on two dimensional (2D) materials progressed along two lines. First, high quality mono-atomic layers of hexagonal boron nitride were grown on single crystalline Rh(111) four-inch wafers [1] and distributed to eight users within and outside the Future and Emerging Technology (FET) Graphene flagship of the European Union. The group continued the efforts for the delamination of single orientation layers of graphene and hexagonal boron nitride from such transition metal substrates by electrochemical means. Second, we explore atom implantation beneath single layer materials by means of low energy ions. It turns out that the created defects, the "nanotents", harbor single atoms beneath an atomically thin "rainfly" and occupy preferential sites within the large 3 nm super unit cells of h-BN/Rh(111) [2, 3] and graphene on Ru(0001) [4]. The ion irradiation also enables the formation of 2 nm voids in single-layer h-BN and graphene, where we succeeded to construct a model for the remarkable nanostructure formation process via the "can-opener" effect, showing that the voids may be annihilated at higher temperatures [5].

- Ultrafast processes at surfaces

The Swiss National Science Foundation (SNF) granted the NCCR MUST (Molecular Ultrafast Science and Technology) for a second period of four years, starting in July 2014. We concluded our series of attosecond measurements in collaboration with ETH Zurich by taking RABBITT traces from various surfaces. Moreover, first time-resolved photoelectron diffraction data were taken from Bi(111). From these data it was possible to extract both electronic and structural dynamics underlying the excitation of coherent phonons in Bi. All these results are currently analyzed and will be submitted for publication in 2015 (see Sec. 14.1). Simulations on the time evolution of the orientation of CO molecules on Pt(111) were performed [6] (see Sec. 14.2). Within the Ambizione project of C. Monney we started to build up a new spectrometer for time-resolved measurements which will be located in the laser-laboratory. This spectrometer will be dedicated to time-resolved two-photon-photoemission experiments and, later on, time-resolved photoelectron spectroscopy experiments using a new high-harmonic gas jet source for obtaining high-energy UV-light [8].

- LightChEC

Within the University Research Priority Program "Light to Chemical Energy Conversion" (LightChEC), we are developing model systems for water reduction and oxidation catalysts, as well as photosensitizers supported on well-defined single-crystal surfaces, with the goal to identify suitable substrates and covalent anchoring units for a heterogeneous water splitting device. Metal complexes like cobalt-pyrphyrin have shown promise for water reduction in homogeneous catalysis [7]. The adsorption of the macrocyclic ligand pyrphyrin synthesized in the group of R. Alberto at UZH was studied on a Au(111) surface. The phase diagram of pyrphyrin on Au(111) in the sub-monolayer regime was established. Two distinct phases were identified and structurally characterized. On the high-coverage phase, deposition of Co atoms at the level of 5% of a monolayer and subsequent annealing lead to the formation of an almost complete monolayer of Co-ligated pyrphyrin molecules.

- Spin Shuttles

The investigation of endohedral single molecule magnets (spin shuttles) [9] was continued within the DACH project "Nitride Cluster Fullerene Spin Shuttles: The role of cluster composition for single molecule magnet behavior" in collaboration with IFW Dresden (A. Popov) and PSI Villigen (C. Piamonteze). With angular dependent x-ray absorption spectroscopy we could demonstrate that in a monolayer of Dy₂ScN@C₈₀ on Rh(111) the endohedral units (Dy₂ScN) orient parallel to the surface and show single molecule magnet behavior at 4 K [10] (see Sec. 14.3). We also installed and commissioned the sub-Kelvin SQUID magnetometer at Irchel (ASKUZI), a joint project with the group of A. Schilling and G. Patzke. Several new endohedral single molecule magnets were found and are further investigated.

[1] A. Hemmi *et al.*, Rev. Sci. Instr. **85**, 035101 (2014).

[2] H. Cun *et al.*, ACS Nano **8**, 1014 (2014).

[3] H. Cun *et al.*, Nano Lett. **13**, 2098 (2013).

[4] H. Cun *et al.*, Surf. Sci. **634**, 95 (2015).

[5] H. Cun *et al.*, ACS Nano, **8**, 7423 (2014).

[6] M. Greif, Ph.D. Thesis, University of Zurich (2015).

[7] S. Schnidrig *et al.* in preparation.

[8] C.M. Heyl, *et al.*,
J. Phys. B: At. Mol. Opt. Phys. **45**, 074020 (2012).

[9] R. Westerström *et al.*,
J. Am. Chem. Soc. **134**, 9840 (2012).

[10] R. Westerström *et al.*,
Phys. Rev. Lett. **144**, 087201 (2015).

In the following, three highlights of last year's research are presented in more detail.

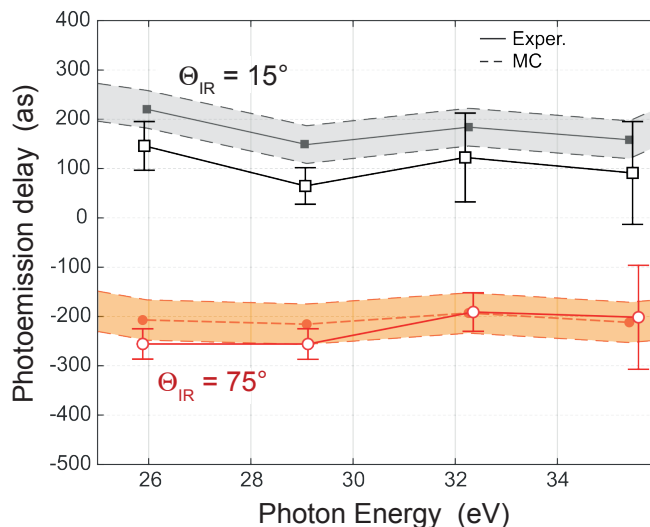
FIG. 14.1 – Delays extracted from the RABBITT traces at two equivalent points in the Brillouin zone of Cu(111), which correspond to angles of light incidence $\Theta_{IR} = 15^\circ$ and 75° (see text). The results of semi-classical Monte Carlo calculations are shown for comparison where the shaded regions represent the uncertainty in the gas phase reference measurement used for time delay calibration. The absolute delay offset is not known, but only the shift between the two incidence angles is important. For this reason the theoretical results were shifted to fit the measurements. From Ref. [5].

14.1 Photoemission delays from attosecond interferometry

In collaboration with: Matteo Lucchini, Lamia Kasmi, Lukas Gallmann, and Ursula Keller (Attoline project), Physics Department, ETH Zurich; NCCR MUST.

We continued to take RABBITT measurements from noble metal surfaces in collaboration with the group of U. Keller at Attoline (ETHZ). RABBITT, which stands for reconstruction of attosecond beating by interference of two-photon transitions [1] was initially used in gas-phase experiments to study atomic photoemission delay at the attosecond time scale [2]. In RABBITT, the absorption of an XUV photon with a specific energy is followed by either absorption or stimulated emission of an IR photon. This two-photon process gives rise to the appearance of sidebands in the temporal overlap of the XUV and IR pulses. Quantum path interference leads to a beating pattern that entails the spectral photoemission phase. The extension of RABBITT to noble-metal surfaces allowed us to extract energy-dependent photoemission delays from interferometric pump-probe experiments using a short attosecond pulse train in the XUV as pump pulse and a few cycle IR probe pulse [3]. The main advantages compared to so-called streaking experiments [4] are the use of fairly long IR pulses and attosecond pulse trains. This simultaneously maximizes the energy *and* temporal resolution without being limited by the time-bandwidth product.

From our previous study [3] one important problem remained to be solved: The description of the transient optical grating generated by incoming and reflected IR fields. We addressed the open question of the effect of the IR probing field and the phase of the transient grating by taking traces from Cu(111) [5]. In order to do so, it was necessary to exclude additional contributions from the photoemission process itself. Therefore, the traces were obtained from equivalent momenta in the Cu Brillouin



zone on the two sides of a mirror plane of the Cu(111) surface. The electrons originate from the same initial states and are excited in identical final states for the two geometries. The only difference is the angle of light incidence and, thereby, a difference in transient grating. The phase will change as well as a consequence of the complex angle-dependent reflection coefficient. As a result, the phase shift observed for the two geometries equals almost exactly the phase difference computed using Fresnel's equations and that of published values for the reflection coefficient at 800 nm, as shown in Fig. 14.1.

- [1] P. M. Paul *et al.*, *Science* **292**, 1689 (2001).
- [2] K. Klünder *et al.*, *Phys. Rev. Lett.* **106**, 143002 (2011).
- [3] R. Locher, L. Castiglioni *et al.*, *Optica* **2**, 405 (2015).
- [4] A. Cavalieri *et al.*, *Nature* **449**, 1029 (2007).
- [5] M. Lucchini *et al.*, submitted for publication (2015).

14.2 Recording molecular motion by photoelectron diffraction

In collaboration with: Tibor Nagy, Maxym Soloviov, and Markus Meuwly, University of Basel; NCCR MUST.

Time-resolved photoelectron diffraction experiments became possible with the availability of ultrashort extreme ultraviolet pulses or x-ray pulses from free-electron lasers [1, 2]. In view of future time-resolved investigations of THz-driven molecular dynamics the group of M. Meuwly (U Basel) and our group simulated the behavior of 50 independent carbon monoxide molecules adsorbed on on-top positions on a Pt(111) surface [3]. Platinum is a well established and efficient catalyst for reactions of CO [4]. There have been many studies of the system CO on Pt(111) with different experimental methods [5]. For low coverage, the molecules adsorb exclusively on energetically favored on top-sites of the platinum surface. With increasing coverage the work function of the CO/Pt(111) system first reaches a minimum at a coverage of $\Theta = 1/6$,

followed by a continuous rise for larger coverage. This behavior was explained by different dipole moments of CO at the two different adsorption sites [6].

For a 1/6 coverage the dipole moments of the molecules point along the CO axis [7, 8]. In this configuration THz-radiation is believed to excite a coherent wagging motion of CO molecules at about 1.8 THz [9]. The 50 simulated molecular trajectories represent atomic coordinates over a temporal range of about 25 ps in steps of 10 fs which were used as input in our single-scattering cluster code. The output of 50 files per time step, summed up incoherently, constitute the simulated experimental photoelectron diffraction pattern. For the simulations, emission out of the C 1s level was assumed using 1 keV x-ray pulses. The electrons undergo scattering at the oxygen atom located above. As a result, the angular distribution of the photoemission intensity exhibits a maximum for the angle of the C-O-bond for each single trajectory. However, since photoelectron diffraction integrates over a large spot and therefore over many molecules, the thermal motions of the molecules are averaging out for negative delays. The THz field aligns and amplifies the motion and induces a coherent combined hindered translation and rotation, well observable by photoelectron diffraction from the C 1s level [3], as shown in Fig. 14.2.

61

- [1] M. Greif *et al.*, *J. El. Spec. Rel. Phen.* **197**, 30 (2014).
- [2] M. Greif, Ph.D. Thesis, University of Zurich (2015).
- [3] M. Greif, T. Nagy *et al.*, submitted to *Struct. Dyn.* (2015).
- [4] I. Langmuir, *Trans. Faraday Soc.* **17**, 621 (1922).
- [5] Y. Y. Yeo, L. Vattuone, and D. A. King, *J. Chem. Phys.* **106**, 392 (1997).
- [6] G. Ertl, M. Neumann, and K. Streit, *Surf. Sci.* **64**, 393 (1977).
- [7] H. Ueba, *Surf. Sci.* **188**, 421 (1987).
- [8] P. Deshlahra, J. Conway, E. E. Wolf, and W. F. Schneider, *Langmuir* **28**, 8408 (2012).
- [9] B. Patterson *et al.*, *Europhys. News* **41**, 28 (2010).

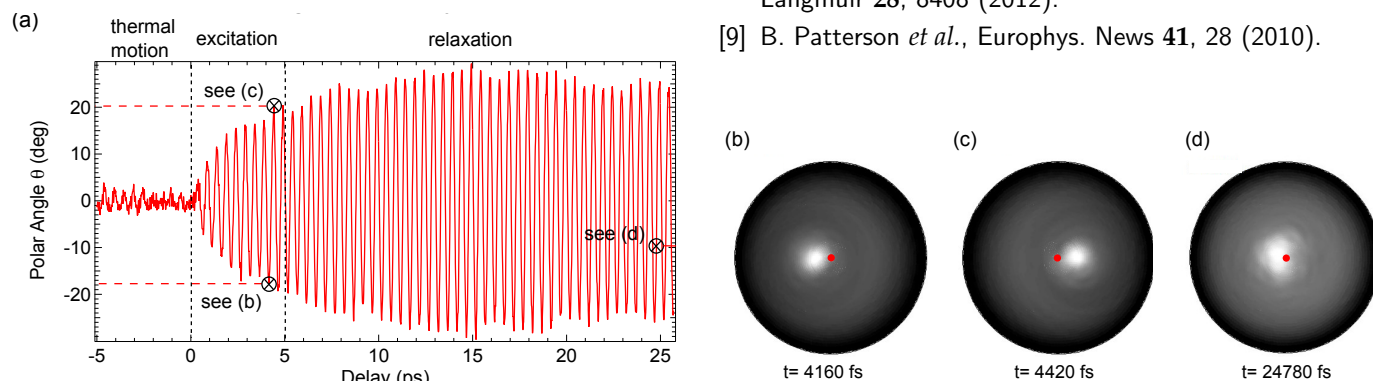


FIG. 14.2 – Results of molecular force field and electron single-scattering calculations, averaged over 50 independent molecular trajectories [3]. (a): angular position of the intensity maximum representing the orientation of the C-O-bond with respect to the surface normal. (b) - (d): diffraction patterns at the indicated delays after the THz excitation pulse. (b) and (c) highlight the orientation of the molecules at different extrema of the coherent oscillation.

14.3 Magnetic hysteresis and anisotropy of metallofullerene nanomagnets on a surface

in collaboration with: Alexey Popov, IFW Dresden; Cinthia Piamonteze, Jan Dreiser, and Bernard Delley Paul Scherrer Institut, Villigen.

The hollow interior of the fullerene [1] carbon cage can be used to encapsulate paramagnetic systems consisting of single atoms [2]. A fascinating example is the dysprosium-scandium based endofullerene-series $\text{Dy}_n\text{Sc}_{3-n}\text{N}@C_{80}$ ($n = 1, 2, 3$) where the different stoichiometries result in distinct ground-state properties like tunneling of magnetization ($n = 1$), remanence ($n = 2$), or frustration ($n = 3$) [3, 4]. Interaction with the ligand fields, mainly from the central N^{3-} ion, imposes an axial anisotropy that restricts the Dy moments to orient along the magnetic easy-axis directed parallel to the corresponding Dy-N bonds. Moreover, the ligand field splits the $2J+1$ degenerate ground state into states separated by an energy barrier that prevents a spontaneous reversal of the magnetization. In the case of the di-dysprosium compound (Fig. 14.3), exchange and dipolar coupling between the two magnetic moments stabilizes hysteresis and a large remanence with a relaxation time of one hour at 2 K are found [4]. These endofullerenes belong to the group of single-molecule magnets [5, 6], a class of molecules that exhibits an intrinsic magnetic bistability at low temperatures. They are particularly promising for molecular spintronics applications [7] and quantum computing [8]. Applications will require that the molecules are transferred from the bulk phase and deposited onto substrates or integrated into different device architectures. Therefore, it is of interest to know how the molecular magnetic properties are modified at low coverages on surfaces.

In order to investigate how the proximity of a metal surface influences the ordering of the magnetic cluster and the magnetic bistability, we have studied molecular films of $\text{Dy}_2\text{ScN}@C_{80}$ on a rodium metal surface [9].

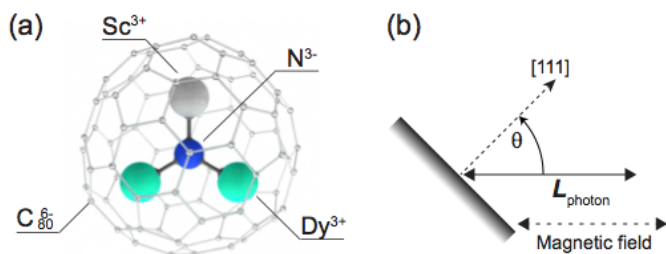


FIG. 14.3 –

(a) Ball-and-stick model of $\text{Dy}_2\text{ScN}@C_{80}$.

(b) Measurement geometry with the angular momentum of the x-rays L_{ph} , parallel or antiparallel to the magnetic field and at an angle of θ with respect to the normal of the sample surface.

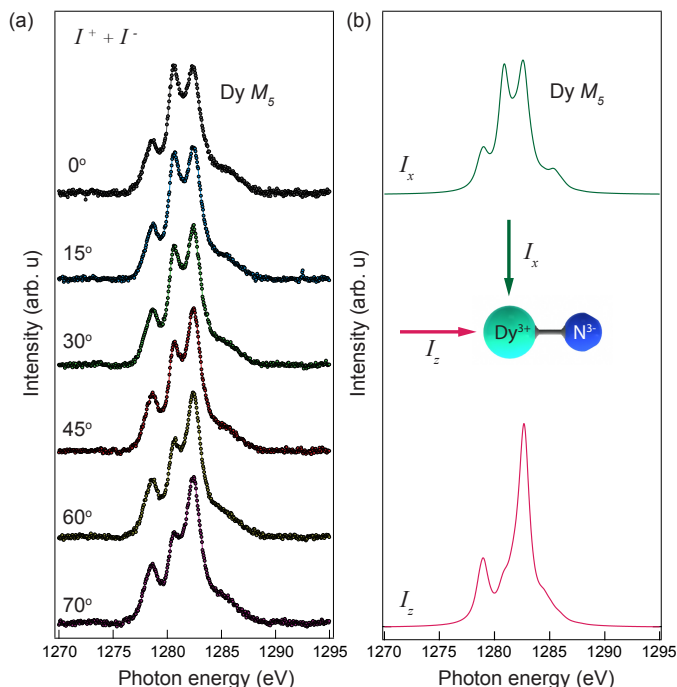


FIG. 14.4 –

(a) XAS measured at the Dy M_5 -edge from a sub-ML of $\text{Dy}_2\text{ScN}@C_{80}/\text{Rh}(111)$ $T = 4$ K, $\mu_0 H = 6.5$ T, measurement geometry in Fig. 14.3 (b). Each data set is normalized to the integrated intensity.

(b) Calculated absorption with the x-ray beam and external field oriented parallel I_z , and perpendicular I_x , to the magnetic easy-axis (Dy-N bond).

For a sub-monolayer coverage is a significant change in the Dy XAS spectra observed as the angle between the surface normal and the x-ray beam is varied (Fig. 14.4 (a)). This effect is a consequence of an anisotropic charge distribution of the 4f orbitals due to a preferential orientation of the Dy_2ScN cluster. A comparison with multiplet calculations reveals that the cluster adopts an orientation parallel to the surface (Fig. 14.4 (b)). Combined with the local magnetic easy axis for the encapsulated Dy ions, the structural orientation of the cluster in the sub-monolayer results in surface aligned magnetic moments and a macroscopic anisotropy [9].

The magnetism of the system was studied by x-ray magnetic circular dichroism (XMCD), a spectroscopy technique that probes the magnetic moments of the individual Dy ions [3]. By measuring the XMCD signal while sweeping the magnetic field, element specific magnetization curves can be recorded. Figure 14.5 displays magnetization curves recorded from a sub-monolayer and a multilayer at 4 K. Hysteresis is observed for both systems, demonstrating that the corresponding magnetic relax-

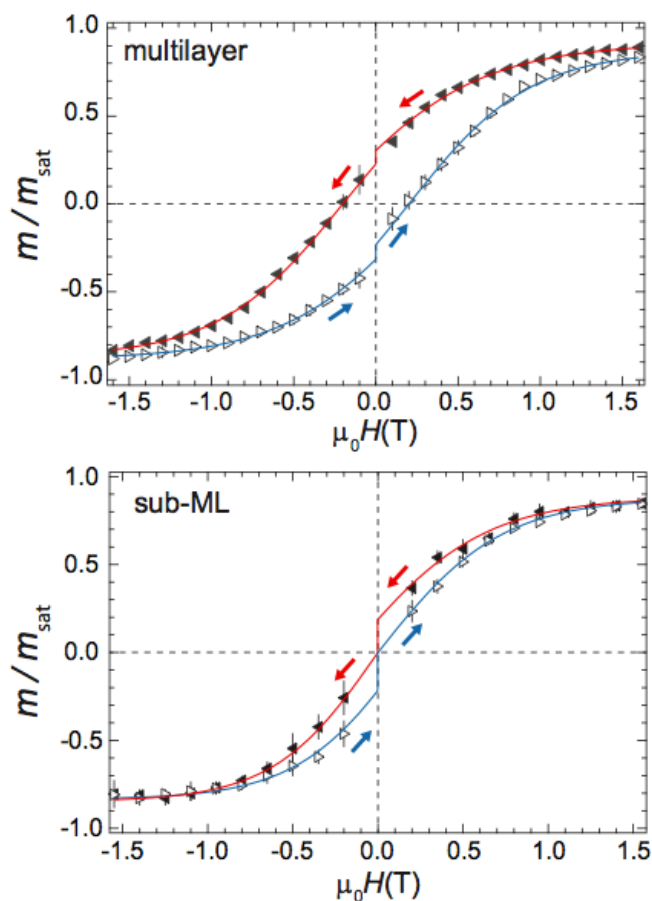


FIG. 14.5 – Hysteresis curves measured from a multilayer and a sub-ML of $\text{Dy}_2\text{ScN}/\text{C}_{80}/\text{Rh}(111)$ at a magnetic field sweep rate of 2 T/min and a sample temperature of ~ 4 K. The data were recorded with the x-ray beam and the magnetic field at an incidence angle of $\theta = 60^\circ$. The magnetization curves correspond to the average of several independent measurements, where the error bars are the standard deviations at each external magnetic field setting. The arrows indicate the ramping direction of the magnetic field, the lines are guides to the eye, and m_{sat} is the saturated magnetisation at ≈ 6.5 T. The drop in magnetization at zero field results from the ≈ 30 s it takes to switch the polarity of the magnet.

ation times are slow compared to the measurement time. However, comparing the magnetization curves from the two systems indicates that the magnetic bi-stability of $\text{Dy}_2\text{ScN}/\text{C}_{80}$ is modified by the proximity of the rhodium metal surface. The comparison to the thicker film (representative of the bulk phase), allows to estimate that the proximity of the metal surface results in four times higher relaxation rates and in a resulting remanence time of about 30 s [9].

In summary, angle dependent XAS from a sub-ML of $\text{Dy}_2\text{ScN}/\text{C}_{80}$ on $\text{Rh}(111)$ reveal a one-to-one correspondence between structural and magnetic ordering: The combined effect of the local magnetic easy-axis for the encapsulated Dy ions, and the preferred absorption geometry of the endohedral cluster, indicates a bistable surface aligned macrospin.

- [1] H. Kroto *et al.*, *Nature*, **318**, 162 (1985).
- [2] A. Popov *et al.*, *Chem. Rev.* **113**, 5989 (2013).
- [3] R. Westerström *et al.*, *J. Am. Chem. Soc.* **134**, 9840 (2012).
- [4] R. Westerström *et al.*, *Phys. Rev. B.* **89**, 060406(R) (2014).
- [5] R. Sessoli, *et al.*, *Nature* **365**, 141 (1993).
- [6] D. Gatteschi *et al.*, *Molecular Nanomagnets*, Oxford University Press, New York, (2006).
- [7] L. Bogani *et al.*, *Nat Mater* **7**, 179 (2008).
- [8] M. N. Leuenberger *et al.*, *Nature* **410**, 789 (2001).
- [9] R. Westerström *et al.*, *Phys. Rev. Lett* **144**, 087201 (2015).

15 Physics of Biological Systems

Conrad Escher, Hans-Werner Fink, Tatiana Latychevskaia, Jean-Nicolas Longchamp, Marianna Lorenzo, Jonas Verges, Flavio Wicki

in collaboration with: Eugen Ermantraut, Clondiag Chip Technologies GmbH (Germany); Prof. Jannik C. Meyer, University of Vienna (Austria); Prof. Ute Kaiser, University of Ulm (Germany); Prof. Klaus Kern, Max Planck Institut, Stuttgart (Germany); Dr. Yuriy Chushkin and Dr. Federico Zontone, The European Synchrotron Radiation Facility, Grenoble (France); Dr. Annette Niehl and Dr. Manfred Heinlein, CNRS Strasbourg (France), Prof. Christian Schönenberger, University of Basel (Switzerland).

Our primary goal is the structural investigation of individual biological objects, which involves both in-line holography with low energy electrons and coherent diffraction imaging, assisted by micro-structuring techniques using a focused gallium ion beam device for miniaturized electron optics and sample preparation.

Our current activities can be grouped in the following interconnected projects:

- Electron Holography and Coherent Diffraction

Major experimental challenges are the improvement of the spatial resolution, the creation of free standing films of graphene transparent for low-energy electrons and the presentation of a single protein molecule to a coherent electron wave front. Another, equally important aspect for achieving high resolution structural information is the optimal hologram reconstruction, developing numerical algorithms to solve the integrals governing these coherent optics problems.

- Coherent Diffraction Imaging of Graphene-Supported Single Biomolecules at Atomic Resolution

This is an independent effort (Ambizione project) of Jean-Nicolas Longchamp. Methods to deposit biomolecules onto freestanding graphene, in particular in-situ electrospray deposition, have been explored. The successful imaging of biomolecules was cross-validated by TEM investigations at the microscopy center of our University. First detailed studies of a single virus are described in some detail below.

- Electron and Ion Point Sources

Field Ion Microscopy and related techniques are employed for fabricating and using bright electron and ion point sources. A novel bright proton source has recently been developed and used for Proton Projection Microscopy which complements imaging with coherent electrons within the very same system.

- Resolution enhancement in X-ray coherent diffraction imaging by extrapolation of diffraction patterns

In collaboration with a group at the European Synchrotron Radiation Facility in Grenoble, we have enhanced the resolution of a non-crystalline object obtained from an X-ray diffraction pattern by extrapolation beyond the detector area. The primary record is missing about 10% information, including the pixels in the center of the diffraction pattern. The extrapolation is based on an iterative routine. A joint publication is currently under review.

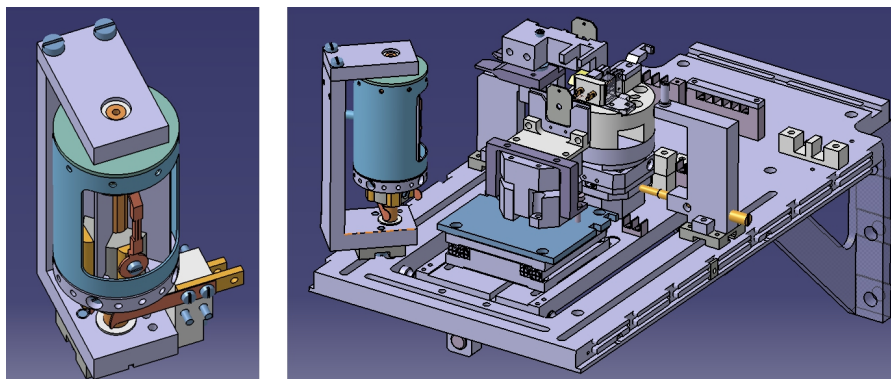
15.1 Instrumentation

A new Low Energy Electron Point Source (LEEPS) microscope has been designed (Fig. 15.1) and built (Fig. 15.2) by our machine shop. The ultra-high vacuum compatible instrument is expected to be in operation by summer 2015.

We have been combining LEEPS microscopy with the functionality of STM for the study of freestanding atomically thin films and objects deposited onto them. These techniques require similar hardware instrumentation but

64

FIG. 15.1 – Overall design of a new LEEPS microscope for exploring in situ adsorption of alkali atoms onto freestanding graphene. Up to four alkali metals can be evaporated. The rotatable evaporator is shown in more detail on the left.



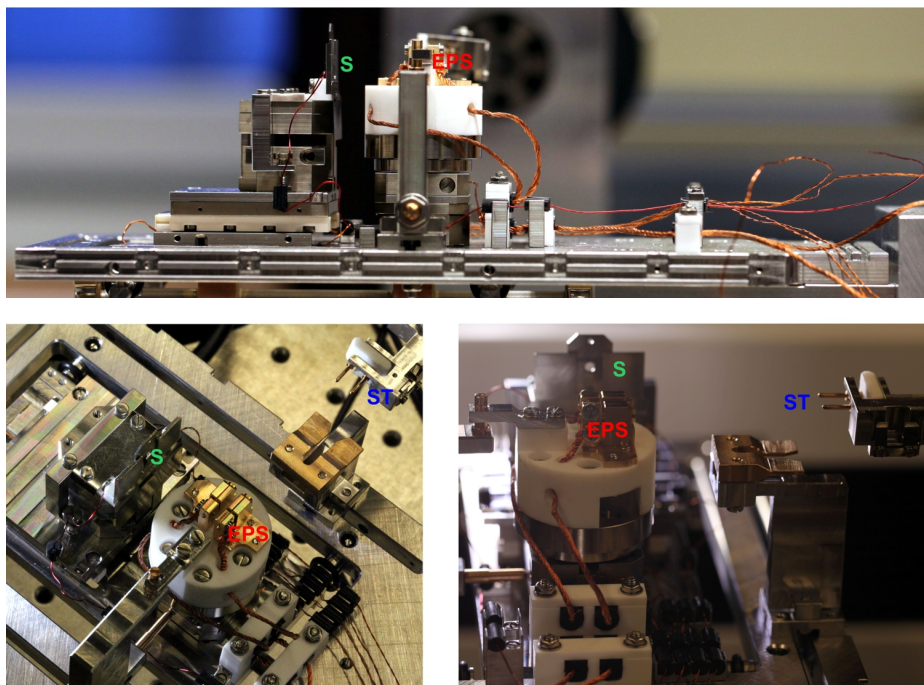


FIG. 15.2 – Status of the new LEEPS system as of March 2015.

EPS: electron point source;
S: sample and
ST: transfer mechanism which allows to move samples and tips (electron point sources) without braking the ultra-high vacuum.

offer different, complementary imaging properties. The most crucial modification to our previous system is the implementation of STM electronics and a software package dedicated to STM signal and data processing.

For our recent review of the subject, see: *Holography and coherent diffraction with low-energy electrons: A route towards structural biology at the single molecule level*, www.sciencedirect.com/science/article/pii/S030439911400240X.

15.2 Imaging tobacco mosaic virus by low-energy electron holography

Jean-Nicolas Longchamp, Tatiana Latychevskaia, Conrad Escher and Hans-Werner Fink

Structural information about biomolecules at nanometer, sub-nanometer or atomic resolution is nowadays predominantly obtained by X-ray crystallography and NMR spectroscopy, whereby samples in the form of crystals or in liquids are studied. This, however, entails important structural information being averaged over many molecules. Thus, relevant details in molecules exhibiting diverse structural conformations remain undiscovered. Besides this drawback, these methods can only be applied to a limited subset of biological molecules that either readily crystallize for use in X-ray studies or are small enough for NMR investigations. A third approach towards imaging single particles is cryo-electron microscopy; however, for biological samples the possible resolution is limited by radiation damage caused by the high electron energy employed in conventional transmission electron microscopes (TEM) [1]. Due to the strong

inelastic scattering of high-energy electrons, there is little hope for obtaining structural information at atomic resolution for a single entity. As the permissible dose is limited to $10 \text{ e}^-/\text{\AA}^2$ only, an individual molecule is destroyed long before an image of high enough quality could be acquired [2, 3]. The radiation damage problem is usually circumvented by averaging over several thousand noisy images in order to attain a satisfactory signal-to-noise ratio [4]. The alignment and averaging routines inherent to high-resolution cryo-electron microscopy limit its application range to symmetric and particularly rigid objects, such as specific classes of viruses.

Despite the shortcomings of the three conventional structural biology tools discussed above, one needs to express respect for the vast amount of data that has been generated over the past decades, reflected by the impressive volume of the current protein database [5]. Nevertheless, a milestone for structural biology would definitely be attained if methods and tools were available, that do away with averaging over an ensemble of molecules and enable structural biology on a truly single molecule level. To obtain atomic resolution information about the structure of any individual biological molecule, different concepts and technologies are needed. One approach of this kind is associated with the recent X-ray free electron laser (XFEL) projects. This approach initially appeared to be a promising method for gaining information from just one single biomolecule at the atomic scale by recording its X-ray diffraction pattern within the short time of just 10 fs, before the molecule is decomposed by radiation damage. Unfortunately, there are now strong indications [6] that again averaging over a large number of molecules is in-

evitable in order to obtain images with a sufficiently high signal-to-noise ratio enabling numerical reconstruction of the diffraction pattern with atomic resolution [7–9].

The approach to structural biology at the single molecule level described here, is motivated by the experimental evidence that electrons with a kinetic energy in the range of 50–250 eV are harmless to biomolecules [10–12]. Even after exposing fragile molecules like DNA or proteins to a total electron dose of 10^6 e-/Å², i.e. more than five orders of magnitude higher than the critical dose in TEM, no radiation damage could be observed. This, combined with the fact that the de Broglie wavelengths associated with this energy range are between 0.7 and 1.7 Å, makes low-energy electron microscopy an auspicious candidate for structural biology at the single molecule level.

During the last three decades, DNA, phages, viruses and individual ferritin proteins attached to carbon nanotubes were imaged by means of low-energy electron holography with nanometer resolution [10, 11, 13–15]. For imaging, the objects of interest used to be placed across bores in a membrane. Unfortunately, after such preparation the holographic record often suffered from biprism distortion limiting the resolution in the reconstruction [16]. This artifact is suppressed if the specimen is placed on an electrically conductive substrate with sufficient transparency for low-energy electrons [17, 18]. Yet, the substrate has to be robust enough to withstand the deposition procedure [19]. It turned out that freestanding graphene, an atomically thin layer of carbon atoms arranged in a honeycomb lattice, fulfills all these requirements. Electron transmission measurements have shown that more than 70% of the low-energy electrons are transmitted through graphene and therefore are available for imaging objects deposited on the two dimensional substrate [17].

The discovery of the tobacco mosaic virus (TMV) at the end of the 19th century marked the beginning of what is now called virology [20–22]. Starting from 1936, TMV was the object of several X-ray diffraction investigations. In that year, Bawden *et al.* could retrieve a repeating pattern with a periodicity of 2.2 nm, a measure nowadays associated with the pitch of the helical TMV structure [23].

Only three years later, Kausche, Pfankuch and Ruska were able to image TMV in an early version of a TEM [24]. In this pioneer work they disclosed the rod-like shape of the virus with dimensions of 300 nm in length and 15 nm in width. These findings are still in good agreement with the current values of 300 nm and 18 nm, respectively. Based on the data available at the time, Watson and Franklin proposed the helical TMV structure in 1954 and 1955, respectively [23]. The first molecular model at atomic resolution was obtained from X-ray fiber diffraction experiments by Namba *et al.* in 1986 [25, 26].

Retrieving information about unstained TMV at the sub-nanometer scale is possible by means of cryo-electron microscopy since the 1980's [27, 28]. The most recent models that can be found in the protein database are either obtained from X-ray fiber diffraction data (2.9 Å resolution) or transmission electron microscopy investigations (5 Å resolution) [5]. In both cases, the Angstrom resolution could only be obtained by averaging over a vast number of entities.

We shall show below that by means of low-energy electron holography, it is possible to image individual TMVs deposited on ultra-clean freestanding graphene. The viruses are imaged with one nanometer resolution exhibiting details of the helical TMV structure.

15.2.1 Materials and Methods

In our low-energy electron holographic setup, inspired by Gabor's original idea of in-line holography [29–31], a sharp (111)-oriented tungsten tip acts as source for a divergent beam of highly coherent electrons [31–34]. The electron emitter can be brought as close as 100 nm to the sample with the help of a 3-axis nano-positioner. The part of the electron wave elastically scattered off the object is called the object wave, while the un-scattered part represents the reference wave. At a distant detector, the resulting interference pattern, the hologram, is recorded. The magnification of the imaging system, given by the ratio between detector-to-source and sample-to-source distances, can be up to hundred.

A hologram, in contrast to a diffraction pattern, contains the phase information of the object wave, and the

66

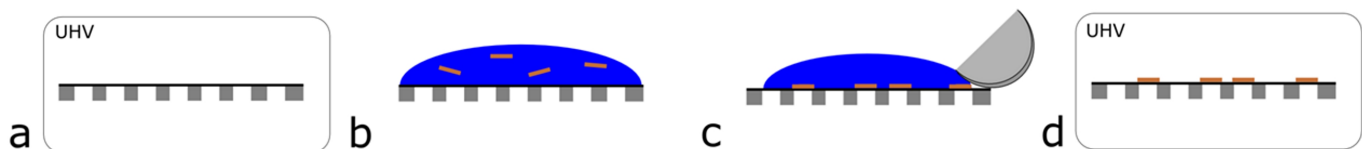


FIG. 15.3 – Virus deposition on ultra-clean freestanding graphene. (a) The cleanliness of the graphene sample carrier is first inspected by means of low-energy electron holography under UHV conditions; (b) A 0.5 ng/ μ l drop of TMV solution is applied onto the substrate; (c) After waiting a few seconds for the sedimentation of the viruses, the excess water is removed with blotting paper and (d) The sample is heated to 125°C for 45 min.

The viruses are now ready to be imaged by means of low-energy electron holography.

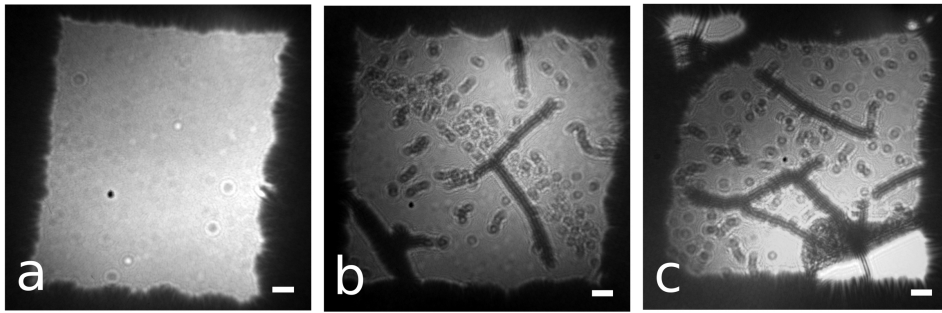


FIG. 15.4 – (a) Low-energy electron hologram of freestanding graphene covering a square aperture milled in a Pd-coated SiN membrane. The graphene layer appears ultra-clean. (b) and (c): Holograms of after TMV deposition. Scale bars correspond to 50 nm.

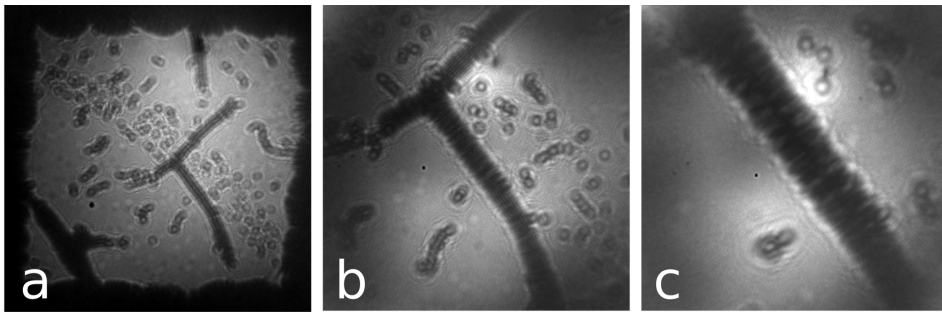


FIG. 15.5 – Low-energy electron holograms with increasing magnification and decreasing source-to-sample distance. The electron energy amounts to 131 eV in (a), 103 eV in (b) and 89 eV in (c) and the source-to-sample distances to 1500 nm, 450 nm and 180 nm, respectively.

object structure can thus be reconstructed unambiguously. The reconstruction is achieved by back propagation of the hologram, which corresponds to a Fresnel-Kirchhoff integral transformation [35–39]. The resolution is limited by the de Broglie wavelength (λ) and the numerical aperture of the detector (NA). With $\lambda = 0.7 \text{ \AA}$ and $NA = 0.54$, atomic resolution shall be possible.

Ultra-clean freestanding graphene, covering ion milled square-like apertures of approximately 500 nm side length, is prepared by the platinum-metal catalysis method [40]. Thereafter, the cleanliness of the graphene is inspected in our low-energy electron holography microscope operating under UHV conditions. Viruses were prepared following the recipe by Niehl *et al.* [41]. They were extracted from ORMV-infected nicotiana benthamiana leaves, purified by precipitation and sedimentation and re-suspended in 10 mM sodium-phosphate buffer. For TMV deposition (see Fig. 15.3), graphene samples

prepared as described above are taken out of the low-energy electron microscope.

15.2.2 Results and Discussion

Figure 15.4 displays low-energy electron holograms recorded at kinetic energies of 131 eV and 125 eV. In these images, the rod-like viruses are apparent besides traces of dirt resulting from the sample preparation procedure.

In contrast to TEM, in low-energy electron holography no lenses are employed and the magnification power of the instrument can be chosen simply by changing the distance between electron source and sample. If the field emission current is maintained constant, the reduction of the source-to-sample distance implies also a decrease of the electron energy (see Fig. 15.5). With increasing magnification, the interference fringes become more and more pronounced.

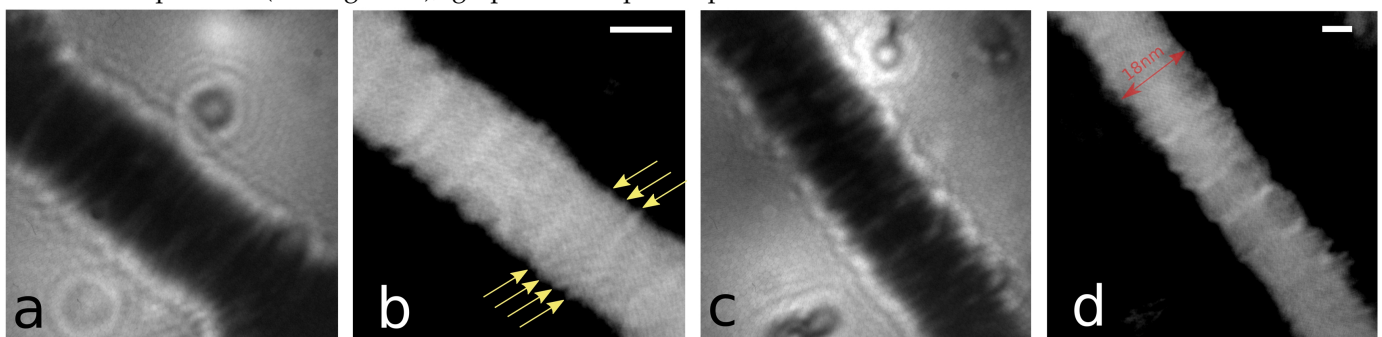


FIG. 15.6 – High-magnification holograms of TMV and the respective reconstructions. (a) and (c) Holograms of TMV recorded with 80 eV, respectively 89 eV electron energy. (b) and (d) reconstructed TMV images from (a) and (c) (inverted grayscale). Arrows emphasize the presence of apex-like features on the rim of the TMV. These details are attributed to the helical structure of the virus. The scale bare corresponds to 10 nm.

FIG. 15.7 – Confronting an atomic TMV model with the measurements.

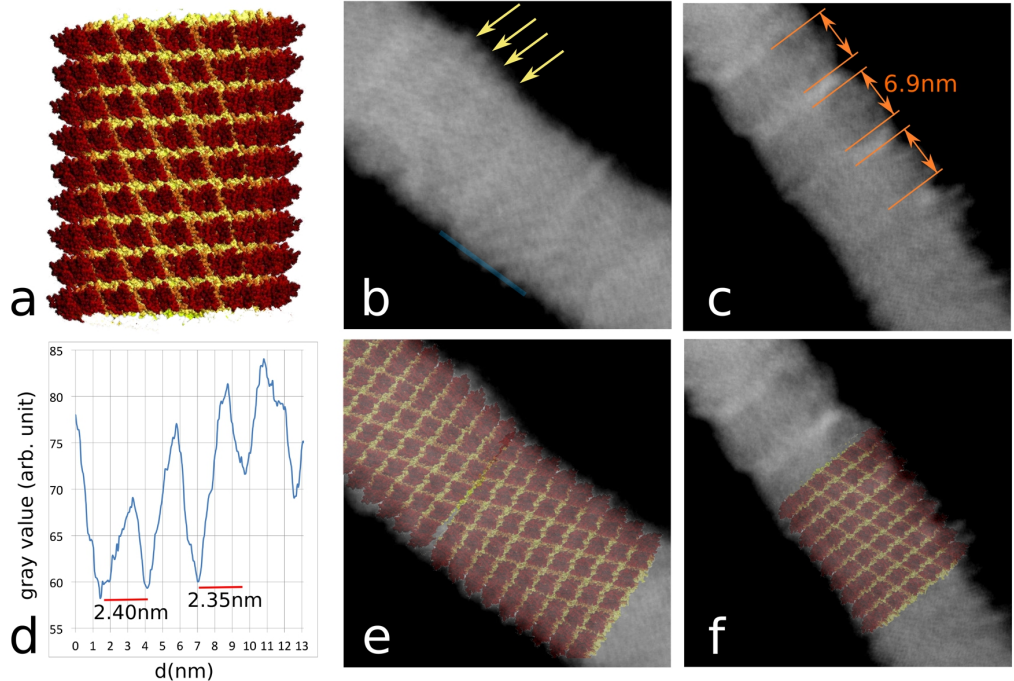
(a) Atomic TMV model constructed from the available coordinates [42].

(b)-(c) Close-ups of the images in Fig. 15.6.

(d) Intensity scan along the blue line in (b).

(e)-(f) Images as in (b)-(c) with the atomic TMV model superimposed.

In (b) arrows mark further apex-like features coinciding with the atomic model. In (c) the distance between bright stripes is marked according to the literature value of 6.9 nm for the thickness of a subunit.



In Figs. 15.6a and 15.6c, two high magnification holograms are displayed. From these holograms the shape of the corresponding viruses is reconstructed at one nanometer resolution (see Figs. 15.6b and 15.6d). The diameter of the virus corresponds to 18 nm as expected. Furthermore, one can observe, as emphasized by arrows in Fig. 15.6b, apex-like features on the rim of the virus, which we attribute to the helical TMV structure.

Given an electron de-Broglie wavelength around 1.4 Å and since in low-energy electron holography the resolution is neither limited by lens aberrations nor by radiation damage, Angstrom resolution may be expected. The nanometer resolution that we report here is attributed to residual mechanical vibrations. In a low-energy electron hologram the spacing between consecutive interference fringes gradually decreases towards higher orders. Hence, high-order interference fringes and thus finest structural details are most susceptible to such vibrations.

Even if the current resolution is of the order of one nanometer, one can already compare the images obtained with low-energy electrons with an atomic TMV model constructed by Jean-Yves Sgro [42] with the atomic coordinates available from the protein database (Fig. 15.7a). Figures 15.7b and 15.7c are close-ups of the TMV images displayed in Fig. 15.6. Once the atomic TMV model is superimposed to match the width of the viruses (see Figs. 15.7e and 15.7f), the apex-like features that we previously attributed to the helical structure of the virus are now coinciding with the peaks of the helical structure in the model.

The agreement between model and experimental data

obtained from a single particle is remarkable. To take into account the kink in the TMV shown in Fig. 15.7e, two copies of the model, rotated by 6° with respect to each other, are superimposed on the low-energy electron images. By this, further details, marked by arrows in Fig. 15.7b, which correspond to the helical structure of the virus are now congruent with the atomic model. In Fig. 15.7d, an intensity plot along the blue line present in Fig. 15.6b is displayed. The distance between depletions in this graph corresponds to approximately 2.35-2.40 nm, a length that almost perfectly fits the expected 2.30 nm helical pitch from X-ray fiber diffraction investigations [5, 43, 44]. Moreover, in Fig. 15.7b-c equidistant bright stripes across the virus are visible. The distance between these features amounts to approximately 7 nm, which most likely corresponds to the literature value of 6.9 nm associated with the thickness of a TMV subunit [44, 45]. Such stripes have been observed in TEM investigations of uranyl acetate stained in-vitro assembled viruses [46, 47] but, to our knowledge, never on in-vivo purified TMV.

With this, we have demonstrated the potential of low-energy electron holography for structural biology at the single particle level. The mapping of any internal structure of the virus is precluded due to the thickness of TMV. However, this limitation is only relevant for objects thicker than 5 nm, i.e. thicker than the majority of proteins for instance.

The current nm resolution will soon be pushed to Å resolution by improving the mechanical stability. Furthermore, we have recently reported that by employing a slightly modified experimental setup, where a parallel

beam of low-energy electrons is illuminating the sample, we could image a region of 210 nm in diameter of free-standing graphene with 2 Å resolution [48]. This scheme will be used to image TMV with a similar resolution.

The sample preparation method used here is certainly only applicable for a very small subset of biological entities that withstand the heat treatment. However, we have recently shown that it is possible to electrospray deposit *in vacuo* gold nanorods of 20 MDa molecular weight onto freestanding graphene without damaging the atomically thin substrate [12]. This demonstrates that the deposition of proteins onto graphene is within reach and consequently structural biology at the single particle level by means of coherent low-energy electron microscopy should soon emerge.

15.2.3 Acknowledgements

We would like to thank Annette Niehl and Manfred Heinlein from the CNRS Strasbourg for the TMV purification and helpful discussions. We also thank Kishan Todkar and Christian Schönenberger from the University of Basel for providing us with their CVD grown graphene.

- [1] R. Henderson, *Rev. Biophys.* 28(2) (1995) 171.
- [2] R.F. Egerton, P. Li, M. Malac, *Micron* 35(6) (2004) 399.
- [3] E. Knapek, J. Dubochet, *J. Mol. Biol.* 141(2) (1980) 147.
- [4] M. van Heel, *et al.*, *Q. Rev. Biophys.* 33(4) (2000) 307.
- [5] Protein Data Bank, www.pdb.org.
- [6] J.W. Miao, *et al.*, *Annu. Rev. Biophys. Biomol. Struct.* 33 (2004) 157.
- [7] R. Neutze, *et al.*, *Nature* 406(6797) (2000) 752.
- [8] V.L. Shneerson, *et al.*, *Acta Crystallogr. Sect. A* 64 (2008) 303.
- [9] H.N. Chapman, *et al.*, *Nature* 470(7332) (2011) 73.
- [10] M. Germann, T. Latychevskaia, C. Escher, H.-W. Fink, *Phys. Rev. Lett.* 104(9) (2010) 95501.
- [11] J.-N. Longchamp, T. Latychevskaia, C. Escher, H.-W. Fink, *Appl. Phys. Lett.* 101(9) (2012) 93701.
- [12] T. Latychevskaia, Longchamp J-N, C. Escher, H.-W. Fink (2014) *Ultramicroscopy*.
- [13] H.-W. Fink, H. Schmid, E. Ermantraut, T. Schulz, *J. Opt. Soc. Am. A - Opt. Image. Sci. Vis.* 14(9) (1997) 2168.
- [14] G.B. Stevens, *et al.*, *Eur. Biophys. J.* 40 (2011) 1197.
- [15] P. Simon, *et al.*, *Micron* 39(3) (2008) 229.
- [16] T. Latychevskaia, J.-N. Longchamp, C. Escher, H.-W. Fink, *Ultramicroscopy* 145 (2014) 22.
- [17] J.-N. Longchamp, T. Latychevskaia, C. Escher, H.-W. Fink, *Appl. Phys. Lett.* 101(11) (2012) 113117.
- [18] J.-N. Longchamp, C. Escher, T. Latychevskaia, H.-W. Fink, *Ultramicroscopy* (2014).
- [19] R.R. Nair, *et al.*, *Appl. Phys. Lett.* 97(15) (2010) 153102.
- [20] D. Ivanowski, *St Petersburg. Acad. Imp. Sci. Bul.* (1892).
- [21] M.W. Beijerinck, *Over een Contagium vivum fluidum als oorzaak van de vlekziekte der tabaksbladeren*, Koninkl. Akademie van Wetenschappen (1898) 229.
- [22] E.F. Smith, *J. Mycol.* 7(4) (1894) 382.
- [23] J.D. Watson, *Biochim. Biophys. Acta* 13 (1954) 10.
- [24] G.A. Kausche, *et al.*, *Naturwissenschaften* 27 (1939) 292.
- [25] K. Namba, G. Stubbs, *Science* 231(4744) (1986) 1401.
- [26] K. Namba, *et al.*, *J. Mol. Biol.* 208(2) (1989) 307.
- [27] T.-W. Jeng, *et al.*, *J. Mol. Biol.* 205(1) (1989) 251.
- [28] C. Sachse, *et al.*, *J. Mol. Biol.* 371(3) (2007) 812.
- [29] D. Gabor, *Nature* 161(4098) (1948) 777.
- [30] D. Gabor, *Holography*, Nobel Lect. (1971).
- [31] H.-W. Fink, W. Stocker, H. Schmid, *Phys. Rev. Lett.* 65(10) (1990) 1204.
- [32] H.-W. Fink, *Ultramicroscopy* 50(1) (1993) 101.
- [33] H.-W. Fink, *IBM J. Res. Dev.* 30(5) (1986) 460.
- [34] H.-W. Fink, W. Stocker, H. Schmid, *J. Vac. Sci. Technol. B* 8(6) (1990) 1323.
- [35] H.J. Kreuzer, *et al.*, *Ultramicroscopy* 45(3-4) (1992) 381.
- [36] H.J. Kreuzer, *Micron* 26(6) (1995) 503.
- [37] T. Latychevskaia, H.-W. Fink, *Phys. Rev. Lett.* 98(23) (2007) 233901.
- [38] T. Latychevskaia, H.-W. Fink, *Opt. Express* 17(13) (2009) 10697.
- [39] T. Latychevskaia, J.-N. Longchamp, H.-W. Fink, *Opt. Express* 20(27) (2012) 28871.
- [40] J.-N. Longchamp, C. Escher, H.-W. Fink, *J. Vac. Sci. Technol. B Microelectron Nanom. Struct.* 31(2) (2013) 020605.
- [41] A. Niehl, *et al.*, *Plant Physiol.* 160(4) (2012) 2093.
- [42] C.M. Fauquet, *et al.*, eds. (2005) *Virus Taxonomy: VIIIth Report of the International Committee on Taxonomy of Viruses* (Academic Press London and New York).
- [43] F. Bawden, *et al.*, *Nature* 138 (1936) 1051.
- [44] R.E. Franklin, *Biochim. Biophys. Acta* 19 (1956) 203.
- [45] A. Kendall, *et al.*, *Virology* 369(1) 226.
- [46] A.C.H. Durham, *et al.*, *Nature* 229(2) (1971) (2007) 37.
- [47] P.J. Butler, *Philos. Trans. R. Soc. Lond. B, Biol. Sci.* 354(1383) (1999) 537.
- [48] J.-N. Longchamp, T. Latychevskaia, C. Escher, H.-W. Fink, *Phys. Rev. Lett.* 110(25) (2013) 255501.

16 Disordered and Biological Soft Matter

M. Ackermann, C.M. Aegerter, D. Assmann (till January 2015), F. Atzeni (since September 2014), D. Dreher (since July 2014), D. Eder, G. Ghielmetti (till June 2014), A. Keller (since November 2014), F. Lanfranconi, A. Mallavalli (since June 2014), A. Pataki (Master student), S. Puri, L. Schertel (Master student), J. Schneider (since December 2014), L. Selvaggi (since August 2014) and S. Urdy (since July 2014)

in collaboration with: Institute of Molecular Life Sciences (K. Basler, T. Aegerter-Wilmsen, S. Luschnig, L. Pelkmans, D. Brunner), ETH Zürich (P. Koumoutsakos), MPI für Pflanzenforschung Köln (R.S. Smith), University of Fribourg (A. Jazwinska), University of Bern (C. Kulemeier, S. Robinson, P. Barbier de Reuille), Biozentrum Basel (M. Affolter), University of Strasbourg (N. Rivier), University of Konstanz (G. Aubry, G. Maret, T. Sperling), MPI für Selbstorganisation Göttingen (C.C. Maass), Deutsches Luft- und Raumfahrtzentrum (M. Sperl), University of Twente (A. Mosk), Université Joseph Fourier Grenoble (S. Skipetrov), Université Paris Denis Diderot (F. Graner), Technion Haifa (E. Akkermans).

The group of Disordered and Biological Soft Matter works at the interface of condensed matter physics and developmental biology. The systems of interest are out-of-equilibrium and also address transport in disordered systems. In particular, we are studying the effects of elastic properties and mechanical forces on biological development, including growth and the formation of structures, such as folds in tissues. In disordered media, we are particularly interested in light transport in turbid, multiple scattering samples. We address both fundamental questions, such as the transition to Anderson localization in three dimensions, and applications in imaging techniques relevant for studies of developmental processes in turbid tissues. Finally, we are studying physical models for disordered out-of-equilibrium structures, such as foams. In particular, we are studying foams under diamagnetic levitation, such that distortions due to gravity, which usually mask several interesting non-equilibrium processes, can be eliminated.

Last year, we made considerable progress in several of these areas. Below we focus on Anderson localization, visco-elastic properties of biological tissues and the dynamics of aging, levitated foams.

16.1 Anderson localization of light

Our recent observation of localization of light in highly turbid media [1–3] shows a transition with turbidity as expected from Anderson localization [4, 5]. These results were achieved in TiO_2 samples, which also exhibit a non-linear optical response [6, 7]. The phenomenon is observed in time-resolved experiments through an enhancement at long times when increasing the incoming intensity, see Fig. 16.1. In addition to this intensity dependent increase, there is however

also a strongly turbidity dependent increase, combined with a saturation of the width of the photon distribution at long time and therefore localization of

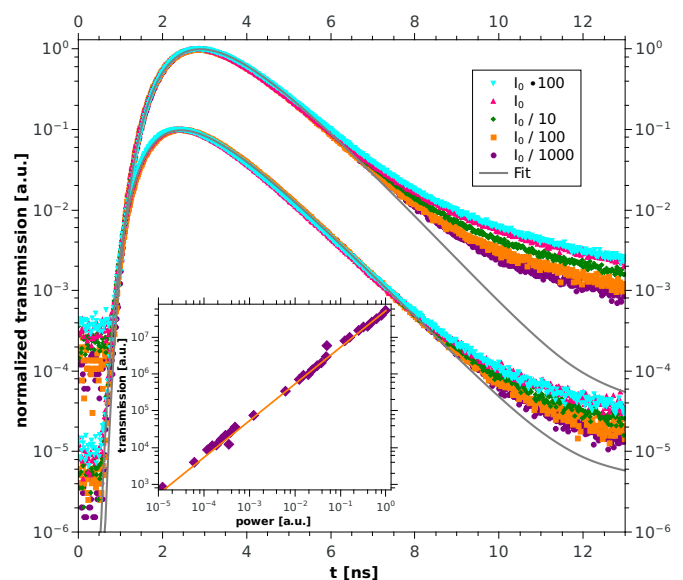


FIG. 16.1 – Characterization of the non-linear response of multiple scattering TiO_2 samples, as given by the power dependence of the time dependent and integrated (inset) optical transmission. The inset shows the transmitted power as a function of input power for a sample with $k \cdot l^* = 2.7$. The time dependent transmission of this sample is shown in the top set of curves for different incident intensities, with $I_0 \simeq 1 \text{ GW/m}^2$. The bottom set of curves shows a different sample with $k \cdot l^* = 5.7$. This shows that non-linear effects are important only at long times and are not discernible in the integrated transmission. The continuous lines are fits to the analytic solution to the diffusion equation for a slab. As can be seen, at high turbidity, the deviations from diffusive behavior at long times are much enhanced.

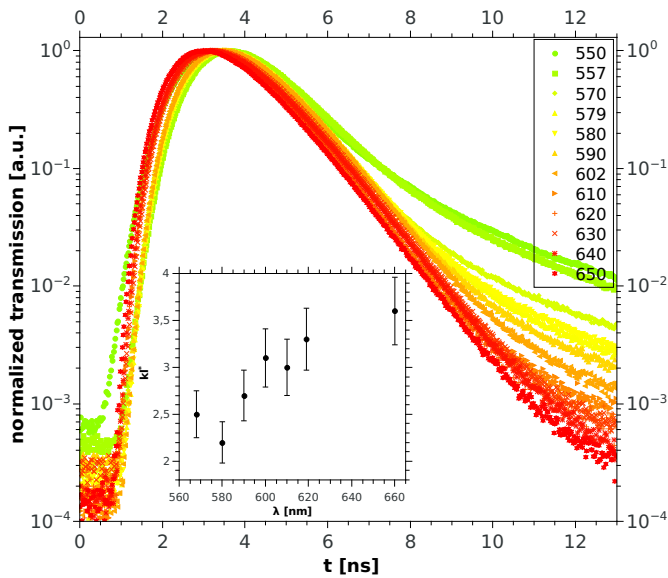


FIG. 16.2 – Wavelength dependence of the time dependent transmission. As the incoming wavelength is increased, the value of $k \cdot l^*$ increases as well (see inset). This means that a scan in wavelength allows for a study of the turbidity dependence of the time dependent transmission. As can be seen by the curves in the main figure, the deviations at long times increase strongly with decreasing $k \cdot l^*$, as expected from a transition to Anderson localization.

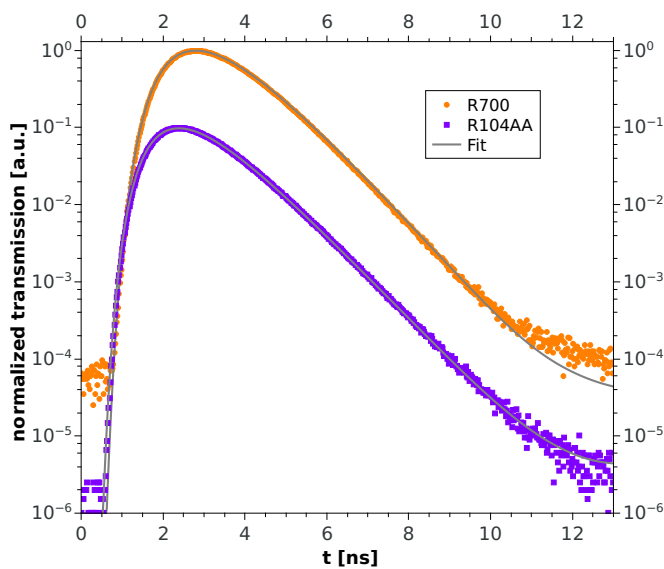


FIG. 16.3 – Time of flight measurement of a sample with $k \cdot l^* = 2.7$ (orange) and $k \cdot l^* = 5.7$ (purple). In order to check for the influence of wave-length shifts in the outgoing signal, a band pass filter centered around the incoming wavelength (590 nm) was placed behind the sample. Thus these data show the purely elastically scattered part of the light. As can be seen, deviations from diffusion (continuous line) are observed for the sample with $k \cdot l^* = 2.7$.

light. The disentanglement of these two effects allows for an experimental study of the interplay between nonlinearities and localization which we have started in this year [8]. The topic receives increasing interest from theory as well [9–11].

When studying the transition to Anderson localization in three dimensions, it is important to characterize the transition as a function of turbidity and thus separate effects that are due to materials properties and effects due to localization. We achieve this by varying the wavelength of the incoming light, which in turn changes the scattering cross-section and hence the turbidity. Thus, as shown in Fig. 16.2, we can tune the value of $k \cdot l^*$, where k is the wavenumber and l^* is the transport mean free path. In addition, we can study the effects of the non-linear processes resulting in a wave-length shift of the outgoing photons due to e.g. mixing and second harmonic effects. Therefore, to study the transition in the elastic component, we are using band pass filters centered around the incoming wave-length, positioned behind the sample. This way, it is still possible to observe long-time deviations from diffusive behavior appearing with increasing turbidity, as expected from localization, see Fig. 16.3. In addition, the increase in the non-linear, frequency shifted component with increasing turbidity can be used to gain information about the intensity distributions of the localized modes. The strong increase in this part of the signal indicates a highly skewed intensity distribution in the sample, as predicted theoretically [12], which we would not be able to discern in these samples otherwise due to temporal fluctuations in the signal averaging out the speckle pattern.

- [1] M. Störzer, P. Gross, C.M. Aegerter and G. Maret, *Phys. Rev. Lett.* **96**, 063904 (2006).
- [2] C.M. Aegerter M. Störzer, and G. Maret, *Europhys. Lett.* **75**, 562 (2006).
- [3] T. Sperling, W. Bührer, C.M. Aegerter, and G. Maret, *Nature Photonics* **7**, 48 (2013).
- [4] P.W. Anderson, *Phys. Rev.* **109**, 5 (1958).
- [5] E. Abrahams *et al.*, *Phys. Rev. Lett.* **42**, 673 (1979).
- [6] R.Adair, L.L.Chase and S.A.Payne, *Phys.Rev.B*, **39**, 3337 (1989).
- [7] C.C. Evans *et al.*, *Optics Express* **21** 18582 (2013).
- [8] T. Sperling, W. Bührer, M. Ackermann, C.M. Aegerter, and G. Maret, *New J. of Phys.* **16**, 112001 (2014).
- [9] C.Conti, *Chin.Phys.Lett.* **31** 030501 (2014).
- [10] S. Fishman, Y. Krivolapov, and A. Soffer, *Nonlinearity* **25** R53 (2012).
- [11] N. Cherroret, B. Vermersch, J.C. Garreau, and D. Delande, *Phys. Rev. Lett.* **112**, 170603 (2014).
- [12] T.M. Nieuwenhuizen and M.C. van Rossum, *Phys.Rev.Lett.* **74**, 2674 (1995).

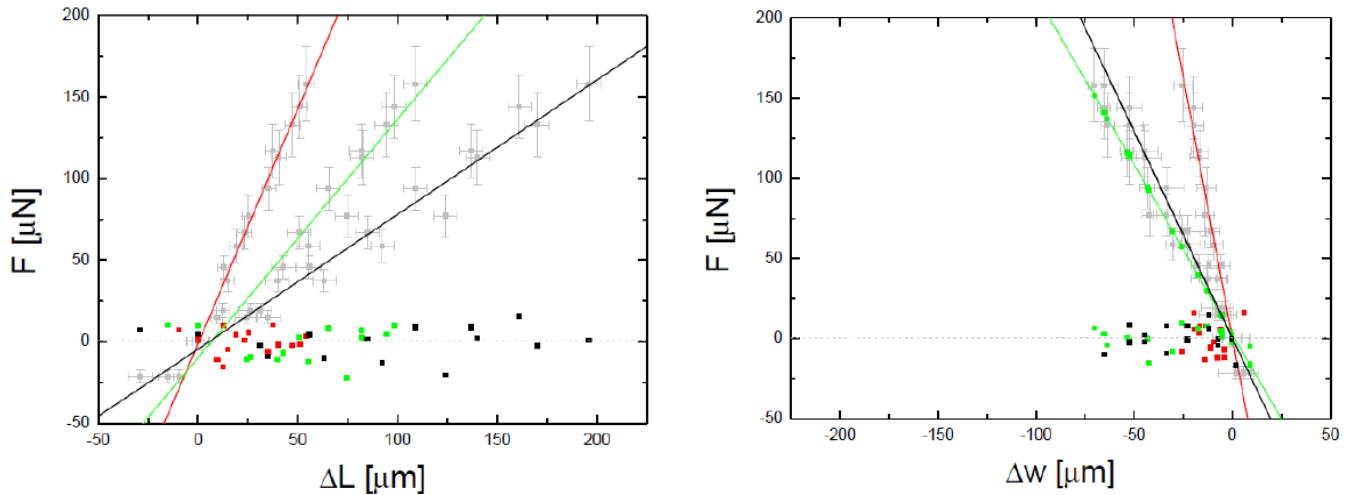


FIG. 16.4 –

Force-extension curves for a wing disc. The left panel shows the length of the disc in the direction of pulling, the right one the width perpendicular to this direction. The curves represent linear fits to different parts of the wing disc (pouch: red, hinge-notum: green, total disc: black). Raw data are grey and the coloured symbols are the residuals of the fits. Even for large deformations the wing discs are surprisingly linear in their elastic behaviour. From a study of the lateral constriction and the extension we find a Poisson ratio very close to 0.5.

16.2 Visco-elastic properties of *Drosophila* wing disc

72

In the course of our investigations into the influence of mechanical force on growth regulation in the wing imaginal disc of *Drosophila* [1–6], we are also studying the visco-elastic properties of this tissue directly using force-extension measurements [7, 8]. For this purpose, we have built a mechanical forcing stage capable of applying forces in the range of 10 to 500 μN onto the tissue in a

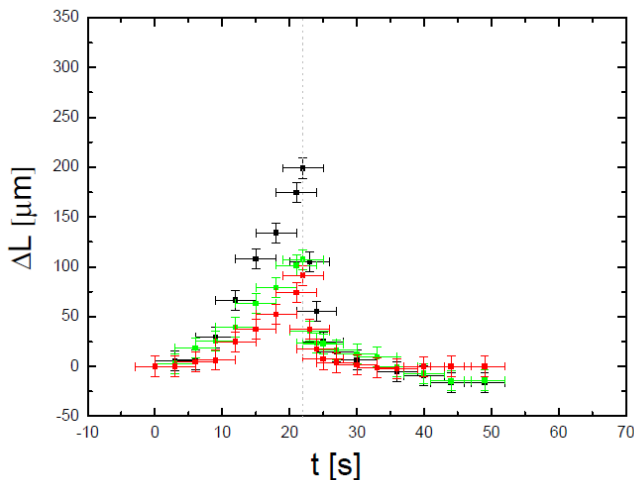


FIG. 16.5 – Determination of the visco-elastic behavior of a wing-disc tissue. When released from tension (dashed vertical line), the wing disc relaxes to the un-stretched state on a time scale of several seconds. Similarly, a temporally increasing force is delayed in the straining of the tissue. This fits well with the description of the tissue as a Kelvin-Voigt material with a high internal viscosity.

temporally varying manner [7]. As can be seen in Fig. 16.4, the mechanical response of the tissue is linear over a very large range of extensions and different parts of the tissue show extensions relative to their lengths, corresponding to a uniform Young's modulus over the whole tissue. This is irrespective of the fact that these different parts of the tissue are developmentally distinct and lead to different structures in the adult fly.

Applying a temporally varying force (linearly increasing until a sudden release), we can study the viscous properties of the tissue as well. An example is shown in Fig. 16.5, where the observed mean time of force application and release is $\tau = 12(3)$ s. This behavior is well described by a Kelvin-Voigt model of the tissue with a Young's modulus of $E = 80(15)$ kPa and a viscosity of $\eta = 1.0(3)$ MPa \cdot s. The results imply that the tissue is insensitive to mechanical stress on time scales shorter than τ , as are for instance incurred due to larval motion [8].

- [1] T. Aegerter-Wilmsen, C.M. Aegerter, E. Hafen, and K. Basler, *Mechanisms of Development* **124**, 318 (2007).
- [2] U. Nienhaus, T. Aegerter-Wilmsen, and C.M. Aegerter, *Mechanisms of Development* **126**, 942 (2009).
- [3] U. Nienhaus, T. Aegerter-Wilmsen, and C.M. Aegerter, *PLoS One* **7**, e47594 (2012).
- [4] T. Aegerter-Wilmsen *et al.*, *Development* **137**, 499 (2010).
- [5] T. Schluck, U. Nienhaus, T. Aegerter-Wilmsen, and C.M. Aegerter, *PLoS One* **8**, e76171 (2013).
- [6] T. Aegerter-Wilmsen *et al.*, *Development* **139** 3221 (2012).

- [7] T. Schluck and C.M. Aegerter, Eur. Phys. J. E **33**, 111 (2010).
 [8] T. Schluck, PhD thesis, University of Zurich (2013).

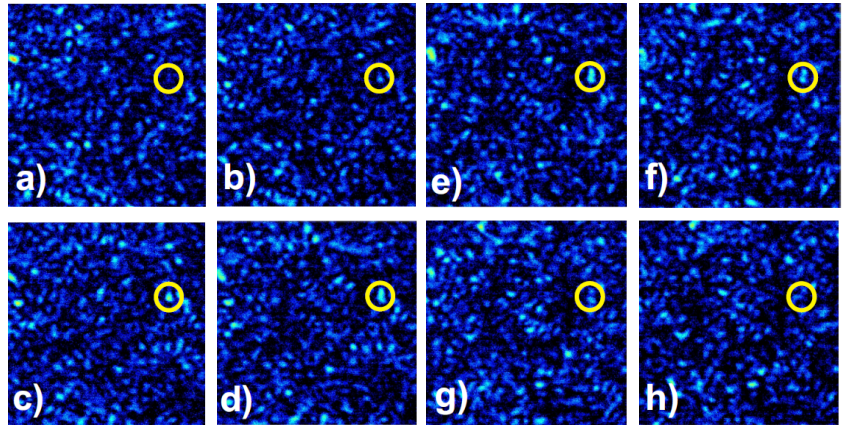


FIG. 16.6 – Time evolution of the speckle pattern of a foam with 20% liquid fraction and an age of about 100 min. The images taken with a movie camera are spaced by 10 ms. The dynamics of the time evolution of the pattern is evidenced by the encircled speckle that comes and goes. From the analysis of all speckles in the images, the correlation time has been obtained as a function of age.

16.3 Dynamics of levitated foams

Using diamagnetic levitation [1–3], we have studied the coarsening behavior of foams of different liquid fractions [4, 5]. While this has been studied theoretically for a long time yielding different predictions for dry foams by von Neumann [6] and wet foams by Ostwald [7], an experimental investigation has proven difficult due to the drainage of liquid by gravity. Given different coarsening dynamics at different liquid fractions according to the predictions [4], we have now studied the microscopic dynamics in the different regimes in more detail. Using diffusing wave spectroscopy [8, 9], i.e. the correlation of speckles in multiply scattered light transmitted through the foam (see Fig. 16.6), we determine the correlation time

of the speckle, thus characterizing the dynamics of the scatterers in the foam. Doing this for several speckles at once using a high speed camera, allows us to study the time dependence of this dynamics on several time scales:

- the time scale of the scatterer movements themselves, which corresponds to the correlation time
- the time scale of the age of the foam, which determines the coarsening behaviour and therefore influences the dynamics of the scatterers
- the intermediate time scale on which the foam as a whole shows movements, resulting in strong fluctuations in the correlation time.

73

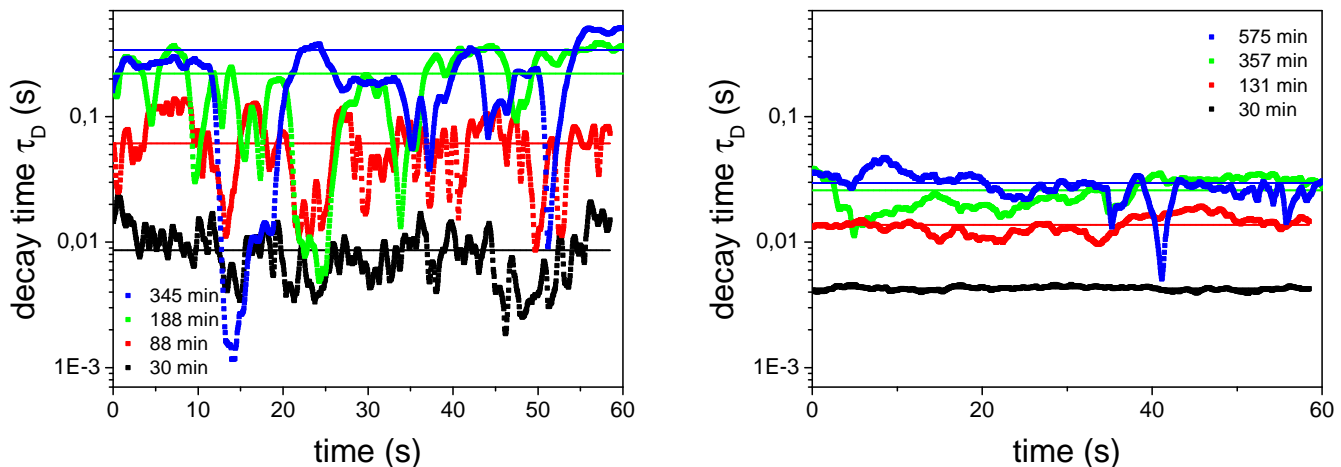


FIG. 16.7 – Time evolution of the DWS decay time as determined from speckle patterns as in Fig 16.6 for two different liquid fractions (left: 19%, right 34 %) for varying ages. Apart from an overall increase of the average decay time caused by the coarsening of the foam, a marked change in the dynamics is seen for the dry foam. At higher age, the dynamics is dominated by intermittent bursts of activity corresponding to large scale rearrangements of bubbles, which become less frequent as the foam coarsens. In wet foams in contrast, the dynamics is not dominated by single events, but rather by random fluctuations. In addition, the time scale of the decay time is much faster, connected to the ballistic motion of bubbles between collisions.

Figure 16.7 indeed shows striking differences in observed dynamics between foams of different liquid fractions [5]. At low liquid fraction, where the bubbles are strongly connected, there are intermittent large bursts of activity, corresponding to macroscopic rearrangements of the bubbles. The frequency of these bursts decreases with age as the foam coarsens according to the predictions of von Neumann [5, 6]. At high liquid fractions, where bubbles are separated from each other, there are no bursts of activity and dynamics does not change greatly with the age of the foam, apart from the change in time scale due to the increase in bubble size. Similarly, the coarsening process is not homogeneous in time, but is described by van Neumanns law at long times, when the larger bubbles start to overlap and by Ostwald ripening at short times, see Fig. 16.8.

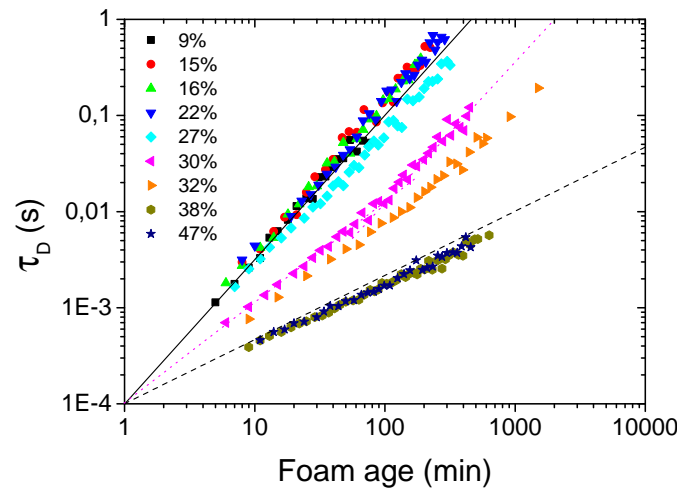


FIG. 16.8 – DWS correlation times obtained from integrating g_2 for several foams as a function of foam age. At low liquid fraction, the correlation time scales with $\text{age}^{3/2}$ (full line), whereas at high liquid fraction it scales as $\text{age}^{2/3}$ (dashed line). Around liquid fractions of 30%, close to the transition, two regimes corresponding to the limiting cases can be seen.

- [1] W. Braunbeck, Z. Phys. **112**, 764 (1939).
 [2] M.V. Berry and A.K. Geim, Europ. J. Phys. **18**, 307 (1997).
 [3] C.C. Maass, N. Isert, G. Maret and C.M. Aegerter, Phys. Rev. Lett. **100**, 248001 (2008).
 [4] N. Isert, G. Maret, C.M. Aegerter, Europ. Phys. J. E **36**, 116 (2013).
 [5] N. Isert, G. Maret, C.M. Aegerter, Colloids and Surfaces A **473**, 40 (2015).
 [6] J. von Neumann, in *Metal Interfaces* (C. Herring ed.), 108 (1952).
 [7] W. Ostwald, Z. Phys. Chem. **37**, 385 (1901).
 [8] G. Maret and P.E. Wolf, Z. Phys. B **65**, 409 (1987).
 [9] D.J. Pine, D.A. Weitz, J.X. Zhu and E. Herbolzheimer, J. Phys. **51**, 2101 (1990).

17 Mechanical Workshop

K. Bösiger, B. Lussi, R. Maier, M. Schaffner, S. Scherr, D. Gabrielli (apprentice), B. Markwalder (apprentice) and P. Weyeneth (apprentice)

Thanks to our state-of-the-art and versatile machinery we could manufacture numerous demanding and complicated parts, for in-house projects, for other departments of the University and the ETH and even for outside contractors. To manage these projects efficiently an Access database software package was purchased. In the reporting period we focused on the maintenance of existing tools: the large VDF lathe, the Kern 480 computer controlled lathe and the Picomax 54 drilling and milling center were examined and refurbished.

Our metal and technical material store supplied more than 30 institutes of the university, universities of applied science and local high schools with materials. Increasingly, we also help to solve technical problems, for example in the selection of materials. This service is actively used and appreciated. The information event organized by the workshop staff in November 2014 proved to be a good platform for the exchange of ideas and demands.

At the beginning of 2015 Reto Maier took over the position of Kurt Bösiger, who has been leading the workshop since 2002 and will retire later this year.

The evaluation of a new high speed laser cutting and engraving system started in June 2014 and the procurement was approved in January 2015 by the administration.

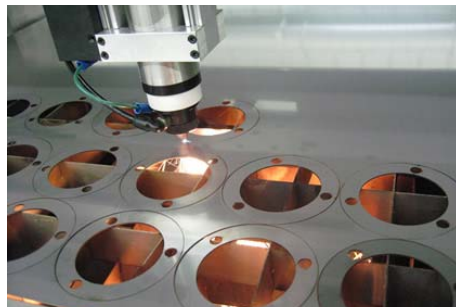


- The new high speed laser cutting and engraving system

75

The device will be commissioned in June 2015. The CO2 laser power is 400 watts which allows to cut also metals (steel up to 4.5 mm, stainless steel 3 mm, aluminum 1.5 mm, brass and tungsten 1 mm) including molybdenum and plastics. The working area of 1320 mm x 1270 mm expands our present possibilities. In addition engravings can be made on working pieces up to this size.

- Engraving process and a fabricated stainless steel workpiece

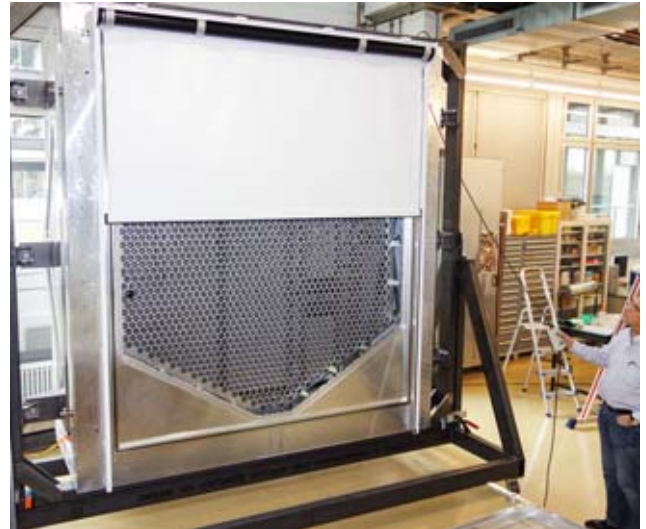


- Cutting tool in action with the pipe rotary cutting option





- Manufacturing of large parts for the FlashCam camera housing on a special table installed in the lock-smithery of the workshop



- The FlashCam camera housing during a shutter test in the assembly hall

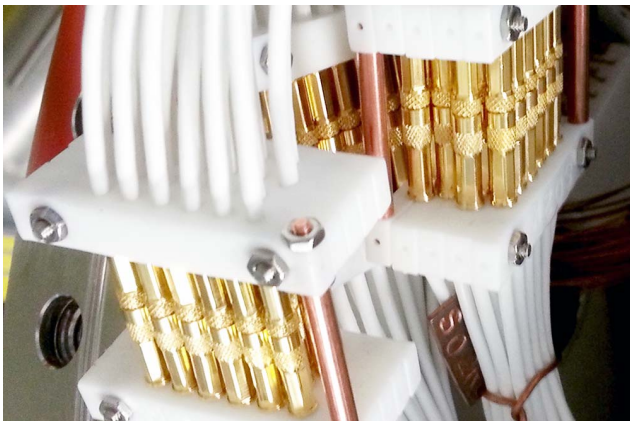
Below we mention a selection of our activities:

- CTA Cherenkov Telescope Array (Sec. 6)
The prototype FlashCam camera was put together in the large assembly hall. Different frames, bushings, mounting brackets used for the installation in the thermal insulated housing were manufactured. Custom designed racks with integrated cooling units for the detector readout electronics as well as a retractable target holder were made. We could only install the components thanks to the installation space with a total height of eight meters available at the institute workshop.
- Astroparticle Physics (Sec. 4)
For the Xenon experiment various test structures were prepared. In particular we produced special parts for connectors made of Teflon, insulators for voltage dividers and various brackets. Thanks to the new milling machine the large XENON1T porcupine

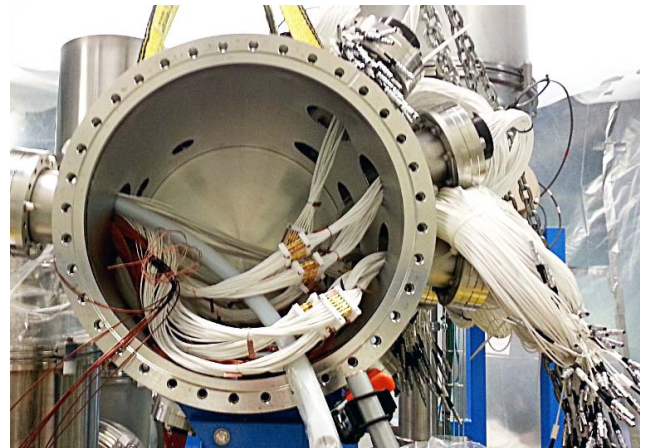
76

chamber could be made. At the beginning of 2015 we started with the preparation of the 85 copper ring electrodes used in the TPC field forming structure. These rings are made of high purity copper purchased specifically for this experiment.

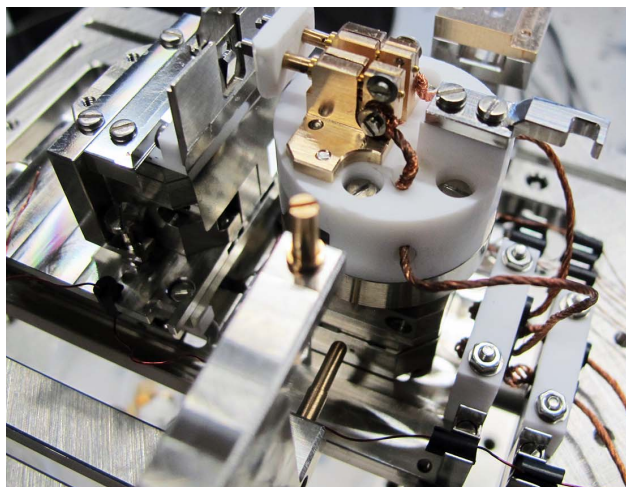
- Physics on the nanometer scale (Sec. 15)
Modifications and maintenance at the six station vapor deposition apparatus were made. We fabricated a load-lock system which enables the rapid transfer of samples into an ultra high vacuum chamber without affecting the chamber pressure. We manufactured and tested parts for the low energy electron point source (LEEPS) microscope. All material used must be suitable for ultra high vacuum and large temperature variations. Thus, the insulators are made of ceramic and the other parts of stainless steel and titanium.



- Closer view of the custom made Teflon connector parts



- The XENON1T porcupine chamber during the cable installation at the underground lab at the Laboratori Nazionali del Gran Sasso (LNGS)



- Detailed view of the LEEPS microscope with field emission tip and sample holder in the center

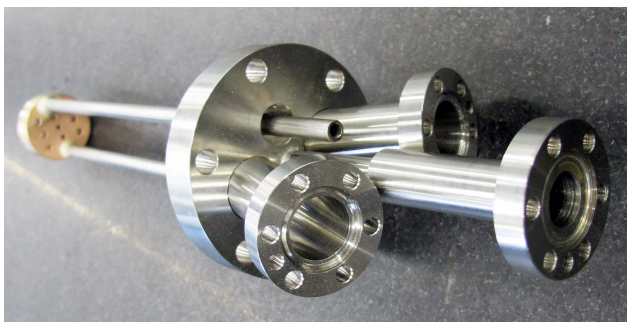
- Surface Physics (Sec. 14)

A new series of borazon cooler and Fasel sources were manufactured and assembled. Throughout the year molybdenum sample holders were adapted and maintained. These sample holders are covered on the inside with an insulating ceramic layer and can withstand temperatures up to 1000⁰C. A small series of standard molybdenum sample holders was made as well.

We produced a detector flange and parts for an electron diffraction experiment, which is installed at the Paul Scherrer Institute. Parts for the Sinergia project were produced. We performed maintenance work and made different modifications.

- CMS Barrel Pixel detector upgrade (Sec. 11)

A new pixel detector has been designed for the CMS experiment at CERN (Phase I Pixel Upgrade) with lightweight mechanics and a CO₂ cooling system. The demanded performances aim for 15 kW of cooling power at -20⁰C evaporation temperature. The cooling



- Base flange of a home-built Knudsen-cell evaporator used for depositing thin films. The material to be evaporated, is contained in a crucible (not shown), which can be heated resistively or by electron-beam bombardment. The setup is water cooled.



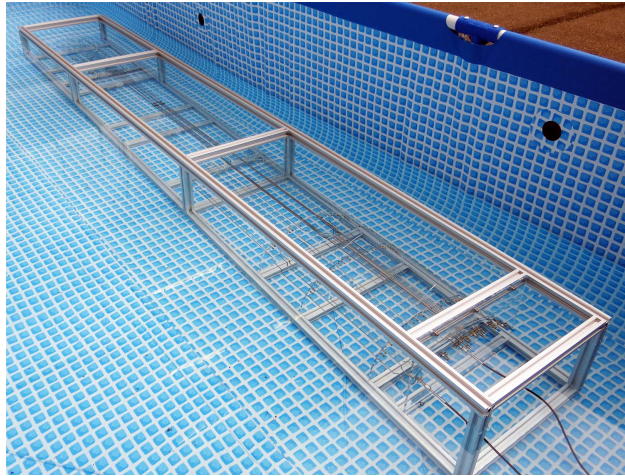
- Load-lock system enabling the rapid transfer of samples into the UHV chamber. An additional port permits the electro-spray deposition of biomolecules onto ultra-clean freestanding graphene.

structures are made of stainless steel tubes with a wall thickness down to 0.05 mm. Tests with the full-size cooling test-system prototypes produced in the workshop showed leakage at the soldering joints. To solve these problems we needed more time than planned. We tried to improve the soldering technology and made tests with different brazing alloys and flux. For the leakage and pressure tests instead of using water we changed to nitrogen gas with a test pressure of 200 bar. To find the leaks efficiently, we submersed the complete 3,2 meter long cooling test-system during the tests in a pool, which was set up outside of the workshop.

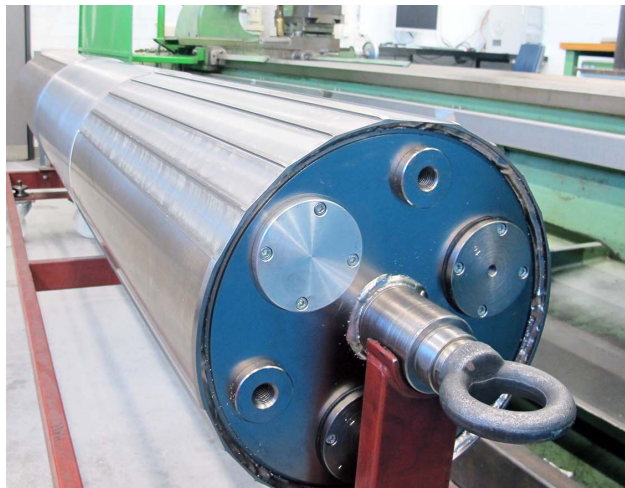
At the end of February 2015 we finally had a working test-system at hand. The setup was then transported to CERN and is meanwhile connected to a CO₂ cooling plant to perform the needed cooling tests. Currently, we continue with various soldering test runs to get a better understanding of the leakage long term effects which occurred. In early February 2015, we



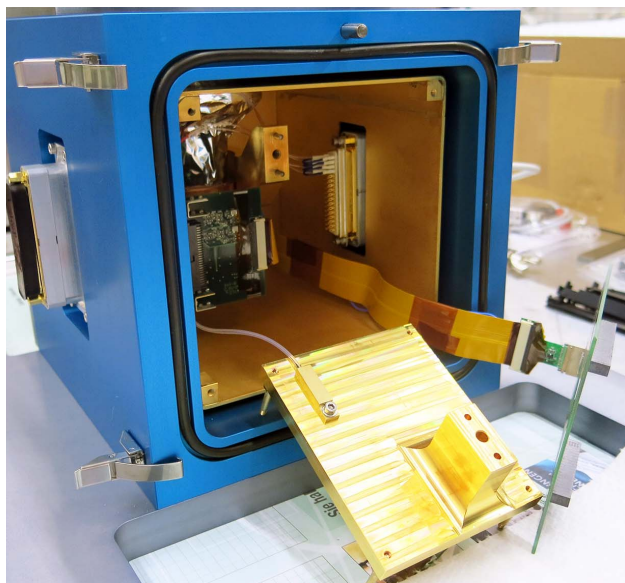
- Parts of an electron diffraction experiment. Electrons back-reflected by a sample produce light on a phosphorous screen after amplification by a micro channel plate. These parts are mounted inside a tube, seen in the middle. The screen is imaged through a vacuum viewport onto an external CCD, seen on the left. The picture on the right shows the detector flange.



- Prototype cooling system during a leakage test in a water pool



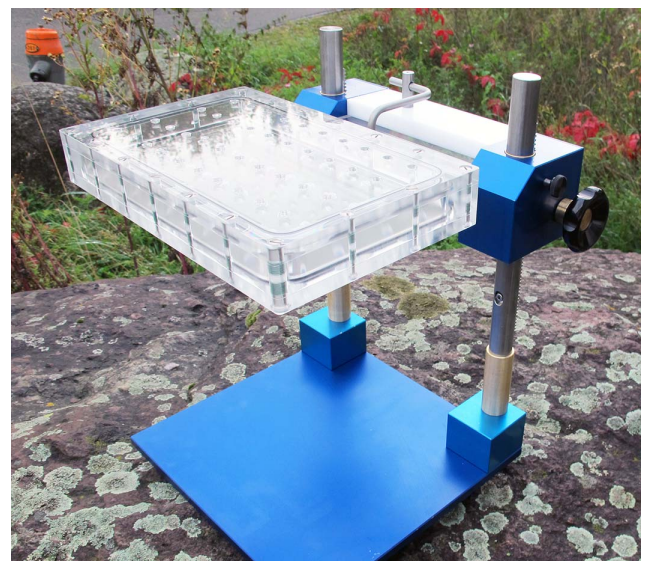
- The cylinder prepared for the fabrication of the Barrel Pixel Supply Tube structures



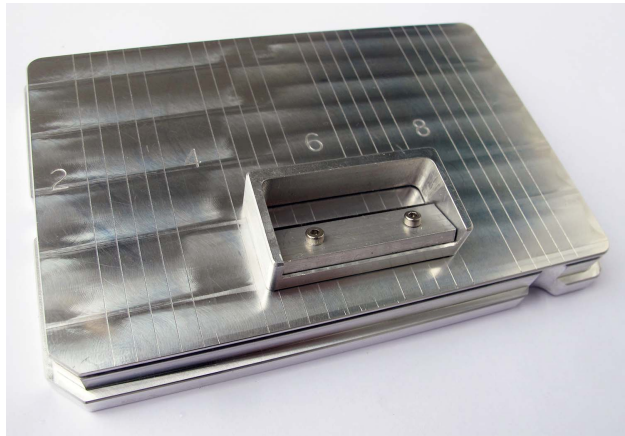
- The Alpine Cube test setup during the installation of the CCD base plate

started with the preparation of the production cylinder needed for the fabrication of the Supply Tube structures for the new detector system. The VDF lathe was re-measured and adjusted to an accuracy of ± 0.02 mm based on the diameter over the length of 3 m.

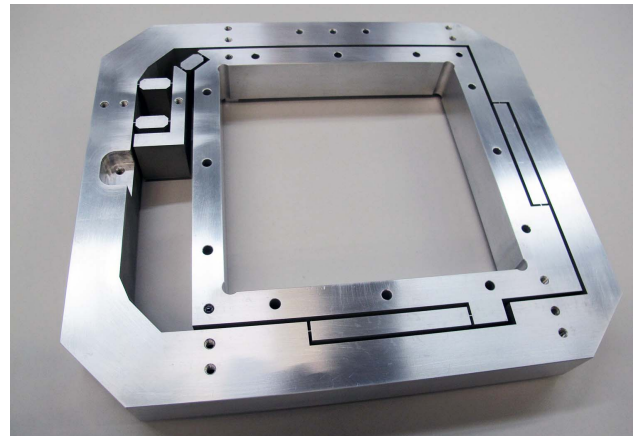
- DAMIC Dark Matter in CCDs (Sec. 5)
We produced additional parts for the AlpineCube test setup used for studies of different CCD types. Various parts were refined (gold-plated) and the system was assembled and tested for vacuum leaks.
- Demonstration and laboratory experiments
We repaired and improved different experiments used for the demonstrations in the basic physics lectures and in the laboratory courses for students of natural sciences and medicine.
- Basic mechanical workshop and welding courses
In August and September 2014 and January and February 2015 the basic mechanical workshop courses for the bachelor students were provided. In total eleven courses were carried out at 35 hours each. In October 2014 the physics laboratory assistant apprentices from the ETH attended the welding courses. For institute staff members we organized an internal basic workshop course in November 2014.
- Education of the apprentices and the workshop staff
Courses in computer aided design (CAD) and manufacturing (CAM) were attended. We took part in welding seminars and went to the regular meetings devoted to the education of the apprentices. We visited machinery and tool manufacturers, and exhibitions. For people interested in a grade as a poly-technician we provided one-week trial apprenticeships in May and August 2014 and several trial days in March 2015.



- Vaporization unit for the Institute of Forensic Medicine.



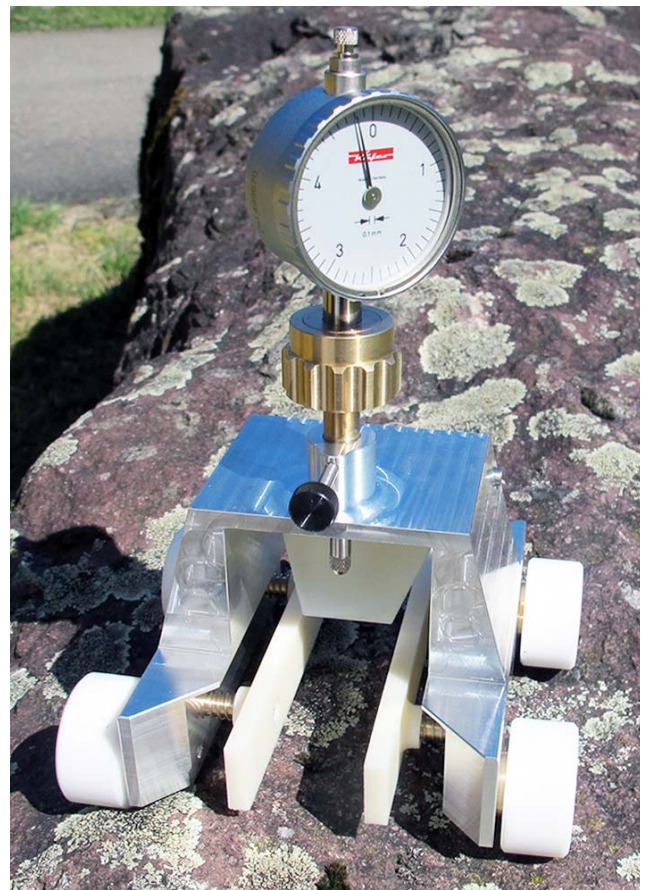
- Sample holder with an integrated hair cleaving tool. With this unit, hair samples can be forensically examined faster.



- Special grid holder for X-ray grating-based phase contrast imaging made for the Centre Suisse d'Electronique et de Microtechnique (CSEM)

For other departments and outside companies:

- Institute of Forensic Medicine
Five sample vaporization devices and a special hair-sample holder
- Institute of Physiology
Sample holders with membranes
- Zoological Museum
Earphone spiral cables
- University of Applied Sciences Rapperswil (HSR)
A high-pressure cell and a special flywheel
- Centre Suisse d'Electronique et de Microtechnique (CSEM)
special grid holders used for the EVITA project
CSEM leads the consortium which aims at new non-destructive inspection methods for the novel fibrous composite airplane materials give a weight (and thus fuel) reduction of >20%.
- A lighting company
Small series of holders for energy-saving LED lights
- Department of Geography
a mobile Augmented Reality 3D sandbox with dimensions 850 mm x 1150 mm x 1950 mm
- An outside company
A series of special measuring carriages, allowing to check the turbine blade positions in gas turbine compressor wheels after their assembly



- Measuring tool to survey the gas turbine compressor wheels after the assembly of the single blades on the rotor spindle

18 Electronics Workshop

D. Florin, P. Soland (until June 2014),
A. Vollhardt and David Wolf (since July 2014)

Besides small repair jobs and prototype tests, performed upon request, we'd like to mention a selection of our activities here.

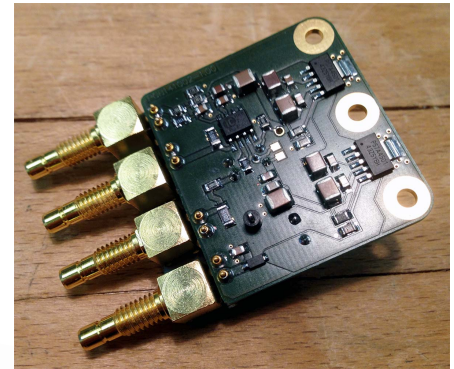
For the XENON1T experiment several PMT bases were designed and produced. Preparations for a larger scale production are underway, as well as the design and construction of a differential instrumentation amplifier for pressure gauges.

For XENON an LED/laser pulse driver with short pulse times was designed and built, to be used for calibrations.

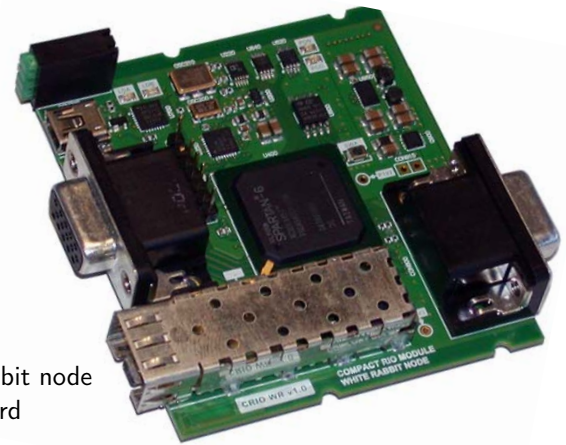
A White Rabbit node, compatible with the National Instruments CompactRIO system, was designed and produced. White Rabbit (WR) is an Open Hardware project initiated by CERN and GSI. Its main task is to transmit accurate timing information to synchronize distributed hardware on a ns scale via standard optical fiber over distances of up to 10 km. Within this project, the Physik-Institut is responsible for development of a WR end node which is compatible with the CompactRIO framework from National Instruments (NI). Several prototypes were successfully commissioned in house and duplicated by CERN for upcoming compliance tests performed by NI. We designed and manufactured a universal converter with five LVDS-CMOS/CMOS-LVDS translators each. Being part of the Open Hardware project, the design including the documentation was published on the White Rabbit Wiki webpages.

For the Flashcam camera for the CTA observatory, a camera safety system has been designed and commissioned, including:

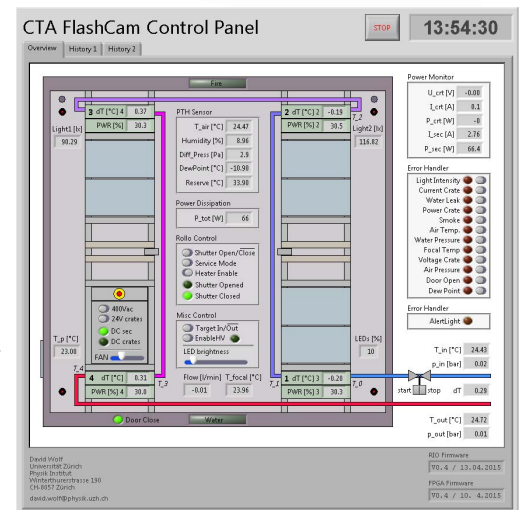
- evaluation and testing of individual components
- planning and documenting the wiring harness
- wiring of the control cabinet and the connected environmental sensors
- development and prototyping of custom made sensors and actuators
- development of a first software version (based on LabVIEW) for initial in-house tests



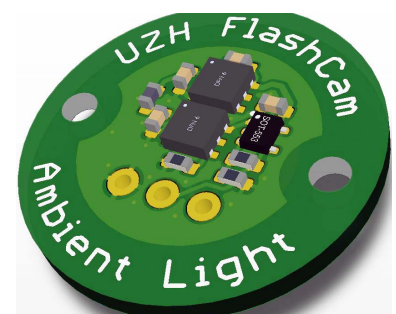
- Pulse driver circuit board



- White Rabbit node circuit board



- Graphical user interface for FlashCam safety control



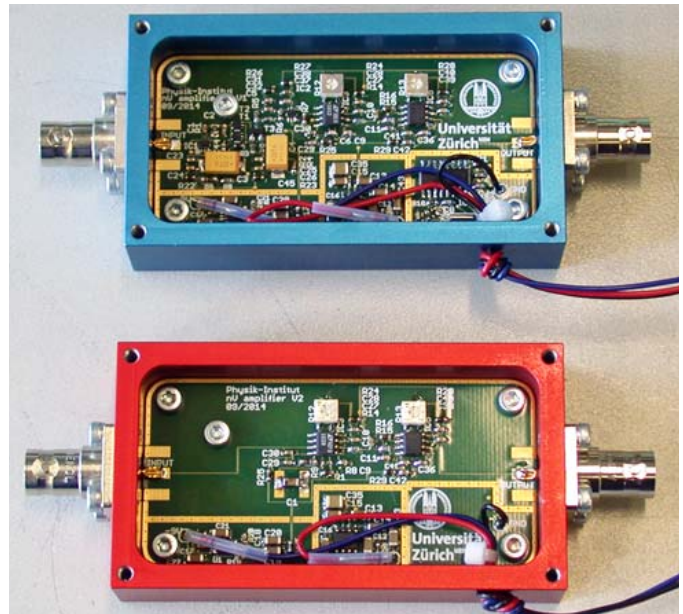
- FlashCam ambient light sensor

Within the CTA consortium, the Cherenkov telescope array requires alignment of 220 mirror segments in each Large Size Telescope (LST). In cooperation with the Institute for Cosmic Ray Research (ICRR) at the University of Tokyo, 220 actuator sets were produced in industry under supervision of the Physik-Institut. Final commissioning and acceptance testing was done in-house.



- Series production of CTA mirror actuators

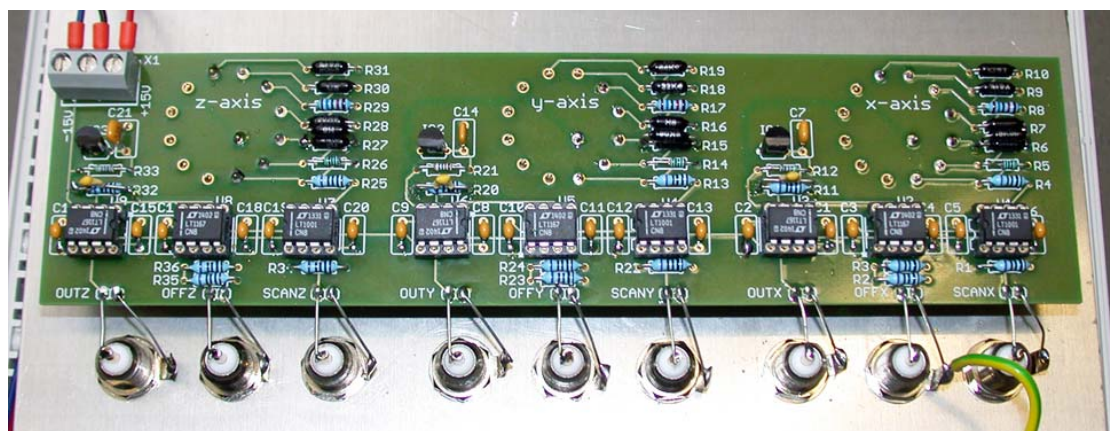
For the Schilling group two ultra-low-noise DC instrumentation amplifiers were developed, to be used for measurements of small resistance variations. The two amplifiers, each with a gain of +1000 but with slightly different design philosophies, were both able to reach noise levels below 5 nV rms at a bandwidth of 1 Hz.



- Ultra-low noise nV amplifiers

During the repair and modifications of a variac used in a laboratory setup of Fink's group, several state-of-the-art upgrades enhancing personal safety were introduced. A dedicated xyz-amplifier was designed to limit the field of view of a scanning tunnel microscope. It allows for switching the field size in powers of 1/2 (1/2 to 1/128) while matching the required voltage offset required by the following piezo driver stage.

- Circuit board of the xyz-amplifier



19 Publications

19.1 Elementary particles and their interactions

19.1.1 Theory of Elementary particles

Articles

- Minimal muon anomalous magnetic moment
C. Biggio and M. Bordone, JHEP 1502 (2015) 099.
- ZZ production at hadron colliders in NNLO QCD
F. Cascioli, T. Gehrmann, M. Grazzini, S. Kallweit, P. Maierhöfer *et al.*, Phys.Lett. B735 (2014) 311-313.
- Two-loop splitting amplitudes and the single-real contribution to inclusive Higgs production at N³LO
C. Duhr and T. Gehrmann and M. Jaquier, JHEP 1502 (2015) 077.
- Higgs boson gluon-fusion production beyond threshold in N³LO QCD
C. Anastasiou, C. Duhr, F. Dulat, E. Furlan, T. Gehrmann *et al.*, JHEP 1503 (2015) 091.
- Precise QCD predictions for the production of Higgs + jet final states
X. Chen, T. Gehrmann, E.W.N. Glover and M. Jaquier, Phys.Lett. B740 (2015) 147-150.
- W⁺W⁻ Production at Hadron Colliders in Next to Next to Leading Order QCD
T. Gehrmann, M. Grazzini, S. Kallweit, P. Maierhöfer, A. von Manteuffel *et al.*, Phys.Rev.Lett. 21 113 (2014) 212001.
- 82 - The $Hb\bar{b}$ form factor to three loops in QCD
T. Gehrmann and D. Kara, JHEP 1409 (2014) 174.
- The two-loop master integrals for $q\bar{q} \rightarrow VV$
T. Gehrmann, A. Manteuffel, L. Tancredi and E. Weihs, JHEP 1406 (2014) 032.
- Calculation of the transverse parton distribution functions at next-to-next-to-leading order
T. Gehrmann, T. Luebbert and L.L. Yang, JHEP 1406 (2014) 155.
- Higgs boson gluon-fusion production at threshold in N³LO QCD
C. Anastasiou, C. Duhr, F. Dulat, E. Furlan, T. Gehrmann *et al.*, Phys.Lett. B737 (2014) 325-328.
- EERAD3: Event shapes and jet rates in electron-positron annihilation at order α_s^3
A. Gehrmann-De Ridder, T. Gehrmann, E.W.N. Glover and G. Heinrich, Comput.Phys.Commun. 185 (2014) 3331.
- BLM Scale Fixing in Event Shape Distributions
T. Gehrmann, N. Häfliger and P.F. Monni, Eur.Phys.J. 6 C74 (2014) 2896.
- Transverse-momentum resummation for heavy-quark hadroproduction
S. Catani, M. Grazzini and A. Torre, Nucl.Phys. B890 (2014) 518-538.
- Associated ZH production at hadron colliders: the fully differential NNLO QCD calculation
G. Ferrera, M. Grazzini and F. Tramontano, Phys.Lett. B740 (2015) 51-55.
- Threshold resummation at N³LL accuracy and soft-virtual cross sections at N³LO
S. Catani, L. Cieri, D. de Florian, G. Ferrera and M. Grazzini, Nucl.Phys. B888 (2014) 75-91.
- Resummation of the transverse-energy distribution in Higgs boson production at the Large Hadron Collider
M. Grazzini, A. Papaefstathiou, Jennifer M. Smillie and B.R. Webber, JHEP 1409 (2014) 056.
- Higher-order QCD effects for associated WH production and decay at the LHC
G. Ferrera, M. Grazzini and F. Tramontano, JHEP 1404 (2014) 039.
- NLO electroweak automation and precise predictions for W+multijet production at the LHC
S. Kallweit, J.M. Lindert, P. Maierhöfer, S. Pozzorini and M. Schönherr, JHEP 1504 (2015) 012.

- Pseudo-observables in Higgs decays
M. Gonzalez-Alonso, A. Greljo, G. Isidori and D. Marzocca, Eur.Phys.J. 3 C75 (2015) 128.
- Softened Gravity and the Extension of the Standard Model up to Infinite Energy
G.F. Giudice, G. Isidori, A. Salvio and A. Strumia, JHEP 1502 (2015) 137.
- LHC Tests of Light Neutralino Dark Matter without Light Sfermions
L. Calibbi, J.M. Lindert, T. Ota and Y. Takahashi, JHEP 1411 (2014) 106.
- Boundary terms in quantum field theory and the spin structure of QCD
P. Lowdon, Nucl.Phys. B889 (2014) 801-816.
- NNLO QCD subtraction for top-antitop production in the $q\bar{q}$ channel
G. Abelof, Aude Gehrmann-De Ridder, P. Maierhöfer and S. Pozzorini, JHEP 1408 (2014) 035.
- Higgs Boson pair production merged to one jet
P. Maierhöfer and A. Papaefstathiou, JHEP 1403 (2014) 126.
- NLO matching for $t\bar{t}b\bar{b}$ production with massive b -quarks
F. Cascioli, P. Maierhöfer, N. Moretti, S. Pozzorini and F. Siegert, Phys.Lett. B734 (2014) 210-214.
- Standard model Higgs boson pair production in the $(b\bar{b})(b\bar{b})$ final state
D.E. Ferreira de Lima, A. Papaefstathiou and M. Spannowsky, JHEP 1408 (2014) 030.
- Higgs boson to di-tau channel in Chargino-Neutralino searches at the LHC
A. Papaefstathiou, K. Sakurai and M. Takeuchi, JHEP 1408 (2014) 176.
- The $\mu \rightarrow e\gamma$ decay in a systematic effective field theory approach with dimension 6 operators
G.M. Pruna and A. Signer, JHEP 1410 (2014) 14.
- Renormalization-group improved fully differential cross sections for top pair production
A. Broggio, A.S. Papanastasiou and A. Signer, JHEP 1410 (2014) 98.
- The infrared structure of QCD amplitudes and $H \rightarrow gg$ in FDH and DRED
C. Gnendiger, A. Signer and D. Stöckinger, Phys.Lett. B733 (2014) 296-304.
- The automated computation of tree-level and next-to-leading order differential cross sections, and their matching to parton shower simulations
J. Alwall, R. Frederix, S. Frixione, V. Hirschi, F. Maltoni *et al.*, JHEP 1407 (2014) 079.
- Higgs pair production at the LHC with NLO and parton-shower effects
R. Frederix, S. Frixione, V. Hirschi, F. Maltoni, O. Mattelaer *et al.*, Phys.Lett. B732 (2014) 142-149.
- Higgs production in association with bottom quarks
M. Wiesemann, R. Frederix, S. Frixione, V. Hirschi, F. Maltoni, and P. Torrielli, JHEP 1502 (2015) 132.
- Transverse momentum resummation for Higgs production via gluon fusion in the MSSM
R.V. Harlander, H. Mantler (CERN) and M. Wiesemann, JHEP 1411 (2014) 116.
- Finite top-mass effects in gluon-induced Higgs production with a jet-veto at NNLO
T. Neumann and Marius Wiesemann, JHEP 1411 (2014) 150.
- Higgs production in bottom quark annihilation: Transverse momentum distribution at NNLO+NNLL
R.V. Harlander, A. Tripathi and M. Wiesemann, Phys.Rev. D90 (2014) 1, 015017.

PhD Theses

- Methods for Multiloop Computations and their Application to Vector Boson Pair Production in NNLO QCD
Lorenzo Trancredi, PhD thesis, 03.07.2014
- A new Generator of One-loop Scattering Amplitudes for Precision Multi-Particle Simulations at the LHC
Fabio Cascioli, PhD thesis, 03.07.2014

- Soft-gluon resummation for four-parton hard scattering processes
Alessandro Torre, PhD thesis, 01.09.2014

Oral Presentations

- S. Borowka: Two-loop computations with SecDec and their application within the MSSM
Seminar, Freiburg, Germany, 11.11.2014
- S. Borowka: News on momentum-dependent 2L QCD contributions to CP-even Higgs-boson masses in the rMSSM
KUTS Workshop, Hamburg, Germany, 20.10.2014
- T. Gehrmann: NNLO correction to dejet production in DIS
DESY workshop on physics with HERA data, Hamburg, 11 November 2014
- T. Gehrmann: Antenna Subtraction Technique
LHCPhenoNet School, Debrecen, Hungary, 23-24 June 2014
- T. Gehrmann: Precision calculations for hadron collider observables
SFB workshop, Karlsruhe, 18 September 2014
- T. Gehrmann: Introduction to QCD
TASI 2014 Summer School, University of Colorado, Boulder, 2-6 June 2014
- M. Grazzini: Perturbative QCD calculations for the LHC
2nd Warsaw Spring Workshop, Warsaw, 8 April 2014
- M. Grazzini: Vector boson pair production at NNLO
Loops and Legs in Quantum Field Theory, Weimar, 29 April 2014
- M. Grazzini: NNLO calculations and resummation
LHCPhenoNet School, Debrecen, Hungary, 23-24 June 2014
- M. Grazzini: Vector boson pair production at NNLO
workshop on EW precision physics at the LHC, CERN, 30 June 2014
- M. Grazzini: The Higgs p_T spectrum in the SM and beyond
Higgs Couplings 2014, Torino, 1 October 2014
- M. Grazzini: WW and ZZ production at NNLO
Higgs (N)NLO MC and Tools Workshop for LHC RUN-2, CERN, Geneva, 18 December 2014
- G. Isidori: Looking for physics beyond the SM via the Flavour Window
ICHEP, Valencia (Spain), 2-9 July 2014
- G. Isidori: Quark and lepton Yukawa couplings: symmetries vs. dynamics
InvisiblesWorkshop 2014, Paris (France), 14-18 July 2014
- G. Isidori: Interpretation of low-energy experiments
Physics Landscape after the Higgs discovery, flavor WE-Heraeus-Seminar, Bad Honnef (Germany), 4-7 Nov 2014
- M. Jaquier: Precision calculation of Higgs plus one jet at NNLO
PhD talks, Zuerich, 12.09.2014
- S. Kallweit: A unified NLO description of top-pair and associated Wt production
Loops and Legs, Weimar 29.04.2014
- S. Kallweit: A unified NLO description of top-pair and associated Wt production
MIAPP summer institute "Challenges, Innovations and Developments in Precision Calculations for the LHC",
Munich, 11.8.2014
- S. Kallweit: NNLO QCD corrections to vector-boson pair production
Seminar at JGU Mainz, 11 July 2014

- J. Lindert: Collider limits on light neutralino dark matter
Planck 2014, Paris, France, 28 May 2014
- J. Lindert: QCD and electroweak corrections with OpenLoops
LHCPhenoNet Final Meeting, Berlin, Germany, November 26, 2014
- P. Lowdon: The proton spin crisis and form factors
Sinergia Project Meeting, Bern, Switzerland, 09.09.2014
- P. Maierhöfer: Next-to-leading order simulations with Sherpa+OpenLoops
Loops and Legs in Quantum Field Theory, Weimar, 29 April 2014
- P. Maierhöfer: Using OpenLoops for one-loop scattering amplitudes
HP2: High precision for hard processes, Firenze, 3 September 2014
- D. Marzocca: Charged lepton contribution to neutrino mixing and stable fermion mass matrices
Seminar at the Scuola Normale Superiore di Pisa, Italy, 22 October 2014
- S. Pozzorini: Scattering Amplitudes and Top phenomenology with OpenLoops
Seminar at RWTH Aachen, 5 June 2014
- S. Pozzorini: Recent results on $t\bar{t}(bb)$ backgrounds
7th Workshop of the LHC Higgs Cross Section Working Group, CERN, Geneva, 12 June 2014
- S. Pozzorini: Applications of OpenLoops to Top and Higgs Physics
Loopfest XIII, New York, 18 June 2014
- S. Pozzorini: Recent progress in Top Physics
QCD@LHC, Suzdal, Russia, 25 August 2014
- S. Pozzorini: New generators for top physics and EW corrections for the HL-LHC
Top2014, Cannes, France, 3 Oct 2014
- S. Pozzorini: $t\bar{t}$ +jets and $t\bar{t}V$ +jets in Sherpa+OpenLoops
Higgs (N)NLO MC and ToolsWorkshop for LHC RUN-2, CERN, Geneva, 18 December 2014
- D. Rathlev: Status of VV' production in NNLO QCD
Loopfest XIII, New York, 20 June 2014
- D. Rathlev: Diboson production in NNLO QCD
HP2, Florenz, 4.9.2014
- D. Rathlev: Diboson production in NNLO QCD
Seminar, Göttingen, 21.11.2014
- D. Rathlev: Diboson production in NNLO QCD
Terascale Meeting, Hamburg, 2.12.2014
- D. Rathlev: Diboson production in NNLO QCD
Seminar, Aachen, 4.12.2014
- D. Rathlev: Diboson production in NNLO QCD
Seminar, Würzburg, 11.12.2014
- H. Sargsyan: $q\bar{q}$ subtraction for top-quark pair production at hadron colliders
LHCPhenonet final meeting 2014, 25.11.2014
- H. Sargsyan: Higgs boson transverse momentum in the Standard Model
Higgs (N)NLO MC and ToolsWorkshop for LHC RUN-2, CERN, Geneva, 17.12.2014
- T. Schmidt: Schwellenresummation in der Higgs Boson Produktion via Gluon Fusion
46. Herbstschule für Hochenergiephysik, Maria Laach, 2.-12. September 2014

- M. Schoenherr: Electroweak corrections for LHC physics
Seminar, Freiburg, Deutschland, 18.11.2014
- M. Schoenherr: Higgs production at NLO in Sherpa
Higgs+Jets workshop, Durham, England, 09.12.2014
- A. Signer: Effective theory approach to top quark production at hadron colliders
Seminar University of Wien, 29 April 2014
- A. Signer: Searching high and low for physics beyond the Standard Model
Colloquium LPSC Grenoble, 22 May 2014
- A. Signer: Effective theory approach to top quark production at hadron colliders
Seminar University Wurzburg, 5 June 2014
- A. Signer: RG improved fully differential top pair cross sections at hadron colliders
MIAPP Top quark workshop, Munich, 11 August 2014
- A. Signer: Top quark physics at a linear collider
5th Linear Collider Physics School, Frauenchiemsee, 13 August 2014
- A. Signer: The impact of a non-vanishing nEDM
Workshop nEDM2014, Ascona, 2 November 2014
- L. Tancredi: Lectures on Methods for multi-loop computations
Bhubaneswar, India, 4-9 March 2014
- L. Tancredi: Schouten identities and the two-loop sunrise graph
Loops and Legs, Weimar 01.05.2014
- L. Tancredi: Schouten identities and the two-loop sunrise graph
New frontiers in Theoretical Physics, Cortona, 01.06.2014
- L. Tancredi: Methods for multi-loop calculations and vector boson pair production in NNLO QCD
TTP Seminar, Karlsruhe, 13.06.2014
- A. Torre: Soft-gluon resummation for four-parton hard-scattering processes
LoopFest XIII, New York, 19 June 2014
- M. Wiesemann:
Supersymmetric Higgs production: Transverse momentum resummation in bottom annihilation at NNLO+NNLL
LHCPhenoNet 2nd Fellows meeting, Paris (France), June 6, 2014
- M. Wiesemann: Analytic resummation for Higgs pT in $gg \rightarrow H$: Choosing the resummation scale for the bottom
MSSM ggH Higgs pT meeting, CERN (Switzerland), June 17, 2014
- M. Wiesemann: Higgs production in bottom annihilation: Transverse momentum spectrum at NNLO+NNLL
LoopFest XIII, New York (USA), June 19, 2014
- M. Wiesemann: Higgs production in association with bottom quarks
Collider Cross Talk, CERN (Switzerland), October 23, 2014
- M. Wiesemann: Finite top-mass effects for Higgs production with a jet-veto at NNLO
LHCPhenoNet Final Meeting, Berlin (Germany), November 24, 2014
- M. Wiesemann: Higgs production in the MSSM: Transverse momentum resummation
HP2 : High Precision for Hard Processes, Florence (Italy), September 5, 2014
- M. Wiesemann: bbH: introduction and theoretical status
bbH cross-group kick off meeting, CERN (Switzerland), November 28, 2014
- M. Wiesemann: Higgs production in association with bottom quarks
Higgs (N)NLO MC and ToolsWorkshop for LHC RUN-2, CERN (Switzerland), December 19, 2014

19.1.2 Astrophysics and General Relativity

Articles

- Testing scalar-tensor theories and parametrized post-Newtonian parameters in Earth orbit
A. Schäfer, R. Angéilil, R. Bondarescu, P. Jetzer and A. Lundgren, *Phys. Rev. D* 90 (2014) 123005.
- Quantum tests of the Einstein Equivalence Principle with the STE-QUEST space mission
B. Altschul, Q. G. Bailey, L. Blanchet, K. Bongs, P. Bouyer, L. Cacciapuoti, S. Capozziello, N. Gaaloul, D. Giulini, J. Hartwig, L. Iess, P. Jetzer, A. Landragin, E. Rasel, S. Reynaud, S. Schiller, C. Schubert, F. Sorrentino, U. Sterr, J. D. Tasson, G. M. Tino, P. Tuckey and Peter Wolf, *Adv. Space Res.* 55 (2015) 501.
- Quasi-universal properties of neutron star mergers
S. Bernuzzi, A. Nagar, S. Balmelli, T. Dietrich and M. Ujevic, *Phys. Rev. Lett.* 112 (2014) 201101.
- Gravitational waves from spinning compact binaries in hyperbolic orbits
L. De Vittori, A. Gopakumar, A. Gupta and P. Jetzer, *Phys. Rev. D* 90 (2014) 124066.
- Planck confirmation of the disk and halo rotation of M31
F. De Paolis, V. Gurzadyan, A. Nucita, G. Ingrosso, A. Kashin, H. Khachatryan, S. Mirzoyan, E. Poghosian, Ph. Jetzer, A. Quadir and D. Vetrugno, *Astron. and Astrophys.* 565 (2014) L3.
- STE-QUEST - Test of the Universality of Free Fall Using Cold Atom Interferometry
D.N. Aguilera, H. Ahlers, B. Battelier, A. Bawamia, A. Bertoldi, R. Bondarescu, K. Bongs, P. Bouyer, C. Braxmaier, L. Cacciapuoti, C. Chaloner, M. Chwalla, W. Ertmer, M. Franz, N. Gaaloul, M. Gehler, D. Gerardi, L. Gesa, N. Gürlebeck, J. Hartwig, M. Hauth, O. Hellmig, W. Herr, S. Herrmann, A. Heske, A. Hinton, P. Ireland, Ph. Jetzer, U. Johann, M. Krutzik, A. Kubelka, C. Lämmerzahl, A. Landragin, I. Lloro, D. Massonnet, I. Mateos, A. Milke, M. Nofrarias, M. Oswald, A. Peters, K. Posso-Trujillo, E. Rasel, E. Rocco, A. Roura, J. Rudolph, W. Schleich, C. Schubert, T. Schuldt, S. Seidel, K. Sengstock, C.F. Sopena, F. Sorrentino, D. Summers, G.M. Tino, C. Trenkel, N. Uzunoglu, W. von Klitzing, R. Walser, T. Wendrich, A. Wenzlawski, P. Wessels, A. Wicht, E. Wille, M. Williams, P. Windpassinger, and N. Zahzam, *Class. and Quantum Gravity* 31 (2014) 115010.
- Limits on compact baryonic dark matter from gravitational microlensing
P. Jetzer, *Phys. Scr.* 89 (2014) 084009.
- Gravitational wave detection from space
P. Jetzer, *EPJ Web. Conf.* 71 (2014) 00060.
- Measuring polarization in microlensing events
G. Ingrosso, S. Calchi Novati, F. De Paolis, P. Jetzer, A. Nucita and F. Strafella, *Mont. Not. R. Astron. Soc.* 446 (2015) 1090.
- Memory effect from spinning unbound binaries
L. De Vittori, A. Gopakumar, A. Gupta and P. Jetzer, 2014 Sant Cugat Forum on Astrophysics, Astrophysics and Space Science, Proceedings 40, C. Sopena Editor,(2015) 259.
- Supermassive Black Hole Tests of General Relativity with eLISA
C. Huwyler, Ed. Porter and P. Jetzer, *Phys. Rev. D* 91 (2015) 024037.
- Effective-One-Body Hamiltonian with next-to-leading order spin-spin coupling
S. Balmelli and P. Jetzer, *Phys. Rev.* 91 (2015) 064011.
- Gravitational lens recovery with GLASS: measuring the mass profile and shape of a lens
J. P. Coles, J.I. Read, and P. Saha, *MNRAS*, vol. 445, pp. 2181–2197, Dec. 2014.
- Gravitational lens modelling in a citizen science context
R. Küng, P. Saha, A. More, E. Baeten, J. Coles, C. Cornen, C. Macmillan, P. Marshall, S. More, J. Odermatt, A. Verma, and J.K. Wilcox, *MNRAS*, vol. 447, pp. 2170–2180, Mar. 2015.
- Mass-galaxy offsets in Abell 3827, 2218 and 1689: intrinsic properties or line-of-sight substructures?
I. Mohammed, J. Liesenborgs, P. Saha, and L.L.R. Williams, *MNRAS*, vol. 439, pp. 2651–2661, Apr. 2014.

- Lensing time delays as a substructure constraint: a case study with the cluster SDSS J1004+4112
I. Mohammed, P. Saha, and J. Liesenborgs, PASJ, vol. 67, pp. 21, Mar. 2015.
- Clocks around Sgr A*
R. Angéilil and P. Saha, MNRAS, vol. 444, pp. 3780–3791, Nov. 2014.
- Feasibility of observing Hanbury Brown and Twiss phase
T. Wentz and P. Saha, MNRAS, vol. 446, pp. 2065–2072, Jan. 2015.

PhD Thesis

- Testing General Relativity with Gravitational Waves
Cédric Huwyler, PhD thesis, 3.12.2014

Oral Presentations

- Simone Balmelli: Quasi-universal properties of neutron star mergers
LISA Symposium X, Gainesville (USA), May 18-23 2014.
- Ruxandra Bondarescu: Probing general relativity, alternative theories of gravity, and relativistic geodesy with atomic clocks
Invited Seminars at Hebrew University, Tel-Aviv University, Weizmann Institute and Technion in Israel, 22nd, 24th, 25th, and 28th December 2014.
- Ruxandra Bondarescu: Testing General Relativity and Alternative Theories of Gravity with Atomic Clocks
3rd International Conference on New Frontiers in Physics, Creta (Greece), July 28-6 August 2014.
- Lorenzo De Vittori: The remains of a spinning, hyperbolic encounter
LISA Symposium X, Gainesville (USA), May 18-23 2014.
- Lorenzo De Vittori: Memory effect from spinning unbound binaries
Sant Cugat Forum on Astrophysics, Sant Cugat (Spain), April 21-25 2014.
- Philippe Jetzer: Gravitational Red-Shift Explorer (GRESE)
2nd Workshop, Planning for a joint scientific space mission, Chinese Academy of Sciences (CAS) - European Space Agency (ESA), Copenhagen (Denmark), 23-24 September 2014.
- Philippe Jetzer: Gravitational wave detection from space
International Conference on Relativistic Astrophysics, Lahore (Pakistan), 10-14 February 2015.

88

19.1.3 GERDA

Articles

- Production, characterization and operation of ^{76}Ge enriched BEGe detectors in GERDA
M. Agostini, M. Allardt, E. Andreotti, A.M. Bakalyarov, M. Balata, I. Barabanov, N. Barros, L. Baudis, C. Bauer *et al.*
(GERDA Collaboration), Eur.Phys.J. C75 (2015) 2, 39.

Lectures and oral presentations

- M. Walter: The GERDA Experiment for the Search of Neutrinoless Double Beta Decay
Discrete 2014, London, 2.- 6. December 2014.
- L. Baudis: GERDA and the nature of neutrinos
Physics Colloquium, Nikhef and University of Amsterdam, Amsterdam, October 24, 2014.

19.1.4 XENON/DARWIN

Articles

- WIMP Dark Matter Direct-Detection Searches in Noble Gases
Laura Baudis, *Physics of the Dark Universe* 4 50 (2014).
- Conceptual design and simulation of a water Cherenkov muon veto for the XENON1T experiment
E. Aprile *et al.* (XENON1T Collaboration) *JINST* 9, P11006 (2014).
- First Axion Results from the XENON100 Experiment
E. Aprile, F. Agostini, M. Alfonsi, K. Arisaka, F. Arneodo, M. Auger, C. Balan, P. Barrow, L. Baudis, B. Bauermeister *et al.*, *Phys. Rev. D* 90, 062009 (2014).
- Observation and applications of single-electron charge signals in the XENON100 experiment
E. Aprile, F. Agostini, M. Alfonsi, K. Arisaka, F. Arneodo, M. Auger, C. Balan, P. Barrow, L. Baudis, B. Bauermeister *et al.*, *J.Phys. G*41 (2014) 035201.

Lectures and oral presentations

- L. Baudis: Dark detection of particle dark matter with underground detectors
Physics Colloquium, Max Planck Institute for Physics, January 20, 2015.
- L. Baudis: DARWIN: an introduction
DARWIN 2015: towards future dark matter experiments, WIS, Rehovot, January 7, 2015.
- L. Baudis: Dark detection of particle dark matter with underground detectors
Physics Colloquium, Max Planck Institute for Plasma Physics, Munich, November 21, 2014.
- L. Baudis: Dark matter detection review
NNN 2014, Paris, November 5, 2014.
- L. Baudis: Dark matter detection: experimental overview
26th Solvay Conference on Physics (Astrophysics and Cosmology), Brussels, October 11, 2014.
- L. Baudis: Dark matter searches: where do we stand, where are we going?
SIF Congresso Nazionale, Pisa, September 25, 2014.
- L. Baudis: Direct detection of WIMPs
COSMO 2014; Chicago, August 28, 2014.
- L. Baudis: Will we detect dark matter soon?
Ascona, July 8, 2014.
- L. Baudis: XENON and DARWIN
SWAPS meeting, Cartigny, June 12, 2014.
- L. Baudis: Direct dark matter detection in the Milky Way
Physics Colloquium, Imperial College, London, April 30, 2014.
- G. Kessler: XENON100 and XENON1T - Dark Matter Search with Liquid Xenon
PANIC2014, Hamburg, Germany, 25. August 2014.
- A. Kish: Direct Dark Matter Detection with XENON and DARWIN
TIPP2014, Beurs Van Berlage, Amsterdam, The Netherlands, June 4 2014.

19.1.5 DAMIC

Lectures and oral presentations

- B. Kilminster: DAMIC results from Snolab
10th Patras Workshop on Axions, WIMPs, and WISPs, CERN (Switzerland), July 3, 2014.
- B. Kilminster: The shape of the Higgs boson
Prospects and Precision of Higgs physics with 13 TeV at the LHC, Galileo Galilei Institute, Firenze (Italy), Sept. 14 2014,
- B. Kilminster: DAMIC: a novel approach for DM searches with CCDs
Strategy Workshop on Astroparticle in Switzerland 2014, Geneva (Switzerland), June 11, 2014.

19.1.6 CTA

Conference contributions

- Q. Weitzel *et. al.*: The FlashCam Camera for the Medium-Sized Telescopes of CTA
Technology and Instrumentation in Particle Physics 2014 (TIPP2014), Amsterdam (Netherlands), PoS(TIPP2014)142.
- G. Pühlhofer *et. al.*: Status of the photomultiplier-based FlashCam camera for the Cherenkov Telescope Array
SPIE.Astronomical Telescopes + Instrumentation (SPIE2014), Montreal (Canada), doi:10.1117/12.2056837.
- A. Gadola *et. al.*: FlashCam: a novel Cherenkov telescope camera with continuous signal digitization
Topical Workshop on Electronics for Particle Physics (TWEPP2014), Aix en Provence (France), doi:10.1088/1748-0221/10/01/C01014.

90

Oral presentations

- A. Gadola: FlashCam: A novel camera for the Cherenkov Telescope Array
SPS Annual Meeting , Fribourg, 02.07.2014.

19.1.7 H1

The 2014 H1 Collaboration has 141 members including K. Müller, P. Robmann, U. Straumann and P. Truöl.

Articles

- Measurement of Feynman- x Spectra of Photons and Neutrons in the Very Forward Direction in Deep-Inelastic Scattering at HERA
H1-Collaboration, V. Andreev *et al.*, Eur. Phys. J. C **74** (2014), 2915.
- Measurement of Multijet Production in ep Collisions at High Q^2 and Determination of the Strong Coupling α_s
H1-Collaboration, V. Andreev *et al.*, Eur. Phys. J. C **75** (2015), 65.
- Measurement of Dijet Production in Diffractive Deep-Inelastic ep Scattering at HERA
H1-Collaboration, V. Andreev *et al.*, JHEP **03** (2015), 092.

Articles in press

- Combination of Differential $D^{*\pm}$ Cross Section Measurements in Deep-Inelastic ep Scattering at HERA
H1- and ZEUS-Collaboration, H. Abramowicz *et al.*, JHEP (2015), in print.
- Diffractive Dijet Production with a Leading Proton in ep Collisions at HERA
H1-Collaboration, V. Andreev *et al.*, JHEP (2015), in print.

19.1.8 LHCb

Articles

- Measurement of B_c^+ production in proton-proton collisions at $\sqrt{s} = 8$ TeV
LHCb-Collaboration, R. Aaij *et al.*, Phys. Rev. Lett. **114** (2015) 132001.
- Study of the rare B_s^0 and B^0 decays into the $\pi^+\pi^-\mu^+\mu^-$ final state
LHCb-Collaboration, R. Aaij *et al.*, Phys. Lett. B **743** (2015) 46.
- LHCb Detector Performance
LHCb-Collaboration, R. Aaij *et al.*, Int. J. Mod. Phys. A **30** (2015) 1530022.
- Measurement of the inelastic pp cross-section at a centre-of-mass energy of $\sqrt{s} = 7$ TeV
LHCb-Collaboration, R. Aaij *et al.*, JHEP **1502** (2015) 129.
- Measurement of the lifetime of the B_c^+ meson using the $B_c^+ \rightarrow J/\psi\pi^+$ decay mode
LHCb-Collaboration, R. Aaij *et al.*, Phys. Lett. B **742** (2015) 29.
- Observation of two new Ξ_b^- baryon resonances
LHCb-Collaboration, R. Aaij *et al.*, Phys. Rev. Lett. **114** (2015) 6, 062004.
- Precision measurement of CP violation in $B_s^0 \rightarrow J/\psi K^+ K^-$ decays
LHCb-Collaboration, R. Aaij *et al.*, Phys. Rev. Lett. **114** (2015) 4, 041801.
- Measurement of the CP-violating phase β in $B^0 \rightarrow J/\psi\pi^+\pi^-$ decays and limits on penguin effects
LHCb-Collaboration, R. Aaij *et al.*, Phys. Lett. B **742** (2015) 38.
- Measurement of the Z+b-jet cross-section in pp collisions at $\sqrt{s} = 7$ TeV in the forward region
LHCb-Collaboration, R. Aaij *et al.*, JHEP **1501** (2015) 064.
- Study of $\eta - \eta'$ mixing from measurement of $B_{(s)}^0 \rightarrow J/\psi\eta^{(\prime)}$ decay rates
LHCb-Collaboration, R. Aaij *et al.*, JHEP **1501** (2015) 024.
- Search for CP violation in $D^0 \rightarrow \pi^-\pi^+\pi^0$ decays with the energy test
LHCb-Collaboration, R. Aaij *et al.*, Phys. Lett. B **740** (2015) 158.
- Precision luminosity measurements at LHCb
LHCb-Collaboration, R. Aaij *et al.*, JINST **9** (2014) 12, P12005.
- Measurement of the semileptonic CP asymmetry in $B^0 - \bar{B}^0$ mixing
LHCb-Collaboration, R. Aaij *et al.*, Phys. Rev. Lett. **114** (2015) 041601.
- Precision Measurement of the Mass and Lifetime of the Ξ_b^- Baryon
LHCb-Collaboration, R. Aaij *et al.*, Phys. Rev. Lett. **113** (2014) 24, 242002.
- Search for the lepton flavour violating decay $\tau \rightarrow \mu^-\mu^+\mu^-$
LHCb-Collaboration, R. Aaij *et al.*, JHEP **1502** (2015) 121.
- Measurement of the CP-violating phase ϕ_s in $\bar{B}_s^0 \rightarrow D_s^+ D_s^-$ decays
LHCb-Collaboration, R. Aaij *et al.*, Phys. Rev. Lett. **113** (2014) 21, 211801.
- Measurement of the $\chi_b(3P)$ mass and of the relative rate of $\chi_{b1}(1P)$ and $\chi_{b2}(1P)$ production
LHCb-Collaboration, R. Aaij *et al.*, JHEP **1410** (2014) 88.
- Measurements of CP violation in the three-body phase space of charmless B^\pm decays
LHCb-Collaboration, R. Aaij *et al.*, Phys. Rev. D **90** (2014) 11, 112004.
- Determination of γ and $-\beta_s$ from charmless two-body decays of beauty mesons
LHCb-Collaboration, R. Aaij *et al.*, Phys. Lett. B **741** (2015) 1.
- Measurement of the forward W boson cross-section in pp collisions at $\sqrt{s} = 7$ TeV
LHCb-Collaboration, R. Aaij *et al.*, JHEP **1412** (2014) 079.

- Measurement of the CKM angle γ using $B^\pm \rightarrow DK^\pm$ with $D \rightarrow K_S^0 \pi^+ \pi^-, K_S^0 K^+ K^-$ decays
LHCb-Collaboration, R. Aaij *et al.*, JHEP **1410** (2014) 97.
- Search for CP violation using T -odd correlations in $D^0 \rightarrow K^+ K^- \pi^+ \pi^-$ decays
LHCb-Collaboration, R. Aaij *et al.*, JHEP **1410** (2014) 005.
- Measurement of the track reconstruction efficiency at LHCb
LHCb-Collaboration, R. Aaij *et al.*, JINST **10** (2015) 02, P02007.
- First observations of the rare decays $B^+ \rightarrow K^+ \pi^+ \pi^- \mu^+ \mu^-$ and $B^+ \rightarrow \phi K^+ \mu^+ \mu^-$
LHCb-Collaboration, R. Aaij *et al.*, JHEP **1410** (2014) 064.
- Measurement of CP asymmetries in the decays $B^0 \rightarrow K^{*0} \mu^+ \mu^-$ and $B^+ \rightarrow K^+ \mu^+ \mu^-$
LHCb-Collaboration, R. Aaij *et al.*, JHEP **1409** (2014) 177.
- First observation of a baryonic B_c^+ decay
LHCb-Collaboration, R. Aaij *et al.*, Phys. Rev. Lett. **113** (2014) 15, 152003.
- Measurement of the $\bar{B}^0 - B^0$ and $\bar{B}_s^0 - B_s^0$ production asymmetries in pp collisions at $\sqrt{s} = 7$ TeV
LHCb-Collaboration, R. Aaij *et al.*, Phys. Lett. B **739** (2014) 218.
- Measurement of CP violation parameters in $B^0 \rightarrow DK^{*0}$ decays
LHCb-Collaboration, R. Aaij *et al.*, Phys. Rev. D **90** (2014) 11, 112002.
- Study of χ_b meson production in pp collisions at $\sqrt{s} = 7$ and 8 TeV and observation of the decay $\chi_b(3P) \rightarrow Y(3S)\gamma$
LHCb-Collaboration, R. Aaij *et al.*, Eur. Phys. J. C **74** (2014) 10, 3092.
- 92 - Dalitz plot analysis of $B_s^0 \rightarrow \bar{D}^0 K^- \pi^+$ decays
LHCb-Collaboration, R. Aaij *et al.*, Phys. Rev. D **90** (2014) 7, 072003.
- Observation of $B_s^0 \rightarrow K^{*\pm} K^\mp$ and evidence for $B_s^0 \rightarrow K^{*-} \pi^+$ decays
LHCb-Collaboration, R. Aaij *et al.*, New J. Phys. **16** (2014) 12, 123001.
- Observation of overlapping spin-1 and spin-3 $\bar{D}^0 K^-$ resonances at mass $2.86 \text{ GeV}/c^2$
LHCb-Collaboration, R. Aaij *et al.*, Phys. Rev. Lett. **113** (2014) 162001.
- Measurement of CP violation and constraints on the CKM angle γ in $B^\pm \rightarrow DK^\pm$ with $D \rightarrow K_S^0 \pi^+ \pi^-$ decays
LHCb-Collaboration, R. Aaij *et al.*, Nucl. Phys. B **888** (2014) 169.
- Measurement of CP asymmetry in $B_s^0 \rightarrow D_s^\mp K^\pm$ decays
LHCb-Collaboration, R. Aaij *et al.*, JHEP **1411** (2014) 060.
- Observation of charmonium pairs produced exclusively in pp collisions
LHCb-Collaboration, R. Aaij *et al.*, J. Phys. G **41** (2014) 11, 115002.
- Evidence for CP violation in $B^+ \rightarrow p \bar{p} K^+$ decays
LHCb-Collaboration, R. Aaij *et al.*, Phys. Rev. Lett. **113** (2014) 14, 141801.
- Measurement of the \bar{B}_s^0 meson lifetime in $D_s^+ \pi^-$ decays
LHCb-Collaboration, R. Aaij *et al.*, Phys. Rev. Lett. **113** (2014) 17, 172001.
- Measurement of CP violation in $B_s^0 \rightarrow \phi \phi$ decays
LHCb-Collaboration, R. Aaij *et al.*, Phys. Rev. D **90** (2014) 5, 052011.
- Measurement of the ratio of B_c^+ branching fractions to $J/\psi \pi^+$ and $J/\psi \mu^+ \nu_\mu$
LHCb-Collaboration, R. Aaij *et al.*, Phys. Rev. D **90** (2014) 3, 032009.
- Effective lifetime measurements in the $B_s^0 K^+ K^-, B^0 K^+$ and $B_s^0 K$ decays
LHCb-Collaboration, R. Aaij *et al.*, Phys. Lett. B **736** (2014) 446.
- Test of lepton universality using $B^+ \rightarrow K^+ \ell^+ \ell^-$ decays
LHCb-Collaboration, R. Aaij *et al.*, Phys. Rev. Lett. **113** (2014) 15, 151601.

- First measurement of the charge asymmetry in beauty-quark pair production
LHCb-Collaboration, R. Aaij *et al.*, Phys. Rev. Lett. **113** (2014) 8, 082003.
- Observation of Z production in proton-lead collisions at LHCb
LHCb-Collaboration, R. Aaij *et al.*, JHEP **1409** (2014) 030.
- Search for CP violation in $D^\pm \rightarrow K_S^0 K^\pm$ and $D_s^\pm \rightarrow K_S^0 \pi^\pm$ decays
LHCb-Collaboration, R. Aaij *et al.*, JHEP **1410** (2014) 25.
- Observation of the $\Lambda_b^0 \rightarrow J/\psi p \pi^-$ decay
LHCb-Collaboration, R. Aaij *et al.*, JHEP **1407** (2014) 103.
- Precision measurement of the mass and lifetime of the Ξ_b^0 baryon
LHCb-Collaboration, R. Aaij *et al.*, Phys. Rev. Lett. **113** (2014) 032001.
- Study of the kinematic dependences of Λ_b^0 production in pp collisions and a measurement of the $\Lambda_b^0 \rightarrow \Lambda_c^+ \pi^-$ branching fraction
LHCb-Collaboration, R. Aaij *et al.*, JHEP **1408** (2014) 143.
- Study of Y production and cold nuclear matter effects in pPb collisions at $\sqrt{s_{NN}}=5$ TeV
LHCb-Collaboration, R. Aaij *et al.*, JHEP **1407** (2014) 094.
- Measurement of the CP-violating phase ϕ_s in $\bar{B}_s^0 \rightarrow J/\psi \pi^+ \pi^-$ decays
LHCb-Collaboration, R. Aaij *et al.*, Phys. Lett. B **736** (2014) 186.
- Observation of the $B_s^0 \rightarrow J/\psi K_S^0 K^\pm \pi^\mp$ decay
LHCb-Collaboration, R. Aaij *et al.*, JHEP **1407** (2014) 140.
- Measurement of CP asymmetry in $D^0 \rightarrow K^- K^+$ and $D^0 \rightarrow \pi^- \pi^+$ decays
LHCb-Collaboration, R. Aaij *et al.*, JHEP **1407** (2014) 041.
- Measurement of the Ξ_b^- and Ω_b^- baryon lifetimes
LHCb-Collaboration, R. Aaij *et al.*, Phys. Lett. B **736** (2014) 154.
- Measurement of the resonant and CP components in $\bar{B}^0 \rightarrow J/\psi \pi^+ \pi^-$ decays
LHCb-Collaboration, R. Aaij *et al.*, Phys. Rev. D **90** (2014) 1, 012003.
- Observation of the resonant character of the $Z(4430)^-$ state
LHCb-Collaboration, R. Aaij *et al.*, Phys. Rev. Lett. **112** (2014) 22, 222002.
- Evidence for the decay $B_c^+ \rightarrow J/\psi 3\pi^+ 2\pi^-$
LHCb-Collaboration, R. Aaij *et al.*, JHEP **1405** (2014) 148.
- Evidence for the decay $X(3872) \rightarrow \psi(2S)\gamma$
LHCb-Collaboration, R. Aaij *et al.*, Nucl. Phys. B **886** (2014) 665.
- Angular analysis of charged and neutral $B \rightarrow K \mu^+ \mu^-$ decays
LHCb-Collaboration, R. Aaij *et al.*, JHEP **1405** (2014) 082.
- Differential branching fractions and isospin asymmetries of $B \rightarrow K^{(*)} \mu^+ \mu^-$ decays
LHCb-Collaboration, R. Aaij *et al.*, JHEP **1406** (2014) 133.
- Study of beauty hadron decays into pairs of charm hadrons
LHCb-Collaboration, R. Aaij *et al.*, Phys. Rev. Lett. **112** (2014) 202001.
- Measurement of polarization amplitudes and CP asymmetries in $B^0 \rightarrow \phi K^*(892)^0$
LHCb-Collaboration, R. Aaij *et al.*, JHEP **1405** (2014) 069.
- Measurement of $\psi(2S)$ polarisation in pp collisions at $\sqrt{s} = 7$ TeV
LHCb-Collaboration, R. Aaij *et al.*, Eur. Phys. J. C **74** (2014) 5, 2872.

- Observation of photon polarization in the $b \rightarrow s\gamma$ transition
LHCb-Collaboration, R. Aaij *et al.*, Phys. Rev. Lett. **112** (2014) 16, 161801.
- Measurement of resonant and CP components in $\bar{B}_s^0 \rightarrow J/\psi\pi^+\pi^-$ decays
LHCb-Collaboration, R. Aaij *et al.*, Phys. Rev. D **89** (2014) 9, 092006.
- Precision measurement of the ratio of the Λ_b^0 to \bar{B}^0 lifetimes
LHCb-Collaboration, R. Aaij *et al.*, Phys. Lett. B **734** (2014) 122.
- Measurement of charged particle multiplicities and densities in pp collisions at $\sqrt{s} = 7$ TeV in the forward region
LHCb-Collaboration, R. Aaij *et al.*, Eur. Phys. J. C **74** (2014) 5, 2888.
- A study of CP violation in $B^\pm \rightarrow DK^\pm$ and $B^\pm \rightarrow D\pi^\pm$ decays with $D \rightarrow K_S^0 K^\pm \pi^\mp$ final states
LHCb-Collaboration, R. Aaij *et al.*, Phys. Lett. B **733** (2014) 36.
- Measurements of the B^+, B^0, B_s^0 meson and Λ_b^0 baryon lifetimes
LHCb-Collaboration, R. Aaij *et al.*, R. Aaij *et al.* [LHCb Collaboration], JHEP **1404** (2014) 114.
- Measurement of Y production in pp collisions at $\sqrt{s} = 2.76$ TeV
LHCb-Collaboration, R. Aaij *et al.*, Eur. Phys. J. C **74** (2014) 4, 2835.
- Searches for Λ_b^0 and Ξ_b^0 decays to $K_S^0 p \pi^-$ and $K_S^0 p K^-$ final states with first observation of the $\Lambda_b^0 \rightarrow K_S^0 p \pi^-$ decay
LHCb-Collaboration, R. Aaij *et al.*, JHEP **1404** (2014) 087.
- Measurement of the B_c^+ meson lifetime using $B_c^+ \rightarrow J/\psi \mu^+ \nu_\mu X$ decays
LHCb-Collaboration, R. Aaij *et al.*, Eur. Phys. J. C **74** (2014) 5, 2839.
- 94 - Observation of associated production of a Z boson with a D meson in the forward region
LHCb-Collaboration, R. Aaij *et al.*, JHEP **1404** (2014) 091.
- Observation of $B_s^0 \rightarrow J/\psi f_1(1285)$ decays and measurement of the $f_1(1285)$ mixing angle
LHCb-Collaboration, R. Aaij *et al.*, Phys. Rev. Lett. **112** (2014) 9, 091802.

LHCb articles in press

- First observation and measurement of the branching fraction for the decay $B_s^0 \rightarrow D_s^{*\mp} K^\pm$
LHCb-Collaboration, R. Aaij *et al.*, arXiv:1503.09086 [hep-ex].
- Observation of the $B^0 \rightarrow \rho^0 \rho^0$ decay from an amplitude analysis of $B^0 \rightarrow (\pi^+ \pi^-)(\pi^+ \pi^-)$ decays
LHCb-Collaboration, R. Aaij *et al.*, arXiv:1503.07770 [hep-ex].
- Observation of the $B_s^0 \rightarrow \eta' \eta'$ decay
LHCb-Collaboration, R. Aaij *et al.*, arXiv:1503.07483 [hep-ex].
- Differential branching fraction and angular analysis of $\Lambda_b^0 \rightarrow \Lambda^0 \mu^+ \mu^-$ decays
LHCb-Collaboration, R. Aaij *et al.*, arXiv:1503.07138 [hep-ex].
- Observation of the decay $\bar{B}_s^0 \rightarrow \psi(2S) K^+ \pi^-$
LHCb-Collaboration, R. Aaij *et al.*, arXiv:1503.07112 [hep-ex].
- Measurement of CP violation in $B^0 \rightarrow J/\psi K_S^0$ decays
LHCb-Collaboration, R. Aaij *et al.*, arXiv:1503.07089 [hep-ex].
- Measurement of the time-dependent CP asymmetries in $B_s^0 \rightarrow J/\psi K_S^0$,
LHCb-Collaboration, R. Aaij *et al.*, arXiv:1503.07055 [hep-ex].
- Measurement of CP asymmetries and polarisation fractions in $B_s^0 \rightarrow K^{*0} \bar{K}^{*0}$ decays
LHCb-Collaboration, R. Aaij *et al.*, arXiv:1503.05362 [hep-ex].
- First observation and amplitude analysis of the $B^- \rightarrow D^+ K^- \pi^-$ decay
LHCb-Collaboration, R. Aaij *et al.*, arXiv:1503.02995 [hep-ex].

- Measurement of forward $Z \rightarrow e^+e^-$ production at $\sqrt{s} = 8$ TeV
LHCb-Collaboration, R. Aaij *et al.*, arXiv:1503.00963 [hep-ex].
- Precise measurements of the properties of the $B_1(5721)^{0,+}$ and $B_2^*(5747)^{0,+}$ states and observation of $B^{+,0}\pi^{-,+}$ mass structures
LHCb-Collaboration, R. Aaij *et al.*, arXiv:1502.02638 [hep-ex]
- Measurement of indirect CP asymmetries in $D^0 \rightarrow K^-K^+$ and $D^0 \rightarrow \pi^-\pi^+$ decays
LHCb-Collaboration, R. Aaij *et al.*, arXiv:1501.06777 [hep-ex].
- Angular analysis of the $B^0 \rightarrow K^{*0}e^+e^-$ decay in the low- q^2 region
LHCb-Collaboration, R. Aaij *et al.*, arXiv:1501.03038 [hep-ex].
- Determination of the branching fractions of $B_s^0 \rightarrow D_s^\mp K^\pm$ and $B^0 \rightarrow D_s^- K^+$
LHCb-Collaboration, R. Aaij *et al.*, arXiv:1412.7654 [hep-ex].
- Search for long-lived particles decaying to jet pairs
LHCb-Collaboration, R. Aaij *et al.*, arXiv:1412.3021 [hep-ex].
- Observation of the rare $B_s^0 \rightarrow \mu^+\mu^-$ decay from the combined analysis of CMS and LHCb data
LHCb-Collaboration, R. Aaij *et al.*, arXiv:1411.4413 [hep-ex].
- Measurement of the $\eta_c(1S)$ production cross-section in proton-proton collisions via the decay $\eta_c(1S) \rightarrow p\bar{p}$
LHCb-Collaboration, R. Aaij *et al.*, arXiv:1409.3612 [hep-ex].

Conference contributions

- Katharina Müller: LHCb results in proton-nucleus collisions at the LHC
Kruger 2014: The International Workshop on Discovery Physics at the LHC, 1 - 5 Dec 2014, Skukuza, South Africa
- Katharina Müller: Central exclusive quarkonia production in the forward region at LHCb
Kruger 2014: The International Workshop on Discovery Physics at the LHC, 1 - 5 Dec 2014, Skukuza, South Africa
- Christian Elsasser: Proton-Ion Physics with LHCb - Results and Prospects
The 2nd International Conference on the Initial Stages in High-Energy Nuclear Collisions, 3 - 7 Dec 2014, Napa, California, U.S.A.
- Albert Bursche: Associated Boson Production in the forward acceptance
6th International Workshop on Multiple Partonic Interactions at the LHC, 3 - 17 Nov 2014, Krakow, Poland
- Marcin Chrzęszcz: Lepton flavour violation in tau decays at LHCb
The 13th International Workshop on Tau Lepton Physics, 15-19 Sep, 2014, Aachen, Germany
- Espen Bowen: Vertexing and tracking software at LHCb
VERTEX2014, 15-19 Sep 2014, Macha Lake, The Czech Republic
- Federica Lionetto: LHCb upgrade : Upstream Tracker
VERTEX2014, 15-19 Sep 2014, Macha Lake, The Czech Republic
- Christian Elsasser: LHCb Silicon Detectors: Operational Experience and Run I \rightarrow Run II Transition
VERTEX2014, 15-19 Sep 2014, Macha Lake, The Czech Republic
- Marcin Chrzęszcz: Lepton flavour and number violation measurements at LHCb
XIIth International Conference on Heavy Quarks and Leptons 2014, 25 - 29 Aug 2014, Mainz, Germany
- Marcin Chrzęszcz: Rare B and charm decays at LHCb
XIIth International Conference on Heavy Quarks and Leptons 2014, 25 - 29 Aug 2014, Mainz, Germany
- Katharina Müller: Measurements with electroweak bosons at LHCb
20th Particles and Nuclei International Conference, 24 - 29 Aug 2014, Hamburg, Germany

- Katharina Müller: LHCb results in proton-nucleus collisions at the LHC
20th Particles and Nuclei International Conference, 24 - 29 Aug 2014, Hamburg, Germany
- Katharina Müller: Electroweak and central exclusive measurements in the forward region at LHCb
Seminar, 8 Jul 2014, Heidelberg, Germany
- Olaf Steinkamp: The LHCb Upgrades
Rencontres du Vietnam 2014: Physics at LHC and beyond, 10 - 17 Aug 2014, Quy Nhon, Vietnam
- Marco Tresch: Electroweak penguin decays to leptons at LHCb
10th Rencontres du Vietnam - Flavour Physics Conference, 27 Jul - 2 Aug 2014, Quy Nhon, Vietnam
- Albert Bursche: QCD and forward physics at LHCb
Low x workshop, 17 - 21 Jun 2014, Kyoto, Japan
- Federica Lionetto: Associated vector boson production in the forward region
Hadron Structure and QCD 2014, 30 Jun - 4 Jul 2014, Gatchina, Russia
- Christian Elsasser: Performance of the LHCb Silicon Tracker during LHC Run I
SPS 2014, 30 Jun - 2 Jul 2014, Fribourg, Switzerland
- Christian Elsasser: Heavy Ion Physics at LHCb
Large Hadron Collider Physics (LHCP) Conference, 2 - 7 Jun 2014, New York, USA
- Katharina Müller: QCD and electroweak measurements in the forward region at LHCb
26th Rencontres de Blois on Particle Physics and Cosmology, 18 - 23 May 2014, Blois, France
- Marcin Chrzęszcz: Searches for New Physics with LHCb
26th Rencontres de Blois on Particle Physics and Cosmology, 18 - 23 May 2014, Blois, France

PhD theses

- The Rare Decays $B_{(s)}^0 \rightarrow \mu^+ \mu^-$ and Z Boson Production at LHCb and Radiation Damage in its Silicon Tracker
Christian Elsasser, PhD Thesis, Universität Zürich, 2014
- Low-Mass Drell-Yan Cross-Section Measurements
Nicola Chiapolini, PhD Thesis, Universität Zürich, 2014
- Z Bosons in LHCb
Albert Bursche, PhD Thesis, Universität Zürich, 2014
- Search for Charged Lepton Flavour Violation at LHCb experiment
M. Chrzęszcz, PhD Thesis, Henryk Niewodniczanski Institute of Nuclear Physics, Kraków, 2014
- Advances in Solar Radiometry
Markus Suter, PhD Thesis, Universität Zürich, 2014

19.1.9 CMS

Articles

- Search for physics beyond the standard model in events with two leptons, jets, and missing transverse momentum in pp collisions at $\sqrt{s} = 8$ TeV
V. Khachatryan *et al.* [CMS Collaboration], JHEP **1504** (2015) 124.
- Measurement of the Z production cross section in pp collisions at 8 TeV and search for anomalous triple gauge boson couplings
V. Khachatryan *et al.* [CMS Collaboration], JHEP **1504** (2015) 164.

- Search for supersymmetry using razor variables in events with b -tagged jets in pp collisions at $\sqrt{s} = 8$ TeV
V. Khachatryan *et al.* [CMS Collaboration], Phys. Rev. D **91** (2015) 052018.
- Search for decays of stopped long-lived particles produced in proton-proton collisions at $\sqrt{s} = 8$ TeV
V. Khachatryan *et al.* [CMS Collaboration], Eur. Phys. J. C **75** (2015) 4, 151.
- Search for resonances and quantum black holes using dijet mass spectra in proton-proton collisions at $\sqrt{s} = 8$ TeV
V. Khachatryan *et al.* [CMS Collaboration], Phys. Rev. D **91** (2015) 5, 052009.
- Search for physics beyond the standard model in dilepton mass spectra in proton-proton collisions at $\sqrt{s} = 8$ TeV
V. Khachatryan *et al.* [CMS Collaboration], JHEP **1504** (2015) 025.
- Searches for supersymmetry based on events with b jets and four W bosons in pp collisions at 8 TeV
V. Khachatryan *et al.* [CMS Collaboration], Phys. Lett. B **745** (2015) 5.
- Measurement of the inclusive 3-jet production differential cross section in proton-proton collisions at 7 TeV and determination of the strong coupling constant in the TeV range
V. Khachatryan *et al.* [CMS Collaboration], Eur. Phys. J. C **75** (2015) 5, 186.
- Measurements of differential and double-differential Drell-Yan cross sections in proton-proton collisions at 8 TeV
V. Khachatryan *et al.* [CMS Collaboration], Eur. Phys. J. C **75** (2015) 4, 147.
- Search for stealth supersymmetry in events with jets, either photons or leptons, and low missing transverse momentum in pp collisions at 8 TeV
V. Khachatryan *et al.* [CMS Collaboration], Phys. Lett. B **743** (2015) 503.
- Search for long-lived particles that decay into final states containing two electrons or two muons in proton-proton collisions at $\sqrt{s} = 8$ TeV
V. Khachatryan *et al.* [CMS Collaboration], Phys. Rev. D **91** (2015) 5, 052012.
- Search for long-lived neutral particles decaying to quark-antiquark pairs in proton-proton collisions at $\sqrt{s} = 8$ TeV
V. Khachatryan *et al.* [CMS Collaboration], Phys. Rev. D **91** (2015) 1, 012007.
- Search for disappearing tracks in proton-proton collisions at $\sqrt{s} = 8$ TeV
V. Khachatryan *et al.* [CMS Collaboration], JHEP **1501** (2015) 096.
- Performance of the CMS missing transverse momentum reconstruction in pp data at $\sqrt{s} = 8$ TeV
V. Khachatryan *et al.* [CMS Collaboration], JINST **10** (2015) 02, P02006.
- Search for a standard model-like Higgs boson in the $\gamma\gamma$ and e^+e^- decay channels at the LHC
V. Khachatryan *et al.* [CMS Collaboration], Phys. Lett. B **744** (2015) 184.
- Study of vector boson scattering and search for new physics in events with two same-sign leptons and two jets
V. Khachatryan *et al.* [CMS Collaboration], Phys. Rev. Lett. **114** (2015) 5, 051801.
- Measurement of the ratio of the production cross sections times branching fractions of $B_c^\pm \rightarrow J/\psi\pi^\pm$ and $B^\pm \rightarrow J/\psi K^\pm$ and $\mathcal{B}(B_c^\pm \rightarrow J/\psi\pi^\pm\pi^\pm\pi^\mp)/\mathcal{B}(B_c^\pm \rightarrow J/\psi\pi^\pm)$ in pp collisions at $\sqrt{s} = 7$ TeV
V. Khachatryan *et al.* [CMS Collaboration], JHEP **1501** (2015) 063.
- Study of Z production in PbPb and pp collisions at $\sqrt{s_{NN}} = 2.76$ TeV in the dimuon and dielectron decay channels
S. Chatrchyan *et al.* [CMS Collaboration], JHEP **1503** (2015) 022.
- Identification techniques for highly boosted W bosons that decay into hadrons
V. Khachatryan *et al.* [CMS Collaboration], JHEP **1412** (2014) 017.
- Measurement of electroweak production of two jets in association with a Z boson in proton-proton collisions at $\sqrt{s} = 8$ TeV
V. Khachatryan *et al.* [CMS Collaboration], Eur. Phys. J. C **75** (2015) 2, 66.
- Searches for heavy Higgs bosons in two-Higgs-doublet models and for $t\bar{t}ch$ decay using multilepton and diphoton final states in pp collisions at 8 TeV
V. Khachatryan *et al.* [CMS Collaboration], Phys. Rev. D **90** (2014) 112013.

- Measurement of Prompt $\psi(2S) \rightarrow J/\psi$ Yield Ratios in Pb-Pb and $p - p$ Collisions at $\sqrt{s_{NN}} = 2.76$ TeV
V. Khachatryan *et al.* [CMS Collaboration], Phys. Rev. Lett. **113** (2014) 26, 262301.
- Measurement of the W boson helicity in events with a single reconstructed top quark in pp collisions at $\sqrt{s} = 8$ TeV
V. Khachatryan *et al.* [CMS Collaboration], JHEP **1501** (2015) 053.
- Search for Monotop Signatures in Proton-Proton Collisions at $\sqrt{s} = 8$ TeV
V. Khachatryan *et al.* [CMS Collaboration], Phys. Rev. Lett. **114** (2015) 10, 101801.
- Search for standard model production of four top quarks in the lepton + jets channel in pp collisions at $\sqrt{s} = 8$ TeV
V. Khachatryan *et al.* [CMS Collaboration], JHEP **1411** (2014) 154.
- Measurement of the production cross section ratio $\sigma(\text{chi}[b2](1P)) / \sigma(\text{chi}[b1](1P))$ in pp collisions at $\sqrt{s} = 8$ TeV
V. Khachatryan *et al.* [CMS Collaboration], Phys. Lett. B **743** (2015) 383.
- Search for Displaced Supersymmetry in events with an electron and a muon with large impact parameters
V. Khachatryan *et al.* [CMS Collaboration], Phys. Rev. Lett. **114** (2015) 6, 061801.
- Long-range two-particle correlations of strange hadrons with charged particles in pPb and PbPb collisions at LHC energies
V. Khachatryan *et al.* [CMS Collaboration], Phys. Lett. B **742** (2015) 200.
- Searches for electroweak neutralino and chargino production in channels with Higgs, Z, and W bosons in pp collisions at 8 TeV
V. Khachatryan *et al.* [CMS Collaboration], Phys. Rev. D **90** (2014) 9, 092007.
- Search for neutral MSSM Higgs bosons decaying to a pair of tau leptons in pp collisions
V. Khachatryan *et al.* [CMS Collaboration], JHEP **1410** (2014) 160.
- Measurements of jet multiplicity and differential production cross sections of Z+ jets events in proton-proton collisions at $\sqrt{s} = 7$ TeV
V. Khachatryan *et al.* [CMS Collaboration], Phys. Rev. D **91** (2015) 5, 052008.
- Search for the associated production of the Higgs boson with a top-quark pair
V. Khachatryan *et al.* [CMS Collaboration], JHEP **1409** (2014) 087 [JHEP **1410** (2014) 106].
- Search for pair production of third-generation scalar leptoquarks and top squarks in proton-proton collisions at $\sqrt{s} = 8$ TeV
V. Khachatryan *et al.* [CMS Collaboration], Phys. Lett. B **739** (2014) 229.
- Measurement of the $t\bar{t}$ production cross section in pp collisions at $\sqrt{s} = 8$ TeV in dilepton final states containing one τ lepton
V. Khachatryan *et al.* [CMS Collaboration], Phys. Lett. B **739** (2014) 23.
- Search for heavy neutrinos and W bosons with right-handed couplings in proton-proton collisions at $\sqrt{s} = 8$ TeV
V. Khachatryan *et al.* [CMS Collaboration], Eur. Phys. J. C **74** (2014) 11, 3149.
- Search for new resonances decaying via WZ to leptons in proton-proton collisions at $\sqrt{s} = 8$ TeV
V. Khachatryan *et al.* [CMS Collaboration], Phys. Lett. B **740** (2015) 83.
- Study of hadronic event-shape variables in multijet final states in pp collisions at $\sqrt{s} = 7$ TeV
V. Khachatryan *et al.* [CMS Collaboration], JHEP **1410** (2014) 87.
- Observation of the diphoton decay of the Higgs boson and measurement of its properties
V. Khachatryan *et al.* [CMS Collaboration], Eur. Phys. J. C **74** (2014) 10, 3076.
- Measurement of top quark-antiquark pair production in association with a W or Z boson in pp collisions at $\sqrt{s} = 8$ TeV
V. Khachatryan *et al.* [CMS Collaboration], Eur. Phys. J. C **74** (2014) 9, 3060.
- Differential cross section measurements for the production of a W boson in association with jets in proton-proton collisions at $\sqrt{s} = 7$ TeV
V. Khachatryan *et al.* [CMS Collaboration], Phys. Lett. B **741** (2015) 12.

- Search for excited quarks in the γ +jet final state in proton-proton collisions at $\sqrt{s} = 8$ TeV
V. Khachatryan *et al.* [CMS Collaboration], Phys. Lett. B **738** (2014) 274.
- Measurement of jet fragmentation in PbPb and pp collisions at $\sqrt{s_{NN}} = 2.76$ TeV
S. Chatrchyan *et al.* [CMS Collaboration], Phys. Rev. C **90** (2014) 2, 024908.
- Measurement of prompt J/ψ pair production in pp collisions at $\sqrt{s} = 7$ TeV
V. Khachatryan *et al.* [CMS Collaboration], JHEP **1409** (2014) 094.
- Measurement of the ratio of inclusive jet cross sections using the anti- k_T algorithm with radius parameters $R=0.5$ and 0.7 in pp collisions at $\sqrt{s} = 7$ TeV
S. Chatrchyan *et al.* [CMS Collaboration], Phys. Rev. D **90** (2014) 7, 072006.
- Measurement of the $pp \rightarrow ZZ$ production cross section and constraints on anomalous triple gauge couplings in four-lepton final states at $\sqrt{s} = 8$ TeV
V. Khachatryan *et al.* [CMS Collaboration], Phys. Lett. B **740** (2015) 250.
- Search for jet extinction in the inclusive jet- p_t spectrum from proton-proton collisions at $\sqrt{s} = 8$ TeV
V. Khachatryan *et al.* [CMS Collaboration], Phys. Rev. D **90** (2014) 3, 032005.
- Searches for electroweak production of charginos, neutralinos, and sleptons decaying to leptons and W, Z, and Higgs bosons in pp collisions at 8 TeV
V. Khachatryan *et al.* [CMS Collaboration], Eur. Phys. J. C **74** (2014) 9, 3036.
- Measurement of differential cross sections for the production of a pair of isolated photons in pp collisions at $\sqrt{s} = 7$ TeV
S. Chatrchyan *et al.* [CMS Collaboration], Eur. Phys. J. C **74** (2014) 11, 3129.
- Description and performance of track and primary-vertex reconstruction with the CMS tracker
S. Chatrchyan *et al.* [CMS Collaboration], JINST **9** (2014) 10, P10009.
- Search for supersymmetry with razor variables in pp collisions at $\sqrt{s}=7$ TeV
S. Chatrchyan *et al.* [CMS Collaboration], Phys. Rev. D **90** (2014) 11, 112001.
- Search for top-squark pairs decaying into Higgs or Z bosons in pp collisions at $\sqrt{s}=8$ TeV
V. Khachatryan *et al.* [CMS Collaboration], Phys. Lett. B **736** (2014) 371.
- Constraints on the Higgs boson width from off-shell production and decay to Z-boson pairs
V. Khachatryan *et al.* [CMS Collaboration], Phys. Lett. B **736** (2014) 64.
- Search for massive resonances decaying into pairs of boosted bosons in semi-leptonic final states at $\sqrt{s} = 8$ TeV
V. Khachatryan *et al.* [CMS Collaboration], JHEP **1408** (2014) 174.
- Search for massive resonances in dijet systems containing jets tagged as W or Z boson decays in pp collisions at $\sqrt{s} = 8$ TeV
V. Khachatryan *et al.* [CMS Collaboration], JHEP **1408** (2014) 173.
- Measurement of pseudorapidity distributions of charged particles in proton-proton collisions at $\sqrt{s} = 8$ TeV by the CMS and TOTEM experiments
S. Chatrchyan *et al.* [CMS Collaboration], Eur. Phys. J. C **74** (2014) 10, 3053.
- Search for anomalous production of events with three or more leptons in pp collisions at $\sqrt{s} = 8$ TeV
S. Chatrchyan *et al.* [CMS Collaboration], Phys. Rev. D **90** (2014) 032006.
- Search for $WW\gamma$ and $WZ\gamma$ production and constraints on anomalous quartic gauge couplings in pp collisions at $\sqrt{s} = 8$ TeV
S. Chatrchyan *et al.* [CMS Collaboration], Phys. Rev. D **90** (2014) 3, 032008.
- Measurement of jet multiplicity distributions in $t\bar{t}$ production in pp collisions at $\sqrt{s} = 7$ TeV
S. Chatrchyan *et al.* [CMS Collaboration], Eur. Phys. J. C **74** (2014) 8, 3014.

- Measurement of the ratio $B(t \rightarrow Wb)/B(t \rightarrow Wq)$ in pp collisions at $\sqrt{s} = 8$ TeV
V. Khachatryan *et al.* [CMS Collaboration], Phys. Lett. B **736** (2014) 33.
- Search for invisible decays of Higgs bosons in the vector boson fusion and associated ZH production modes
S. Chatrchyan *et al.* [CMS Collaboration], Eur. Phys. J. C **74** (2014) 2980.
- Measurement of the t-channel single-top-quark production cross section and of the $|V_{tb}|$ CKM matrix element in pp collisions at $\sqrt{s} = 8$ TeV
V. Khachatryan *et al.* [CMS Collaboration], JHEP **1406** (2014) 090.
- Measurement of WZ and ZZ production in pp collisions at $\sqrt{s} = 8$ TeV in final states with b-tagged jets
S. Chatrchyan *et al.* [CMS Collaboration], Eur. Phys. J. C **74** (2014) 8, 2973.
- Alignment of the CMS tracker with LHC and cosmic ray data
S. Chatrchyan *et al.* [CMS Collaboration], JINST **9** (2014) P06009.
- Search for new physics in the multijet and missing transverse momentum final state in proton-proton collisions at $\sqrt{s} = 8$ TeV
S. Chatrchyan *et al.* [CMS Collaboration], JHEP **1406** (2014) 055.
- Measurements of the $t\bar{t}$ charge asymmetry using the dilepton decay channel in pp collisions at $\sqrt{s} = 7$ TeV
S. Chatrchyan *et al.* [CMS Collaboration], JHEP **1404** (2014) 191.
- Search for $W' \rightarrow tb$ decays in the lepton + jets final state in pp collisions at $\sqrt{s} = 8$ TeV
S. Chatrchyan *et al.* [CMS Collaboration], JHEP **1405** (2014) 108.
- Measurement of the production cross sections for a Z boson and one or more b jets in pp collisions at $\sqrt{s} = 7$ TeV
S. Chatrchyan *et al.* [CMS Collaboration], JHEP **1406** (2014) 120.
- Measurement of inclusive W and Z boson production cross sections in pp collisions at $\sqrt{s} = 8$ TeV
S. Chatrchyan *et al.* [CMS Collaboration], Phys. Rev. Lett. **112** (2014) 191802.
- Evidence for the direct decay of the 125 GeV Higgs boson to fermions
S. Chatrchyan *et al.* [CMS Collaboration], Nature Phys. **10** (2014) 557.
- Evidence for the 125 GeV Higgs boson decaying to a pair of τ leptons
S. Chatrchyan *et al.* [CMS Collaboration], JHEP **1405** (2014) 104.
- Studies of dijet transverse momentum balance and pseudorapidity distributions in pPb collisions at $\sqrt{s_{NN}} = 5.02$ TeV
S. Chatrchyan *et al.* [CMS Collaboration], Eur. Phys. J. C **74** (2014) 7, 2951.
- Observation of the associated production of a single top quark and a W boson in pp collisions at $\sqrt{s} = 8$ TeV
S. Chatrchyan *et al.* [CMS Collaboration], Phys. Rev. Lett. **112** (2014) 23, 231802.
- Measurement of the $t\bar{t}$ production cross section in the dilepton channel in pp collisions at $\sqrt{s} = 8$ TeV
S. Chatrchyan *et al.* [CMS Collaboration], JHEP **1402** (2014) 024.
- Measurement of the production cross section for a W boson and two b jets in pp collisions at $\sqrt{s} = 7$ TeV
S. Chatrchyan *et al.* [CMS Collaboration], Phys. Lett. B **735** (2014) 204.
- Measurement of four-jet production in proton-proton collisions at $\sqrt{s} = 7$ TeV
S. Chatrchyan *et al.* [CMS Collaboration], Phys. Rev. D **89** (2014) 9, 092010.
- Event activity dependence of $Y(nS)$ production in $\sqrt{s_{NN}} = 5.02$ TeV pPb and $\sqrt{s} = 2.76$ TeV pp collisions
S. Chatrchyan *et al.* [CMS Collaboration], JHEP **1404** (2014) 103.
- Measurement of the muon charge asymmetry in inclusive $pp \rightarrow W + X$ production at $\sqrt{s} = 7$ TeV and an improved determination of light parton distribution functions
S. Chatrchyan *et al.* [CMS Collaboration], Phys. Rev. D **90** (2014) 3, 032004.
- Study of double parton scattering using $W + 2$ -jet events in proton-proton collisions at $\sqrt{s} = 7$ TeV
S. Chatrchyan *et al.* [CMS Collaboration], JHEP **1403** (2014) 032.

- Measurement of the properties of a Higgs boson in the four-lepton final state
S. Chatrchyan *et al.* [CMS Collaboration], Phys. Rev. D **89** (2014) 9, 092007.
- Evidence of b-Jet Quenching in PbPb Collisions at $\sqrt{s_{NN}} = 2.76$ TeV
S. Chatrchyan *et al.* [CMS Collaboration], Phys. Rev. Lett. **113** (2014) 13, 132301.
- Search for Flavor-Changing Neutral Currents in Top-Quark Decays $t \rightarrow Zq$ in pp Collisions at $\sqrt{s} = 8$ TeV
S. Chatrchyan *et al.* [CMS Collaboration], Phys. Rev. Lett. **112** (2014) 17, 171802.
- Search for top squark and higgsino production using diphoton Higgs boson decays
S. Chatrchyan *et al.* [CMS Collaboration], Phys. Rev. Lett. **112** (2014) 161802.
- Search for top-quark partners with charge 5/3 in the same-sign dilepton final state
S. Chatrchyan *et al.* [CMS Collaboration], Phys. Rev. Lett. **112** (2014) 17, 171801.
- Studies of azimuthal dihadron correlations in ultra-central PbPb collisions at $\sqrt{s_{NN}} = 2.76$ TeV
S. Chatrchyan *et al.* [CMS Collaboration], JHEP **1402** (2014) 088.
- Measurement of Higgs boson production and properties in the WW decay channel with leptonic final states
S. Chatrchyan *et al.* [CMS Collaboration], JHEP **1401** (2014) 096.
- Inclusive search for a vector-like T quark with charge $\frac{2}{3}$ in pp collisions at $\sqrt{s} = 8$ TeV
S. Chatrchyan *et al.* [CMS Collaboration], Phys. Lett. B **729** (2014) 149.
- Search for new physics in events with same-sign dileptons and jets in pp collisions at $\sqrt{s} = 8$ TeV
S. Chatrchyan *et al.* [CMS Collaboration], JHEP **1401** (2014) 163.
- Measurement of the triple-differential cross section for photon+jets production in proton-proton collisions at $\sqrt{s}=7$ TeV
S. Chatrchyan *et al.* [CMS Collaboration], JHEP **1406** (2014) 009.
- Probing color coherence effects in pp collisions at $\sqrt{s} = 7$ TeV
S. Chatrchyan *et al.* [CMS Collaboration], Eur. Phys. J. C **74** (2014) 6, 2901.
- Search for pair production of excited top quarks in the lepton + jets final state
S. Chatrchyan *et al.* [CMS Collaboration], JHEP **1406** (2014) 125.
- Search for supersymmetry in pp collisions at $\sqrt{s}=8$ TeV in events with a single lepton, large jet multiplicity, and multiple b jets
S. Chatrchyan *et al.* [CMS Collaboration], Phys. Lett. B **733** (2014) 328.
- Measurements of $t\bar{t}$ spin correlations and top-quark polarization using dilepton final states in pp collisions at $\sqrt{s} = 7$ TeV
S. Chatrchyan *et al.* [CMS Collaboration], Phys. Rev. Lett. **112** (2014) 18, 182001.
- Searches for light- and heavy-flavour three-jet resonances in pp collisions at $\sqrt{s} = 8$ TeV
S. Chatrchyan *et al.* [CMS Collaboration], Phys. Lett. B **730** (2014) 193.
- Measurement of higher-order harmonic azimuthal anisotropy in PbPb collisions at $\sqrt{s_{NN}} = 2.76$ TeV
S. Chatrchyan *et al.* [CMS Collaboration], Phys. Rev. C **89** (2014) 4, 044906.
- Measurement of the differential and double-differential Drell-Yan cross sections in proton-proton collisions at $\sqrt{s} = 7$ TeV
S. Chatrchyan *et al.* [CMS Collaboration], JHEP **1312** (2013) 030.
- Search for the standard model Higgs boson produced in association with a W or a Z boson and decaying to bottom quarks
S. Chatrchyan *et al.* [CMS Collaboration], Phys. Rev. D **89** (2014) 1, 012003.
- Search for baryon number violation in top-quark decays
S. Chatrchyan *et al.* [CMS Collaboration], Phys. Lett. B **731** (2014) 173.
- Measurement of associated W + charm production in pp collisions at $\sqrt{s} = 7$ TeV
S. Chatrchyan *et al.* [CMS Collaboration], JHEP **1402** (2014) 013.

- Modification of jet shapes in PbPb collisions at $\sqrt{s_{NN}} = 2.76$ TeV
S. Chatrchyan *et al.* [CMS Collaboration], Phys. Lett. B **730** (2014) 243.
- Observation of a peaking structure in the $J/\psi\phi$ mass spectrum from $B^\pm \rightarrow J/\psi\phi K^\pm$ decays
S. Chatrchyan *et al.* [CMS Collaboration], Phys. Lett. B **734** (2014) 261.
- Searches for new physics using the $t\bar{t}$ invariant mass distribution in pp collisions at $\sqrt{s}=8$ TeV
S. Chatrchyan *et al.* [CMS Collaboration], Phys. Rev. Lett. **111** (2013) 21, 211804, Phys. Rev. Lett. **112** (2014) 11, 119903.
- Measurement of the $W\gamma$ and $Z\gamma$ inclusive cross sections in pp collisions at $\sqrt{s} = 7$ TeV and limits on anomalous triple gauge boson couplings
S. Chatrchyan *et al.* [CMS Collaboration], Phys. Rev. D **89** (2014) 9, 092005.
- Measurement of the top-quark mass in all-jets $t\bar{t}$ events in pp collisions at $\sqrt{s}=7$ TeV
S. Chatrchyan *et al.* [CMS Collaboration], Eur. Phys. J. C **74** (2014) 4, 2758.
- Study of the production of charged pions, kaons, and protons in pPb collisions at $\sqrt{s_{NN}} = 5.02$ TeV
S. Chatrchyan *et al.* [CMS Collaboration], Eur. Phys. J. C **74** (2014) 6, 2847.
- Determination of the top-quark pole mass and strong coupling constant from the t t -bar production cross section in pp collisions at $\sqrt{s} = 7$ TeV
S. Chatrchyan *et al.* [CMS Collaboration], Phys. Lett. B **728** (2014) 496, Phys. Lett. B **728** (2014) 526.

Lectures and oral presentations

102

- Y. Yang: Search for dark matter in CMS
Workshop on Effective Theories and Dark Matter, March 16-27, 2015 - Heidelberg, Germany.
- D. Pinna: Dark Matter produced in association with top quark pair
Moriond Electroweak Interactions and Unified Theories, March 14-21, 2015 - La Thuile, Italy.
- F. Canelli: The top quark at 20
AEC Seminars on Particle Physics, February 25, 2015 - University of Bern, Switzerland.
- V. Chiochia: New heavy flavour results from CMS
Kruger 2014: The International Workshop on Discovery Physics at the LHC, December 1-5, 2014 - Kruger Parc, South Africa.
- J. Ngadiuba: Overview of di-bosons searches
CMS Exotica Workshop, November 12-14, 2014 - Madrid, Spain.
- F. Canelli: Beyond the standard model with top quarks
LBNL Research Progress Meeting, October 28, 2014 - Berkeley, California, US.
- A. De Cosa: DarkMatter B2G analyses: Preparation for Run2
CMS B2G Workshop, October 23-24, 2014 - Fermilab, Batavia, US.
- Y. Yang: Search for dark matter at the LHC
Seminar on particle and astrophysics, October 22, 2014 - University of Zurich, Switzerland.
- L. Caminada: Determination of the strange content of the proton using LHC data
Seminar on particle and astrophysics, October 8, 2014 - University of Zurich, Switzerland.
- F. Canelli: Searches with top quarks beyond the standard model
TOP 2014, September 29 - October 3, 2014 - Cannes, France.
- C. Lange: Beyond Standard Model Higgs
XXXIV Physics in Collision Symposium Bloomington, September 16-20, 2014 - Bloomington, Indiana, US.
- A. De Cosa: CMS pixel detector: Operational Experience and Run1 to Run2 transition
VERTEX2014, 15-19 Sep 2014, Macha Lake, The Czech Republic

- B. Kilminster: The shape of the Higgs Boson
Prospects and Precision of Higgs physics with 13 TeV at the LHC, September 14, 2014 - Firenze, Italy.
 - C. Galloni: Search for new bosons decaying to boosted tau and b pairs at CMS
PhD Seminar, September 11, 2014 - University of Zurich, Switzerland.
 - J. Ngadiuba: Search for new heavy bosons with boosted b-tagged jets in the final state with CMS
PhD Seminar, September 11, 2014 - University of Zurich, Switzerland.
 - D. Pinna: Search for Dark Matter associated top pair production in single-lepton channel with the CMS detector
PhD Seminar, September 11, 2014 - University of Zurich, Switzerland.
 - D. Salerno: Search for associated ttH production in the Hbb decay channel at CMS using the Matrix Element Method
PhD Seminar, September 11, 2014 - University of Zurich, Switzerland.
 - D. Pinna: CMS Search for Dark Matter produced in association with top quarks
DM@LHC conference, September 25-27, 2014 - Oxford, UK.
 - A. Hinzmann: Jet substructure measurements in ATLAS+CMS
BOOST 2014, August 18-22, 2014 - London, UK.
 - A. Hinzmann: Searches for exotic new physics in CMS
ICNFP 2014, July 28 - August 6, 2014 - Kolymbari, Greek.
 - M. Verzetti: Higgs boson decay channels with fermions
Higgs Hunting 2014 conference, July 21-23, 2014 - Orsay, France.
 - C. Galloni: Search for heavy resonances decaying into a pair of Higgs Bosons in the tau+ tau- b bbar final state at CMS
SPS Annual Meeting, July 1-2, 2014 - Fribourg, Switzerland.
 - D. Salerno: Search for associated t tbar H production in the H to bbar channel at CMS using the Matrix Element Method
SPS Annual Meeting, July 1-2, 2014 - Fribourg, Switzerland.
 - D. Pinna: Search for Dark Matter associated top pair production in single-lepton channel with the CMS detector
2014 EUROPEAN SCHOOL OF HIGH - ENERGY PHYSICS, 18 June - 1 July, 2014 - Garderen, Netherlands.
 - Y. Yang: Search for dark matter in CMS
20th International Symposium on Particles, Strings and Cosmology, 22-27 June, 2014 - Warsaw, Poland.
- PhD thesis
- Search for the Standard Model Higgs in Tau Decays in Association with a W Boson
M. Verzetti, PhD Thesis, Universität Zürich, CMS TS-2015/003.

19.2 Condensed matter

19.2.1 Superconductivity and Magnetism

Articles

- Pressure Effects in the Iron Chalcogenides
M. Bendele, E. Pomjakushina, K. Conder, R. Khasanov, and H. Keller, *J. Supercond. Nov. Magn.* **27**, 965 (2014).
- Negative Oxygen Isotope Effect on the Static Spin Stripe Order in $\text{La}_{2-x}\text{Ba}_x\text{CuO}_4$ ($x = 1/8$) Observed by Muon-Spin Rotation
Z. Guguchia, R. Khasanov, M. Bendele, E. Pomjakushina, K. Conder, A. Shengelaya, and H. Keller, *Phys. Rev. Lett.* **113**, 057002 (2014).
- Spin-lattice coupling induced weak dynamical magnetism in EuTiO_3 at high temperatures
Z. Guguchia, H. Keller, R.K. Kremer, J. Köhler, H. Luetkens, T. Goko, A. Amato, and A. Bussmann-Holder, *Phys. Rev. B* **90**, 064413 (2014).

- Effect of pressure-driven local structural rearrangement on the superconducting properties of $\text{FeSe}_{0.5}\text{Te}_{0.5}$
M. Bendele, Z. Guguchia, F. von Rohr, T. Irifune, T. Shinmei, I. Kantor, S. Pascarelli, B. Joseph, and C. Marini, *Phys. Rev. B* **90**, 174505 (2014).
- Superconductivity in a new layered bismuth oxyselenide: $\text{LaO}_{0.5}\text{F}_{0.5}\text{BiSe}_2$
A. Krzton-Maziopa, Z. Guguchia, E. Pomjakushina, V. Pomjakushin, R. Khasanov, H. Luetkens, P.K. Biswas, A. Amato, H. Keller, and K. Conder, *J. Phys.: Condens. Matter* **26**, 215702 (2014).
- The Unique Properties of Superconductivity in Cuprates
K.A. Müller, *J. Supercond. Nov. Magn.* **27**, 2163 (2014).
- Local disorder investigation in $\text{NiS}_{2-x}\text{Se}_x$ using Raman and Ni K-edge x-ray absorption Spectroscopies
C. Marini, B. Joseph, S. Caramazza, F. Capitani, M. Bendele, M. Mitrano, D. Chermisi, S. Mangialardo, B. Pal, M. Goyal, A. Iadecola, O. Mathon, S. Pascarelli, D.D. Sarma, and P. Postorino, *J. Phys.: Condens. Matter* **26**, 452201 (2014).
- Controlling the near-surface superfluid density in underdoped $\text{YBa}_2\text{Cu}_3\text{O}_{6+x}$ by photo-illumination
E. Stilp, A. Suter, T. Prokscha, Z. Salman, E. Morenzoni, H. Keller, P. Pahlke, R. Huehne, C. Bernhard, L. Ruixing, W.N. Hardy, D.A. Bonn, J.C. Baglo, and R.F. Kiefl, *Scientific Reports* **4**, 6250 (2014).
- Probing the multi gap behavior within '11' and '122' families of iron based superconductors: the μSR studies
R. Khasanov and Z. Guguchia, *Superconductor Science and Technology* **28**, 034003 (2015).
- Over Half a Century of Research in Oxides
K.A. Müller, *J. Supercond. Nov. Magn.* **28**, 739 (2015).
- The intrinsic heterogeneity of superconductivity in the cuprates
A. Shengelaya and K.A. Müller, *EPL* **109**, 27001 (2015).

104

PhD theses

- Photo-Induced Effects in Cuprate Systems
Evelyn Stilp, PhD Thesis, Physik-Institut, Universität Zürich, 2014.
- Structural and Magnetic Properties of the Insulating $T'-RE_2\text{CuO}_4$ Parent Compounds of Electron-Doped Superconductors
Gwendolyne Banasan Pascua, Physik-Institut, Universität Zürich, 2014.

Conference reports

- Oxygen isotope effects on the superconducting and magnetic states in the static stripe phase of $\text{La}_{2-x}\text{Ba}_x\text{CuO}_4$ ($x = 1/8$)
Z. Guguchia, R. Khasanov, M. Bendele, E. Pomjakushina, K. Conder, A. Shengelaya, and H. Keller, $\mu\text{SR}2014$, Grindelwald, Switzerland, June 1-6, 2014.
- Modifications of the Meissner screening profile due to illumination with visible light of underdoped $\text{YBa}_2\text{Cu}_3\text{O}_{7-\delta}$
E. Stilp, A. Suter, T. Prokscha, Z. Salman, E. Morenzoni, H. Keller, P. Pahlke, R. Huehne, C. Bernhard, L. Ruixing, W.N. Hardy, D.A. Bonn, J.C. Baglo, and R.F. Kiefl, $\mu\text{SR}2014$, Grindelwald, Switzerland, June 1-6, 2014.
- Influence of gold nanoparticles on the Meissner screening profile of $\text{YBa}_2\text{Cu}_3\text{O}_{7-\delta}$ thin films
E. Stilp, A. Suter, T. Prokscha, Z. Salman, E. Morenzoni, H. Keller, C. Katzer, F. Schmidl, and M. Döbeli, $\mu\text{SR}2014$, Grindelwald, Switzerland, June 1-6, 2014.
- Controlling the near-surface superfluid density in underdoped $\text{YBa}_2\text{Cu}_3\text{O}_{6+x}$ by photo-illumination
E. Stilp, A. Suter, T. Prokscha, Z. Salman, E. Morenzoni, H. Keller, P. Pahlke, R. Huehne, C. Bernhard, L. Ruixing, W.N. Hardy, D.A. Bonn, J.C. Baglo, and R.F. Kiefl, Annual Meeting of the Swiss Physical Society, Fribourg, Switzerland, June 30 - July 2, 2014.
- Tuning the static spin stripe phase and superconductivity in $\text{La}_{2-x}\text{Ba}_x\text{CuO}_4$ ($x = 1/8$) by hydrostatic pressure
Z. Guguchia, A. Maisuradze, G. Ghambashidze, R. Khasanov, A. Shengelaya, and H. Keller, *Condensed Matter in Paris*, Paris, France, August 24-29, 2014.

Invited lectures

- H. Keller: Pressure effects in unconventional superconductors studied by muon spin rotation
4th Intl. Conf. on Superconductivity and Magnetism (ICSM 2014), Antalya, Turkey, April 27 - May 2, 2014.
- H. Keller: Tuning the structural and magnetic phase transitions of EuTiO_3 by Sr doping
4th Intl. Conf. on Superconductivity and Magnetism (ICSM 2014), Antalya, Turkey, April 27 - May 2, 2014.
- H. Keller: 30 years of μSR - looking back to the future
 $\mu\text{SR}2014$, Grindelwald, Switzerland, June 1-6, 2014.
- H. Keller: Pressure effects in unconventional superconductors studied by muon spin rotation
Intl. Conf. on Magnetic Resonance: Fundamental Research and Pioneering Applications (MR70), Kazan, Russia, June 23 -27, 2014.
- Z. Guguchia: Negative oxygen isotope effect on the static spin-stripe order in $\text{La}_{2-x}\text{Ba}_x\text{CuO}_4$ ($x = 1/8$)
6th Georgian-German School and Workshop in Basic Science, Tbilisi, Georgia, July 7-12, 2014.
- Z. Guguchia: Muon spin rotation studies of spin fluctuations in the paramagnetic phase of EuTiO_3
Condensed Matter in Paris, Paris, August 24-29, 2014.
- Z. Guguchia: Hydrostatic pressure and oxygen isotope effects on the static spin-stripe order and superconductivity in $\text{La}_{2-x}\text{Ba}_x\text{CuO}_4$ ($x = 1/8$)
Max Planck Institute for Solid State Research, Stuttgart, Germany, February 25-26, 2015.

19.2.2 Phase transitions and superconducting photon detectors

Articles

- Superconductivity in rubidium-substituted $\text{Ba}_{1-x}\text{Rb}_x\text{Ti}_2\text{Sb}_2\text{O}$
F. von Rohr, R. Nesper, and A. Schilling, *Phys. Rev. B* **89** (2014) 094505.
- Low-temperature magnetic fluctuations in the Kondo insulator SmB_6
P.K. Biswas, Z. Salman, T. Neupert, E. Morenzoni, E. Pomjakushina, F. von Rohr, K. Conder, G. Balakrishnan, M. Ciomaga-Hatnean, M.R. Lees, D. McK. Paul, A. Schilling, C. Baines, H. Luetkens, R. Khasanov, and A. Amato, *Phys. Rev. B* **89** (2014) 161107(R).
- Superconductivity and correlated Fermi liquid behavior in noncentrosymmetric $\text{Ca}_3\text{Ir}_4\text{Ge}_4$
F. von Rohr, H. Luo, N. Ni, M. Wörle, and R.J. Cava, *Phys. Rev. B* **89** (2014) 224504.
- Influence of disorder on the structural phase transition and magnetic interactions in $\text{Ba}_{3-x}\text{Sr}_x\text{Cr}_2\text{O}_8$
H. Grundmann, A. Schilling, M. Medarde, D. Sheptyakov, *Phys. Rev. B* **90** (2014) 075101.
- Monodisperse colloidal gallium nanoparticles: Synthesis, low temperature crystallization and surface plasmon resonance
M. Yarema, M. Wörle, M.D. Rossell, R. Erni, R. Caputo, L. Protesescu, D.N. Dirin, K. Lienau, F. von Rohr, A. Schilling, M. Nachtegaal, and M. V. Kovalenko, *J. Am. Chem. Soc.* **136** (2014) 12422.
- Effect of pressure driven local structural rearrangement on the superconducting properties of $\text{FeSe}_{0.5}\text{Te}_{0.5}$
M. Bendele, Z. Guguchia, F. von Rohr, T. Irifune, T. Shinmei, I. Kantor, S. Pascarelli, B. Joseph, and C. Marini, *Phys. Rev. B* **90** (2014) 174505.

PhD-Theses

- Superconductivity in the Vicinity of Structural and Electronic Phase Boundaries
Fabian von Rohr, PhD Thesis, Physik-Institut, Universität Zürich, 2014.
- Tuning the Bose-Einstein Condensation in Spin Dimer Quantum Magnets
Henrik Grundmann, PhD Thesis, Physik-Institut, Universität Zürich, 2014.

Contributed Conference Presentations

- H. Grundmann: Structure and magnetic interactions in $\text{Ba}_{3-x}\text{Sr}_x\text{Cr}_2\text{O}_8$
European Conference Physics of Magnetism, Poznań (Poland), 25.06.2014.
- H. Grundmann: Structure and magnetic interactions in $\text{Ba}_{3-x}\text{Sr}_x\text{Cr}_2\text{O}_8$ (Poster)
Swiss Physical Society Annual Meeting, Fribourg (Switzerland), 30.6.2014.
- X. Zhang: Superconducting and normal state properties of a-WSi films (Poster)
Swiss Physical Society Annual Meeting, Fribourg (Switzerland), 30.6.2014.
- F. von Rohr: Superconductivity and charge-density-wave ordering in $\text{BaTi}_2\text{Sb}_2\text{O}$ (Poster)
Gordon Research Conference in Solid State Chemistry, New London (NH, USA) 1.8.2014.
- A. Gazizulina: Structure and magnetic interactions in $\text{Ba}_{3-x}\text{Sr}_x\text{Cr}_2\text{O}_8$
DPG Spring Meeting 2015, Berlin (Germany), 16.03.2016.
- F. von Rohr: How to find new noncentrosymmetric superconductors by the example of $\text{Ca}_3\text{Ir}_4\text{Ge}_4$ (Poster)
Chemistry meets Physics Meeting, Ringberg (Germany), 18.3.2015.

Invited Lectures

- F. von Rohr: How to find new superconductors
Solid State Chemistry Seminar, Ludwig-Maximilians-Universität München (Germany), 29.4.2014.
- F. von Rohr: New Materials for superconductors and topological insulators
Solid State Physics Seminar, Max Planck Institut für Festkörperforschung in Stuttgart (Germany), 1.7.2014.
- A. Engel: Simple numerical model gives deep insights into the detection mechanism in SNSPD
Applied Superconductivity Conference, Charlotte (NC, USA), 13.8.2014.
- F. von Rohr: Superconductivity in the vicinity of structural and electronic phase boundaries
Materials Theory Seminar, ETH Zürich (Switzerland), 31.10.2014.
- A. Engel: X-ray sensitive superconducting nanowire single-photon detectors: development and perspectives
Joint Instrumentation Seminar at DESY, Hamburg University and XFEL, Hamburg (Germany), 28.11.2014.
- H. Grundmann: Tuning the Bose-Einstein Condensation of Triplons
Helmholtz-Zentrum für Materialien und Energie, Berlin (Germany), 20.3.2015.

106

19.2.3 Surface Physics

Articles

- Surface Aligned Magnetic Moments and Hysteresis of an Endohedral Single-Molecule Magnet on a Metal
R. Westerström, A.-C. Uldry, R. Stania, F. Dreiser, C. Piamonteze, M. Muntwiler, F. Matsui, S. Rusponi, H. Brune, S. Yang, A. Popov, B. Büchner, B. Delley, and T. Greber, *Phys. Rev. Lett.* 114, 087201 (2015).
- Response of the topological surface state to surface disorder in TlBiSe_2
F. Pielmeier, G. Landolt, B. Slomski, S. Muff, J. Berwanger, A. Eich, A. A. Khajetoorians, J. Wiebe, Z. S. Aliev, M. B. Babanly, R. Wiesendanger, J. Osterwalder, E. V. Chulkov, F. J. Giessibl, and J. H. Dil, *New J. Phys.* 17, 023067 (2015).
- Direct measurement of the bulk spin structure of noncentrosymmetric BiTeCl
G. Landolt, S. V. Ereemeev, O. E. Tereshchenko, S. Muff, K. A. Kokh, J. Osterwalder, E. V. Chulkov, and J. H. Dil, *Phys. Rev. B* 91, 081201(R) (2015).
- Ar implantation beneath graphene on $\text{Ru}(0001)$: Nanotents and "can-opener" effect
H. Cun, M. Iannuzzi, A. Hemmi, J. Osterwalder, and T. Greber, *Surf. Sci.* 634, 95 (2015).

- Rashba-type spin splitting and spin interference of the Cu(111) surface state at room temperature
J. H. Dil, F. Meier, and J. Osterwalder, *J. Electr. Spec. and Rel. Phen.* (2015).
- The Metallofullerene Field-Induced Single-Ion Magnet HoSc₂N@C₈₀
J. Dreiser, R. Westerström, Y. Zhang, A. A. Popov, L. Dunsch, K. Krämer, S.-X. Liu, S. Decurtins, and T. Greber, *Chem. Eur. J.* 20, 13536 (2014).
- Acquisition of photoelectron diffraction patterns with a two-dimensional wide-angle electron analyzer
M. Greif, L. Castiglioni, D. Becker-Koch, J. Osterwalder, and M. Hengsberger, *J. Electr. Spec. and Rel. Phen.* 197, 30 (2014).
- X-ray induced demagnetization of single-molecule magnets
J. Dreiser, R. Westerström, C. Piamonteze, F. Nolting, S. Rusponi, H. Brune, S. Yang, A. Popov, L. Dunsch, and T. Greber, *Appl. Phys. Lett.* 105, 032411 (2014).
- Cluster-size dependent internal dynamics and magnetic anisotropy of Ho ions in HoM₂N@C₈₀ and Ho₂MN@C₈₀ families (M = Sc, Lu, Y)
Y. Zhang, D. Krylov, S. Schiemenz, M. Rosenkranz, R. Westerström, J. Dreiser, T. Greber, B. Büchner, and A. Popov, *Nanoscale*, 6, 11431 (2014).
- Two-Nanometer Voids in Single-Layer Hexagonal Boron Nitride: Formation via the "Can-Opener" Effect and Annihilation by Self-Healing
H. Cun, M. Iannuzzi, A. Hemmi, J. Osterwalder, and T. Greber, *ACS Nano*, 8, 7423 (2014).

PhD theses

- Electronic Properties of Atomically Precise Graphene Nanoribbons
Hajo Söde, PhD Thesis, EMPA and Physik-Institut, Universität Zürich, 2015.
- Time-resolved Photoelectron Diffraction
Michael Greif, PhD Thesis, Physik-Institut, Universität Zürich, 2015.
- Large Scale Single Layer Hexagonal Boron Nitride Growth, Process Control and Application
Adrian Hemmi, PhD Thesis, Physik-Institut, Universität Zürich, 2014.
- Spin- and Angle-Resolved Photoelectron Spectroscopy on Topological Insulators and Bulk Rashba Systems
Gabriel Landolt, PhD Thesis, Physik-Institut, Universität Zürich, 2014.

Contributed conference presentations

- Time-resolved photoelectron diffraction from solids
M. Hengsberger, Workshop on ultrafast dynamical imaging of Matter (UDIM), Grindelwald, 11.3.15.
- Magnets inside C₈₀
T. Greber, 30th Workshop on High T_c, Obertraun, Austria, 13.2.15.
- Ion implantation beneath a corrugated monolayer of boron nitride: Nanotents, "can-opener" effect and self-healing
H. Cun, SAOG meeting 2015, Fribourg, 23.1.15.
- Ion implantation beneath a corrugated monolayer of boron nitride: Nanotents, "can-opener" effect and self-healing
H. Cun, International Symposium on Surface Science (ISSS 7), Matsue, Japan, 3.11.14.
- Adsorption study of porphyrin molecules on a Au(111) surface
G. Mette, Summerschool, Les Diablerets, 10.9.14.
- Photoelectron Diffraction in the x-ray and ultraviolet regime: Towards real-time measurements of structural dynamics
M. Greif, European Conference on Surface Science (ECOSS 30), Antalya, Turkey, 2.9.14.
- Origin of attosecond delays in photoemission from noble metal surfaces
L. Castiglioni, European Conference on Surface Science (ECOSS 30), Antalya, Turkey, 2.9.14.

- Attosecond dynamics of photoelectric effect in surfaces
M. Hengsberger, European Conference on Surface Science (ECOSS 30), Antalya, Turkey, 1.9.14.
- Adsorption study of a new polypyridine macrocycle on Au(111)
G. Mette, European Conference on Surface Science (ECOSS 30), Antalya, Turkey, 1.9.14.
- Attosecond interferometry for the determination of photoemission delays and ultrafast electron dynamics in solids
L. Castiglioni, International Workshop on Photoionization and Resonant Inelastic X-Ray Scattering, Erice, Italy, 27.8.14
- CVD growth and transfer of single-crystalline hexagonal boron nitride monolayers and graphene
J. Osterwalder, Swiss Nanoconvention, Brugg, 21.5.14.
- Ion Implantation beneath a corrugated Single Layer of Boron Nitride: Nanotent Formation and "can-opener" effect
H. Cun, MRS spring meeting, San Francisco, USA, 22.4.14.
- Lateral Segregation in Pt₅₀Rh₅₀(111) induced by a *h*-BN nanomesh
R. Stania, DPG Frühjahrstagung, Dresden, Germany, 2.4.14.

Invited lectures

108

- H. Cun: Nanotents - and controlled 2 nm hole formation in monolayers of hexagonal boron nitride and graphene
Seminar Institute of Electronic Materials Technology (ITME), Warsaw, Poland, 17.2.15
- T. Greber: Spinshuttles
Symposium on Surface and Nanoscience (SSNS'15), Furano, Japan, 15.1.15
- J. Osterwalder: Zweidimensionale Festkörper: Graphen und hexagonales Bornitrid
Physikalische Gesellschaft Zürich, 27.11.14
- T. Greber: Cutting and Assembling 2 Nanometer Voids in Single Layer hexagonal Boron Nitride
American Vacuum Society (AVS) 61st International Symposium and Exhibition, Baltimore, MD, USA, 10.11.14
- J. Osterwalder: Graphene on hexagonal boron nitride heterostacks grown by UHV-CVD on metal surfaces
American Vacuum Society (AVS) 61st International Symposium and Exhibition, Baltimore, MD, USA, 10.11.14
- T. Greber: Looking inside spin-shuttles
SPinMol 2014, Monte Verita, Switzerland, 28.10.14
- T. Greber: Self-assembly of 2 nanometer voids in hexagonal boron nitride on rhodium: Creation and annihilation
73th IUVESTA Workshop, Eisenerz, Austria, 26. 9.14
- H. Cun: Ion implantation beneath a corrugated monolayer of Boron Nitride: Nanotents, "can-opener" effect and self-healing
Seminar EMPA, Dübendorf, Switzerland, 29.8.14
- T. Greber: Steering stiction of a liquid on a surface
International Workshop on Nanomaterials and Nanodevices, Wuhan, China, 4.7.14
- T. Greber: Nanotent and 2 nm void-formation in sp² hybridized single layers on metals
International Workshop on Nanomaterials and Nanodevices, Beijing, China, 1.7.14
- T. Greber: From C₆₀ to Spin-Shuttle-Single-Molecule Magnets on Surfaces
Seminar Peking University, Beijing, China, 30.6.14
- J. Osterwalder: Boron nitride and graphene on single crystal substrates: CVD growth of heterostructures and film transfer
2nd European Workshop on Epitaxial Graphene (EWEG), Primosten, Croatia, 17.6.14
- J. Osterwalder: Functionalization from corrugated hexagonal boron nitride monolayers
Seminar Donostia International Physics Center, San Sebastian, Spain, 16.4.14

19.2.4 Biological systems

Articles

- Low-energy electron holographic imaging of gold nanorods supported by ultraclean graphene
J.-N. Longchamp, C. Escher, T. Latychevskaia, and H.-W. Fink, *Ultramicroscopy* 145 (80-84) (2014).
- On artefact-free reconstruction of low-energy (30-250 eV) electron holograms
T. Latychevskaia, J.-N. Longchamp, C. Escher, and H.-W. Fink, *Ultramicroscopy* 145 (22-27) (2014).
- Holographic time-resolved particle tracking by means of three-dimensional volumetric deconvolution
T. Latychevskaia, and H.-W. Fink, *Opt. Express* 22 (17), pp. 20994-21003 (2014).
- Terahertz in-line digital holography of dragonfly hindwing: amplitude and phase reconstruction at enhanced resolution by extrapolation
L. Rong, T. Latychevskaia, D. Wang, X. Zhou, H. Huang, Z. Li, and Y. Wang,
Opt. Express 22 (14), pp. 17236-17245 (2014).
- Atomically resolved structural determination of graphene and its point defects by employing extrapolation assisted phase retrieval
T. Latychevskaia, and H.-W. Fink, *Applied Physics Letters* 106, pp. 021908 (2015).
- Terahertz in-line digital holography of human hepatocellular carcinoma tissue
L. Rong, T. Latychevskaia, D. Wang, Z. Yu, X. Zhou, C. Chen, H. Huang, Y. Wang, Z. Li, and Z. Zhou,
Scientific Reports 5, 8445 (2015).
- Practical algorithms for simulation and reconstruction of digital in-line holograms
T. Latychevskaia, and H.-W. Fink, Vol. 54, Issue 9, pp. 2424-2434 (2015).
- Reconstruction of purely absorbing, absorbing and phase-shifting, and strong phase-shifting objects from their single-shot in-line holograms
T. Latychevskaia and H.-W. Fink, *Applied Optics* 54, Issue 13, 3925-3932 (2015).

109

Article in press

- Holography and coherent diffraction with low-energy electrons: A route towards structural biology at the single molecule level
T. Latychevskaia, J.-N. Longchamp, C. Escher, and H.-W. Fink, *Ultramicroscopy*.

Contributed Conference Presentations

- M. Lorenzo, J. Verges and H.-W. Fink:
LEEPS microscope and alkali metals adsorption dynamics on freestanding graphene (poster)
Low-energy electrons: Lithography, Imaging, and Soft Matter (LEELIS), Amsterdam, Nov. 4 -5th, 2014.
- F. Wicki, J.-N. Longchamp and H.-W. Fink:
Combining LEEPS microscopy and STM to study Atomically thin freestanding films (poster)
Low-energy electrons: Lithography, Imaging, and Soft Matter (LEELIS), Amsterdam, Nov. 4 -5th, 2014.
- T. Latychevskaia and H.-W. Fink: Coherent imaging beyond detector area and Abbe limit, towards atomic resolution
International Microscopy Congress, Prague (Czech Republic), Sept. 7 -12th, 2014.
- J.-N. Longchamp: Coherent Low-Energy Electron Microscopy of Single Biomolecules
Seminar, June 10th 2014, Stuttgart (Germany)
- J.-N. Longchamp, C. Escher, H.-W. Fink:
Ultraclean freestanding graphene as substrate for electrospray deposition of biomolecules
Graphene Week, Gothenburg (Sweden), June 23-27th 2014.

- H.-W. Fink: Holographie und kohärente Beugung mit langsamen Elektronen: Perspektiven zur Strukturbestimmung eines individuellen Proteins
Physik-Kolloquium, Erlangen, 23. June 2014.
- H.-W. Fink: Holography and Coherent Diffraction with Low Energy Electrons
opening plenary talk, Atom Probe Tomography & Microscopy 2014, Stuttgart (Germany), 1. - 5. Sept. 2014.
- T. Latychevskaia and H.-W. Fink: Coherent imaging beyond detector area and Abbe limit, towards atomic resolution
International Microscopy Congress, Prague (Czech Republic), September 7-12th, 2014.
- H.-W. Fink: Imaging with Coherent Electrons
Quantum-Electron-Microscope Workshop, G. and B. Moore Foundation, Erlangen (Germany), 19./20. Sept. 2014.
- T. Latychevskaia, J.-N. Longchamp, C. Escher and H.-W. Fink: Coherent imaging with ultra-low energy electrons
Sub-Angstrom Low-Voltage Electron Microscopy (SALVE) Symposium, Ulm (Germany), Febr. 2015.
- T. Latychevskaia: Phase retrieval methods applied to coherent imaging
MECMATPLA, Montgenèvre (France), Febr. 2015.

19.2.5 Disordered and Biological Soft Matter

Articles

110

- Studying foam dynamics in levitated, dry and wet foams using diffusing wave spectroscopy
N. Isert, G. Maret, and C.M. Aegerter, *Colloids and Surfaces A*, **473**, 40 (2015).
- Probing Anderson localization using weak non-linear effects
T. Sperling, W. Bührer, M. Ackermann, C.M. Aegerter, and G. Maret, *New Journal of Physics* **16**, 112001 (2014).
- Direct imaging of fluorescent structures behind turbid layers
G. Ghielmetti, and C.M. Aegerter, *Optics Express* **22**, 1981 (2014).
- On growth and form of irregular coiled-shell of a terrestrial snail: *Plectostoma concinnum*
T. Liew, A.C.M. Kok, M. Schilthuizen, and S. Urduy, *PeerJ* **2**, e383 (2014).
- A viscoelastic damage model for polycrystalline ice, inspired by Weibull-distributed fiber bundle models. Part I: Constitutive models
A. Keller and K. Hutter, *Continuum Mechanics and Thermodynamics* **26**, 879 (2014).
- A viscoelastic damage model for polycrystalline ice, inspired by Weibull-distributed fiber bundle models. Part II: Thermodynamics of a rank-4 damage model
A. Keller and K. Hutter, *Continuum Mechanics and Thermodynamics* **26**, 895 (2014).
- Conceptual thoughts on continuum damage mechanics for shallow ice shelves
A. Keller and K. Hutter, *Journal of Glaciology* **60**, 685 (2014).
- Method and apparatus for imaging a structure marked with a fluorescent dye
S. W. Hell, J. Schneider, J. Engelhardt, US Patent Application US2014/0097358 A1, April 2014.

PhD-Thesis

- Microscopy through turbid layers using wave-front shaping
G. Ghielmetti, PhD Thesis, Universität Zürich, 2014

Conference reports

- Applying forces to wing discs
F. Lanfranconi, Workshop "Forces in tissues", Paris, France (May 21 - 25 2014).

- Determination of the transmission matrix through thick turbid samples (poster)
M. Ackermann, T. Sperling, G. Maret, and C.M. Aegerter, Workshop "Waves and Disorder", Cargese, France (June 30 - July 11, 2014).
- The Role of Mechanical Forces in the Regulation of Tissue Growth (poster)
D. Eder, K. Basler and C.M. Aegerter, EMBL Advanced Course: Fluorescence Imaging Techniques, Heidelberg, Germany July 07-11 2014.
- Folding of growing epithelial tissues in a stochastic cell-based model (poster)
S. Urdy , D. Laman-Trip , R. Merks, 2nd international conference on Systems Biology, Lausanne, Switzerland October 20-23 2014.
- Applying forces to wing discs
F. Lanfranconi, SystemsX retreat, Emmetten (March 5 - 6 2015).
- Imaging with a light sheet
J. Schneider, SystemsX retreat, Emmetten (March 5 - 6 2015).
- Magnetic force Microscope
L. Selvaggi, SystemsX retreat, Emmetten (March 5 - 6 2015).
- Finite element modeling of growing tissues
A. Keller, SystemsX retreat, Emmetten (March 5 - 6 2015).
- Folding of growing epithelial tissues in a stochastic cell-based model
S. Urdy, SystemsX retreat, Emmetten (March 5 - 6 2015).
- Finite element modeling of pulsed, contractile forces
F. Atzeni; SystemsX retreat, Emmetten (March 5 - 6 2015).
- MuViSPIM and 4D tissue analysis
D. Dreher, SystemsX retreat, Emmetten (March 5 - 6 2015).

Invited lectures

- C.M. Aegerter: Forces and elastic properties in the wing imaginal disc of *Drosophila*
Workshop "Forces in tissues", Paris, France (23.05.2014).
- C.M. Aegerter: Probing Anderson localization using weak nonlinear effects
Summerschool "Waves and Disorder", Cargese, France (09.07.2014).
- C.M. Aegerter: Musterbildung in Physik, Chemie und Biologie
Weiterbildung für Gymnasiallehrpersonen, University of Zurich (07.11.2014).
- C.M. Aegerter: Physical Biology and Biological Physics
IMLS Seminar, University of Zurich (09.01.2015).
- C.M. Aegerter: Physik der ungeordneten Systeme ausserhalb des Gleichgewichts
MNG Rämibühl, Zurich (02.02.2015).
- C.M. Aegerter: Mechanical regulation of growth in the *Drosophila* wing disc
Forces at cell junctions workshop, Göttingen (11.02.2015).
- C.M. Aegerter: Measuring and modelling forces in tissues
SystemsX retreat, Emmetten (05.03.2015).
- A. Keller: Deterioration and failure of glacier ice - a damage mechanics approach to glacier calving
IMLS Seminar, University of Zurich (12.09.2014).
- J. Schneider: Ultrafast STED nanoscopy
IMLS Seminar, University of Zurich (06.10.2014).

19.3 Bachelor and Master Theses

19.3.1 Bachelor theses

- Development of a fault tolerant CAN bus interface based on the Raspberry Pi single board computer
Timothy Dominik Widmer
- Measurement of W production cross section in proton-lead collisions
Chris Marentini
- Kinetic energy spectra of Ar, Ne and He ions
Annina Spescha
- RABBITT on Cu(111) at different points in the Brillouin zone
David Becker-Koch
- μ SR investigation of the high-temperature superconductor $(Cu_{0.75}Mo_{0.25})Sr_2(Y)Cu_2O_{7+\delta}$
Leonid Leiva Ariosa
- Bau und Test eines HF-Messtandes Temperaturen für kryogene Temperaturen
Andreas Meier
- Tuning the Critical Field of the Bose-Einstein Condensation in $Ba_{3x}Sr_xCr_2O_8$
Philippe Hasler
- Untersuchung amorpher supraleitender Filme unterschiedlicher Dicke
Julia Lonsky
- 112 - Kalibrierung und Weiterentwicklung eines Teststandes zur Charakterisierung von supraleitenden Photonenzählern
Stefan Holenstein
- SandBox: A Facility for XENON Photosensors Characterization and Measurements of Photocathode Uniformity
Sandro D'Amato

19.3.2 Master theses

- The linear memory effect in gravitational waves
Yannick Bötzel
- Measurement of the $Z\gamma$ production cross section at $\sqrt{s} = 8$ TeV at the LHCb experiment
Moritz Küng
- A dedicated boosted Higgs boson tagging algorithm in CMS
Thea Årestad
- In situ Ion Implantation beneath Boron Nitride Nanomesh
Rubina Arulanantham
- First steps towards Graphene Nanoribbon device application
Beat Lauber
- Sauberes Graphen durch katalytische Zersetzung von PMMA
Simon Bachmann
- Characterization and Calibration of a Liquid Xenon Time-Projection Chamber
Hrvoje Dujmović